A Multi-instrument Study of Magnetic Reconnection and Substorm Events

Pia Christiane Hauger Garaas

Thesis submitted for the degree
Master of Science

UNIVERSITY OF OSLO

March 2010

Abstract

Magnetic reconnection is a plasma process where magnetic energy is converted into kinetic particle energy in the Earth's magnetosphere and causes topological changes in the magnetic field. Certain solar wind conditions can cause magnetic reconnection to occur in different regions of the magnetopause and some of these solar wind configurations can cause substorms to develop. A substorm can be described as a local process characterized by magnetic and auroral activity in the ionosphere. Several theories explaining these phenomena involve magnetic reconnection in the near-Earth magnetotail. A way to investigate a reconnection in the Earth's near magnetotail is to use data from the Cluster satellites.

In this study we investigate the signatures of a collisionless magnetic reconnection based on observations by the Cluster satellites. We combine Cluster studies with data from the IMAGE satellite and ground based observations of the auroral and geomagnetic activity, including UV images of the auroral zone, magnetometer data, and auroral indices. We show that the signatures of magnetic reconnection temporarily coincide with enhanced auroral activity and variations in the auroral indices. The comparison of data is discussed within the scope of existing substorm models.

2010

A Multi-instrument Study of Magnetic Reconnection and Substorm Events

Pia Christiane Hauger Garaas

http://www.duo.uio.no/

Print: Reprosentralen, University of Oslo

Acknowledgements

First of all I want to thank Anette Lauen Borg, my main supervisor, for guiding me, helping me and supporting my ideas, and for proofreading the thesis. I want to thank her for motivating me during the master period, for inviting me work with her at ESTEC and letting me stay at her place during my visit. Without her help, this thesis would not have been possible. I'm really grateful! I would also thank my internal supervisor Jan A. Holtet for feedback on my thesis and for providing me with a trip to ESTEC and Arne Pedersen for all the help with the EFW data analysis and the comments on my thesis.

I acknowledge the CIS (PI Iannis Dandouras, French/Hellenic) team, the FGM (PI Elizabeth Lucek, UK) team, the EFW (PI Mats André, Sweden) team and the Cluster Active Archive for providing me with Cluster data. I thank Harald Frey at the Space Science Laboratory University of California, Berkeley for preparing the datasets from IMAGE WIC and Professor K. Yumoto, Kyushu University, Japan for providing me with the CPMN-network data. I thank the national institutes that support the magnetic observatories and INTERMAGNET for the geomagnetic field data. I thank the Wold Data Center for Geomagnetism, Kyoto, Japan for providing the data for the AE-index, and I acknowledge the Space Physics Data Facility and National Space Science Data Center at the NASA's Goddard Space Flight Center for providing the OMNI web data.

I am grateful for every person who has spent time on me and my work, who have helped me with analyse of my datasets and commented on my thesis. A special thanks to my father Stein, my father-in-law Erik and Ervin Thorn for all the precious advices and helpful feedback on my written English.

I would like to thank Knut Stanley Jacobsen for helping me with my problems in MATLAB and for answering all possible questions I may have had regarding my thesis, Espen Trondsen for helping me with my computer programs and for providing me with a laptop and Bjørn Lybekk for providing among other things the expert knowledge on travel expense records.

I would like to thank all my good friends for nice coffee breaks, lunches, talks and quality time, and for most of all, just being there for me when I have needed it. I would also thank my sister Tina, my mother Elsi and my father Stein for being the best family, for believing in me and encourage me to make my own choices, and always been supportive.

At last, but not least, I would like to thank my lovely husband Sjur, for all the support, for the MS Office help, for providing me dinner at my office, for picking me up late at night from school and most of all for just having an enormous faith in me.

Pia Christiane Hauger Garaas

Oslo, March 2010

Table of contents

¡Vamos a flipando tío!

1 Introduction

On a clear sky at night we can sometimes see the dancing northern lights which may be a consequence of an eruption on the Sun. Such solar eruptions do not only create the northern lights, but can also have damaging consequences too. Endangering astronauts and satellites, damaging communications, navigation systems, power supplies and computers are effects caused by eruptions on the Sun.

In the Oxford Dictionary of Astronomy, space weather is used as a description of the conditions in the near-Earth space environment [*Ridpath*, 2007]. By studying the processes in the near-Earth space environment, it might in the future be possible to predict the space weather and take necessary precautions in order to prevent or reduce damages caused by solar eruptions.

Our knowledge of space physics has grown rapidly during the last decades. Satellites provide large amounts of datasets from the Earth's space environment containing detailed information about the processes in our magnetosphere, and one of the main topics studied by the Plasma and Space Research group at the University of Oslo is the interaction between the solar wind, the magnetosphere and the ionosphere. The Cluster satellites provide data that makes it possible to study plasma processes in three dimensions (3-D) in the plasma sheet and lobe region of the magnetotail at distances 15 – 20 R_E from the Earth. Data from the Cluster satellites have been collected in a database of observations of the magnetotail by the Oslo group. This database is available through the Cluster Team at the University of Oslo, and the group also has expertise on analysing data from the instruments on the Cluster satellites. The satellite data used in this thesis are selected based upon this expertise of the research group at the University of Oslo.

Much effort has been put into satellite data analysis and there have been some conclusive results. But yet some topics are still debated, and one such topic is how a magnetic substorm is triggered, where it is triggered and how the solar wind influences the triggering process.

1.1 Motivation

A substorm is a very complex process and there exist many substorm models explaining how a substorm is triggered. The models can be classified into two categories which contain the main ideas. The two main models of substorm trigger theories provide different timing signa-

tures for observation of signatures in the magnetotail, in the ionosphere and in ground based measurements. In the Near-Earth Neutral Line (NENL) model a magnetic reconnection initiates the substorm, hence the reconnection will occur prior to the substorm signatures. In the Near-Earth Current Disruption (NECD) the substorm can be initiated by a number of plasma instabilities in the near-Earth region. The disturbed region propagates tailward where magnetic reconnection is initiated. In the NECD model the substorm signatures occur prior to the magnetic reconnection. Since the two scenarios suggest different sequence of the signatures, studies regarding a precise determination of the timing are important.

Motivated by the large amount of available data from satellites in the International Solar Terrestrial Physics (ISTP) program and ground based measurements, we establish the timing between magnetic reconnection signatures in data observed by the Cluster satellites and substorm signatures.

Using two already identified magnetic reconnection events, we investigate the signatures regarding reconnection (fast plasma jets, simultaneous change in the vertical component and the quadrupole Hall magnetic field), and we study the context of the process by including a study of the ambient of the Cluster satellites and determine a rough location of the spacecraft with respect to the reconnection region. Based on the timing from the reconnection signatures we use IMAGE WIC data in order to establish the onset of an auroral substorm observed in the ionosphere. We then search for substorm signatures in regions on the ground. Such signatures include development of magnetic bays, Pi 2 pulsations and an investigation of the AE-index. We proceed by doing a timing analysis of the signatures of magnetic reconnection and substorm. Finally we discuss our findings and compare the two events, and we also investigate the large and small scale context prior to and after the two reconnection events including the solar wind conditions prior to the events. In order to perform such an analysis, a large amount of data have been collected, studied and even discarded.

The reconnection event on the 26th September 2005 was identified by *Sergeev et al.* [2007] and studied in some detail by *Sergeev et al.* [2008]. The event on 22nd August 2001 has been studied by *Borg* [2006], where the event was one of a list of thirteen magnetic reconnection events. The 2001 event has also been partly investigated by *Østgaard et al.* [2009] who investigated whether the particles accelerated in the magnetic reconnection region could have produced the observed aurora in the ionosphere. The event has also been studied by *Louarn et al.* [2004] who investigated the low frequency fluctuations observed in the plasma sheet by the Cluster satellites, and by *Volwerk et al.* [2003] who investigated a kink mode

oscillation of the neutral sheet during the time interval. Some of the results from these papers are used in this thesis to support our findings.

1.2 Structure of the thesis

The chapters in the thesis are structured as follows:
In chapter 2 a brief introduction to space physics and the relevant regions in space is given. The main focus of this chapter is the processes leading to magnetic reconnection and substorms, and the identification of the signatures that may be observed by satellite and ground based observations. In chapter 3 we give a presentation of the satellites and the instruments used. In chapter 4 the methods used when presenting and analysing the datasets from the satellites and instruments presented in chapter 3 are introduced. In chapter 5 the datasets from the 26th September 2005 and 22nd August 2001 are presented and analysed. The presentation starts with Cluster data, then proceeds with IMAGE data and is completed with data from the ground instruments. At the end of each event analysis, the timing of the signatures is investigated. A summary and a discussion of the results are presented in chapter 6 and the events are seen in context with the geomagnetic activity the current day. The solar wind conditions prior to the events are also discussed.

2 Background

2.1 Space weather – interaction between the solar wind and the near-Earth space environment

The Sun emits the solar wind, which is a thin hot ionised gas that carries particles and magnetic fields outward from the Sun. The particles in the solar wind are mainly ionised hydrogen and electrons in nearly equal numbers, which makes it neutral on average. The magnetic fields in the solar wind originate at the Sun and are called the Interplanetary Magnetic Field (IMF). The solar wind can best be described as a fluid consisting of freely moving charged particles. This thin hot ionised fluid is called plasma fluid [*Gurnett and Bhattacharjee*, 2005].

Observations of the solar wind at the Earth's distance from the Sun were first made in the mid-1960s. These observations indicated a density in the solar wind with a typical value of ~ 7 particles pr. cm^{-3}, a temperature of $\sim 10^5$ K and a velocity of $\sim 4 * 10^2$ km/s [*Kivelson and Russell*, 1997].

The Earth's magnetic field, located inside of the purple line in Figure 2-1, forms an effective shield against the solar wind, protecting the Earth's environment. The magnetic field forms a magnetospheric cavity, which is stretched outwards in the direction away from the Sun [*Chapman and Ferraro*, 1930]. This magnetospheric cavity also referred to as the magnetosphere (described in further details in chapter 2.2), consists of a magnetic field and plasma. The magnetosphere forms equilibrium with the solar wind, causing the magnetosphere to change with the changing conditions in the solar wind. This makes the magnetospheric cavity a dynamic system.

Because the solar wind contains magnetic fields, an interaction between the IMF and the Earth's dipolar magnetic field will occur when the solar wind hits the Earth's magnetic field lines. Figure 2-1 gives an illustrated example of the interaction between the Sun and the Earth. The solar wind is constantly streaming out in radial directions from the Sun, interacting with the Earth's magnetic field and causing changes in the near-Earth space environment. During the interaction between the IMF and the Earth's geomagnetic field, the particles in the solar wind are transported from the interplanetary space into the magnetosphere. This magnetic interaction takes place at the boundary of the magnetosphere, called the magnetopause, shown by the purple line in Figure 2-1. Depending on the internal structure of the IMF, the interaction process can occur in different locations at the magnetopause [*Sonnerup et al.*, 1981]. The magnetic field interaction between the IMF and the Earth's magnetic field in the

magnetosphere may play a part in the generation of magnetic storms, which are sudden changes in the near-Earth space environment. The magnetic interaction processes are elaborated in chapter 2.5 and the storms in chapter 2.6.

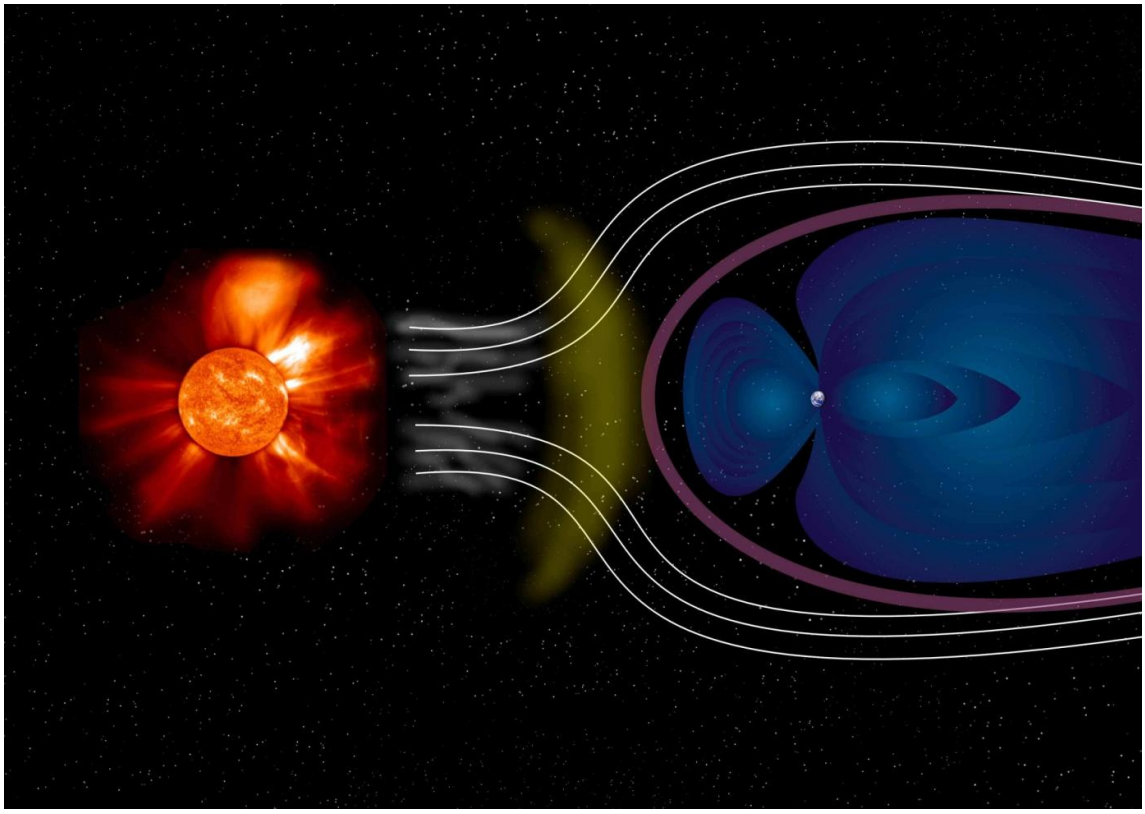

Figure 2-1: An example of an interaction between the Sun and the Earth. An explosion at the Sun sends the solar wind out into space. When the solar wind arrives close to the Earth, its magnetic field can interact with the Earth's magnetic field. Figure from ESA [2004] © ESA.

2.2 Magnetosphere

The Earth's magnetosphere, illustrated by the blue lines in Figure 2-1, is the region containing the Earth's magnetic field lines. The Earth's magnetosphere consists of different regions, all containing plasma and magnetic field lines. The magnetosphere covers a huge area in space compared to the size of the Earth itself. The stand-off distance, which is the distance from the Earth to the point where the magnetopause is closest to the sun, is normally located in the range of 11 – 12 Earth radii (R_E). 1 R_E is the mean value of the radius of the Earth at the equator and has a length of 6378 km. The magnetotail, where the magnetic field lines of the Earth are dragged out on the night side of the Earth due to the solar wind pressure, can be more than 200 R_E long [*Campell*, 2003].

The Earth's magnetic field can be described as a dipole field up to a distance of approximately 2 R_E, see Figure 2-2. The blue lines represent magnetic field lines and the arrows indicate the orientation of the field. The magnetic field strength is strongest at the poles and decreases rapidly with increasing distance from the Earth [*Kivelson and Russell*, 1997].

The Earth's magnetic field is mainly produced by the Earth's core, but the currents flowing in the Earth's magnetosphere contribute to the total field as well. Changes in the magnetospheric currents will affect the Earth's magnetic field configuration and give rise to processes as magnetospheric storms and substorms. These currents and the processes will be described in further detail later in this section.

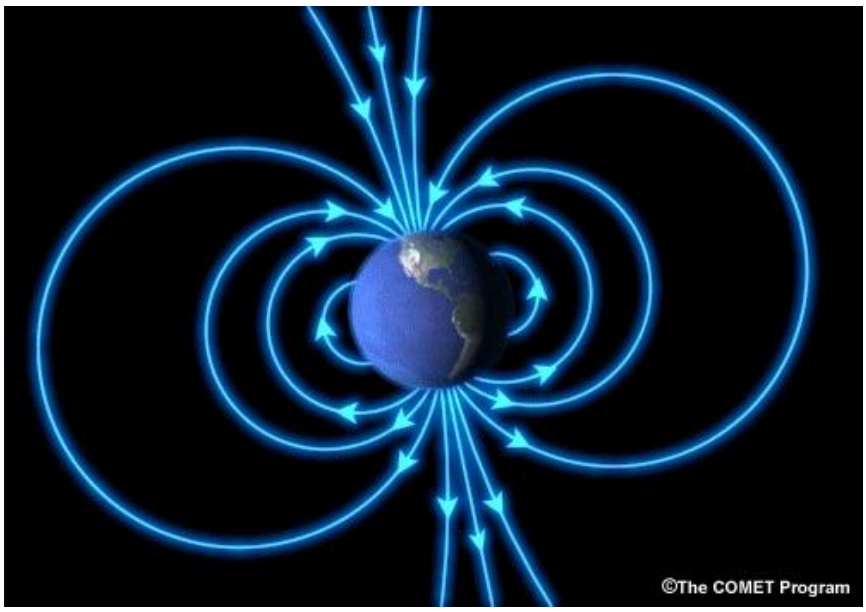

Figure 2-2: An illustration of the Earth's magnetic dipole field close to Earth. The blue lines illustrate the magnetic field lines and the arrows show the direction of the field. Figure from *WU Team* [2008] © The Regents of the University of Michigan.

Outside the dipole region of the Earth's magnetic field the topology of the magnetic field changes dramatically. The magnetosphere is a dynamic system with different regions. Each region consists of a composition of different plasma populations and magnetic field lines with different orientation. The magnetic field lines in the magnetotail outside the dipole region are directed early parallel to the Earth-Sun line. The magnetic field lines are directed towards the sun in the northern hemisphere and away from the sun in the southern hemisphere, see Figure 2-3. The magnetosphere is separated from the solar wind by the magnetopause, and at a distance of 30 R_E into the magnetotail the magnetosphere has a diameter of approximately 40 R_E [*Ness*, 1965] in the yz plane in Figure 2-3.

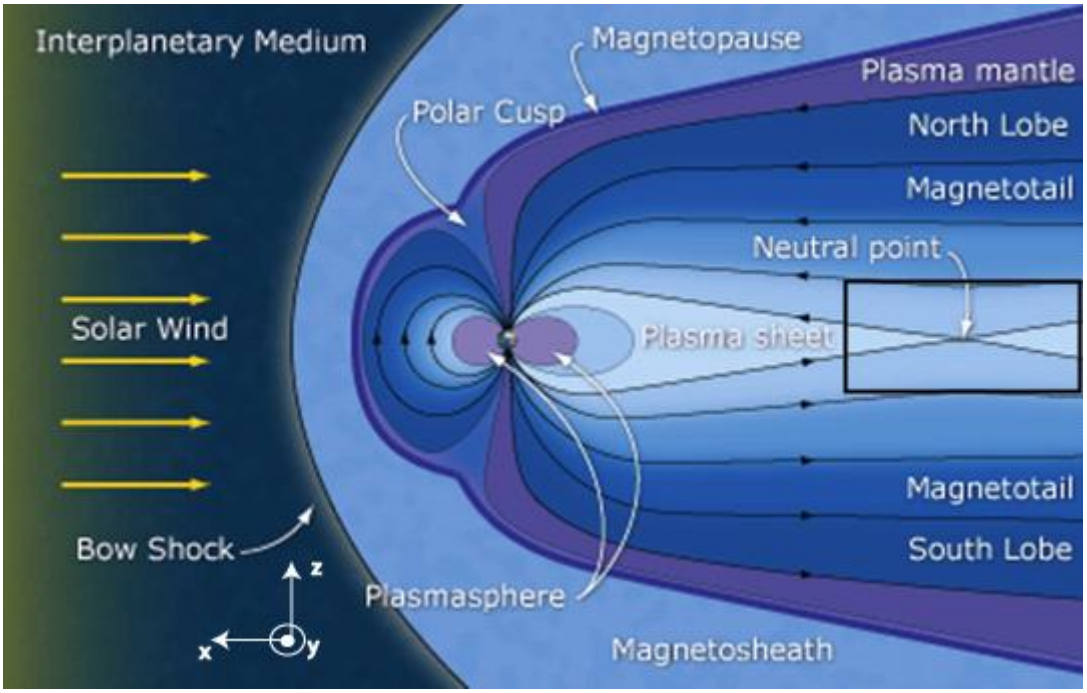

Figure 2-3: The different regions in the Earth's magnetosphere. In this thesis the region of interest is marked with the black square. Figure from *ESA* [2007a] © ESA.

In this thesis the main focus is on the night side of the Earth: The magnetotail region marked with a square in Figure 2-3. Within the square, only the neutral point and the plasma sheet are included, but disturbances within the magnetotail may cause the lobe regions to enter the square as well. In the tail lobes, the magnetic field lines are generally connected to the solar wind at one end, and to the Earth at the other end. They are referred to as open field lines, and are divided into the northern and southern lobe in Figure 2-3. The magnetic field orientation in the northern hemisphere is opposite that of the southern hemisphere. The magnetic field strength here is on average ~ 20 nT [*Kivelson and Russell*, 1997]. The density is small, $n < 3 * 10^{-2}$ particles pr cm^{-3}, compared to the denser region located between the lobes. This region is the plasma sheet, which has a density of $\sim 3 * 10^{-1}$ particles pr. cm^{-3} [*Kivelson and Russell*, 1997].

As illustrated in Figure 2-3, the plasma sheet is located in the centre of the magnetotail where it separates the lobes and stretches out horizontally from the Earth and outward in the magnetotail. The magnetic field lines in the plasma sheet are closed but stretched out tailwards. The plasma sheet can be divided into a boundary region, called the plasma sheet boundary layer, a central layer, referred to as the central plasma sheet, and a current sheet. The plasma sheet boundary layer is generally a transition zone between the dense plasma sheet and the "empty" lobes. The current sheet is embedded within the plasma sheet and is directed along the horizontal plasma sheet midplane between the stretched magnetic field

lines of opposite polarity. The current sheet is also referred to as the neutral sheet. In one dimension (1D) this would be as if the magnetic field vanishes along a line in the x direction. The current which flows in the neutral sheet is called The Neutral Sheet Current flows [*Kivelson and Russell*, 1997] (see Figure 2-4).

2.2.1 The magnetospheric currents

The magnetosphere contains a complex current system. The Chapman-Ferraro current [*Chapman and Ferraro*, 1930] flows along the magnetopause and is therefore called the Magnetopause Current, see Figure 2-4. The Neutral Sheet Current, flowing across the centre of the tail from east to west, forms a closed loop with the eastward flowing Tail Current.

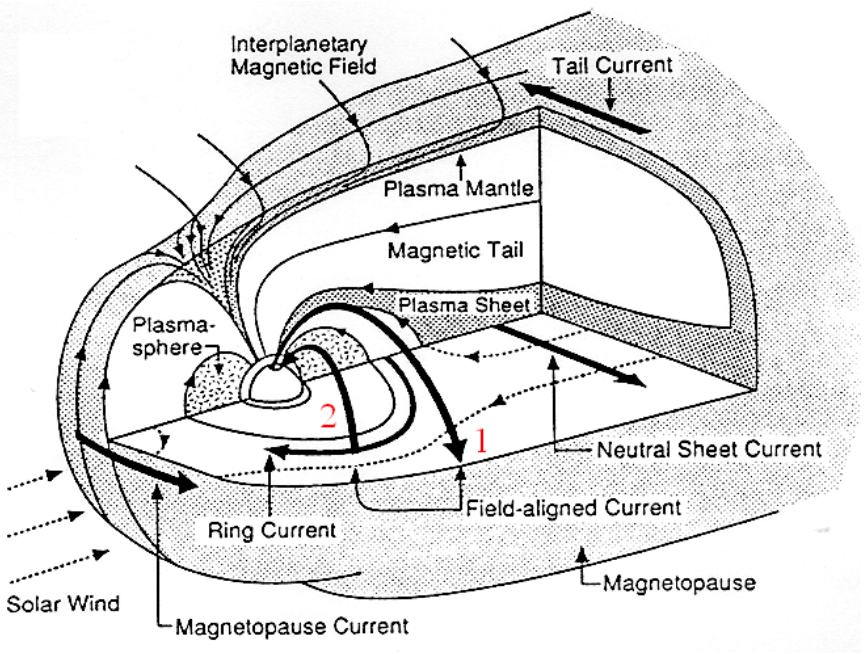

Figure 2-4: A sketch of the different current systems in the magnetosphere: The Magnetopause Current, the Ring Current, the Neutral Sheet (cross-tail) Current and the Field Aligned Currents. The region 1 FAC is marked with the number 1, and the region 2 FAC is marked with the number 2. Figure modified from *Russell et al.* [1995].

Closer to Earth there is a westward flowing Ring Current. This current is caused by a population of charged particles which is confined to the inner part of the magnetosphere. The drift of those charged particles cause an electric current, the ring current [*Prölss*, 2003]. This current is connected to the Tail Current and to the Magnetopause Current by currents flowing along the magnetic field lines in and out of the ionosphere. (The ionosphere is the ionised upper part of the Earth's atmosphere, and is described in further detail in section 2.3). The currents flowing along magnetic field lines are referred to as Field Aligned Currents (FACs)

or Birkeland Currents [*Cummings and Dessler*, 1967] and are separated into region 1 and region 2 FACs, marked with the numbers in Figure 2-4. The region 1 FACs connect the Magnetopause Current with the ionosphere while the region 2 FACs connect the Ring Current with the ionosphere. In the ionosphere the FACs are connected with the ionospheric currents.

The FACs are the electrodynamic elements which couple the ionosphere with the magnetosphere on a large scale. The FACs are primarily carried by electrons, but during disturbed conditions the current density becomes too large to be carried by thermal particles. This gives rise to an electric field parallel to the magnetic field in order to maintain the current continuity [*Paschmann et al.*, 2002].

2.3 Ionosphere

The ionosphere is the ionised part of the Earth's upper atmosphere. The ionisation at polar latitudes is caused by energetic particles from the magnetosphere and by EUV and X-ray radiation from the sun [*Prölss*, 2003]. From 90 km above the surface of the Earth and into space, the ionosphere contains a quasi-neutral mixture of charged particles, i.e. the amount of positive ions is equal to the amount of negative ions and electrons.

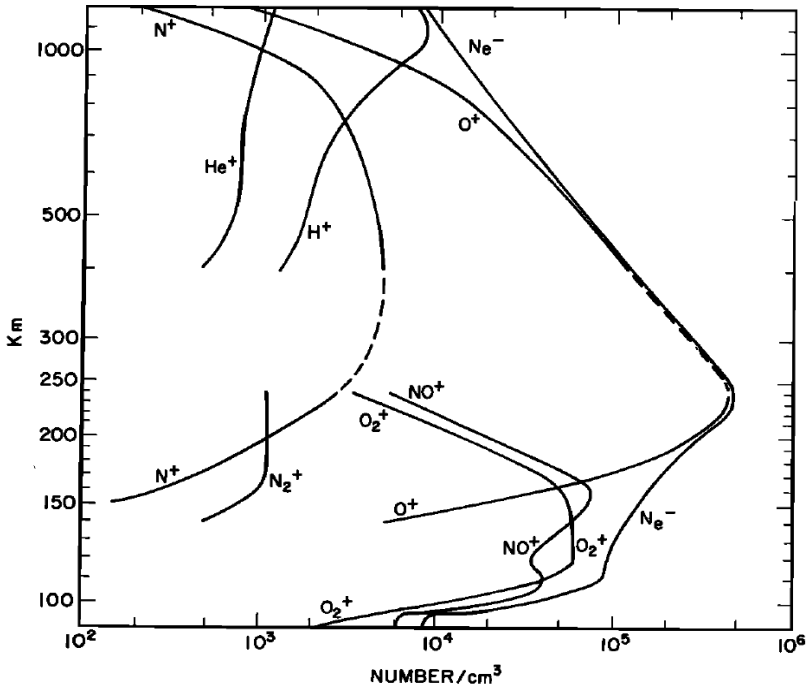

Figure 2-5: The density profile of different ions in the ionosphere in daytime as a function of altitude. The density profile is valid for periods of low solar activity. The dashed part in the N^+ and O^+ lines is due to lack of data in that certain region [*Johnson*, 1966]. Figure from *Johnson* [1966].

In order to divide the ionosphere into separate layers, the D-, E- and F- layers, the electron density distribution has been used. The density profile in the ionosphere changes during the day- and night-time due to variations in radiation and energized particles. Figure 2-5 illustrates the electron density profile in the ionosphere and how the density varies in altitude.

2.3.1 The ionospheric currents

Figure 2-6 illustrates a horizontal cut of polar ionosphere to show the different regions and currents. Along the magnetic field lines the conductivity is high, but there is also conductivity perpendicular to the field which is caused by the interaction between the charged particles from the magnetosphere and the Earth's neutral atmosphere [*Kivelson and Russell*, 1997]. This conductivity allows currents to flow perpendicular to the magnetic field in the ionosphere. The Pedersen current is such a current flowing perpendicular of the electric and magnetic field. The Hall current in the ionosphere flows sunward inside the polar cap and antisunward in the auroral oval. The strength of the currents depends on the conductivity in the ionosphere and the strength of the electric fields. A combination of strong electric fields in the auroral oval and high conductivity will therefore cause strong currents in the oval [*Cowley*, 2000]. These currents are called the auroral electrojets and are illustrated with red arrows in Figure 2-6. The eastward electrojet flows in the dusk part of the oval and the westward electrojet in the dawn side of the oval.

The region 1 FACs are located at a high latitude while the region 2 FACs are located at a lower latitude, see Figure 2-6. In the figure, the FACs flowing out of the ionosphere are indicated with dots and the FACs flowing into the ionosphere are indicated with circled cross. The current pattern is an almost permanent pattern in the magnetosphere-ionosphere system, but the current strength varies with magnetic activity. During quiet times the region 1 current strength is ~ 1.6 MA and for the region 2 it is ~ 1.1 MA [*Paschmann et al.*, 2002]. During disturbed conditions the current increases to ~ 2.7 MA and ~ 2.5 MA respectively. Region 1 FACs are fed by the Pedersen current flowing from dawn to dusk in the polar cap, and from north to south in the auroral zone, as illustrated in Figure 2-6. Region 2 currents close the current system in the auroral zone. The FACs are also referred to as the Birkeland currents.

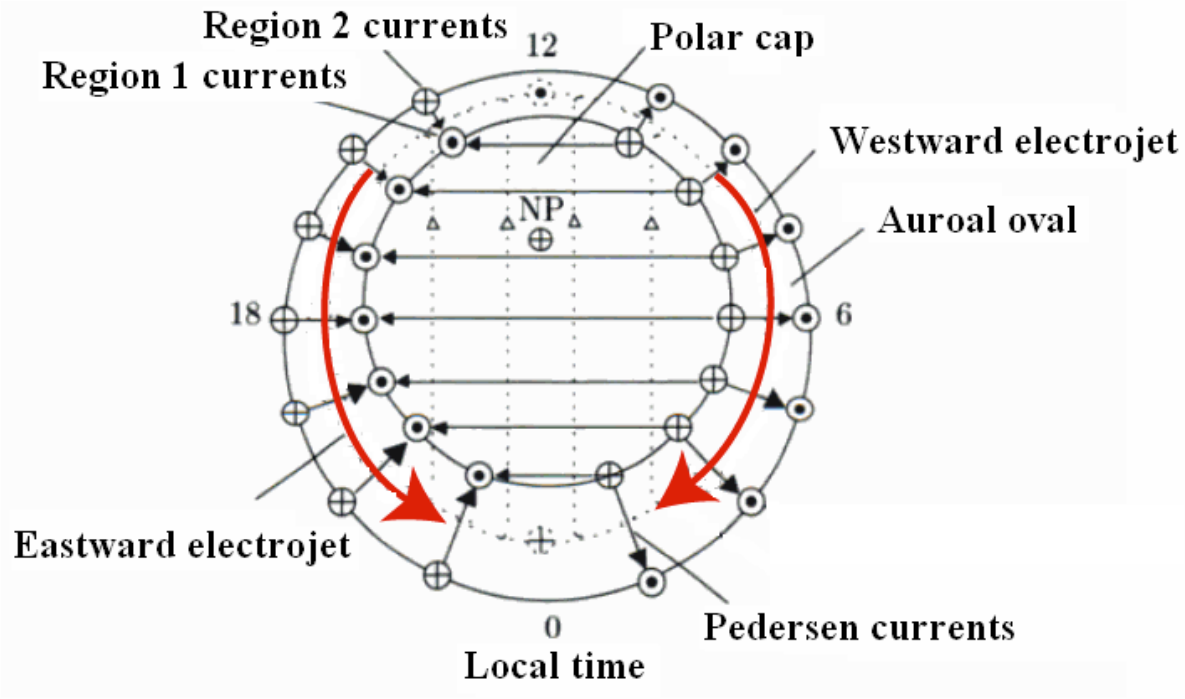

Figure 2-6: The current distribution in the ionosphere. The details about the current systems are described in the text. The red arrows are the auroral electrojets and NP is the geographic North Pole. Figure modified from *Pölss* [2003].

2.3.2 The topology of the polar upper atmosphere and ionospheric footpoints

So far the magnetosphere and ionosphere have been described during steady conditions. The picture changes when extra energy together with increased magnetic flux is deposited into the magnetosphere. Such conditions are referred to as disturbed conditions.

The upper polar ionosphere consists of three distinguished regions: The polar cap, the auroral oval and the subpolar latitudes. The three different regions are characterised by their electric field, current and footpoints. A footpoint is the geographic location of the end of a magnetic field line when followed from space down into the Earth's ionosphere. The auroral oval is the footpoint of the plasma sheet, and around the edges of the oval is the footpoint of the plasma sheet boundary layer. The polar caps are where the footpoints of the tail lobes are located.

The polar cap is the circular area surrounding the magnetic pole with a diameter of ~30° latitude. The auroral oval is an oval at a certain radius from the magnetic pole and it has an extent of a few degrees in latitudinal width. If the location of the oval is plotted in magnetic local time and latitude (MLT) coordinates, it is a circle with the centre located at ~4°

from the magnetic pole. In geographical coordinates, however, it is an oval, hence its name. Details on the MLT coordinates are given in chapter 3. During disturbed conditions in the magnetosphere, the oval expands and shrinks depending on the dynamical processes in the magnetotail. When the aurora changes its characterization, the oval changes as well. Some of these changes will be described further in section 2.6.

Figure 2-7 shows the upper polar ionosphere during a period of enhanced auroral activity. Inside the oval, the polar cap appears as a clear area without any auroral activity.

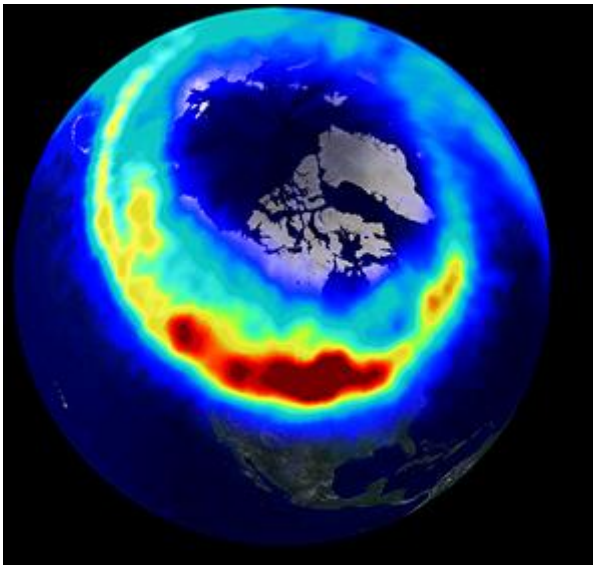

Figure 2-7: An example of the auroral oval in the northern hemisphere. The red area in the picture shows the enhanced particle precipitation. Figure from *Bogdanova* [2006] .

2.3.3 The aurora

The interaction between the molecules in the upper atmosphere and particles from the magnetosphere create the aurora borealis and aurora australis (the northern and southern lights). Energized precipitating particles collide with the atoms and molecules of the Earth's upper atmosphere. Their kinetic energy is converted into energy stored in the chemically excited states of the atmospheric atoms and molecules. The excited states relax and give off photons of wavelengths determined by the processes during the relaxation. The photon emissions are in the UV-, visible- and IR-spectrum. In the visible range the common colours are yellow-green, red, blue-violet and dark red. The emission depends on the composition of the molecules in the atmosphere where the particles interact. The red and yellow-green correspond to the oxygen emissions, the blue-violet to the nitrogen ion emission and the dark red to the nitrogen emission [*Prölss*, 2003]. The most intense aurora appears at the night side of the auroral oval. The red and yellow-green spectra have the most emission rate per volume, and are

also the most common aurora. Figure 2-8 shows the red aurora which is located at a higher altitude than the yellow-green.

The height distribution of the aurora is mainly in the range of 95 – 150 km in altitude for the night aurora, and for the day aurora, the altitude is in the range of 100 – 200 km [*Størmer*, 1955]. The height profile of the aurora depends on the energy distribution of the magnetospheric charged particles.

Figure 2-8: Red and green aurora above Göttingen. Figure from *ESA* [2000] ©Till Credner, AlltheSky.com.

The intensity of the aurora is measured in rayleigh, R, where 1 R corresponds to the emission rate of one million photons per second in an atmospheric column with a cross section of 1 cm^2. Typical intensities during a night with intense auroral activity may reach a level of several hundreds kilorayleighs [*Kivelson and Russell*, 1997].

2.4 Plasma physics

In the Oxford dictionary of astronomy, plasma is defined as

"a state of matter consisting of ions and electrons moving freely….. External magnetic and electric fields can affect a plasma, and the charged particles themselves can interact magnetically and electrically" [*Ridpath*, 2007].

In order to express some of the dynamics in a fluid consisting of plasma in a context such as a magnetic reconnection, some basic parameters have to be established. A plasma fluid consists of charged particles and is therefore strongly affected by magnetic and electric fields. Small charge separations can give rise to huge currents and forces. The dynamics of a plasma are

described by the magnetohydrodynamic (MHD) model, which is a mathematical model describing the plasma as a fluid.

2.4.1 Single-particle motion

The gyromotion of charged particles is a result of movement in a uniform magnetic field but with no electric field present. The z-axis of the Cartesian coordinate system in which the particles move is given by the magnetic field orientation $\vec{B} = (0, 0, B_z)$. The velocity $\vec{V} = (V_x, V_y, V_z)$ and the electric field $\vec{E} = 0$, see illustration Figure 2-9. The magnetic field exerts a force on the charged particle, the Lorentz force denoted as $\overrightarrow{F_L}$ which is given as

$$\overrightarrow{F_L} = q(\vec{V} \times \vec{B}) \Rightarrow m\frac{d\vec{V}}{dt} = q\vec{V} \times B\overrightarrow{e_z} \tag{2.1}$$

where q is the charge, m is the mass and $\frac{d\vec{V}}{dt}$ is the acceleration of the particle. $\overrightarrow{F_L}$ is directed perpendicular to particle movement and does not accelerate the particle (see Figure 2-9). When differentiating equation (2.1) with respect to time and mutually substituting, gives two solutions

$$\begin{aligned} V_x &= V_0 \sin \omega t \\ V_y &= V_0 \cos \omega t \end{aligned} \tag{2.2}$$

where ω is the gyrofrequency. The motion described by equation (2.2) is a gyromotion where the charged particle gyrates with a constant speed V_0 with the magnetic field at the centre of motion. The gyrofrequency is given by $\omega = \frac{2\pi}{\tau} = \frac{|q|B}{m}$ where $\tau = \frac{2\pi r}{V_\perp} = \frac{2\pi m}{|q|B}$ is the gyroperiod and $V_\perp$ is the velocity of a charged particle moving in a circular path as shown in Figure 2-9. r is the gyroradius and is given by $r = \frac{mu_\perp}{|q|B}$. If an electric field is present, only the field components parallel to the magnetic field will contribute to an acceleration of the particles along the magnetic field.

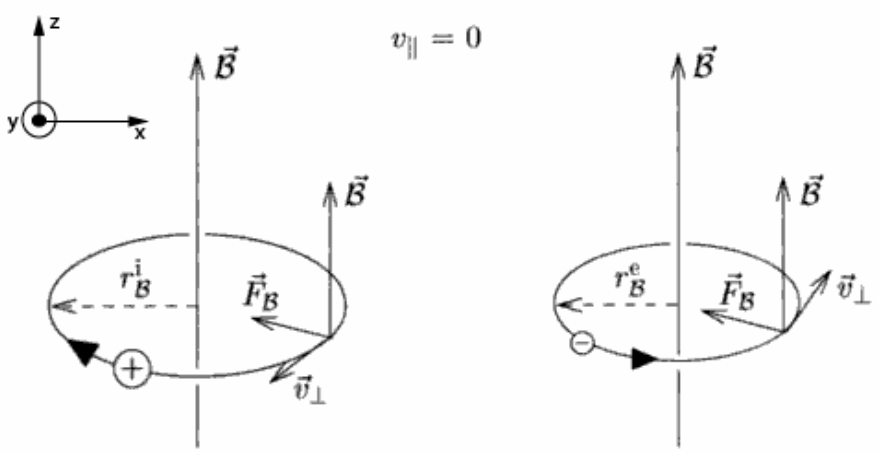

Figure 2-9: The movement of charged particles in a uniform magnetic field. The illustration to the left are for positive ions and the illustration to the left are for negative ions and electrons. Figure from *Prölss* [2003].

2.4.2 A magnetohydrodynamic description of space plasma

The dynamics of an ionised gas in the presence of magnetic and electric fields is described by the MHD model. The MHD-model is a self-consistent fluid description of a neutrally charged ionised gas where the charged ions and electrons move freely, and can be used as a model describing the plasma of the interplanetary medium.

On timescales larger than the gyroperiod of ions and electrons and spatial scales larger than the ion and electron gyroradius, Maxwell's equations can be expressed as

$$\nabla \cdot \vec{E} = \frac{\rho_q}{\epsilon_0} \tag{2.3}$$

$$\frac{\partial \vec{B}}{\partial t} = -\nabla \times \vec{E} \tag{2.4}$$

$$\nabla \times \vec{B} = \mu_0 \vec{J} + \epsilon_0 \mu_0 \frac{\partial \vec{E}}{\partial t} \tag{2.5}$$

$$\nabla \cdot \vec{B} = 0 \tag{2.6}$$

where $\vec{E}$ is the electric field, $\rho_q$is the charge density and ε_0 is the electrical permittivity in vacuum, $8.854 \cdot 10^{-12}\mathrm{F/m}$. $\vec{B}$ is the magnetic field, $\vec{J}$ is the current density and μ_0 is the magnetic permeability in vacuum, $4\pi \cdot 10^{-7}\mathrm{H/m}$. The last term on the right hand side of equation (2.5) is referred to as Maxwell's displacement current. In the MHD-approximation, this term can be neglected, assuming the plasma velocity in vacuum is much less than the speed of light, c. Equation (2.5) then reduces to $\nabla \times \vec{B} = \mu_0 \vec{J}$.

A self consistent set of equations, which describes the fully ionised plasma as a fluid, consists of a continuity equation, a momentum equation, an equation of state for the fluid and

the generalized Ohm's law. It is assumed that the plasma consists of an equal amount of electrons and positive charged ions, $n_e \approx n_i = n$, but that the charges move with different speeds. The continuity equation describing any medium is given as

$$\frac{\partial \rho}{\partial t} + \nabla \cdot (\vec{V}\rho) = 0 \tag{2.7}$$

where ρ is the density of the plasma and $\vec{V}$ is the velocity. In the momentum equation of the fluid, equation (2.8), the viscosity of the fluid is not taken into consideration. Here the $\vec{J}$ is the current density and $\vec{B}$ is the magnetic field, ∇p is the pressure gradient and $\vec{g}$ is the gravitational acceleration

$$\rho\left(\frac{\partial \vec{V}}{\partial t} + \vec{V} \cdot \nabla \vec{V}\right) = -\nabla p + \vec{J} \times \vec{B} + \rho \vec{g} \tag{2.8}$$

The electromagnetic forces in a plasma are significantly larger than the gravitational force experienced by each charged particle experiences. The gravitational force is therefore not taken into consideration in further calculations. Another equation, the equation of state, describes the state of the fluid, whether it is adiabatic, incompressible or described as an ideal gas. The physical conditions in the system determine which equation of state should be applied for the system.

The last equation in the self-consistent equation set is Ohm's law in its general form

$$\vec{E} + \vec{V} \times \vec{B} = \frac{\vec{J}}{\sigma} - \frac{1}{ne}\nabla p_e + \frac{m_e}{ne^2}\left[\frac{\partial \vec{J}}{\partial t} + \nabla \cdot (\vec{J}\vec{V})\right] + \frac{1}{ne}\vec{J} \times \vec{B} \tag{2.9}$$

Equation (2.9) is derived from the momentum equation, equation (2.8), of mixed plasma. m_e is the electron mass, e is the elementary charge and σ is the electrical conductivity of the plasma. Equation (2.9) may be reduced to

$$\vec{E} + \vec{V} \times \vec{B} = \frac{\vec{J}}{\sigma} \tag{2.10}$$

by introducing certain parameter scale lengths. Such parameter length scales represent the spatial scales, at which the processes described by the different terms in (2.9), add contribution to the equation, hence the terms cannot be neglected. The parameter length scale of each term in equation (2.9) has been calculated by *Vasyliunas et al.* [1975]. The results from the calculations are:

- First term on the right side is the resistive term. The characteristic length scale of this term is $\frac{\lambda_\eta V_A}{V}$. λ_η is the diffusion length scale given as $\lambda_\eta = \frac{\eta}{\mu_0 |\vec{V}|}$ where η is the resistivity in the plasma (inverse proportional to the plasma conductivity σ) and $\vec{V}$ is the

plasma velocity. V_A is the Alfvén speed and is defined as $V_A \equiv \frac{B}{\sqrt{\mu_0 \rho_0}}$, where ρ_0 is the density of the plasma. On length scales larger than $\frac{\lambda_\eta V_A}{V}$, the resistive term can be neglected in equation (2.9).

- Second term on the right hand side is the pressure term. The characteristic length scale when the pressure term is important is given as $\lambda_i \beta^{\frac{1}{2}}$. λ_i is the ion skin depth. The ion skin depth is the gyro radius of the ions when they move with the Alfvén velocity. β is the ratio between the plasma pressure and the magnetic pressure. The β will be explained in further details later in this section. On length scales larger than $\lambda_i \beta^{\frac{1}{2}}$, the pressure term in equation (2.9) can be neglected.
- Third and fourth term on the right hand side is related to the electrons in the plasma. The characteristic length scale of the two terms is the electron skin depth, λ_e. The electron skin depth is the gyroradius of the electrons when they move with the Alfvén velocity. On length scales larger than λ_e, the fourth and fifth term of equation (2.9) can be neglected.
- The fifth term is the Hall term. The characteristic length scale of the term is the ion skin depth λ_i. On length scales larger than λ_i, the Hall term can be neglected.

The average ion and electron skin depths in the magnetotail plasma sheet are ~ 700 km for ions and ~ 20 km for electrons [*Oieroset et al.*, 2001].

In the ideal MHD plasma, the conductivity σ is assumed to be infinite. The magnetotail plasma is assumed to be almost collisionless and highly conductive so the ideal MHD approximation is valid [*Schindler and Birn*, 1978]. With a large conductivity ($\sigma \to \infty$), equation (2.10) reduces to

$$\vec{E} + \vec{V} \times \vec{B} = 0 \tag{2.11}$$

in order to obtain a finite current density. Equation (2.11) is the ideal Ohm's law. Inserting equation (2.11) into equation (2.4), the electric field in equation (2.4) is eliminated, hence

$$\frac{\partial \vec{B}}{\partial t} = \nabla \times \left(\vec{V} \times \vec{B}\right) \tag{2.12}$$

Equation (2.12) relates the magnetic field to the plasma velocity, so that the magnetic flux will convect with the plasma fluid, which means the plasma is bound to the magnetic field.

Inserting the reduced (2.5), $\nabla \times \vec{B} = \mu_0 \vec{J}$, into equation (2.8) by replacing the current density, the momentum equation reduces to

$$\rho\left(\frac{\partial\vec{V}}{\partial t}+\vec{V}\cdot\nabla\vec{V}\right)=-\nabla p+\frac{1}{\mu_0}(\nabla\times\vec{B})\times\vec{B} \tag{2.13}$$

The equations (2.8) – (2.13), except equation (2.10), are the equations describing the ideal MHD plasma.

Summary of the main assumptions and results from the mathematical derivation of the MHD: If the gravitational force is neglected and the plasma moves with a velocity $V \ll c$ and that the characteristic scale length is larger than the ion and electron skin dept, the plasma in the magnetosphere is collisionless. This implies a large conductivity, and the ideal MHD approximation can describe the dynamics of the space plasma. If the scale lengths are less than the ion and electron skin depth, the assumptions of an ideal MHD plasma are no longer valid, and the momentum of each particle has to be considered.

2.4.3 The frozen-in concept

One of the consequences of equation (2.12) is a concept referred to as "frozen-in". The frozen-in concept says that if a fluid element flowing through a surface S is followed through a system, then the total flux through the surface will remain the same even if the surface changes its location or shape. The total magnetic flux Φ through a surface S is given as

$$\Phi(S,B)\equiv\int\vec{B}\cdot\vec{d}S \tag{2.14}$$

Assuming the flux remains constant with time, $\frac{\partial\Phi}{\partial t}=0$, equation (2.14) can be written as

$$\frac{\partial\Phi(S,B)}{\partial t}=\frac{\partial}{\partial t}\int\vec{B}\cdot\vec{d}S=0 \tag{2.15}$$

When inserting the equation (2.12) into equation (2.15), the frozen-in condition can mathematically be given by

$$\frac{\partial\Phi(S,B)}{\partial t}=\int\left[\frac{\partial\vec{B}}{\partial t}-\nabla\times\left(\vec{V}\times\vec{B}\right)\right]\cdot d\vec{S}=0 \tag{2.16}$$

Equation (2.16) states that the magnetic flux flowing through a surface S, and moves with the plasma fluid, remains constant [*Boyd and Sanderson*, 2003]. The frozen-in condition is valid only if all the assumptions leading to $\vec{E}+\vec{V}\times\vec{B}=0$ are satisfied. The consequence of the frozen-in concept is that plasma along different magnetic field lines does not mix until the frozen-in condition is broken. The plasma can only flow along the magnetic field line, not perpendicular to it.

2.4.4 The plasma beta

The plasma β is defined as the ratio between the plasma pressure and the magnetic pressure [*Chen*, 1983]. It is derived from a simple static solution where $\vec{V} = 0$, hence the momentum equation, equation (2.8), reduces to

$$-\nabla p + \frac{1}{\mu_0}(\nabla \times \vec{B}) \times \vec{B} = 0 \tag{2.17}$$

Using vector identities, equation (2.17) can be written as

$$\nabla\left(p + \frac{1}{2\mu_0}B^2\right) = \frac{1}{\mu_0}(\vec{B} \cdot \nabla)\vec{B} \tag{2.18}$$

If the magnetic field lines are divergence free, and the pressure depends on the Cartesian coordinate $p = p(x)$, then assuming the magnetic field points in the z direction, $\vec{B} = (0,0,B_z)$, equation (2.18) yields

$$\frac{d}{dx}\left(p + \frac{1}{2\mu_0}{B_z}^2\right) = 0 \tag{2.19}$$

or

$$p + \frac{1}{2\mu_0}{B_z}^2 = \text{constant} \tag{2.20}$$

The first term on the left side of equation (2.20) is the thermal plasma pressure given by the ideal gas law, $p = nkT$ where n is the density, $k = 1.380 * 10^{-23} J/K$ is Boltzmann's constant and T is the temperature. The second term on the left side is called the magnetic pressure and is given as $p_B = \frac{B^2}{2\mu_0}$. The plasma β is given as

$$\beta \equiv \frac{2\mu_0 n_{ions} k T_{ions}}{B^2} \tag{2.21}$$

In the statistical studies done by Baumjohann in 1988 and 1989, plasma β was found to be the quantity which varied the most across the plasma sheet [*Baumjohann et al.*, 1988, *Baumjohann et al.*, 1989]. In the inner central plasma sheet and close to the neutral sheet, plasma β takes values between 3 and 10. Typical values of the plasma β in the central plasma sheet are > 0.3. In the plasma sheet boundary layer (PSBL) the values have a range between $0.02 < \beta < 0.05$ from the outer to the inner PSBL. In the lobes $\beta < 0.02$. When studying the plasma β observed by satellites, it is therefore possible to distinguish the different plasma regions in the magnetotail.

2.5 Magnetic reconnection

Magnetic field line merging (magnetic reconnection) is the most important process for plasma transport and energy conversion in space plasma. Magnetic reconnection is a process which is present in coronal mass ejections (CME) [*Gosling et al.*, 1995]. Magnetic reconnection contributes to coronal heating [*Hones*, 1984] and enables the solar wind plasma and its electromagnetic energy to enter the magnetosphere [*Paschmann et al.*, 1979]. Magnetic reconnection in the magnetotail converts the stored magnetic energy in the tail lobes into kinetic particle energy by accelerating particles in the reconnection region.

2.5.1 The Dungey Cycle

The Dungey Cycle was first described by J. W. Dungey in [1961] and in Figure 2-10 the cycle structure is schematically displayed. The Dungey Cycle describes the coupling between the magnetic field lines and the IMF at the magnetopause. The cycle also describes how the magnetic flux is stored in the magnetotail leading to another magnetic reconnection in the distant magnetotail in an estimated mean distance at $100 - 200$ R_E tailwards of the Earth, in order to prevent a magnetic flux pile-up in the magnetotail.

The principles behind the Dungey Cycle illustrate the importance of the magnetic field line merging between the solar wind and the Earth's magnetic field [*Kivelson and Russell*, 1997]. Figure 2-10 illustrates how an interplanetary magnetic field (IMF) line (1') in the solar wind couples to an Earth magnetic field line (1). In this illustration it is assumed that the IMF is directed mainly southward. Instead of an IMF in the interplanetary space, and an Earth magnetic field line connected to the Earth at both ends, the new coupled field lines are attached with one end close to one of the Earth's geographical poles and the other end stretched out into the interplanetary space (2 and 2'). These field lines are called open field lines. The open field lines are dragged towards the night side of the Earth's magnetosphere (3 and 3') and (4 and 4') due to the pressure and electric field, $\vec{E}_{SW}$, caused by the solar wind. $\vec{E}_{SW} = \vec{V}_{SW} \times \vec{B}_{SW}$ where $\vec{V}_{SW}$ is the velocity and $\vec{B}_{SW}$ is the magnetic field in the solar wind. On the night side of the Earth, the open magnetic field lines form the lobes of the Earth's magnetotail (5 and 5'). If there was no return flux of the magnetic field in this process, the whole geomagnetic field would be connected to the interplanetary field, which is not the case. In the magnetotail the open field lines from the northern and southern regions move towards each other and reconnect (6 and 6'). The new field line (7), now with both ends connected to

the Earth, is stretched and is being pulled earthward (8). The other new field line (7') becomes again a part of the solar wind. Due to mechanisms, which are not a part of this thesis, the closed field lines will move from the Earth's night side (8) back to the dayside (9) (either on the dusk or dawn side). This renewal of the Earth's magnetic field lines in the magnetotail is known as the open magnetosphere model. The areas where reconnection occurs in this model are marked with **p** (the magnetopause) and **pp (**the magnetotail).

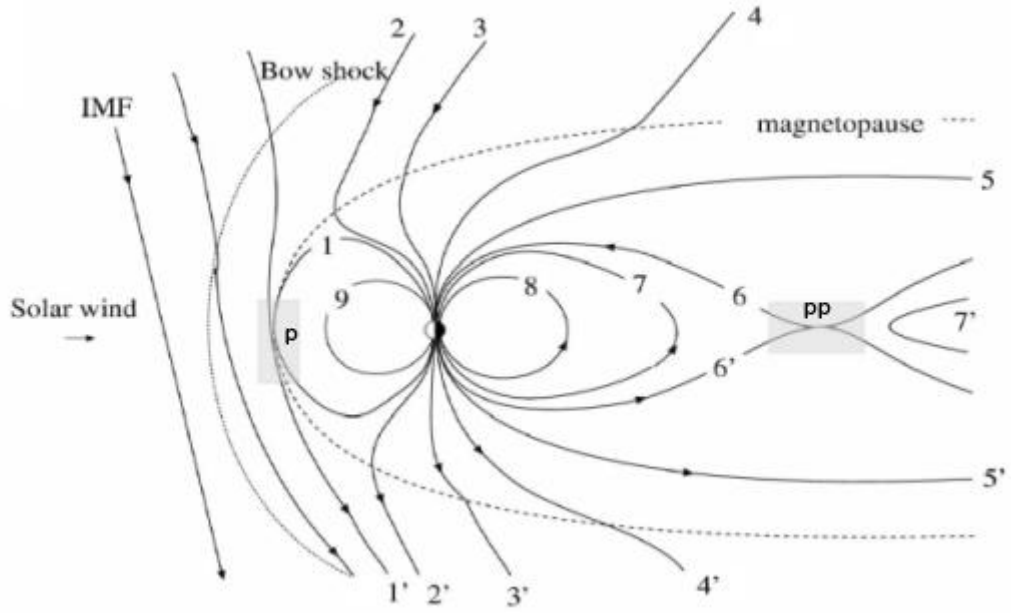

Figure 2-10: Panel a) Topology of the magnetosphere during the Dungey Cycle. The gray shaded areas marked with "**p**" and "**pp**" are the two regions in the Dungey model where magnetic reconnection occurs. Figure modified from *Jordan* [2008].

Magnetic field line coupling in the Earth's magnetotail can also occur at other places in the magnetotail, not only in the distant tail as described in the Dungey Cycle.

2.5.2 Magnetic reconnection in the Earth's magnetotail

Magnetic reconnection in the magnetotail is based on the breakdown of the frozen-in concept of the ideal MHD description of the plasma (see section 2.4). The frozen-in concept is valid when $\vec{E} - \vec{V} \times \vec{B} = 0$. A direct consequence of the frozen-in concept is the formation of thin boundaries between regions containing different plasma populations and magnetic field configuration. The reason for this is that the plasma only moves parallel to the magnetic field lines, and not in the perpendicular direction in regions that are of length scales larger than the ion and electron skin depth. If the magnetic field lines in two regions of opposite or nearly opposite polarity meet, the boundary between them will then fulfil the criteria of a current

sheet, also called a neutral sheet [*Kivelson and Russell*, 1997]. An example of such a magnetic field configuration is found in the magnetotail, where the polarity of the magnetic field lines in the northern and southern lobes are opposite. These field lines of opposite polarity meet in the magnetotail current sheet. When the magnetic flux increases in the lobes, an imposed external electric field in the dawn-dusk direction (E_y) will drive the magnetic field lines in the two hemispheres towards the plasma sheet midplane and the current sheet becomes thinner. If the size of the current sheet is less than the ion skin depth, the ideal MHD model will no longer be valid, and the frozen-in concept will therefore also no longer be valid. When the frozen-in condition is broken, plasma populations from different magnetic field lines are then free to move across the field lines and mix and magnetic reconnection is made possible.

The x-line, illustrated in Figure 2-11, is a line out-of-plane in the dawn-dusk direction where the magnetic field lines from the northern and southern lobes touch and reconnect.

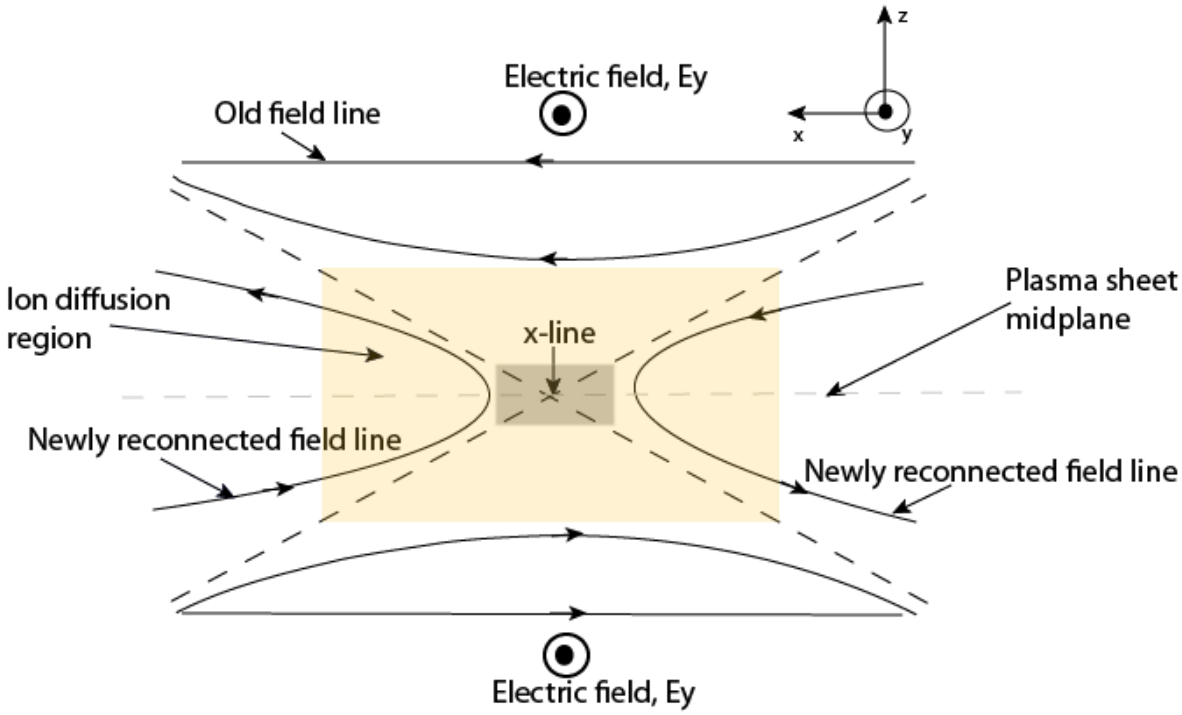

Figure 2-11: An illustration of the reconnection region. An external electric field E_y forces the plasma and the magnetic field to convect towards the plasma sheet midplane. The field lines touch in the x-line and become reconnected. The yellow area is the ion diffusion region while the gray shaded area is the electron diffusion region.

The areas north and south of this x-line are referred to as the inflow regions, and consist of magnetic flux and frozen-in plasma which move towards the plasma sheet midplane from both hemispheres. The left side (earthward) and the right side (tailward) of the x-line are the outflow regions, which consist of accelerated magnetic flux and frozen-in plasma moving

away from the x-line. In this simple MHD magnetic reconnection model the outflow velocity is larger than the inflow velocity of the plasma [*Nagai et al.*, 2001]. The relative transfer rate of a reconnection is the ratio $\frac{V_{inflow}}{V_A}$. Theory predicts an upper limit of the inflow velocity (V_{inflow}) to be ~ 0.1 – 0.2 V_A [e.g., *Levy et al.*, 1964]. The existence of the magnetic x-line has been verified by observations [e.g, *Scudder et al.*, 2002, *Xiao et al.*, 2006].

The region surrounding the x-line is called the reconnection region. The yellow area in Figure 2-11 is the ion diffusion region, and this is where the frozen-in concept breaks down for the ions, $\vec{E} + \vec{V_i} \times \vec{B} \neq 0$. The gray shaded region shows where the frozen-in concept breaks down for the electrons, $\vec{E} + \vec{V_e} \times \vec{B} \neq 0$ and this area is therefore referred to as the electron diffusion region. Since the ion and electron length scales are dependent on mass, the size of the ion diffusion region is much larger than the size of the electron diffusion region. The in-flow and outflow regions, which contain different magnetic field structures and plasma, are separated with the dashed dark lines in Figure 2-11. Those lines are called the separatrices [*Vasyliunas*, 1975] and may extend far out from the x-line. This has been confirmed by observations [e.g., *Retino et al.*, 2006]. As the ions and electrons leave the diffusion region (in the outflow region) they are again frozen into the magnetic field. Since the magnetic field lines after a reconnection in the x-line are curved, a strong tension force will accelerate the field lines out from the region in the horizontal direction (along plasma sheet midplane). Since the plasma is frozen into the field lines in this region outside the diffusion region, it will be accelerated as well during this process.

Magnetic reconnection in the distant magnetotail is believed to be a part of the Dungey Cycle [*Dungey*, 1961]. Such magnetic reconnection occurs at distances ≥ 100 R_E from the Earth. Magnetic reconnection can also take place in the near-Earth magnetotail. A statistical study done by Nagai in 2005 [*Nagai et al.*, 2005] concludes that magnetic reconnection takes place in the near-Earth plasma sheet, inside 25 R_E from the Earth for high solar wind energy input, and outside 25 R_E for low solar wind energy input. Several studies have also confirmed the occurrence of magnetic reconnection inside of 19 R_E [e.g., *Baker et al.*, 2002, *Runov et al.*, 2003, *Borg et al.*, 2005]. The probability of a satellite observing the electron diffusion region is relatively small because of the region`s small size compared to that of the magnetotail size [*Vaivads et al.*, 2006] and due to the short time the satellite would have spent in the region. The ion diffusion region has been observed in-situ for example by *Øieroset et al.* [2001] and by *Borg et al.* [2005] in the magnetotail and by *Mozer et al.* [2002] at the magnetopause. The existence of the electron diffusion region has been confirmed by

Mozer et al. [2003], who reported the breakdown of the frozen-in concept for electrons in strong current channels at the subsolar magnetopause.

2.5.3 The physics of magnetic reconnection

Most of the understanding of the structure and the dynamical processes of the ion and electron diffusion regions are based on numerical studies and simulations [*Hoshino et al.*, 2000, *Pritchett*, 2001]. Depending on the resistive scale given in equation (2.9) magnetic reconnection can be accomplished by different processes. If the resistive length scale is smaller than the ion skin depth, the reconnection is said to be collisionless. In a collisionless magnetic reconnection a charge separation between the ions and electrons will form. This thesis will focus on the collisionless reconnection process.

The scale of the diffusion region is limited by the characteristic length scale given for the general Ohm's law. Inside the diffusion region the ideal Ohm's law is no longer valid, hence $\vec{E} + \vec{V} \times \vec{B} \neq 0$. Because of the difference between the electron mass and the ion mass, the ion and electron skin depth are of different scales. The charge separation, created by the relative motion of the ions, $\vec{V_i}$ and electrons, $\vec{V_e}$ in the inflow region towards the neutral sheet, will therefore generate an electric field. Their inflow velocities are marked with grey and white arrows in Figure 2-12.

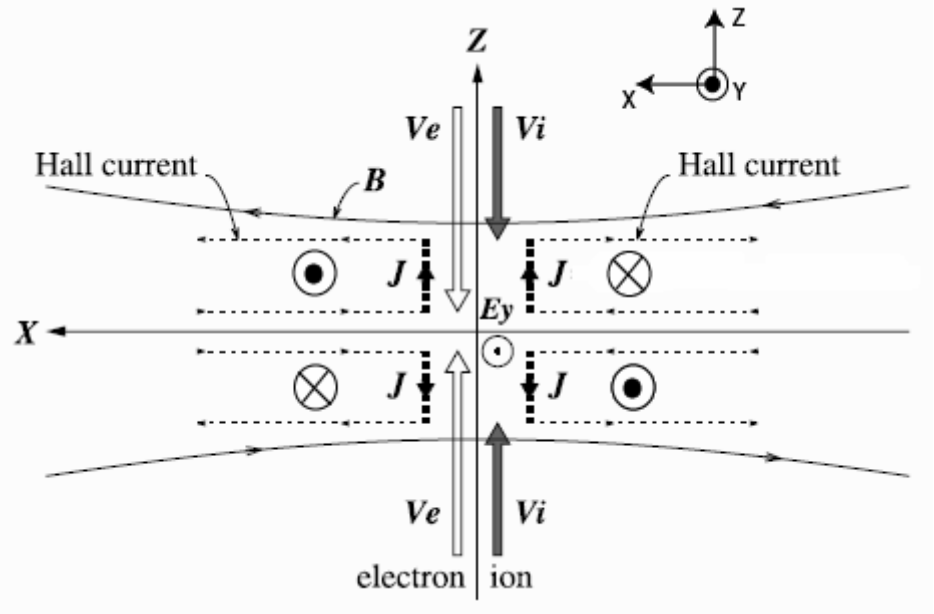

Figure 2-12: A sketch of the Hall current system around the x-line in a magnetic reconnection with the Hall magnetic field marked as circles with dots – out-of-plane (positive y direction), and crosses – into the plane (negative y direction). Figure modified from *Ueno et al.* [2003].

The generated electric field E_z, which is negative in the northern hemisphere and positive in the southern hemisphere, further generates a current J which flows lobeward inside the diffusion region, see Figure 2-12. Due to charge conservation a currents are required to flow into the diffusion region close to the x-line and out of the diffusion region close to the mid-plane as illustrated in Figure 2-12. This current flow is referred to as the Hall current system and is a current system created around the x-line in a collisionless magnetic reconnection [*Sonnerup*, 1979, *Hesse et al.*, 1999]. The Hall currents form four current loops as illustrated in the figure. In a resistive reconnection there is no charge separation, and consequently no generation of the Hall current [*Oieroset et al.*, 2001].

The Hall current system induces a quadrupole Hall out-of-plane magnetic field, from now on referred to as the Hall magnetic field. This magnetic field structure is a characteristic signature of a magnetic reconnection [*Hesse and Winske*, 1994, *Pritchett*, 2001] and is illustrated in Figure 2-12 by the circles with dots and crosses, where a dot is out-of-plane (positive y direction) and a cross is into-plane (negative y direction). The Hall magnetic field varies in strength, and has been observed at some distance from the reconnection region [*Ueno et al.*, 2003].

The quadrupole Hall magnetic field near the magnetic reconnection region, has been verified many times by observations done by a single spacecraft [e.g., *Oieroset et al.*, 2001] and by using multiple spacecraft [e.g., *Runov et al.*, 2003, *Borg et al.*, 2005, *Laitinen et al.*, 2007]. In a statistical study by *Ueno et al.* [2003], 4022 events of ion flow reversals and simultaneous B_z variations were studied. They found that the correlation between the out-of-plane Hall magnetic field measured as the B_y-component, and the horizontal component B_x indicates a quadrupole structure as in the Hall magnetic field. Such an ideal quadrupole field is illustrated in Figure 2-13. Panel a) illustrates the typical correlation between the B_x- and B_y-components earthward of the magnetic reconnection region. For $B_x < 0$ (southern hemisphere), $B_y < 0$, and for $B_x > 0$ (northern hemisphere), $B_y > 0$. Panel b) illustrates the anti-correlation between the B_x- and B_y-components tailward of the reconnection region [e.g., *Laitinen et al.*, 2007]. For $B_x < 0$ (southern hemisphere), $B_y > 0$, and for $B_x > 0$, (northern hemisphere) $B_y < 0$.

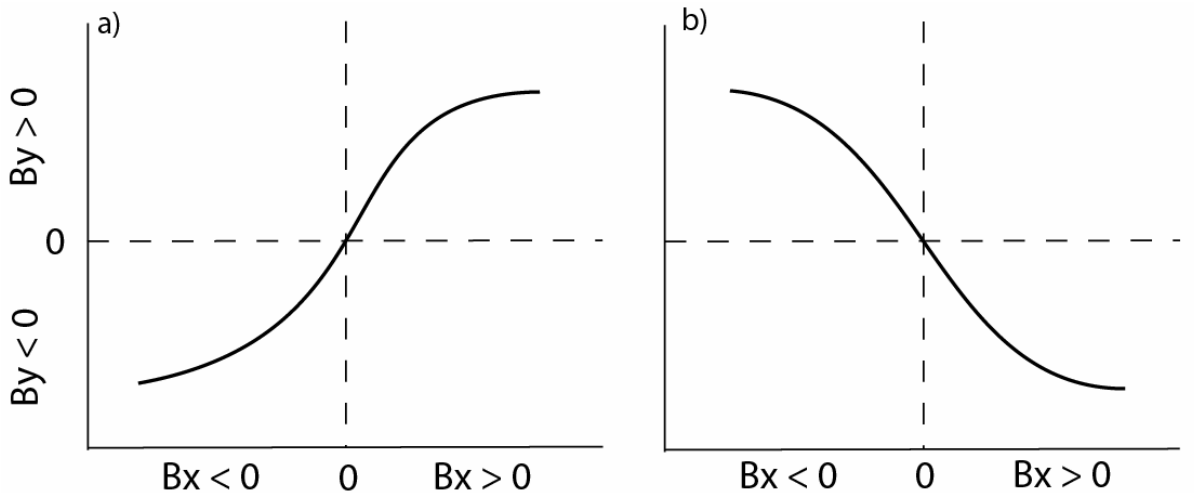

Figure 2-13: The ideal correlation and anticorrelation between the B_x- and B_y-component from the quadrupole structure of the Hall magnetic field. Panel a) displays the signature of the Hall magnetic field if the spacecraft is located earthward of the reconnection region. Panel b) shows the signature of the Hall magnetic field if the space craft is located tailward of the reconnection region.

In papers by *Borg et al.* [2005] and by *Østgaard et al.* [2009], the velocity of ions was used as well as the B_x- and B_y-components in order to visualise the Hall magnetic field. By using the fact that the B_x-component and the x-component of the velocity changes polarity depending on the location within the reconnection region (see Figure 2-15) the spacecraft position within the ion diffusion region can be found. Figure 2-14 illustrates what such an ideal structure of the Hall magnetic field would look like using the B_x- and V_x-components.

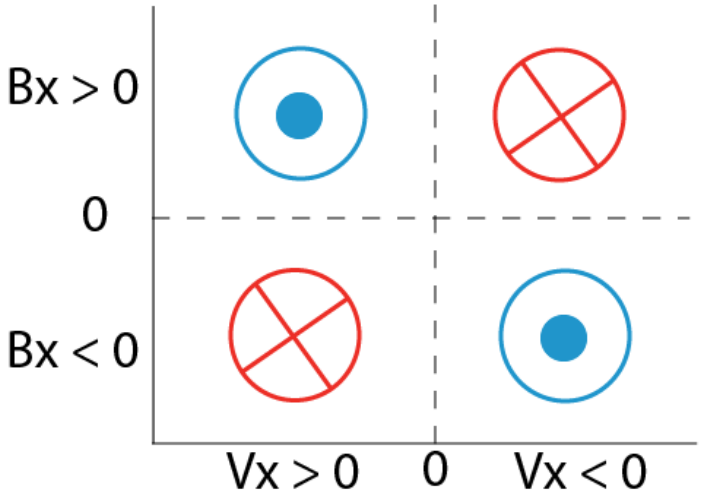

Figure 2-14: A sketch of the ideal quadrupole Hall magnetic field using measurements of the velocity and the magnetic field done by a satellite. The red circles indicate a negative B_y-component into-plane, while the blue circles indicate a positive B_y-component out-of-plane.

The displayed colours represent the direction of the B_y-component, blue for out-of-plane, and red for into-the-plane.

The magnetic energy released in the reconnection process is converted into kinetic particle energy, accelerating the particles in the outflow region. The outflow velocity is measured as the V_x-component and is shown in Figure 2-15.

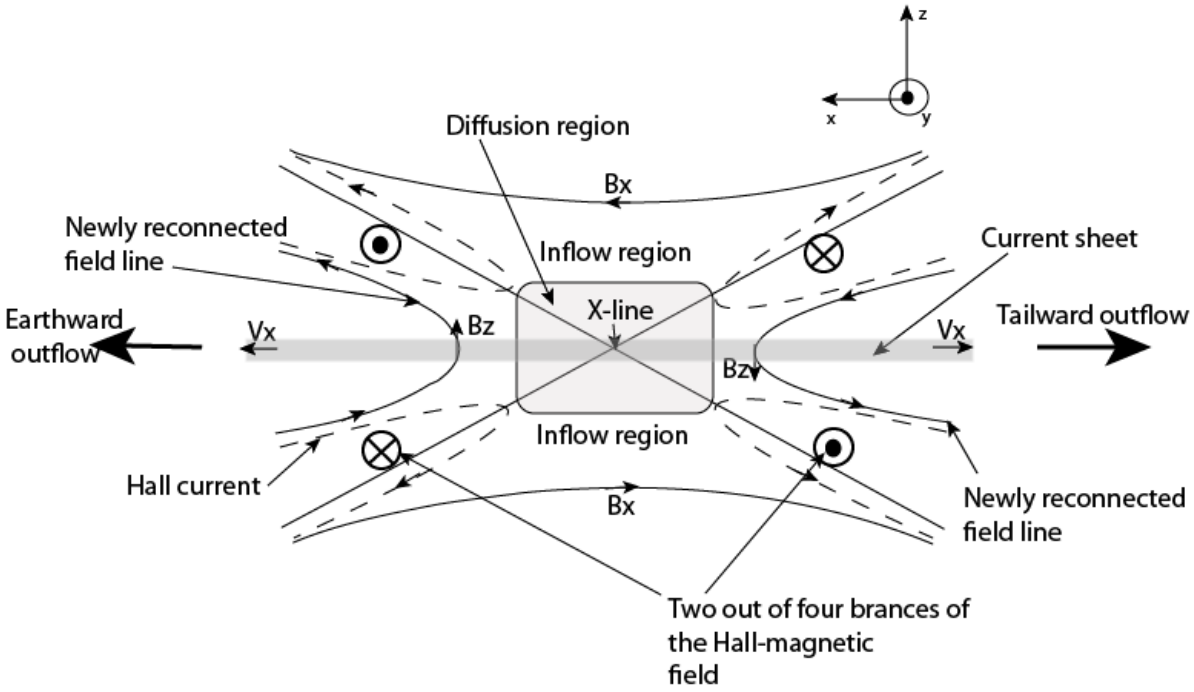

Figure 2-15: An illustration of the reconnection region with the Hall currents (dashed lines) and the four branches of the quadrupole Hall magnetic field (in- and out-of-plane circles). The current sheet is located in the centre of the region. The illustration shows the expected signatures of a collisionless magnetic reconnection in datasets from in situ measurements. Details regarding this figure are given in the text.

Observations of high speed plasma jets in the reconnection region, both earthward and tailward has been reported by a number of studies [e.g., *Oieroset et al.*, 2001, *Baker et al.*, 2002, *Runov et al.*, 2003, *Borg et al.*, 2005, *Nakamura et al.*, 2006, *Laitinen et al.*, 2007, *Angelopoulos et al.*, 2008]. Typical ion bulk velocities of such high speed jets exceeds values of 400 km/s [*Shiokawa et al.*, 1997]. These observed jets are signatures of energy conversion from magnetic field to plasma [*Vaivads et al.*, 2006]. Figure 2-15 also illustrates the topological structure of the magnetic field in a reconnection region. As seen in the figure, close to the diffusion region the magnetic field tailwards of the diffusion region has a strong positive B_z-component, and a negative earthward of the diffusion region. Close to the neutral sheet the B_x-component is very weak. The arrows in Figure 2-15 only illustrate the direction of the components, not the magnitude. The direction of the Hall magnetic field is illustrated as circles with crosses and dots.

Observations of strong amplitude fluctuations in the x- and y-components of electric field measurements has been reported during an observed magnetic reconnection event [*Borg*

et al., 2005]. The high values of the E_y-component during this event corresponded to instances of low plasma density and large magnitude B_x-component, implying that the large scale electric field is located in the vicinity of the separatrices.

When searching for collisionless magnetic reconnection in satellite datasets the signatures used in this thesis are:

- Fast plasma jets directed earthward and tailward, visible as a flow reversal in the V_x-component
- Simultaneous reversals in the vertical magnetic field component
- Quadrupole Hall magnetic field seen in the B_y-component

The signatures are included in Figure 2-15.

When searching for these signatures two assumptions have been made. The first assumption is that the reconnection region is a 2-D structure in the xz plane. The second assumption is that the reconnection region moves relative to the satellites in approximately the x direction.

When the reconnection signatures are established, the interval in which the reconnection is observed is used to analyse data observed by different instruments.

2.6 Magnetospheric substorms

Magnetospheric substorms are considered the most important dynamical process resulting from the solar wind-magnetosphere interaction. A magnetospheric substorm is described as a magnetically disturbed time period when the magnetic energy, stored in the tail lobes of the magnetosphere, is deposited into a region confined mostly to the auroral oval region [*McPherron*, 1979]. The start of a magnetospheric substorm, the onset, is signaled by the explosive increase in the auroral activity in the midnight sector [*Rostoker et al.*, 1980]. During the interval of a substorm the auroral electrojet can strengthen and return to a ground state several times, each time accompanied with bursts of micropulsations and westward travelling surges (WTS). A WTS is an auroral form which looks like a wave and moves westward, hence the name. All such features associated with the substorm (auroral electrojet, micropulsations and the WTS) are signatures which can be observed by satellites and by using data from ground stations which measure the geomagnetic field.

A substorm can be divided into three main phases. The growth phase, the expansion phase and the recovery phase [*McPherron et al.*, 1973]. During the growth phase, the energy from the solar wind is being stored in the magnetotail by the Dungey Cycle [*Baker et al.*,

1996]. As the magnetic flux increases, a build-up of magnetic pressure forces the plasma sheet to thin [*Schindler and Birn*, 1993]. The expansion phase is a result of the sudden disrupt of the flux that caused the energy build-up. The expansion phase is also associated with plasma jets in the plasma sheet [*Baumjohann et al.*, 1990]. After the expansion phase, the magnetotail configuration again seeks the equilibrium state. Within a magnetospheric substorm, several substorm onsets with a following expansion phase can occur. Such onsets are referred to as substorm intensifications [*Rostoker et al.*, 1980]. During substorms which contain several substorm intensifications, the expansion phase ends when the maximum poleward expansion of the auroral oval is reached.

The physic behind the onset of the expansion phase are not fully understood and remains as a longstanding issue [e.g., *Baker et al.*, 1996]. It is generally believed that the onset is caused by a release of the energy in the magnetotail, but how this release is triggered is still a debated question [e.g., *Angelopoulos et al.*, 2008, *Angelopoulos et al.*, 2009, *Lui*, 2009]. There are a number of theories regarding the triggering of the substorm onset, and the two paradigms which contain the main ideas of the processes are referred to as the "near-Earth neutral line" (NENL) and the "near-Earth current disruption" (NECD) paradigms. In the near-Earth neutral line model a magnetic reconnection located in the midtail (~20 R_E) generates high speed ion flows both earthward and tailward. The flows transporting energy from the reconnection region towards the Earth are stopped in the region between the dipolar shaped magnetic field and the tail-like field in the plasma sheet (~13 - ~15 R_E) [*Shiokawa et al.*, 1997]. In this region there will be a magnetic flux pile-up leading to an even more dipolar shape of the inner tail region. The pressure gradient caused by the breaking of the plasma flows causes the cross-tail current to divert and form the substorm current wedge (SCW) [*McPherron et al.*, 1973], thus triggering the substorm onset. In the near-Earth current disruption model, the cross-tail current is disrupted by some local instability within the near-Earth region and generates a SCW [*Lui*, 1991], thus triggering the substorm onset. The disturbed region propagates tailwards [*Jacquey et al.*, 1991] causing the plasma sheet to thin which again leads to a formation of magnetic reconnection at ~20 R_E.

In the SCW, the currents flow into the ionosphere along the magnetic field lines on the dawn side of the tail and out of the ionosphere on the dusk side of the tail, as illustrated in Figure 2-16. In the ionosphere an auroral electrojet is formed due to current continuity and acts as a closure of the field aligned currents. The auroral electrojet flows in the midnight sector from east to west both in the southern and northern hemisphere, and moves together with the auroral intensification in the WTS. Intense enhancement of the auroral electrojet in

the midnight sector of the ionosphere acts as a closure of the SCW and the FACs during active periods.

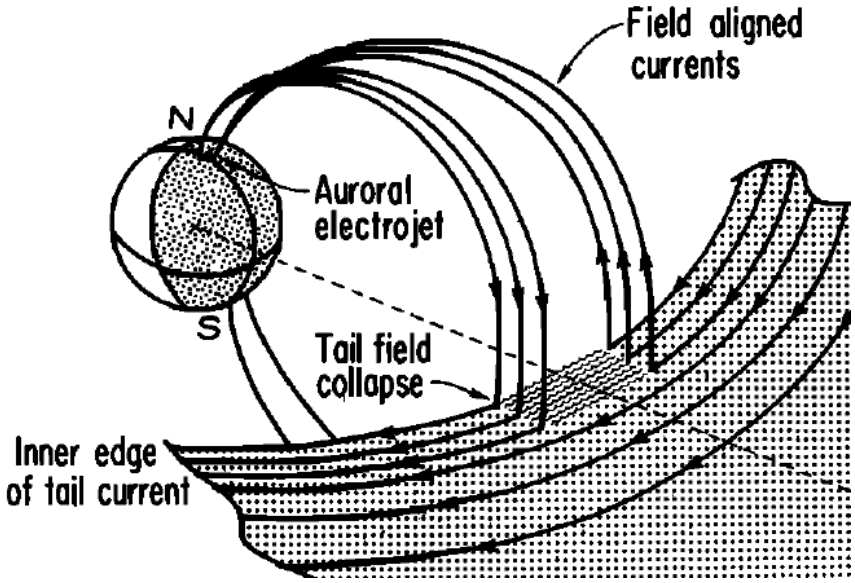

Figure 2-16: A schematic drawing of the substorm current wedge. The figure shows the current disruption in the tail current and the creation of the currents along the magnetic field lines (FACs). The FACs propagate in and out of the ionosphere and the current system is closed by the dawn-to-dusk flowing auroral electrojet in the ionosphere. Figure from *McPherron et al.* [1973].

It is assumed that along with the formation of the SCW micropulsations are formed [*Olson*, 1999]. Such pulsations are presumably generated by an oscillating SCW and the bouncing of field-aligned currents between the plasma sheet and the ionosphere [*Olson*, 1999], and are referred to as Pi 2 pulsations.

The ultimate driver of the substorm process is the solar wind and the energy dissipation from the solar wind into the magnetosphere. In order to understand the solar wind conditions prior to a substorm, a study was done by *Nagai et al.* [2005] where the solar wind conditions prior to the reconnection events associated with substorm onsets was investigated. The main result from the investigation, was that prior to near-Earth magnetic reconnection ($-15 < x_{GSM} < -25$ R_E) events, the velocity of the solar wind had an average value of ~ 520 km/s and a 60 minute period of southward directed component ($B_z < 0$) of the IMF. If such conditions occur prior to the onset of a magnetic reconnection, this may be a result of a build-up of energy in the magnetosphere.

2.6.1 Substorm signatures

In August 1978 a workshop was held in Victoria, British Colombia, in order to create a definition of a magnetospheric substorm and substorm signatures. Among the signatures estab-

lished during the workshop were the auroral signature, the magnetic signature, the Pi micropulsation signature and the AE-index [*Rostoker et al.*, 1980].

Auroral signature

An auroral substorm is the visual ionospheric response of the substorm disruption, and it is an eruption of auroral activity described as a sudden brightening in the night side of the auroral oval [*Akasofu*, 1964]. The signatures, which are illustrated in Figure 2-17, were first described by *Akasofu* [1964]. An auroral substorm consists of different phases. Its growth phase is recognised by the equatorward motion of the auroral oval which is seen in panel a). The onset is characterised by an initial arc brightening, as seen in panel b). The oval then expands poleward and the brightening spreads out and moves east and west. Sometimes a westward travelling surge (WTS) forms at the western edge of the auroral intensification. The WTS is characterized by intense upward FACs which define the westward edge of the SCW. The expansion phase of an auroral substorm is characterised by the formation of a WTS, displayed in panel c) and d). The brightening then fades away and the auroral oval moves equatorward. This last part is called the recovery phase.

In an auroral breakup, where the bright arc which identifies the onset of an auroral substorm dims before it develops, is referred to as a pseudobreakup [*Elphinstone et al.*, 1996]. Pseudobreakups are small auroral activations which look like substorm onsets, but the activity decays before an expansion phase evolves [*Elvey*, 1957]. The pseudobreakups can be observed during the growth phase of a substorm, as a result of plasma flows in the plasma sheet during plasma sheet thinning in front of a substorm onset [see *Nakamura et al.*, 2002 and references therein]. The pseudobreakups can be observed during all levels of geomagnetic activity, not only during substorms.

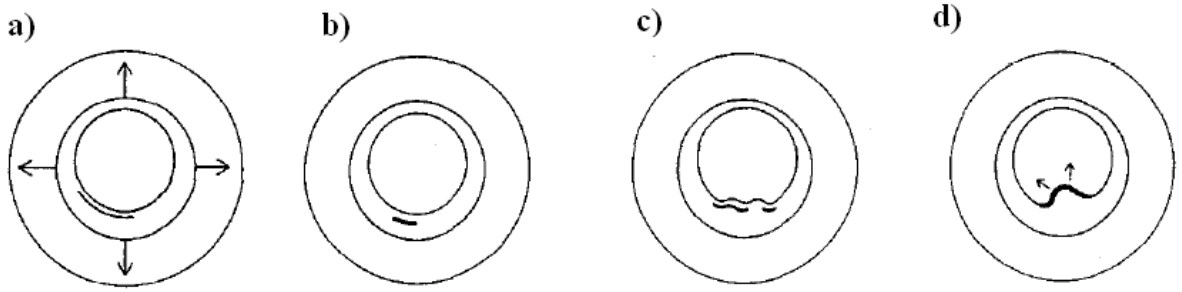

Figure 2-17: An illustration of the different phases during an auroral substorm in the ionosphere. Panel a) shows the growth phase, panel b) shows the onset phase, panel c) shows the expansion phase and panel d) shows the late expansion/recovery phase of the auroral substorm. Figure modified from *Lui* [1991].

Magnetic signature, the magnetic bay

During an auroral substorm the magnetic activity in the auroral zone changes. Data from magnetometer stations on the ground which measure the magnetic disturbances in the auroral region can with caution be used in order to determine the substorm onset and recovery. A magnetometer is a vector measuring instrument designed to measure the magnetic field intensity and orientation [*Webster*, 1999]. A consequence of the formation of a SCW in the magnetotail is the generation of the auroral electrojet in the ionosphere which generates a local magnetic field. Magnetic signatures created by the auroral electrojet will therefore give an indication of the substorm development.

A station in the auroral oval would measure a positive (negative) vertical change in the component (Z) if it is located north (south) of the auroral electrojet [*Rostoker et al.*, 1980]. If the station is located on the dusk side below the auroral electrojet, the horizontal component will be deflected when the auroral electrojet passes above. This negative magnetic compression caused by the auroral electrojet looks like a coastal bay, hence the name magnetic bay.

In the southern hemisphere the same happens, but the WTS moves eastward and enters the westward flowing electrojet in the dusk side of the MLT system. The signatures in the geomagnetic field measurements are the same as described above.

Pi micropulsation, Pi 2

A committee of the International Union of Geodesy and Geophysics established in 1963 a general notation of micropulstations in the geomagnetic field. Their definition of Pi 2 pulsations is impulsive pulsations of the geomagnetic field in the period range of 40 – 150 s. The Pi 2 pulsations are presumably generated by two processes, the onset of field-aligned currents flowing into the polar ionosphere and compressional waves in the plasma sheet that propagate inward and affect the magnetic structures in the inner magnetosphere [*Olson*, 1999]. The electrons travelling with the waves increases the conductivity in the ionosphere, which again can generate new waves [*Maltsev et al.*, 1974]. The Pi 2 pulse follows the transient changes in FACs which connects the ionosphere with the plasma sheet. It is in the auroral oval the maximum Pi 2 amplitudes appears [*Jacobs and Sinno*, 1960] and the evolution of the Pi 2 pulse is related to the substorm current wedge and westward travelling surge in the aurora.

Pi 2 pulsations can be observed as dampened wave trains where the initial pulse is recognised in data from stations located at and around the auroral oval, and in the mid and low latitudes on the night side of the Earth [*Olson*, 1999]. A Pi 2 pulsation does not have any limitation in amplitude [*Rostoker et al.*, 1980].

The auroral indices

The auroral electrojet indices were defined as an attempt to describe the global variation of the auroral electrojets in the auroral oval region, not just the local variation as that of the magnetic bay signatures. The indices describe the variations in the auroral oval caused by the electrojets [*Davis and Sugiura*, 1966]. The indices are derived from variations in the horizontal component of the magnetic field at ground level, as observed by the 10-13 observatories located at high latitudes in the northern hemisphere, see Figure 2-18 [*Weimer*, 1994]. The AE-index can be as a rough determination of the geomagnetic activity and is often used to define the onsets of a substorm and to identify the recovery phase [*Rostoker et al.*, 1980].

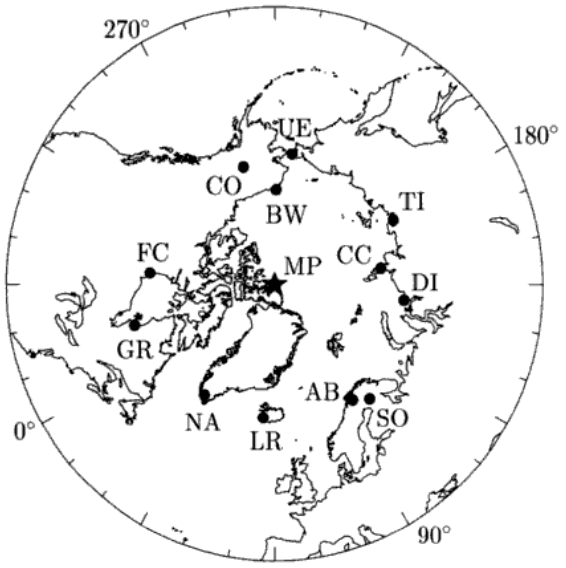

Figure 2-18: The stations which contribute to the AE-index (1974). The position of the Magnetic North Pole (MP) is marked with a star. The different abbreviations in the map are: AB – Abisko, LR – Leirvogur, NA – Narsarsuaq, GR – Great Whale River, FC – Fort Churchill, CO – College, BR – Barrow, UE – Cape Uelen, TI – Tixie Bay, CC – Cape Chelyuskin, DI – Dixon Island and SO – Sodankyla. The magnetic longitudes are marked at the boundary of the circle. Figure from *Prölss* [2003].

The indices consist of an auroral upper (AU)-index which is the maximum disturbance in the H-component of the magnetic field, and the auroral lower (AL)-index which is the minimum disturbance in the H-component of the magnetic field. The difference between the two indices is defined as the auroral-electrojet (AE)-index. The AE-index is calculated with a resolution of one minute [*Davis and Sugiura*, 1966]. An enhancement in the AE-index is a ground

signature of the substorm expansion phase where the auroral electrojet flowing in the ionosphere in the midnight sector is strengthened [*Nakamura*, 2006]. The classical signatures of a substorm in the auroral indices are shown in Figure 2-19. The signatures shown in the figure are an average of the AU-, AL-, and the AE-index, made using an analysis of 55 different substorm events done by *Weimer et al*. [1994]. The upper panel of Figure 2-19 shows the AU-, and the AL-index with the different stages of a substorm, where (1) is the growth phase, (2) is the expansion phase and (3) is the recovery phase when the electrojet starts to decay and returns to quiet conditions.

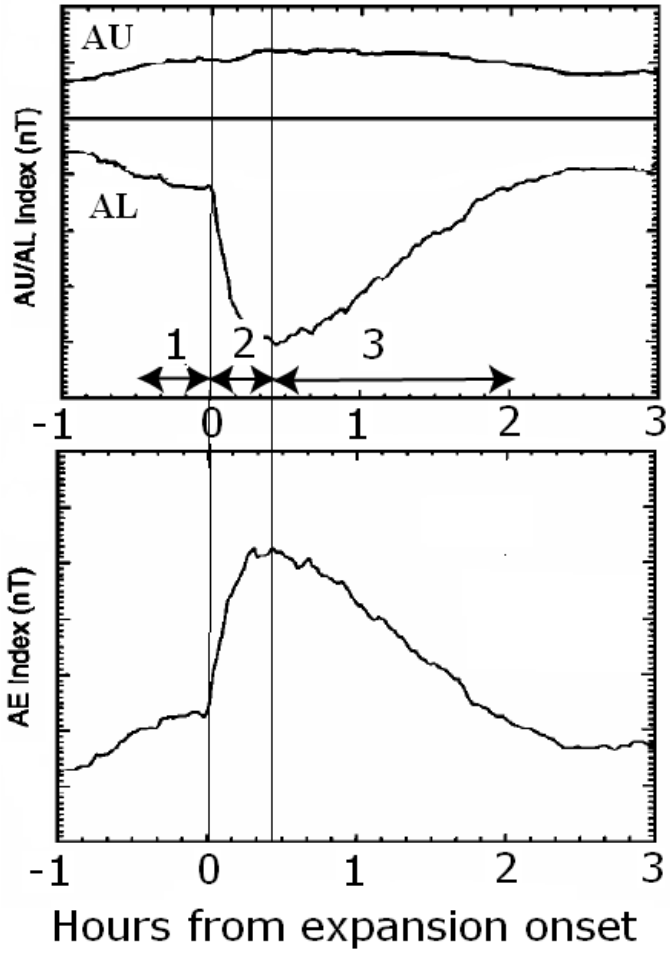

Figure 2-19: The upper panel shows the average AU-, and AL-index of 55 substorm events. The shape is a classical signature of a substorm signature where the growth (1), expansion (2) and the recovery (3) phase is shown. The lower panel shows the AE-index of the same 55 substorms. Figure modified from *Weimer* [1994].

2.6.2 Timing of the signatures

The two substorm triggering paradigms predict different timing of the substorm signatures. In NENL, the fast flows in the plasma sheet precede the auroral intensifications and the ground signatures by 1-3 minutes [*Kepko et al.*, 2004]. In NECD, the auroral brightening will precede the fast flows and perhaps the Pi2 pulsations as well by 1-3 minutes [*Liou et al.*, 2000].

The auroral intensification is an easily observed signature of an auroral substorm onset because of the dramatic change in the aurora. The auroral intensification is often used as a parallel for the substorm onset [*Kepko et al.*, 2004]. The changes from a pre-substorm state to a substorm onset are very apparent and happen during a short time scale. The uncertainties related to timing of an auroral substorm are therefore limited to the resolution of the instrument observing the aurora.

3 Satellites and ground stations

3.1 Common coordinate systems in space physics

The Geocentric Solar Ecliptic (GSE) and the Geocentric Solar Magnetospheric (GSM) are the coordinate systems which are most frequently used in magnetospheric physics. The coordinate systems are illustrated in Figure 3-20. In the GSE coordinate system, the x-axis is directed towards the sun, and the z-axis points in the direction of the ecliptic north pole and the y-axis completes the orthogonal system. The GSE coordinate system is used for example when presenting satellite trajectories or when measuring the IMF or other features of the solar wind.

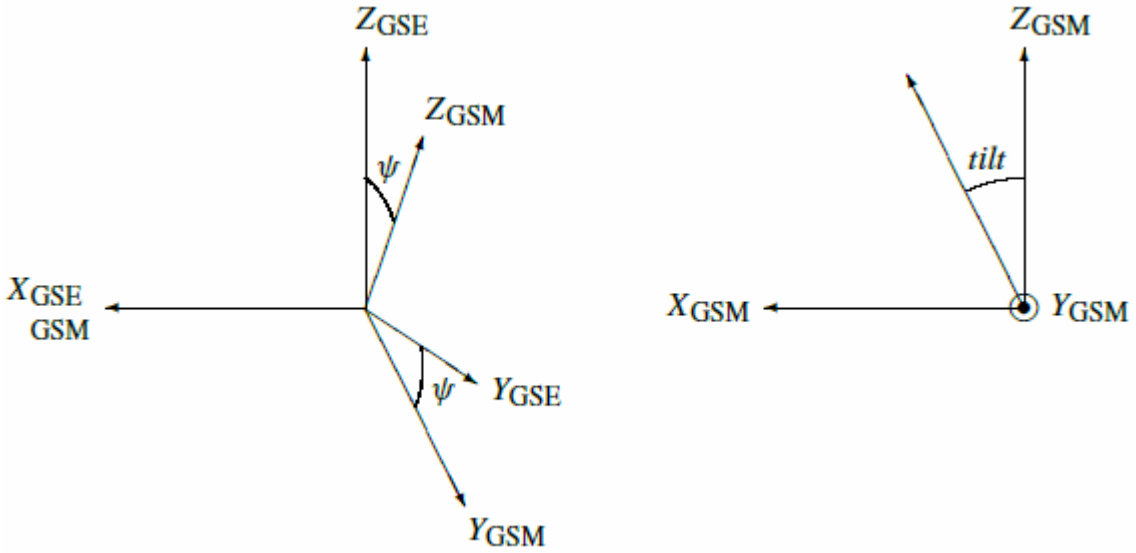

Figure 3-20: The GSE and GSM coordinate system with respect to each other. The tilt is referred to as the dipole-tilt between the GSM z-axis and the vector pointing from the centre of the Earth to the magnetic pole located in the northern hemisphere. The coordinate systems shear a common x-axis but the y- and z-axes differs with an angle ψ. Figure from *Daly* [2008].

The GSM coordinate system shares the x-axis with the GSE system, but the z-axis is the projection of the Earth's magnetic dipole axis onto a plane which is perpendicular to the x-axis. The y-axis is perpendicular to the magnetic dipole, which means that it lies in the magnetic equator, pointing toward dusk. The GSM coordinate system is used for example when displaying the magnetotail magnetic field. The GSM coordinate system varies not only throughout the year, but also during a 24 hour interval. The origin of both the coordinate systems is in the centre of the Earth.

The geomagnetic local time (MLT) is defined relative to the magnetic dipole system by using the magnetic longitude and latitude. The system is illustrated in Figure 3-21. The MLT com-

bines the magnetic latitude (the blue numbers) with a local time (the black numbers) reference system. The system has a fixed axis where noon is always directed towards the sun.

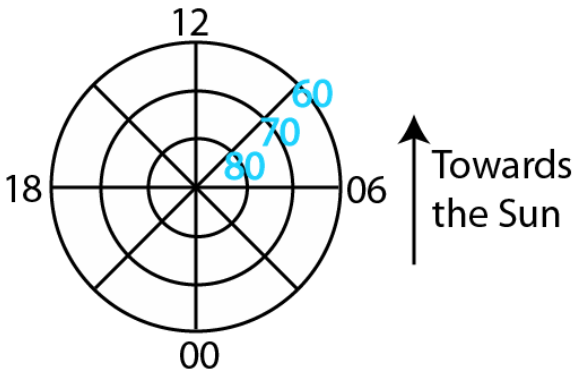

Figure 3-21: An illustration of the MLT system. The circles indicate the magnetic latitudes, also marked by the blue numbers (e.g. 80° magnetic latitude). The time sectors are divided into eight sectors where 00 is midnight and 12 is noon. The system is always located so that noon points towards the Sun.

12 MLT is referred to as "magnetic noon" and 0 MLT is referred to as the "magnetic midnight". The sector before midnight is the pre-midnight sector. The sector after midnight is the post-midnight sector. The MLT system is used in order to eliminate the local latitude variations, and to see how for example the aurora develops in time and space [*Langel and Hinze*, 1998, *Campell*, 2003].

Both the GSE and the GSM system are used when measuring quantities in space and when scientists present the measurements in papers. When presenting datasets from the Cluster satellites in the region < 20 R_E from the Earth in the magnetotail, the data are normally transformed into GSM coordinates [e.g., *Angelopoulos et al.*, 2008, *Baker et al.*, 2002, *Laitinen et al.*, 2007, *Nagai et al.*, 2005, *Nakamura et al.*, 2006, *Nakamura et al.*, 2002, *Ostgaard et al.*, 2009, *Petrukovich et al.*, 2005, *Runov et al.*, 2003, *Sergeev et al.*, 2008, *Sergeev et al.*, 2004, *Sergeev et al.*, 2003, *Sergeev et al.*, 2007, *Snekvik*, 2009, *Volwerk et al.*, 2003, *Volwerk et al.*, 2008, *Zhang et al.*, 2002].

When measuring the Earth's magnetic field on the ground, a different system is used. Historically the measurements of the Earth's magnetic field on the ground have been made in accordance with a topocentric system. The topocentric system consists of two type of systems: The HDZ- and the XYZ-component system [*Campell*, 2003] and is shown in Figure 3-22. In the first system, H is the horizontal component, D is the eastward angular direction of the horizontal component and Z is the vertical component of the magnetic field. The second system, the XYZ-components, consists of three orthogonal vectors, where the positive x direction is pointing towards the geographic north, the positive y direction is pointing towards

the geographic east and the positive z direction is the vertical component directed into the centre of the Earth.

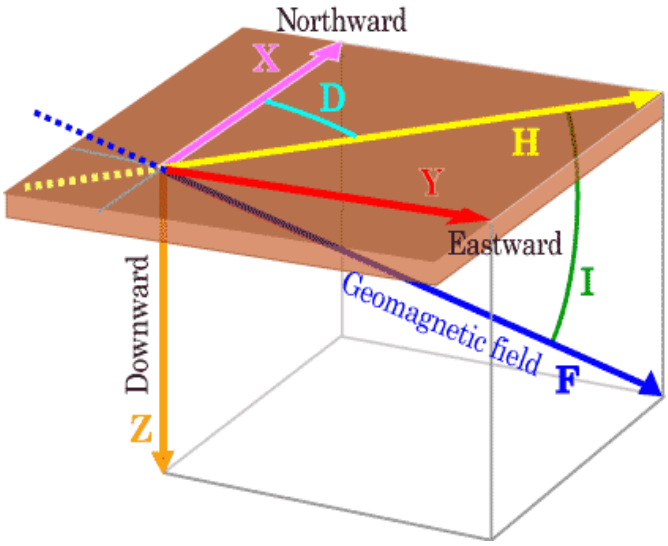

Figure 3-22: The vectors describing the topocentric coordinate system of the magnetic dipole field. The figure illustrates the XYZ-component (pink, red, orange) system, and the HDZ-component system (yellow, light blue, orange). I is the inclination of the geomagnetic field F. D is the angle between geographic north(x) and the horizontal component H of the magnetic field. Figure from *Wold Data Center for Geomagnetism* [2010].

The time used in the datasets is Universal Time (UT). Universal time is a time scale counted from 0 hours to midnight. The time scale is define to be as uniform as possible despite the variations related to the rotation of the Earth [*NMOC*, 2010].

3.2 The Cluster satellites and Cluster Active Archive

3.2.1 The Cluster mission and the satellite instruments

The Cluster mission consists of four identical satellites each containing 11 different scientific instruments, which have provided scientists with in situ data in the near-Earth space environment from 2001 through to the present day [*Escoubet et al.*, 2001]. The main goal of the mission is to study the plasma structures including the magnetotail, the polar cusps and the auroral zones. The satellites are named Rumba, Salsa, Samba and Tango but they are usually named SC1, SC2, SC3 and SC4, or C1, C2, C3 and C4, respectively. The satellites forming Cluster have a configuration which forms a tetrahedron with a common barycentre, i.e. an average of centre of mass. Such a structure is favourable when studying small scale structures in the magnetosphere region. After the first launch failure of Cluster I in 1996, a new launch was planned to take place during the summer of 2000, and was called the Cluster II-mission. The Cluster II-mission was successfully launched and on the first of February 2001 the mis-

sion was declared operational. The Cluster I mission was, and the Cluster II mission is a part of the Solar Terrestrial Science Program (STSP), the first "cornerstone" of the European Space Agency's (ESA) Horizons 2000 Program [*Escoubet et al.*, 2001]. Figure 3-23 illustrates the orbit of the Cluster satellites in late December 2004.

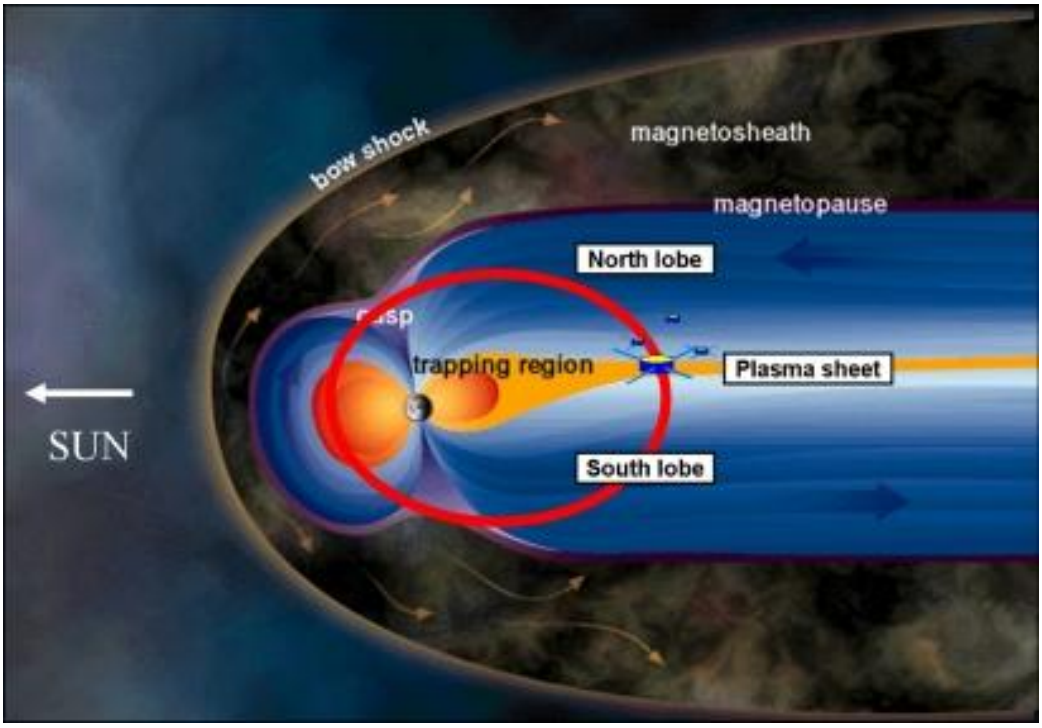

Figure 3-23: The red ellipse illustrates the polar orbit of the Cluster satellites during December 2004. The satellites have a favourable tetrahedral configuration in order to observe small scale plasma structures in the magnetotail. Figure from ESA [2007b] © ESA.

The Cluster satellites move in an elliptical polar orbit with perigee at $1.9 * 10^4$ km (ca 3.0 R_E) and apogee at $1.2 * 10^5$ km (ca 19 R_E) from the Earth [*ESA*, 2000]. The perigee is the point in an elliptical orbit that is closest to the Earth's centre, while apogee is the point that is farthest from the Earth's centre. The orbit period of the Cluster satellites are about 57 hours [*ESA*, 2000].

In this thesis data from the Fluxgate Magnetometer (FGM) [*Balogh et al.*, 2001], the Electric Field and Wave (EFW) [*Gustafsson et al.*, 2001] and the Cluster Ion Spectrometry (CIS) [*Réme and al.*, 2001] experiments are used.

3.2.2 Cluster Active Archive

The data used in this thesis from the Cluster satellites are downloaded from the Cluster Active Archive (CAA). The data that is used are the CAA-parameter (CP) data, which means that the data are prepared for scientific usage [*Harvey et al.*, 2008]. The data have been calibrated and are presented in the physical SI-units. If the variable from the calibrated file is not

in SI-units, the SI-conversion is given in the parameter information. The GSE coordinate system is the preferred coordinate system used in the CAA. The spacecraft position data are measured in a GSE centred coordinate system. The time is given in the Universal Time (UT).

The FGM instrument provides magnetic field measurement data to the CAA. The magnetic field B_x-, B_y- and B_z-components are transformed from the instrument sensor coordinate system into the GSE coordinates during the calibration process of the raw data. The calibration is done using a Fourier analysis [*French et al.*, 2001]. The accuracy of the magnetic field data depends on the instrument range, which is determined by the strength of the magnetic field the instrument should measure. The instrument range therefore changes when measuring different magnetic field magnitudes. The instrument range varies from 1 to 4 and is found in the data file the CAA. The instrument range of the instrument during the observation of the magnetic field data used in this thesis have range 2, which means that if measured magnetic field magnitude lies within $\pm$ 64 nT, then the magnetic field measurements have an achieved accuracy level of $0.1 - 0.2$ nT for the calibrated data [*French et al.*, 2001].

The CIS instrument provides data to the CAA on the velocity distribution of ions. The instrument consists of two sensors, the Hot Ion Analyzer (HIA) and the COmposition and DIstribution Function (CODIF) sensor. The preferred datasets from CIS when the spacecraft are located in the outer region of the magnetosphere, including the plasma sheet, is the CIS-CODIF mode [*Dandouras et al.*, 2004]. The CIS-CODIF experiment has not been operational at spacecraft 2 at all. On spacecraft 1 this experiment was in operation until 2004. In spacecraft 4 the experiment has been in normal operation during the whole period. After November 2003 the data quality from the experiment on spacecraft 3 was not reliable enough to be applied [*Dandouras et al.*, 2004]. The velocity datasets from the CAA are in the GSE coordinates.

The EFW instrument provides data to the CAA on measurements taken of the electric field. The electric field is measured as the potential difference between probe 1 and 2 and probe 3 and 4 (see Figure 3-24). Such measuring technique requires special attention to the data in order to know whether the measured electric field is the correct one, and not caused by any wake effects caused by the measuring spacecraft. A wake is a disturbance in the electric field measurements due to the satellite movement in the ambient plasma and affects the spacecraft potential of which the electric field are derived from [*Lindquist*, 1983]. The raw data signal is in the form of a sine wave, where the amplitude of the wave is the electric field amplitude and the electric field direction is given by the phase of the wave.

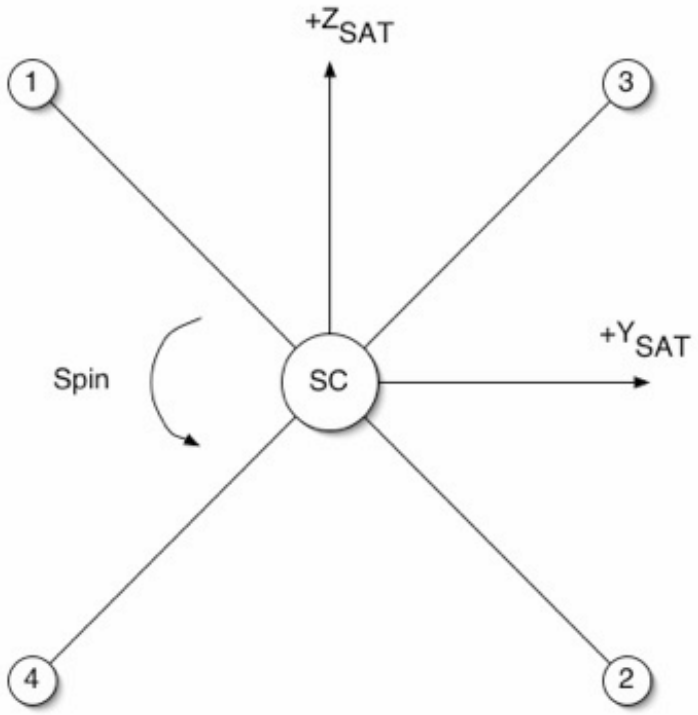

Figure 3-24: An illustration of one of the Cluster spacecraft (SC) with its four electrical probes. The satellite's coordinate system and the direction of spin is also included in this illustration. Figure from *Lindquist and EFW-Team* [2001].

The measurements are carried out in the satellite spin plane, or the ISR2 coordinate system, which is approximately the same as the GSE coordinates. The E_x- and E_y-components are found from a least-square-fit to the raw data of the form

$$y = A + Bsin(\omega t) + Ccos(\omega t) + Dsin(2\omega t) + Ecom(2\omega t) + .. \quad (3.1)$$

averaged over four seconds, which corresponds to one spin period of a Cluster satellite. Details regarding the terms of equation (3.1) are given in the user guide of the EFW instrument [*Lindquist and EFW-Team*, 2001]. The sine wave is first fitted to the raw data, then outliers are removed, and finally the sine wave re- fitted. The outliers are measurements which are larger than 2* the standard deviation from the first fitted sine wave.

The quality of the electric field data from the CAA is given in the form of a number between 0-4. When analysing electric field datasets, this quality number should be taken into consideration. Whereas level 3-4 represents data of good quality, for publication use, the data of quality level 0-2 is rated as poor and should be used with caution [*Lindquist and EFW-Team*, 2001]. The quality number reports whether the electric fields measured are due to wake effect or actual electric fields not caused by the spacecraft. The data file containing the E_x and E_y measurements contain also a measure of the standard deviation of the raw data points from the least-square fit sine wave, given as "E_sigma", and the quality number of the

instrument. The E_z-component is calculated by subtracting the $V \times B$-field induced by the spacecraft and by assuming that $\vec{E} \cdot \vec{B} = 0$ [*Harvey et al.*, 2008].

The EFW data contain also the spacecraft potential. The spacecraft potential is a measurement of the electron flux in the region where the spacecraft is located. A large electron flux will contribute to a small spacecraft potential, while a smaller electron flux will contribute to a larger spacecraft potential. The spacecraft potential in the CAA is the average of the potentials of the four probes relative to the spacecraft potential [*Lindquist and EFW-Team*, 2001], see Figure 3-24 for an illustration of the probes. Because a decrease in the electron flux results in an increase in the spacecraft potential, it is usual to plot the inverse of the spacecraft potential so that an increase in the graph corresponds to an increase in the electron density [*Pedersen et al.*, 2008].

3.3 The IMAGE satellite

The Far Ultraviolet imaging system on the satellite named IMAGE is designed in order to observe several substorm phenomena like auroral formation, poleward expansion and recovery. The IMAGE satellite provides data which are suitable for the investigation of auroral substorm signatures in this thesis.

The IMAGE was the first space borne program for observing the magnetosphere by remote sensing techniques only. The IMAGE satellite has an elliptical polar orbit with an apogee of $40 * 10^3$ km (6.3 R_E) and a perigee of 10^3 km (0.2 R_E) from the Earth. During the first two years of operation the apogee was in the northern hemisphere. The orbit period is approximately 14 hours.

The Far Ultraviolet (FUV) imaging system on the IMAGE satellite is designed to monitor a substorm development in the Earth's ionosphere, to observe the extent and the form of the auroral activity and to record periodic structures seen in the aurora. The FUV imaging system contains a Wideband Imaging Camera (WIC), a Spectrographic Imager (SI) and a Geocorona (GEO) photometer. In this thesis only datasets from WIC are used. All of the instruments of the FUV imaging system are located in such a way that the field of view points radially outward away from the spin axis. The spacecraft rotates with a spin period of 2 minutes which is why the data from WIC are provided each second minute. Figure 3-25 gives an illustration of the cross section of the field of view from FUV when the IMAGE satellite is located near apogee [*Mende et al.*, 2000b]. The cross section is marked with the gray area.

WIC [*Mende et al.*, 2000a] is a wideband imaging camera which observes auroral emissions in the wavelength range 140 – 190 nm. This means that at an altitude of 4-5 R_E the entire auroral oval is covered. WIC has an exposure time of 10 seconds, which means that each auroral feature spends 10 seconds in WIC's field of view per image. The data from the IMAGE WIC used in this thesis are given in the MLT coordinate system.

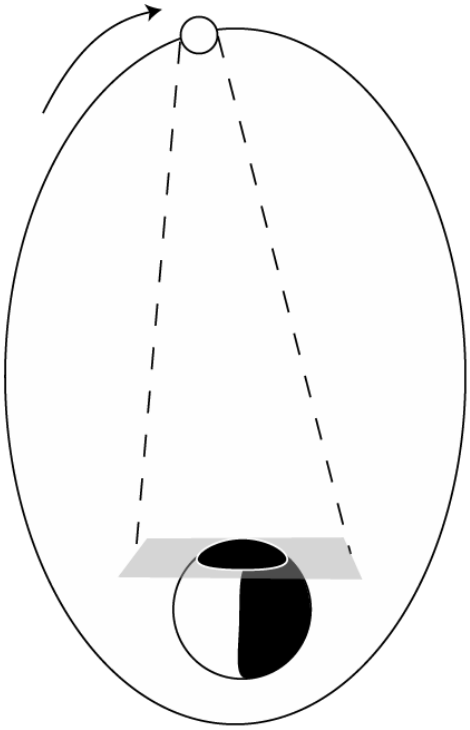

Figure 3-25: An illustration of the cross section of the IMAGE satellite field of view marked as the grey area in the figure from near apogee. Figure inspired from *Mende et al*. [2000b].

3.4 Magnetic ground station measurements

3.4.1 The Circum-pan Pacific Magnetometer Network

The Circum-pan Pacific Magnetometer Network (CPMN) consists of a group of fluxgate magnetometer observatories that are mostly located along the 210° magnetic meridian [*Yumoto*, 1996, *Yumoto and Grp*, 2001]. Figure 3-26 displays a global view station map of the CPMN, which clearly illustrates that the stations are located at different geographical latitude and longitude around the world. The data used in this thesis from the CPMN chain are high time resolution data, with a resolution of averagely one second. Using a magnetometer network like the CPMN makes it possible to study the magnetospheric processes by distin-

guishing both changes in time and spatial variations. The datasets are in the HDZ dipole coordinate system and have a sufficient resolution in order to observe the Pi 2 signatures.

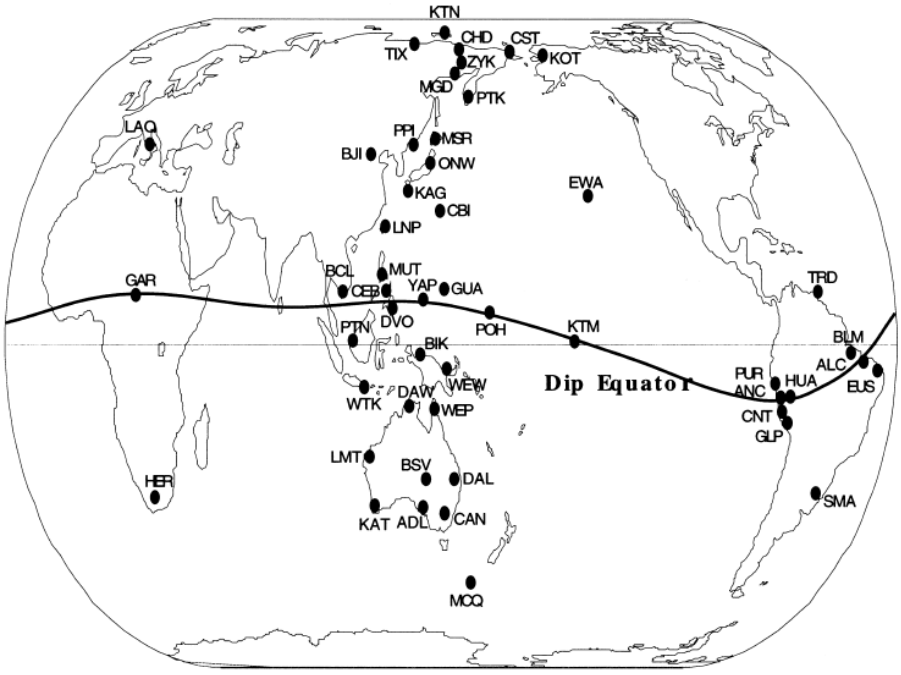

Figure 3-26: A map of the CPMN stations that are situated around the world. The stations are mostly located along the 210° magnetic meridian. Figure from *Yumoto and the CPMN group* [2001].

3.4.2 The INTErnational Real-time MAGnetic Observatory NETwork

The INTErnational Real-time MAGnetic observatory NETwork (INTERMAGNET) consists of a wide range of ground stations with locations distributed all over the world both in the northern and in the southern hemisphere (see Figure 3-27). INTERMAGNET is a global network for observatories monitoring the geomagnetic field. INTERMAGNET was established in 1987 as a result of data merging between two organisations working with geomagnetic field data. Figure 3-27 illustrates the location of each station in the network marked with the station code. The full name of each station is given at the homepage of INTERMAGNET [*INTERMAGNET*, 2009b]. The data being used are definitive data: They have been verified in a process where contaminations of the data have been removed. Such corrections include the removal of spikes and the filling in of gaps in the data. The daily average measurements of the geomagnetic field caused by the eastward and westward flowing electrojets in the dusk and dawn sides respectively, have also been removed from the definitive data [*INTERMAGNET*, 2010]. The datasets from INTERMAGNET are in the HDZ dipole coordinate system, where Z is positive towards the nadir and H is the intensity of the horizontal

component. Nadir is the opposite of zenith and so is positive in the vertical direction pointing towards the centre of the Earth.

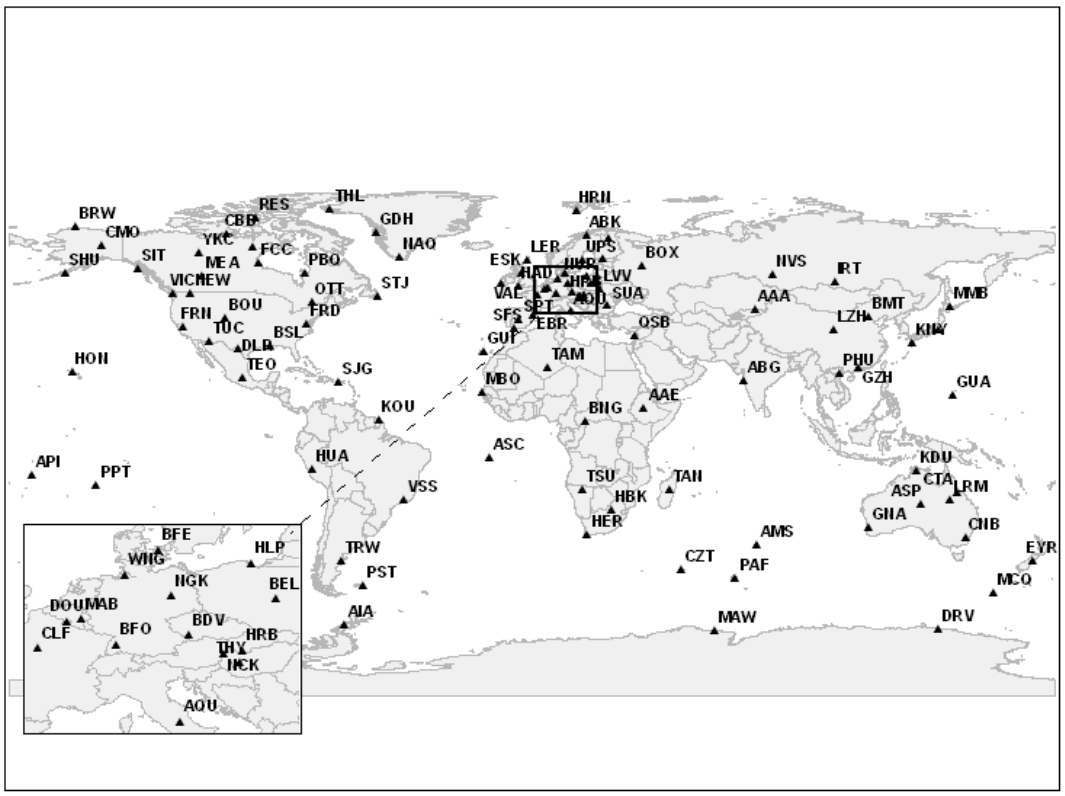

Figure 3-27: The geographic locations of the stations in the INTERMAGNET network of stations monitoring the geomagnetic field around the world. Figure from *INTERMAGNET* [2009a].

3.5 OMNI web

OMNI data are used for investigating the solar wind in advance of a magnetic reconnection. The OMNI web is a part of the NASA Goddard space flight center data facility website. The solar wind data used in this thesis are an average of the magnetic field and plasma data measured from the satellites Advanced Composition Explorer (ACE) Geotail and Wind located within the solar wind when measuring. Geotail, Wind and Cluster are a part of the International Solar Terrestrial Physics (ISTP) program where the goal is to obtain simultaneous observations of the Sun-Earth space environment. The project is a collaboration between NASA, ESA and the Institute of Space and Astronautical Science (ISAS) of Japan [*Acuna et al.*, 1995]. To simplify the analysis of solar wind-magnetosphere interaction, the data from the satellites have been time-shifted. This means that the solar wind data, which are measured by different satellites located at different places in the solar wind, are time-shifted to a com-

mon place at the magnetopause. The datasets provided by OMNI are time-shifted from the satellites to the Earth's bow shock nose (for details regarding the time-shift, see *King et al.* [2006]). The ACE datasets in OMNI are level 2, which means the data are verified for scientific use, with a 16 second averaged magnetic field data and 64 second averaged plasma data. The Geotail datasets are created by using an average of 15 second of the 3 second resolution data in the available datasets. The Wind datasets are 15 second averaged from the available 3 second average data. The details regarding the time-shift calculations and assumptions are found on the OMNI web [*King et al.*, 2006].

4 Methods

The methods used to analyse and present the data in chapter 5 are explained here. The calculations were carried out in Matlab 7.7.0, and the Matlab codes used are found in appendix E as the MVA.m file.

4.1 Variance analysis of the magnetic field

Close to midnight in the Earth magnetotail the main magnetic field component is directed approximately along the $\hat{\boldsymbol{x}}_{GSM}$ direction, but away from the midnight sector there is a contribution to the $B_{y\,GSM}$-component due to the flaring of the magnetotail [*Kaymaz et al.*, 1994]. Flaring of the magnetic field can be seen as the dipole spreading of the field lines in the y direction, see Figure 4-28.

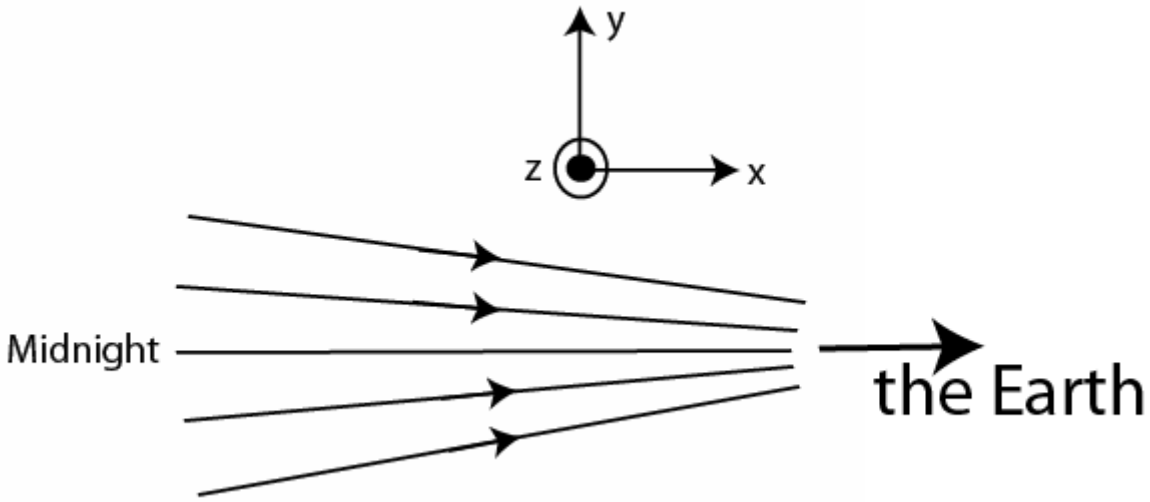

Figure 4-28: An illustration of the flaring of the magnetic field with increasing distance from midnight in the east-west direction. The lines with arrows are magnetic field lines in the northern hemisphere.

The flaring increases with an increasing distance from midnight. By performing a variance analysis on the magnetic field measurements, local time effects due to flaring can be removed [*Nakamura et al.*, 2002] and underlying structures in the magnetic field measurements may appear more distinct. This method is illustrated in Figure 4-29 where the measured data points of the magnetic field components are represented by the blue dots and the black coordinate system corresponds to the GSM coordinate system. A new coordinate system (shown in red in Figure 4-29) can be constructed based on the direction of maximum variance. When rotating the data into the modified coordinate system the data do not change, only the representation. The data points plotted in the modified coordinate system are seen to be located

mainly along one of the axes. In the GSM coordinate system they are not associated with any of the axes. This means that when presenting the data in the modified coordinates system, structures in the dataset are more apparent than when the dataset was presented the GSM coordinates.

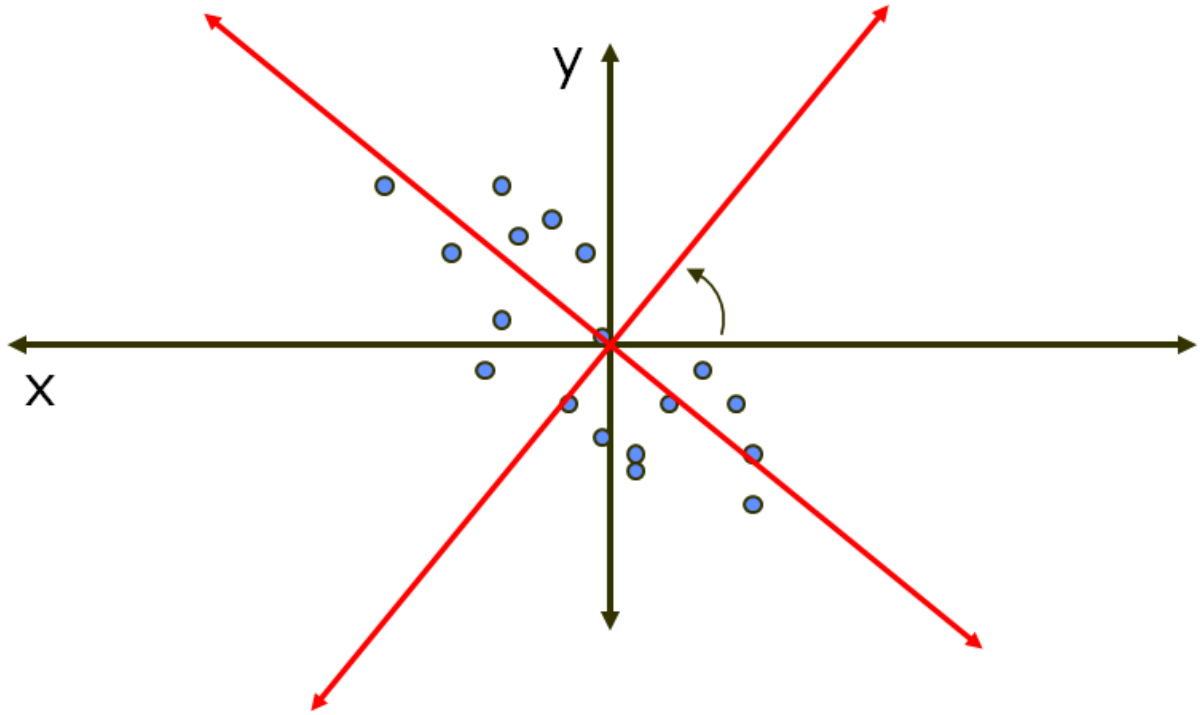

Figure 4-29: The principles of the main component analysis. The original coordinate system is black and the red coordinate system is the new, calculated system. The blue dots are the measured data points.

In this thesis a coordinate system that is fitted to the current sheet in the magnetic reconnection region, i.e. a coordinate system with the z-axis pointing in a direction perpendicular to the current sheet, as the modified coordinate system. The coordinate system is found by performing a variance analysis on the magnetic field measurements. The B_x- and B_y-components are then plotted in this coordinate system in order to reveal structures in the dataset which may reflect the signatures of the Hall magnetic field.

In order to perform a variance analysis it must be assumed that the current sheet can be described as a time stationary structure and that the structure is crossed by the Cluser satellites [*Dunlop et al.*, 1995]. The first application of the variance method on satellite data was done by Sonnerup and Cahill in 1967 [*Sonnerup and Cahill*, 1967] while they investigated the direction of the normal to the magnetopause current sheet.

4.1.1 The mathematical approach to a variance analysis

Since $\nabla \cdot \boldsymbol{B} = 0$, the normal $\hat{\boldsymbol{n}}$ of an ideal thin electromagnetic structure must be continuous across the structure. This condition may be applied to a current sheet, when the current sheet thickness is much smaller than current sheet length (in the xz plane). When a spacecraft measures the magnetic field vector $\boldsymbol{B} \cdot \hat{\boldsymbol{n}}$ M times during a current sheet crossing, the direction in which the normal vector of the current sheet points will be the direction where the vector field has minimum variance [*Sonnerup and Cahill*, 1967]. The variance of the $\boldsymbol{B} \cdot \hat{\boldsymbol{n}}$ vector is given as

$$\sigma^2 = \frac{1}{M}\sum_{i=1}^{M}\left|\left(\boldsymbol{B^i} - \langle \boldsymbol{B} \rangle\right) \cdot \hat{\boldsymbol{n}}\right|^2 \tag{4.1}$$

where $\langle \boldsymbol{B} \rangle = \frac{1}{M}\sum_{i=1}^{M} \boldsymbol{B}^i$ and $\boldsymbol{B^i}$ are the individual magnetic field measurements and consists of $\boldsymbol{B^i} = (B_x, B_y, B_z)$ measured in a Cartesian coordinate system (e.g. GSM or GSE). The normal of the current sheet can be found by minimising equation (4.1). Such a minimisation is equivalent to finding the smallest eigenvalue and corresponding eigenvector of the covariance matrix

$$M^B_{\mu\nu} \equiv \langle B_\mu B_\nu \rangle - \langle B_{\boldsymbol{\mu}} \rangle \langle B_{\boldsymbol{\nu}} \rangle \tag{4.2}$$

where the subscripts $\mu, \nu = 1, 2, 3$ denotes the Cartesian components of the magnetic field, i.e. the B_x-, B_y- and B_z-components. The eigenvectors of (4.2) represent a new coordinate system, rotated with respect to the original coordinate system. The normal $\hat{\boldsymbol{n}}$ to the current sheet is pointing along the direction of minimum variance of the components in the magnetic field dataset [*Sonnerup and Cahill*, 1967], and the main component of the current sheet is directed along the maximum variance [*Johnson and Wichern*, 2007]. In order to use the eigenvalues obtained from the variance analysis in such a minimum and maximum variance analysis, the components should be well determined. This means that the ratio between the intermediate and the minimum eigenvalue should be larger than 1.5 [*Sonnerup and Cahill*, 1967] in order to be able to use the eigenvector corresponding to the smallest eigenvalue as the normal of the current sheet. When using the maximum variance analysis the qualification multiplier ω, can be used. ω is the ratio of each eigenvalue to the sum of eigenvalues. If most of the total variance ($\omega > 80 - 90$ %) is located in one main direction, then this direction can "replace" the original without losing too much information [*Johnson and Wichern*, 2007]. The calculated eigenvalues and the qualification multiplier of the magnetic field datasets used in this thesis are given in chapter 5.

The neutral sheet in the Earth's magnetotail region studied here, is mainly oriented in the xy_{GSM} plane [*Kaymaz et al.*, 1994] and it is assumed that an average plasma sheet normal is directed parallel to $\hat{\boldsymbol{z}}_{GSM}$ [*Ostgaard et al.*, 2009]. The orthogonal unit vectors in the Cartesian coordinate system are given as

$$\hat{\boldsymbol{e}}_{GSM}: \left\{ \begin{pmatrix} 1 \\ 0 \\ 0 \end{pmatrix}, \begin{pmatrix} 0 \\ 1 \\ 0 \end{pmatrix}, \begin{pmatrix} 0 \\ 0 \\ 1 \end{pmatrix} \right\} \tag{4.3}$$

The xy_{GSM}-coordinate system is shown as the black axes in Figure 4-29. The new coordinate system is calculated by using the maximum variance analysis eigenvector of the maximum eigenvalue as the x-axis. The reason for using the maximum variance analysis as the x-direction is because the main direction of the current sheet is in the x-direction.

Assuming $\hat{\boldsymbol{x}}'$ is the eigenvector corresponding to the largest eigenvalue obtained from the variance analysis, the eigenvector forming the x-component of the new coordinate system is given as

$$\hat{\boldsymbol{e}}_{NEW_x} = \hat{\boldsymbol{x}}' = \begin{pmatrix} x_1 \\ y_1 \\ z_1 \end{pmatrix} \tag{4.4}$$

The $\hat{\boldsymbol{z}}'$ is defined as the normal to the current sheet plane and is given by

$$\hat{\boldsymbol{e}}_{NEW_z} = \hat{\mathbf{z}}' \approx \hat{\mathbf{z}}_{\mathrm{GSM}} = \begin{pmatrix} 0 \\ 0 \\ 1 \end{pmatrix} \tag{4.5}$$

The y-component in the new coordinate system y' is given by

$$\hat{\boldsymbol{e}}_{NEW_y} = \hat{\boldsymbol{y}}' = \hat{\mathbf{z}}' \times \hat{\mathbf{x}}' = \begin{pmatrix} 0 \\ 0 \\ 1 \end{pmatrix} \times \begin{pmatrix} x_1 \\ y_1 \\ z_1 \end{pmatrix} \tag{4.6}$$

These three vectors constitutes the current sheet coordinate system with a normal $\hat{\boldsymbol{z}}' = \hat{\boldsymbol{z}}_{GSM}$, into which the magnetic field components B_x and B_y are rotated when the Hall magnetic field is presented.

4.2 Timing analysis

As a supplement to the variance analysis, multipoint timing analysis can be used in order to determine the direction of the normal to a plane surface crossing a satellite. When using multiple spacecraft, the easiest way to perform a multipoint timing analysis is to find an instance when the satellites measures a common feature (e.g. when B_x changes polarity). It is assumed that the feature has an approximately constant velocity when crossing the satellites and that it can be described in 1D. By selecting the timing one of the spacecraft's observations as a basis

for the method, the time delay until the other spacecraft observe the same feature are obtained. The separation distance between the spacecraft is known and so it is possible to calculate the normal to and the velocity of the feature crossing the satellite. The program used here requires four spacecraft to observe the same feature.

4.3 Mapping of magnetic field lines

The method for finding the footpoint of a magnetic field line is called topological or magnetic field mapping [*Paschmann et al.*, 2002]. The mapping method is based on models of the magnetic field around the Earth using the frozen-in assumption that the flow of the particles follows the magnetic field lines through space, i.e. the frozen-in assumption. Such mapping models are developed based upon large amounts of datasets which have been collected from high-altitude spacecraft, together with modelling of the magnetosphere current system. Since the magnetosphere is a dynamic system the mapping method is a complex issue. By using different mapping models, the position of the average footpoint can be limited inside an area with boundaries given by the footpoint in each model.

In order to determine the ionospheric footpoint of the magnetic field lines located in the same region as the Cluster satellites, different models that perform field line mapping have been used. The models used in this thesis are the Tsyganenko models 87, 89 and 96 [*Tsyganenko*, 1987, *Tsyganenko*, 1989, *Tsyganenko*, 1995]. There is also a Tsyganenko 01 model. The T01 model is, however, an empirical model of the inner part of the Earth's magnetosphere ($x_{GSM} > -15$ R_E) [*Tsyganenko*, 2002], and is therefore not possible to use in this thesis due to the > 15 R_E location of the Cluster satellites. Each model provides one footpoint and by studying all the footpoints simultaneously, it is possible to draw a circle surrounding the footpoints. Within this circle it is most likely to find the actual footpoint of the magnetic field lines at that extend out to the Cluster satellites. This circle is used when searching for ground stations providing geomagnetic field measurements that may contain substorm signatures.

The Tsyganenko models simulate the structure of the magnetosphere based on the major current system in the magnetosphere. Each part of the current system is parameterised by factors that depend on the location in the magnetosphere, the dipole tilt angle, the level of the geomagnetic activity, the solar wind pressure and the interplanetary magnetic field properties. After using a least-square fitting technique in order to minimize the errors between the ob-

served values and the model, the Earth external magnetic field is given [*Tsyganenko*, 1987, *Tsyganenko*, 1989, *Tsyganenko*, 1995].

In the T87 and T89 models the Kp-index[*Bartels*, 1950] is used as a model parameter[*Tsyganenko*, 1987, *Tsyganenko*, 1989]. The Kp-index is obtained from the WDC Kyoto Observatory and is an index based on data from magnetic observatories at middle and high northern latitudes. The index is generated with a three hour time resolution, and has a range of 0 to 9. A Kp-index equal to 0 corresponds to very quiet conditions and 9 correspond to very disturbed conditions.

In the T96 model the D_{ST}- index [*Campell*, 2003] is used as a parameter together with the B_x-, B_y- and B_z-component of the interplanetary magnetic field and the solar wind pressure [*Tsyganenko*, 1995]. The average of the IMF components over the time interval when reconnection is observed by the Cluster satellites is used. The D_{ST}-index is obtained from the WDC Kyoto Observatory with an hourly resolution. This index is a global mean value of the geomagnetic activity at low latitudes.

The Orbit Visualization Tool (OVT) for Cluster uses the Tsyganenko models. The program is developed in order to visualize the satellite orbits in the Earth's magnetic field in 3D [*Stasiewicz et al.*, 2003]. Documentation of the software is found at the OTV-homepage [*Khotyaintsev*, 2000].

5 The reconnection and substorm events

In this section, the data analyses are presented including analyses of the magnetic reconnection and substorm signatures, and the timing of the onset of the different signatures. The data from the Cluster satellites are analysed based on the magnetic reconnection signatures given in chapter 2.5. These being: Reversal of fast plasma outflow jets, simultaneous reversal of the vertical magnetic field component and the presence of a quadrupole Hall magnetic field. Ionospheric and ground measurements are presented for each event, and the analysis of these data is based on the substorm theory described in chapter 2.6.1. The two events are presented in this chapter as the 26th September 2005 event and as the 22nd August 2001 event. The data programs used in the analyses are found in appendix E.

5.1 The 26th September 2005 event

Sergeev et al. [2007] reported about three plasma injections between 08 UT and 10 UT observed by the Cluster satellites at ~ -15 R_E in the magnetotail on the 26th September 2005. The first injection started at 08.43 UT and was followed by another at 09.31 UT and a final one at 09.41 UT. These three injections corresponded in time with an enhancement of auroral activity that was observed by the IMAGE satellite. In this thesis the time period of investigation was set between 09.30 and 10.00 UT.

The GSM z-axis during this event was tilted ~ 33° towards dawn in the GSE coordinate system. The difference between the first and last measured tilt angle in the time interval was 0.4°, which is much less than the total angle of ~ 33°. A mean value of the rotation angle was therefore used when transforming the datasets from the GSE system into the GSM system.

5.1.1 Data analysis and observations in the magnetosphere

From 09.30 UT to 10.00 UT, 26th September 2005, the Cluster constellation of satellites was located at $(x, y, z)_{GSM} = (-15, 3.7, -1.0)$ R_E, 15 R_E from the Earth into the magnetotail.

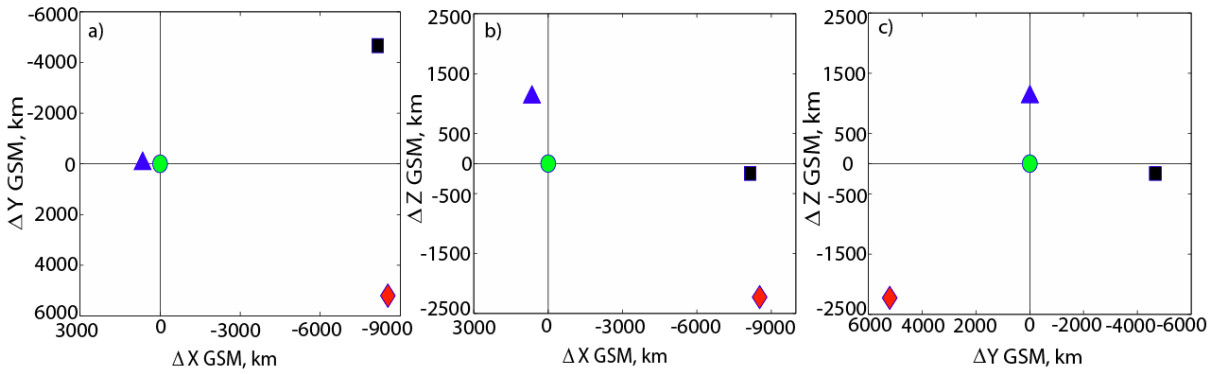

Figure 5-30: The position of the Cluster satellites in the GSM coordinate system, using the SC3 location as the origin. Each spacecraft is represented with its colour identifier. The Cluster colours are SC1-black, SC2-red, SC3-green and SC4-blue.

The Cluster tetrahedron configuration in the GSM coordinate system during the chosen time interval is shown in Figure 5-30. Panel a) is in the xy_{GSM} plane, panel b) is in the xz_{GSM} plane and panel c) is in the yz_{GSM} plane. As seen from the figure, spacecraft (SC) 4 – the blue triangle – was located closest to Earth. SC2 - the red diamond – was located further south in the z_{GSM} direction compared with the other spacecraft. SC1 – the black square – and SC3 – the green circle – were located at nearly the same level in both the yz_{GSM} and xz_{GSM} plane. The maximum separation distance was $1.1 * 10^4$ km, between SC2 and SC4, and the minimum separation distance was $1.2 * 10^3$ km, between SC3 and SC4. The Cluster barycentre moved at a speed of 1.4 km/s, which was a speed much less than the speed in the plasma registered by the satellites, which will be shown later. The satellites were therefore assumed to be stationary compared to the plasma during the studied time interval.

The location of the Cluster satellites in the magnetosphere

The plasma β for this event was calculated (see chapter 2.4.4) using datasets from the FGM- and CIS-experiment. Since the CIS-experiment only worked on SC4 in 2005, the plasma β was calculated for this spacecraft only. A plasma sheet has a typical plasma β value > 0.3 and in the plasma sheet boundary layer $0.02 < \beta < 0.05$ [*Baumjohann et al.*, 1988, *Baumjohann et al.*, 1989]. Registered values below 0.02 indicate a position of the spacecraft in the lobes. The spacecraft potential was here used as a supplement to the plasma β in order to establish the position of the spacecraft in the magnetotail. The spacecraft potential can be used as a good estimate of the electron density in the region near the spacecraft [*Pedersen et al.*, 2008]. Large values of spacecraft potential have been observed in the lobe region with

values from $|20| - |50|$ V. Spacecraft potential values between $|10| - |15|$ V correspond to the plasma sheet region [*Lindquist*, 1983].

In Figure 5-31 panel a) shows the calculated plasma β for SC4 between 09.30 and 10.00 UT. By zooming into the low plasma β values, it is easier to distinguish between the different regions of the plasma sheet, the plasma sheet boundary layer and the lobes. This is shown in Figure 5-31 panel b) where the values of β are shown between 0 – 0.3. The upper limit was chosen due to the low values of plasma β in the plasma sheet region. Panel c) shows the spacecraft potential from all four spacecraft.

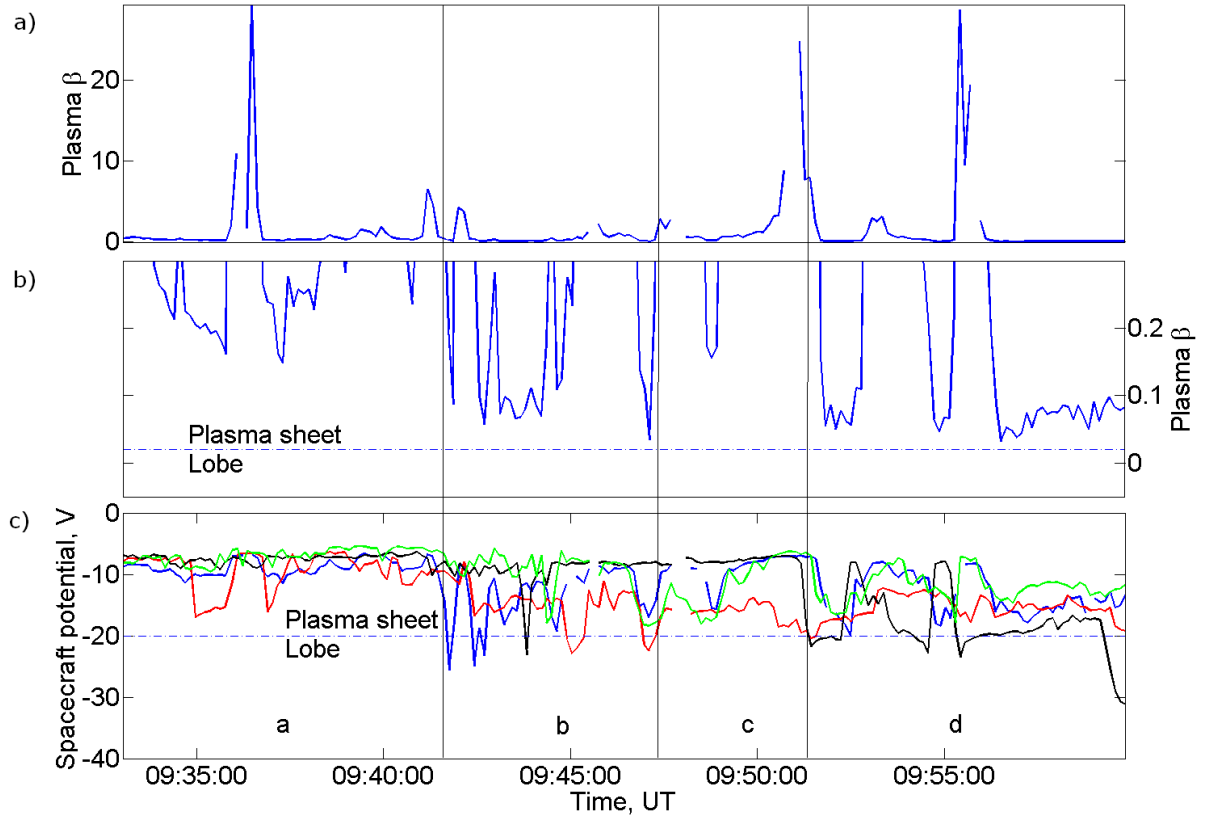

Figure 5-31: The plasma β values from SC4 are drawn in blue. The spacecraft potential for each spacecraft is drawn in the respective Cluster colours: SC1-black, SC2-red, SC3-green and SC4-blue. The plasma β values presented in panel b) are the same as presented in panel a), but in panel b) the plasma β values are limited between 0 – 0.3.

Based on the plasma β values in Figure 5-31 panel a) and panel b) which were above 0.02 during the whole interval, SC4 was probably located within the plasma sheet and plasma sheet boundary layer during the whole time period. The β value 0.02 is marked in Figure 5-31 panel b) with a dashed line. Studying the spacecraft potential of the four spacecraft during the same interval shows that there were two periods when the spacecraft potential exceeded |20| V. Those two periods are marked with "b" and "d". During those two periods SC1, SC2 and SC4 may have entered the plasma sheet boundary layer or the lobe for very

short time periods, seen as the spikes in the spacecraft potential measurements during period "b" and for SC1 during period "d". Since there are no strong boundaries between the lobes and the plasma sheet, and the values which were used here as a distinction between the regions are not finite, it was difficult to determine whether or not the spacecraft did enter the lobe or whether they were only located in the plasma sheet boundary layer.

Observations

The data from the Cluster satellites used in the examination of this event have been collected from the CAA. The data used are H^+ (CIS) data from SC4, the magnetic field (FGM) data and the electric field (EFW) data from all four spacecraft, and the spacecraft potential data from SC4. See chapter 3.2 for further details concerning the experiments on Cluster. The CIS data had a sampling period of 8 seconds which corresponds to an average of two spin periods. The FGM and EFW data were averaged to a sampling rate of 4 seconds and were so-called spin resolution data.

Figure 5-32 shows the H^+ velocity, the magnetic field, the electric field, the H^+ density and the spacecraft potential between 09.30 UT and 10.00 UT. The GSM coordinates were used unless otherwise specified.

As seen from Figure 5-32 panel a), SC4 observed four intervals of earthward and tailward directed high speed flows, shown as the positive and negative excursions in the V_x-component. During the first interval, marked as "1" in Figure 5-32, the ions reached an outflow velocity of $\sim$500 km/s directed earthward ($V_x > 0$). In the second interval, marked as "2" in Figure 5-32, SC4 observed first an earthward high speed flow reaching $\sim$400 km/s, then a tailward high speed flow reaching $\sim$1000 km/s. From 09.43.30 UT to 09.50.00 UT V_x fluctuated around zero. During the third interval SC4 observed a new earthward directed high speed flow reaching $\sim$500 km/s. In the last interval, marked as "4" in Figure 5-32, the spacecraft observed mainly earthward directed high speed flows reaching $\sim$900 km/s. Figure 5-32 panel e) displays the B_z measurements of the Cluster satellites. For SC4 the component was positive during the first interval reaching values of ~5 nT, before it started fluctuating around zero until the start of the second interval. During the second interval there was a reversal of the B_z-component, it was positive during the first part of the interval and negative during the second part of the interval reaching negative values of ~15 nT. The component stayed mainly negative until the start of the third interval.

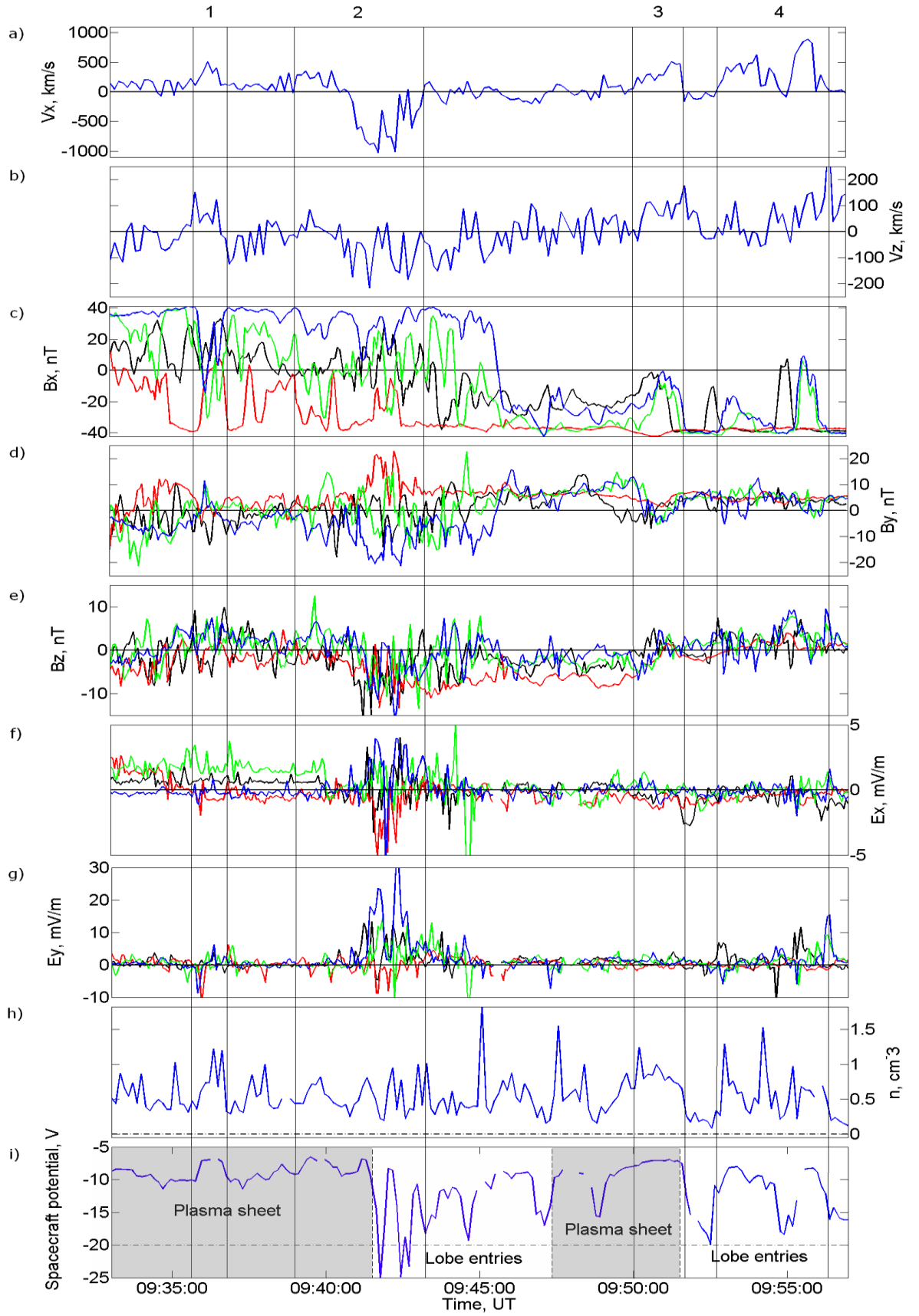

Figure 5-32: H^+ velocity, magnetic and electric field, density and spacecraft potential data from all four Cluster spacecraft. The velocity, the density and the spacecraft potential are from SC4. Details regarding the data are given in the text.

During the third and the last part of the fourth interval where high speed outflows were registered, the B_z the component was mainly positive and reached a value of ~10 nT during the last outflow. During the first part of the last outflow interval the spacecraft did not register a reversal in the B_z component.

The correlation between the V_x and B_z reversals during the high speed intervals indicates that SC4 went from being located at the earthward side of the reconnection region to being located at the tailward side. The second outflow period coincided with the period when the spacecraft potential of SC4 (panel i)) suggested plasma sheet boundary layer or lobe entries. This indicates that SC4 was located in the plasma sheet boundary layer. During the most intense outflow period (when V_x was largest) the spacecraft was located far from $B_x = 0$.

If SC1, SC2 and SC3 entered the reconnection region, the B_z measurements should have revealed similar signatures as those registered by SC4. The B_z measurements from SC1 fluctuated around zero until ~09.40 UT. During the period from 09.40 UT to 09.47 UT the component was mainly negative with a few crossings to positive. A reversal of B_z from negative to positive occurred in the middle of the third high speed flow observed by SC4, and after 09.51 UT the component was mainly positive with only a few crossings. The B_z-component measured at SC2 went from being negative in the beginning of the first interval, to fluctuating around zero until the start of the second interval. During the period from the start of the second interval and on to the middle of the third interval, the component values were mainly negative. During the third outflow the component went from being negative to slightly positive. At the same time as the last high speed outflow, measured by SC4, the B_z measurements increased again reaching a value of ~ 4 nT. The B_z measurements from SC3 showed the same tendency as the B_z measurements from SC4. The SC3 measured a positive B_z during the first interval, negative during the second outflow period and was positive during the last high speed outflows. During the last high speed outflow, there was a significant increase in the B_z measurements registered by SC3 and SC4. The values changed from 0 nT to ca 10 nT. The correlation between the B_z measurements from SC3 and SC4 indicates that the two spacecraft observed the same signatures during the four high speed intervals marked in Figure 5-32. It is therefore possible to assume that SC3 was located tailward of the reconnection region during the second interval, and earthward during the other intervals.

The correlation between the B_z measurements from SC1 and SC4 indicates that the two spacecraft observed similar signatures during the second and third outflow intervals. It is

therefore possible to assume that also SC1 was located tailwards of the reconnection region during the second interval, and earthward during the third interval. However, due to lack of ion data from SC1 it is difficult to determine the location of the spacecraft with respect to the reconnection region during the other intervals marked in Figure 5-32.

The measurements of B_z from SC2 differ from the other spacecraft B_z measurements. During the first high speed outflow interval the component was close to zero. Then the component was negative during the second interval of high speed flows, and became positive during the third and fourth interval when the earthward flows were detected by SC4. This suggests that the spacecraft may have seen some of the same signatures as those registered by SC3 and SC4 during the third and fourth interval, but the signatures were weaker, suggesting that SC2 was located further away from the reconnection region in the z direction than the other spacecraft. An additional lack of ion data means that it is not possible to determine the position of the spacecraft relative to the reconnection region.

During the time interval between 09.34 UT and 09.57 UT the Cluster satellites crossed the neutral sheet several times (see Figure 5-32, panel c)). The neutral sheet is located approximately at $B_x = 0$ [*Ness*, 1965]. During the first interval in Figure 5-32, SC1, SC3 and SC4 approached $B_x = 0$ from the northern hemisphere ($B_x > 0$) and SC2 from the southern hemisphere ($B_x < 0$). SC2 stayed mainly in the southern hemisphere during the whole time interval investigated here (09.30 – 10.00 UT). These changes in the B_x measurements, which corresponded with the observations of a high speed flow and an increasing B_z, indicated a sudden change of magnetic field topology toward the dipole shape. The changes were rapid and happened twice during the second interval.

From 09.37 UT to 09.45 UT there were small but rapid fluctuations the B_x measurements registered by SC1 and SC3. Such rapid changes indicate a fluctuating current sheet during the first part of the reconnection interval. The small fluctuations measured by SC3 were systematically delayed compared to the ones registered by SC1, suggesting that the fluctuations moved towards the tail centre in the xy_{GSM} plane, and were directed earthward in the xz_{GSM} plane. The spatial extent of the fluctuations was limited within a region of $\sim$1000 km in z_{GSM} since they were only detected by SC1 and SC3.

SC4 was located in the northern hemisphere ($B_x > 0$) until ~ 09.45 UT when the spacecraft crossed the neutral sheet (large plasma β in Figure 5-31). During the rest of the interval SC4 was mainly located in the southern hemisphere ($B_x < 0$). In the period after 09.50 UT SC1, SC3 and SC4 registered large amplitude variations in the B_x measurements

($B_x > |50|$ nT). The fluctuations were observed by SC1 before they reached SC3 and SC4. The fluctuations were larger and slower than the fluctuations registered by SC1 and SC3 between 09.37 and 09.45 UT. The fluctuations measured by SC4 corresponded in time with the third and the fourth high speed outflow. Due to lack of ion data from SC1 and SC3, it is not possible to say whether the fluctuations corresponded to high speed outflows registered by the spacecraft. Such large amplitude variations have frequently been observed in the magnetotail by satellites and can be a feature of a flapping current sheet or of large scale waves in the plasma sheet [*Sharma et al.*, 2008]. Such flapping motions have been seen by satellites as fast current sheet crossings, and they have been reported in the region between 10 and 30 R_E in the magnetotail. The flapping motions are more frequent in the central part of the tail. Statistically, such flapping motions tend to occur during substorm expansion phases, and in association with enhanced magnetic reconnection activity [*Sergeev et al.*, 2006]. SC2 did not observe the flapping motions.

The B_y measurements, shown in Figure 5-32 panel d), imply the presence of large out-of-plane magnetic fields, especially during the second outflow interval. In this interval B_y reached a magnitude close to -20 nT measured by SC4. The B_y measurements are analysed in further detail in the Hall magnetic field section of this thesis.

If SC4 encountered the inflow region during any of the four intervals in Figure 5-32 it would be recognised by a slow velocity (from 25 km/s) mainly in the z direction (V_z) while V_x would be close to zero. Panel b) shows the measurements of V_z from SC4. The V_z component was observed to fluctuate mainly around zero except for some periods: During the second outflow interval V_z had a negative tendency, but in the interval when V_x fluctuated around zero, V_z also fluctuated around zero until the start of the third high speed outflow period. It was during this interval, when the both components fluctuated around zero, that SC4 crossed the neutral sheet from the northern hemisphere to the southern hemisphere. These observations suggest that SC4 did not enter the inflow region, neither during the crossing of the neutral sheet, nor when the spacecraft went from being located tailward of the reconnection region to being located earthward of it. During the third outflow, the vertical velocity showed the same tendency as the horizontal velocity, where V_z increased and reached value of ca 100 km/s. During this interval SC4 was located to the south of the neutral sheet ($B_x < 0$), where an earthward flow originating in the central plasma sheet would have had a vertical velocity as the flow diverged along the field lines outside the diffusion region. This feature with the

correlating V_x- and V_z-components was also present during the fourth interval of the earth-ward directed high speed flow.

In Figure 5-32, panel f) and g) show the E_x- and the E_y-component of the electric field. The electric field is measured in the ISR2 coordinate system, which is approximately the same as the GSE coordinate system. Only two of the components (E_x and E_y) are derived from these measurements. If the electric field were to be transformed in to the GSM coordinate system, the third component (E_z) would have been determined. This is possible by including the magnetic field data, but however, this will add further errors to the electric field measurements. The coordinate system in which the data from the EFW experiment originally were measured was therefore used. The electric field data (mostly E_y) showed an occurrence of large electric fields during the first, second and forth high speed flow intervals, with the largest electric field amplitudes were present during the second period. The E_y-component was mainly positive reaching values up to ~ 34 mV/m. The E_x-component fluctuated more and was both positive and negative during the outflow intervals. The values were, however, lower, reaching only ~ -5 mV/m and ~ 4 mV/m. A further investigation of the electric fields is given in the next section.

The H^+ density measurements from SC4 are shown in panel h). The density fluctuated between values of 0.1 – 1.5 particles pr. cm^3 during the studied time interval. The lowest values of the density was present when the spacecraft potential (see panel i)) decreased. The largest intervals of density occurred during the first and the third high speed outflows. During the second large outflow, however, the density decreased at the same time as the spacecraft potential values indicated that the spacecraft entered the plasma sheet boundary layer or the lobe.

The quality of the electric field data

The quality of the electric field data should be investigated before continuing the analysis of the electric fields. The quality numbers of the electric field measurements reveal that there are intervals when wake effects may have influenced the measurements. The quality flags of the electric field measurements are given in appendix B. The plots indicate that the measurements taken between 09.45 UT and 09.46 UT by all four spacecraft, and also the measurements registered by SC1 between 09.50 UT and 09.52 UT, were not reliable due to wake effects [*Lindquist and EFW-Team*, 2001]. As seen from measurements presented in Figure 5-32 there were no significant electric fields measured between 09.45 and 09.46 UT. This means

that in the following analysis of the electric fields, the results were most likely not influenced by wake effects.

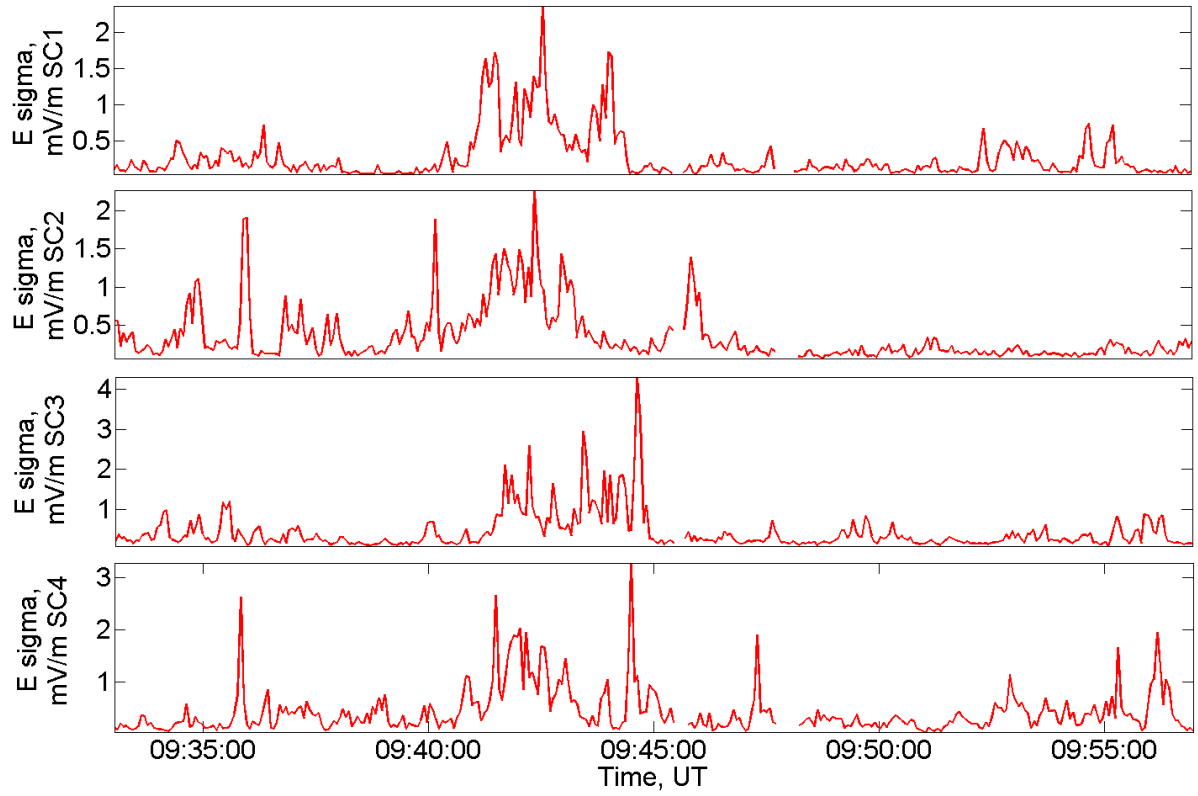

Figure 5-33: "E_sigma" from the EFW-instrument during the reconnection interval.

Another indication of the reliability of the electric field measurements is the "E-sigma" quantity (see 3.2.2). Figure 5-33 presents the E_sigma values from all four spacecraft during the investigated time interval. Note that E_sigma is a positive quantity. As seen from the figure, E_sigma values were low, and during the outflow periods the parameter reached values of only ~ 2 mV/m. Low E_sigma values signifies a good correlation between the raw data and the least-square-fit sine wave. This suggests that the electric field fluctuations presented in Figure 5-32 represent real electric fields.

As a final check, the E_y-component raw data (see Figure 5-34) and the E_y-component of the spin resolution data (Figure 5-32) are compared. There were some large spikes seen in the E_y raw data where the magnitude of the raw data component exceeded the magnitude of the spin resolution data, but most of the time the raw data had the same magnitude as the spin resolution data. The low values of the E_sigma and the similarity between the raw data and the spin resolution data suggest that the calibrated spin resolution dataset presented in this event show the actual electric fields in the surroundings of the Cluster satellites during the

investigated time interval. The spin resolution dataset was therefore used in the following section.

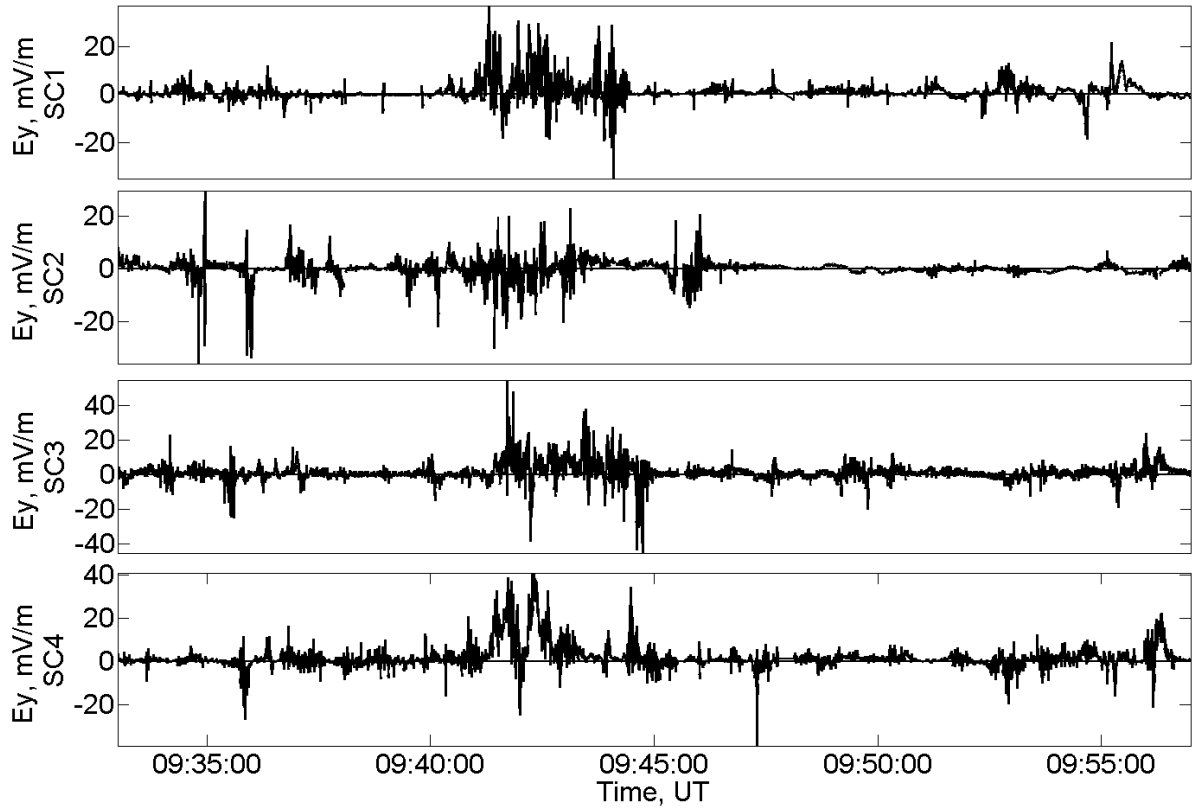

Figure 5-34: The raw data of the E_y-component from the EFW-instrument during the reconnection interval.

Electric fields in the reconnection region

Large electric fields in association with reconnection have been shown to appear in regions with small density and large $\pm B_x$ values [*Borg et al.*, 2005]. The conclusion of such studies have been that the electric fields were located in the vicinity of the separatrices and were most likely correlated with the electric fields found in simulations where also density depletions at the separatrices were proposed [*Shay et al.*, 2001]. Figure 5-35 presents a scatter plot of density versus E_y (panel a)), and B_x versus E_y (panel b)), for the time period between 09.30 UT and 10.00 UT using measurements from SC4. Figure 5-35 panel b) shows a correlation between large B_x- and E_y- values both in the southern ($B_x < 0$) and in the northern ($B_x > 0$) hemisphere. Close to the neutral sheet where $B_x = 0$, there were no large electric fields. In Figure 5-35 panel a), however, there are some large electric fields occurring in regions with low density, but also in regions with higher density. It is not possible to say whether this unclear picture was caused by the low resolution of the density data (2 spin periods) which necessitated a removal of electric field data points, or by the calibration process of

the electric field measurements where some of the large amplitude spikes may have been removed. Based on these results it is not possible to determine whether the large electric fields seen in this reconnection event occurred at the separatrices or not.

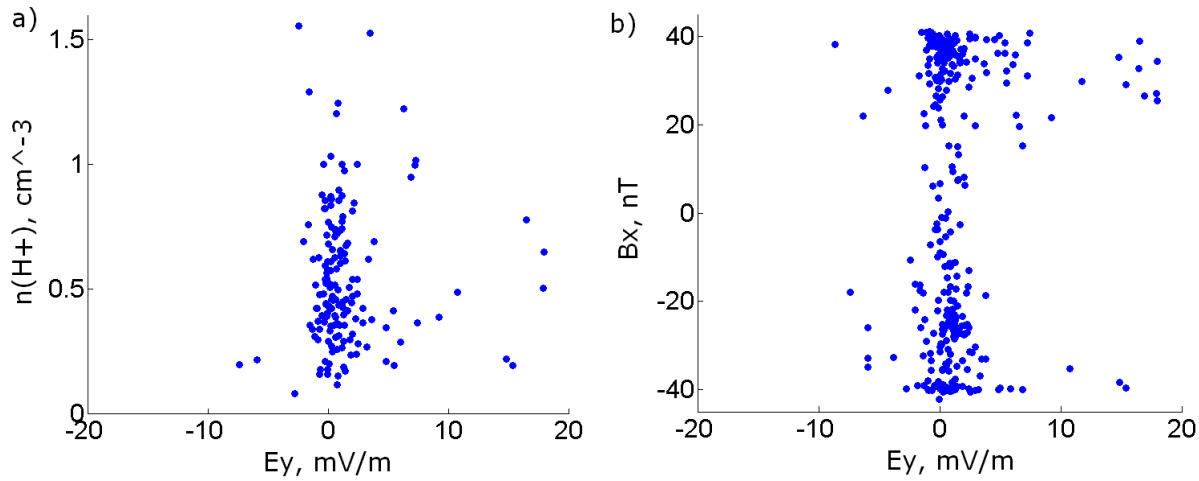

Figure 5-35: Scatter plot in the time period between 09.30 UT and 10.00 UT using measurements from SC4. Panel a) n_{H^+} versus $E_y$and panel b) B_x versus E_y.

The variance analysis calculations and the Hall magnetic field

When looking for the Hall magnetic field, the magnetic field data should be corrected for local variations due to flaring [*Kaymaz et al.*, 1994]. The method used is elaborated in chapter 4.1 and the results from the calculations for this event are given in Table 5-1. The covariance matrix was based on magnetic field measurements with a resolution of 0.04 seconds, and the time window for the calculations was set from 09.30 UT to 10.00 UT, in order to include the entire time interval when magnetic reconnection occurred.

Spacecraft	**Eigenvalues, λ**	$\omega = \frac{\lambda_{max}}{\lambda_1 + \lambda_2 + \lambda_3}$
SC1	$\lambda_1 = 13, \lambda_2 = 19, \lambda_3 = 510$	$\omega = 0.94$
SC2	$\lambda_1 = 13, \lambda_2 = 19, \lambda_3 = 285$	$\omega = 0.90$
SC3	$\lambda_1 = 15, \lambda_2 = 20, \lambda_3 = 839$	$\omega = 0.96$
SC4	$\lambda_1 = 13, \lambda_2 = 21, \lambda_3 = 1111$	$\omega = 0.97$

Table 5-1: The calculated eigenvalues for all four Cluster spacecraft in the time period between 09.30-10.00 UT.

The x-component in the modified coordinate system was given by the eigenvector corresponding to the largest eigenvalue. As seen from Table 5-1 this eigenvalue was well deter-

mined for all the spacecraft in this event which is seen by the large qualification multipliers (more than 90 % of the magnetic field variation was located in the modified x direction). In the method used for calculating the modified coordinate system (see chapter 4.1.1), it was assumed that the normal of the current sheet is directed along $\hat{\boldsymbol{z}}_{GSM}$. When comparing the eigenvector of the smallest eigenvalue, corresponding to the normal of the current sheet, $\hat{\boldsymbol{n}}_{VA} = (-0.02, -0.17, 0.98)$, it seemes that the assumption of a normal directed approximately along the $\hat{\boldsymbol{z}}_{GSM}$ was a correct assumption. The rotation angles between the GSM coordinate system's and the modified system's x- and y-axis were in order of magnitude ~9° for SC1, ~12° for SC2, ~10° for SC3 and ~10° for SC4.

In Figure 5-36 the black curve shows the original B_y while the red curve shows the same measurements transformed into the modified coordinate system. As seen in the figure, there is a significant difference between the B_y component and that of the modified B_y' component for all spacecraft. The differences were in the range of 5 nT which is a larger value than the uncertainty of the FGM instrument (see chapter 3.2.2). By using the modified coordinate system, effects related to flaring of the magnetic field are reduced.

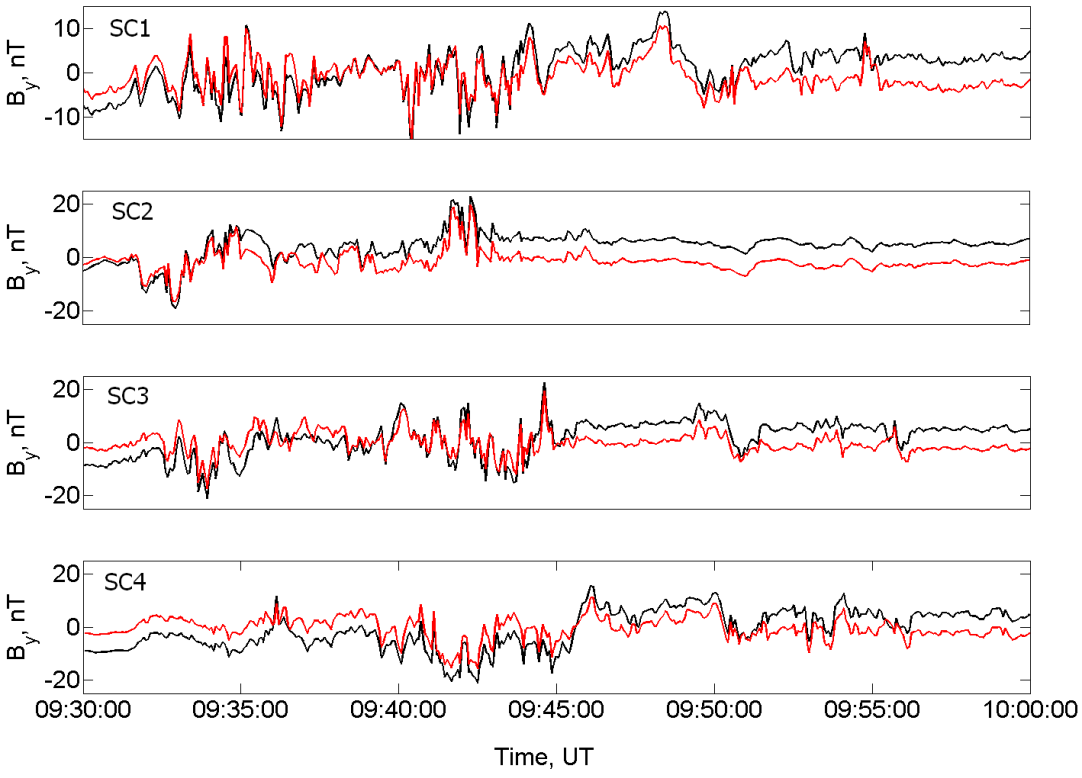

Figure 5-36: The result of the variance analysis on the B_y-component on each satellite. The black curve is the original magnetic field and the red curves are the modified magnetic field.

When looking for the Hall magnetic field, data from each time period which contained high speed outflows were used. The challenge in identifying the Hall magnetic field for this

event was the lack of ion data from SC1, SC2 and SC3. The ion data from SC4 made it possible to determine the intervals of high speed outflows for this spacecraft. The outflow intervals corresponded to intervals with excursions of the V_x and B_z components, which are the expected signatures if the spacecraft did enter the reconnection region. In order to determine whether the other spacecraft did enter the reconnection region or not, the B_z measurements from SC1, SC2 and SC3 were compared with the measurements from SC4. As found in the preceding section, SC3 and SC4 did most likely register the same signatures. SC1 registered the same signatures as SC4 during the last part of the second outflow interval and during the third outflow interval, while SC2 was located further away from the reconnection region than the other spacecraft. The Hall magnetic field plots, presented in Figure 5-37, are based on these findings. During the investigated interval, all four spacecraft were located within the plasma sheet, except for some short possible crossings into the plasma sheet boundary layer or lobes (the intervals "b" and "d" in Figure 5-31).

Figure 5-37 panel a) – panel e) contain data from a high speed outflow period. The scatter plots are based on data transformed into the modified coordinate system from the variance analysis, and are presented in the Cluster satellite colours. The second outflow interval is split into two separate figures due to the reversal of the flow inside the interval where an earthward directed outflow (panel b)) would provide a different signature of the Hall magnetic field than a tailward directed outflow (panel c)). Panel a) and panel b) contain data from SC3 and SC4. Panel c) – panel e) contain data from SC1, SC3 and SC4. In panel a) there is a correlation between the B_x' and the B_y' measurements as would be expected if the spacecraft were located earthward of the reconnection region. This observation is consistent with the direction of the first high speed outflow, which was earthward. In panel b) the sense of the relation changes. In panel c) there is a correlation between the B_x' and the B_y' corresponds to a quadrupole Hall magnetic field. The sense of the variation corresponded to a tailward location of the satellites, which is consistent with the direction of the high speed outflow during the second period. In panel d) the picture is somewhat cluttered, and it is not possible to identify any Hall magnetic field signature. The lack of a clear quadrupole Hall magnetic field signature in panel d) may be due to the fact that the spacecraft did not cross the current sheet. In panel e) a new correlation corresponding to the Hall magnetic field is apparent, where the sense of the correlation corresponds to an earthward location of the reconnection region.

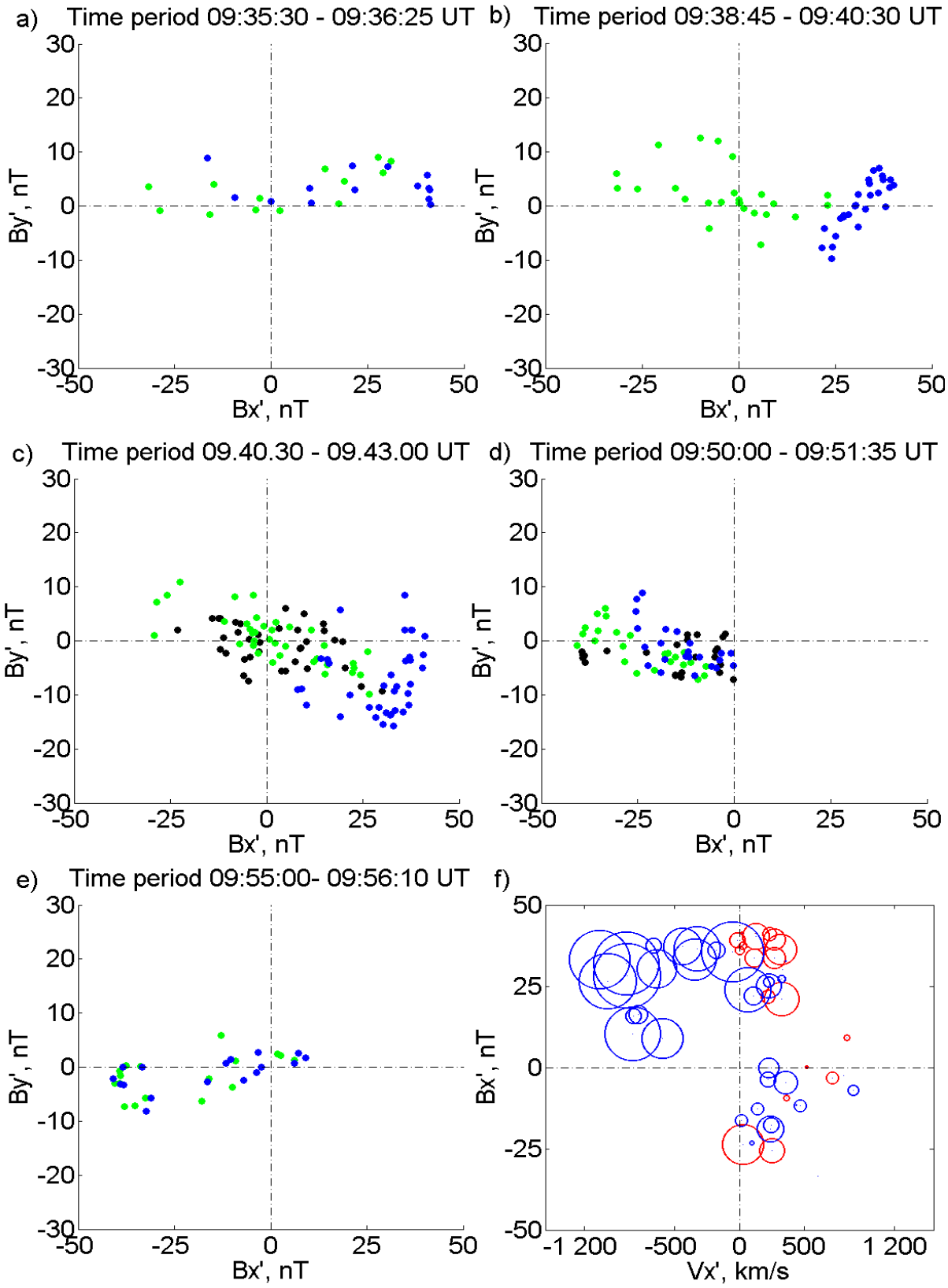

Figure 5-37: Panel a) – panel e) show scatter plots of B_y' versus B_x'. Panel a) during the first high speed outflow, panel b) during the first part of the second high speed outflow, and panel c) during the last part of the second high speed outflow. Panel d) shows B_y' versus B_x' during the third high speed outflow and panel e) during the fourth high speed outflow. Panel f) shows B_x' versus V_x' with B_y' represented as circles, and contains data from all four intervals (not in Cluster colours). The size of the circles represents the magnitude of B_y'.

In panel e) measurements of B_x' and B_y' only from the last part of the fourth high speed outflow are used. The reason was the lack of the B_z' reversal during the first part of this outflow interval.

Panel f) differ from the other panels. The plot was generated based on measurements from SC4 during the three first high speed outflow intervals and from the last part of the fourth outflow. If SC4 had encountered both the earthward and the tailward regions of the reconnection region in both northern and southern hemisphere, four of the quadrupole Hall-magnetic field branches should be detected (see illustration of the ideal quadrupole in chapter 2.5.3, Figure 2-14). Panel f) shows a plot of B_x' versus V_x' with B_y' data presented as circles. The blue circles represents positive, out-of-plane B_y', and the red circles presents the negative, into-plane B_y'. The size of the circles are relative to the size of B_y'. In the figure a quadrupole pattern is seen, where the positive B_y' dominated the positive B_x'- negative V_x'-region and the negative B_x'- and positive V_x'- region, while negative B_y' dominated the positive B_x'- positive V_x'- region. The magnitude of B_y was between 5 – 15 nT, during the outflow periods. The signature of the quadrupole Hall out-of-plane magnetic field presented in Figure 5-37 panel f) suggested that SC4 did encounter the reconnection region between 09.35 UT and 09.50 UT. Such a quadrupole Hall magnetic field was not apparent when making the same plot using data in the GSM coordinate system. When the scatter plots in panels a) - e) were constructed based on the B_x and B_y measurements in the GSM coordinate system, they showed the same tendency as the plots presented here.

These results indicates that SC1, SC3 and SC4 entered a collisionless magnetic reconnection region during the three first high speed outflows, and that SC3 and SC4 did enter a reconnection during the last part of the fourth high speed outflow. The sense of the correlations presented in Figure 5-37 suggests that the spacecraft were located both earthward and tailward of the reconnection region during the studied time interval.

The Cluster satellites' location in the reconnection region

Based on the signatures between 09.40 UT and 09.43 UT of a tailward directed high speed outflow, along with a similar excursion in the B_z-component and the quadrupole Hall out-of-plane magnetic field, a rough location of the spacecraft can be determined (Figure 5-38). The signatures suggest a location of the Cluster satellites positioned in the tailward part of the reconnection region.

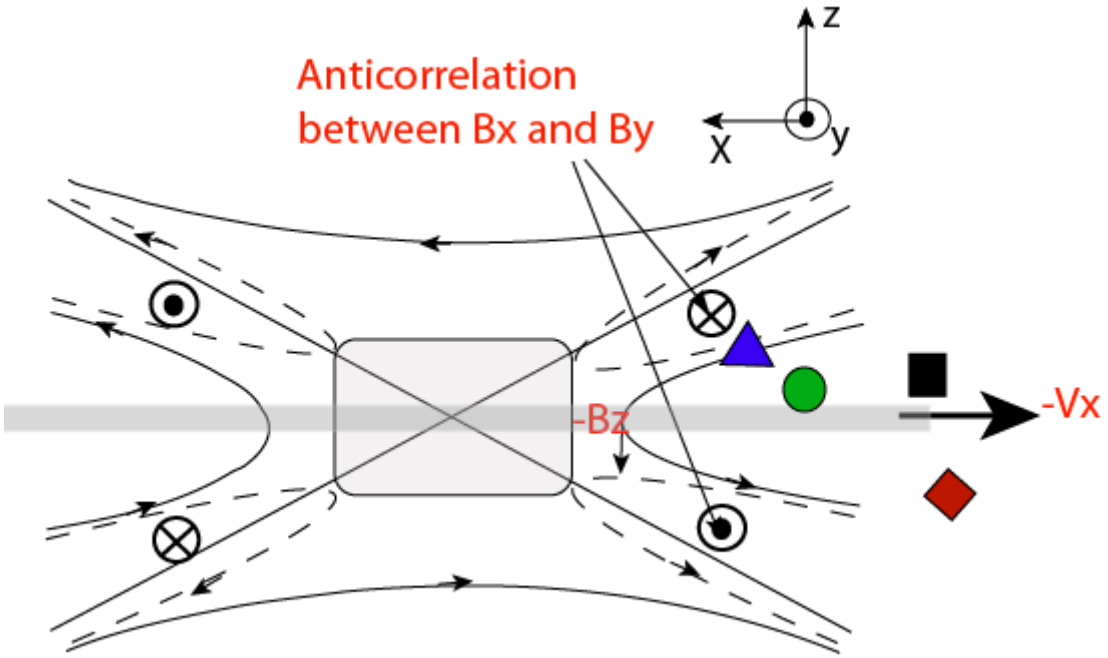

Figure 5-38: A rough sketch of the location of the Cluster satellites in the reconnection region during the second time period. The determination of the location is based on the observed signatures from the Cluster data. The red font writing indicates the signatures observed by the Cluster satellites during the dipolarization interval. The signatures are not to scale.

5.1.2 Magnetic field line footpoint in the ionosphere

The OVT program provided three footpoints, simulated using three models, of magnetic field lines located in the same region as the Cluster satellites. The time when the footpoints were calculated was during the beginning of the reconnection interval at 09.40 UT. The values used for the different Tsyganenko models are given in appendix C. Circles surrounding the footpoints calculated by T87, T89 and T96 models are shown as red circles in Figure 5-39, panel a) and b). The red circles are from now on referred to as the footpoint regions. The grey circles in the figures show the geographic latitudes and longitudes. The footpoint region in the northern hemisphere shown in panel a) was located between 60° and 70° latitude north, in Alaska and in northern parts of Canada. The region in the southern hemisphere shown in panel b), was located around 60° south in the ocean south of New Zealand. It should be pointed out that the calculations of footpoints are very uncertain, and therefore they only provide a rough estimate of the footpoint region.

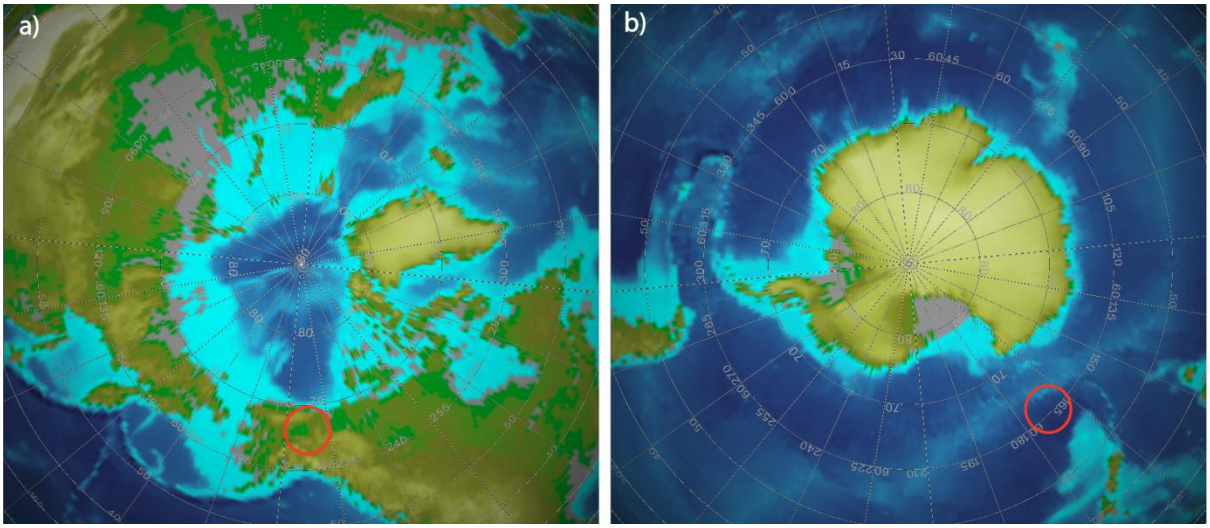

Figure 5-39: The footpoint of the magnetic field lines extending out to the Cluster satellites during a time interval of two hours. The estimated footpoint region is shown by the red circle enveloping three calculated footpoints using T87, T89 and T96.

5.1.3 Data analysis and observations in the ionosphere

Enhanced auroral activity in the auroral oval was observed by the IMAGE WIC instrument [*Mende et al.*, 2000a] during the time period when the Cluster satellites observed signatures of a magnetic reconnection in the magnetotail (see details regarding the IMAGE and its instruments in chapter 3.3). Figure 5-40 shows the UV pictures of the auroral oval in the southern hemisphere during the time period. The auroral intensity is measured in rayleighs.

As seen in Figure 5-40 there is some activity at 09.32 UT. An auroral spot appeared at 09.32 UT near 23 MLT at ~ 65° magnetic latitude. This spot faded away before it developed into any larger activity. Such a small auroral activity can be described as a pseudobreakup (see chapter 2.6.1) and could be a result of the plasma sheet thinning during a substorm growth phase [*Nakamura et al.*, 2002]. At 09.41 UT a new auroral spot appeared within the same region as the previous, and was located just north of the footpoint region. The aurora grew in size and became more intense and at 09.43 UT it covered almost the entire pre-midnight sector between 22 MLT and 00 MLT, between $-60°$ and $-70°$ magnetic latitude. The footpoint region was almost covered with aurora at this time. The intensity reached 3000 R in most of the aurora, only the edges had a lower intensity of $\sim$2000 R. At 09.45 UT, the aurora moved eastward while it started to fade. This first auroral intensification corresponded in time with the Cluster satellites encountering of the second period of the tailward directed high speed outflow. Between 09.45 UT and 09.53 UT the intensity of the aurora became weaker. At 09.55 UT a new auroral spot appeared in the pre-midnight sector in the northern

part of the footpoint region. This most intensive region grew in size and much of the oval was now filled with weaker particle precipitation, which is shown by the lower intensity. At 09.59 UT the aurora started to dim. This second intensification corresponded in time with the Cluster satellites observing the last periods of earthward directed ion outflows. Based on the signatures from chapter 2.6.1 and the timing from chapter 2.6.2, the intensification which appeared at 09.41 UT was the onset of an auroral substorm.

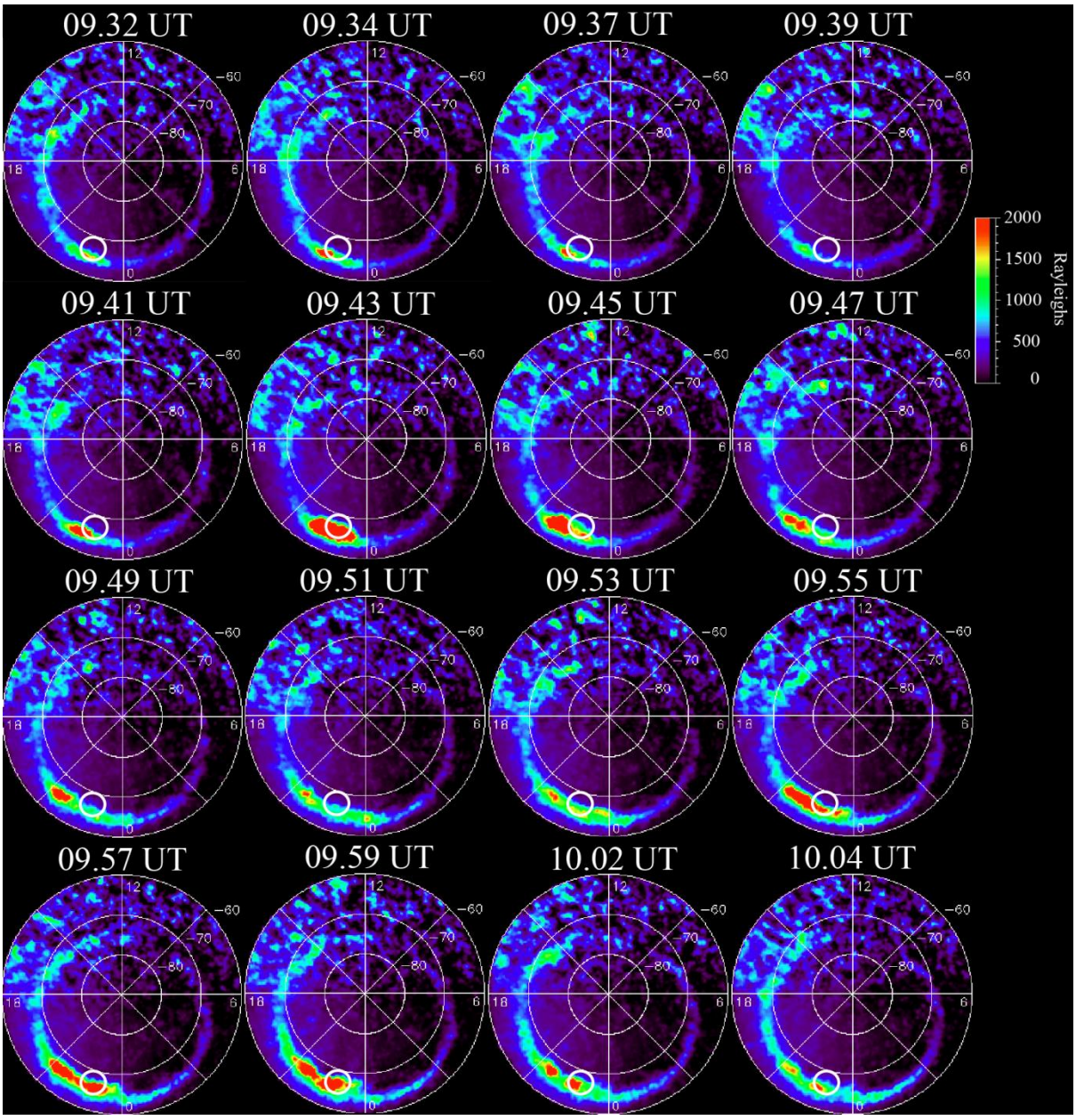

Figure 5-40: Image WIC pictures of the auroral oval before, during and after the reconnection interval observed by the Cluster satellites. The region where the simulated footpoints are located is marked with the small white circle. IMAGE WIC observed the southern hemisphere at this time which is shown by the negative latitudes. The colour bar represents the intensity of the aurora measured in Rayleighs.

5.1.4 Ground measurements

Magnetic bays

Because the footpoint region in the southern hemisphere located in the ocean outside Antarctica on this day, the available magnetometer stations were very limited. The ground magnetometer stations Dumont d'Urville (DRV) in Antarctica and Macquarie Island (MCQ) and Eyrewell (EYR) on New Zealand were located in the same region as the footpoint region and the observed auroral activity. The locations of the stations are given in Table 5-2.

Station name, north	**Geographical longitude**	**Geographical latitude**
Barrow, BRW	203°	71°
Collage, CMO	212°	65°
Sitka, SIT	225°	57°
Station name, south		
Dumont d'Urville, DRV	140°	-67°
Macquarie Island, MCQ	159°	-55°
Eyrewell, EYR	172°	-43°

Table 5-2: The INTERMAGNET stations in the northern and southern hemispheres used in the analysis of the geomagnetic field. The stations are sorted by geographical latitude.

The stations were located in the in the dusk sector in the MLT system. Figure 5-41 shows the measurements of the horizontal intensity (H) and the vertical (Z) component of the geomagnetic field between 09.00 UT and 11.00 UT, from stations identified as DRV, MCQ and EYR. The stations were sorted by latitude where DRV was located farthest south and EYR was located farthest north in the southern hemisphere. The resolution in the data was one minute and when studying the start time in the plots 2 minutes of uncertainty should be added when manually determine the start of a signature. At 09.41 UT the first changes of the geomagnetic field were detected at the stations MCQ and EYR. This is marked by the black line to the left in Figure 5-41. At 09.45 UT a negative magnetic bay ($H < 0$) developed at the MCQ station. The bay lasted for 45 minutes and reached a value close to 40 nT. At the same time as the bay developed a small increase in vertical component was registered. The signatures indicated that the MCQ station was located north of the dawn-to-dusk flowing auroral electrojet.

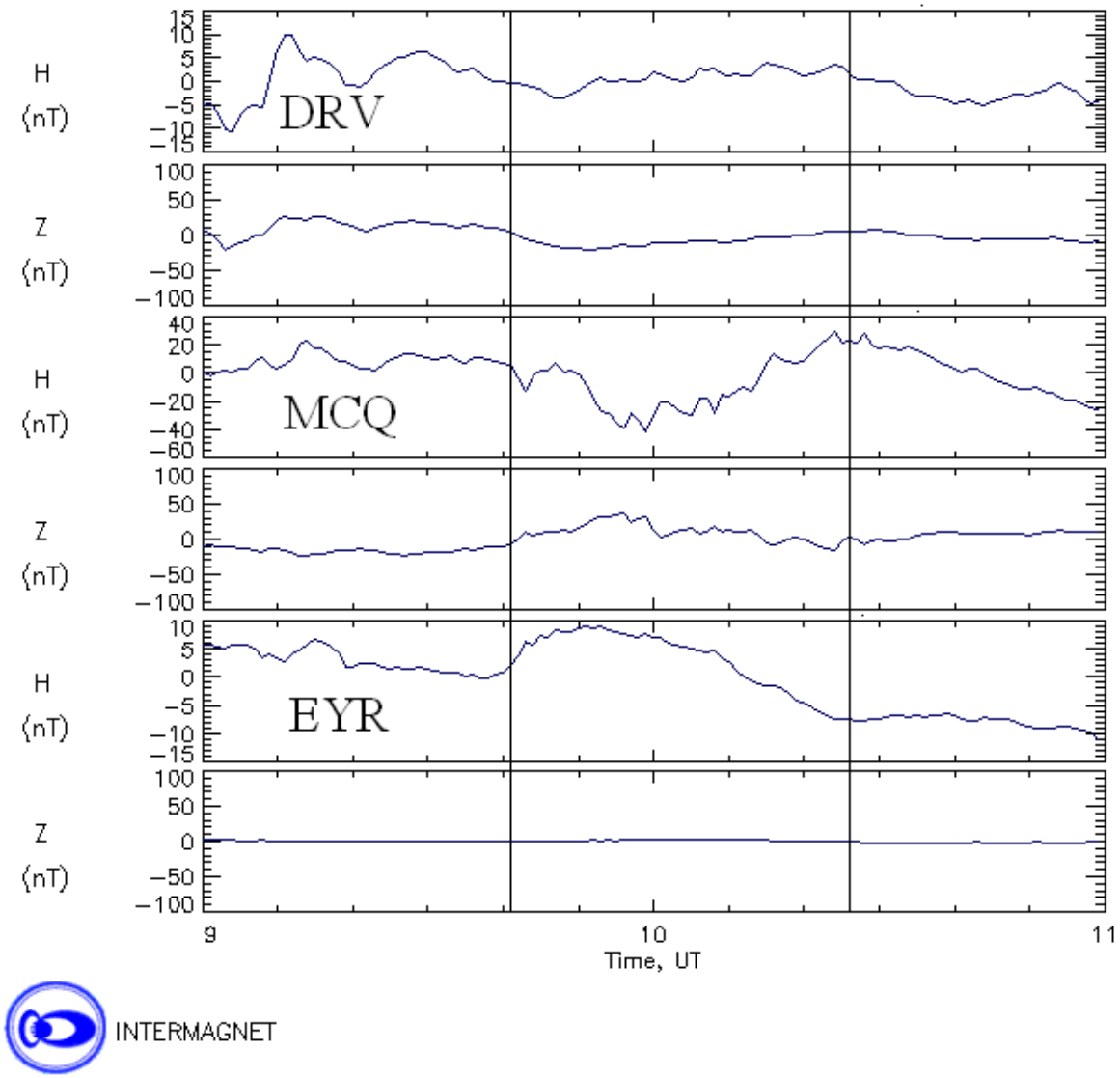

Figure 5-41: The ground magnetic field data from Dumont d'Urville (DRV), Macquarie Island (MCQ) and Eyrewell (EYR) stations which are located in footpoint region in the southern hemisphere. The start and the end of the magnetic bay are marked by the black lines in the figure.

The geomagnetic field measurements at EYR showed no fluctuations in the vertical component, but the horizontal intensity measured a positive magnetic bay (H > 0). The amplitude of the bay was very small (H ~ 5 nT) compared to the amplitude measured at MCQ, and therefore it was difficult to say if the bay at EYR was an effect of the auroral electrojet. The measurements from the DRV station showed no significant geomagnetic activity during this time interval. The MCQ station was located closest to the footpoint region.

In Figure 5-42, the geomagnetic field measurements from stations located in the northern hemisphere are presented.

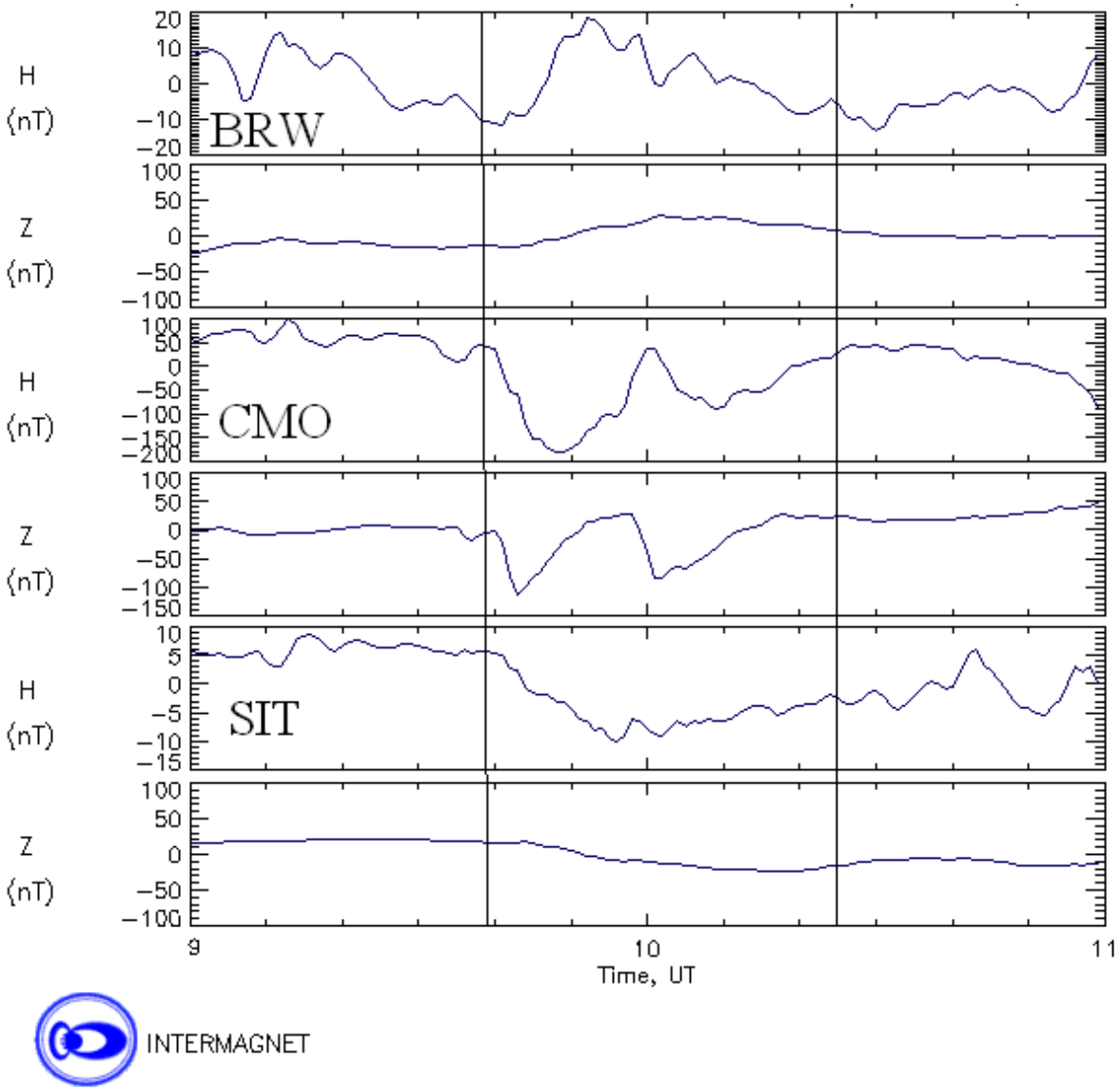

Figure 5-42: The ground magnetic field data from Barrow (BRW), Collage (CMO) and Sitka (SIT) stations which are located in the footpoint region in the northern hemisphere. The start and the end of the magnetic bay are marked by the black lines in the figure.

At 09.39 UT a negative magnetic bay (H < 0) developed at the CMO station and reached an amplitude > 150 nT. This station was located within the same region as the footpoint region. The vertical component at the same station decreased when the bay developed, indicating a dawn-to-dusk auroral electrojet north of the CMO station (Z < 0). The magnetic bay development (H < 0) suggested that the WTS was close to the station. At ~ 10.00 UT a new negative magnetic bay developed at the same station. The shape of the new signatures in the horizontal intensity and vertical component were similar to the signatures of the previous magnetic bay development at the same station. This observation implies that a new intensification of the auroral electrojet occurred, and that the dawn-to-dusk auroral electrojet flowed north of the CMO station (Z < 0). Again the WTS was close to the station. The magnitude of the sec-

ond bay (> 50 nT) was less than the magnitude of the first bay. If the station was located further away from the electrojet the second time, this would reduce the intensity of the horizontal measurements. The development of the second bay suggests that the auroral electrojet intensified twice between 09.00 UT and 11.00 UT passing through the region north the CMO station. At the SIT station the measurements showed a small (~10 nT) negative fluctuation at ~09.42 UT in the horizontal intensity and the variation in the vertical component was not significant. The BRW station measured fluctuations of the horizontal intensity and very little variation in the vertical component. The observations in the vertical component from BRW and SIT were too small to use to identify a possible location of the auroral electrojet.

Magnetic bays were observed in both hemispheres at approximately at the same time during the studied time interval. The footpoint region in both hemispheres was close to the stations which measured the most geomagnetic activity between 09.00 UT and 11.00 UT. The activity at the CMO station in the northern hemisphere was larger than the activity measured at the MCQ station in the southern hemisphere. This could be explained by the different location in longitude of the stations, which means that the CMO station was located closer to the auroral electrojet than the MCQ station.

Pi 2 signatures

The Pi 2 signatures are described in chapter 2.6.1 and the stations of the CPMN-network used in the event on 26th September 2005 are listed in Table 5-3 with respect to their location in geographical latitude.

Station name(South)	**Geographic latitude**	**Geographic longitude**
Macquarie Isl., MCQ	-55º	159º
Canberra, CAN	-35º	149º
Weipa, WEP	-13º	142º
Wewak, WEW	-4º	144º
Stations name(North)	**Geographic latitude**	**Geographic longitude**
Magadan, MGD	60º	151º
Rikubetsu, RIK	44º	144º
Kagoshima, KAG	32º	131º

Table 5-3: The geographic locations of the selected stations in the CPMN chain used in this thesis. Their locations are taken from the homepage of the CPMN stations[*CPMN*, 1995].

The stations listed in the table were selected due to their different location in latitude (see the map in chapter 3.4.1). The reason for this was that the magnitude of the Pi 2 pulsations may change with latitude. During the time period between 09.00 UT and 10.00 UT the stations in the CPMN-network were located in the pre-midnight sector between 18 MLT and 21 MLT.

Figure 5-43 shows the H-component (not filtered by frequency) of the datasets from the CPMN stations in the southern hemisphere.

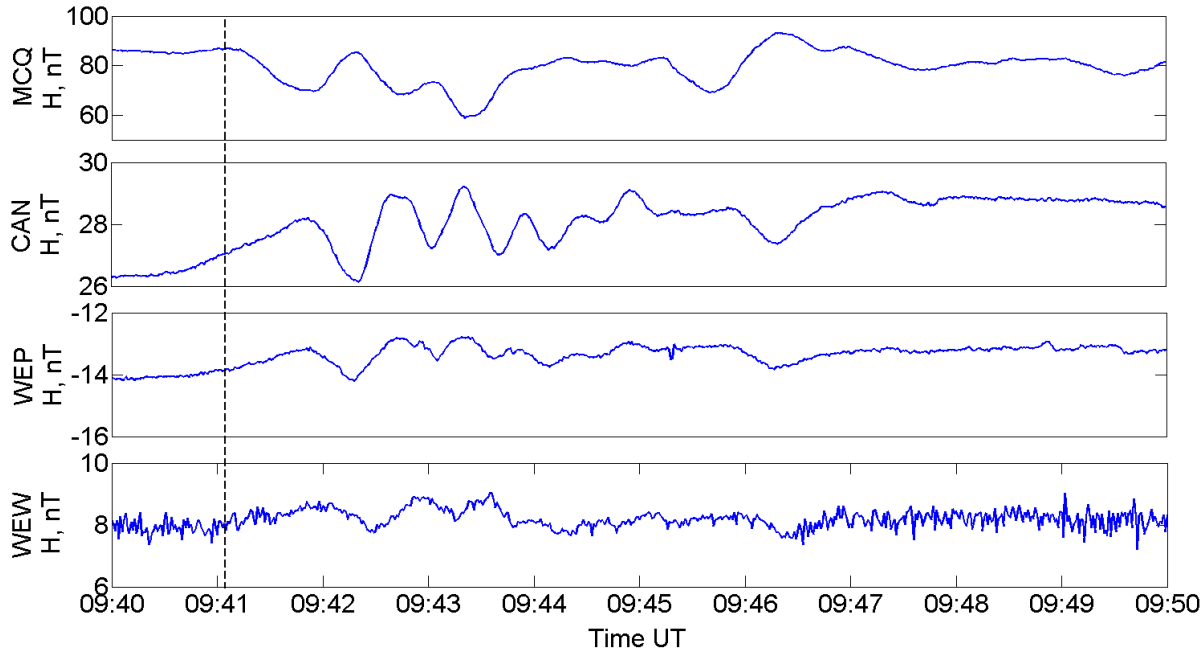

Figure 5-43: The Pi 2 pulsation registered at different stations in the CPMN chain in the southern hemisphere. The most southern station, MCQ, registered the largest Pi 2 pulse amplitude. As seen in the figure, the pulse was damped further north. The dashed line in the figure marks the start of the Pi 2 pulse wave train.

The stations were arranged by latitude where Macquarie Island (MCQ) was located the most south and Wewak (WEW) the most north. The Pi 2 pulse started just after 09.41 UT (marked by the dashed line in the Figure 5-43) and the largest amplitude was registered at the MCQ station, where the amplitude reached 16 nT peak-to-peak during the first pulse. The other stations (CAN, WEP and WEW) also observed a Pi 2 wave train but the amplitudes were smaller. The pulsations at MCQ were shifted 180° in phase with respect to the other measurements. Ground based observations have shown that the pulses with the minimum or maximum amplitude tend to occur in measurements taken by stations located at L = 3-4 and that a -180° phase change occures at the L-shell with largest amplitude (as the one seen in the measurements from the MCQ station) [see *Takahashi et al.*, 1995 and references therein]. The L-shell is the distance, measured in R_E, from the centre of the Earth to the point where the magnetic field line crosses the equator [*Kivelson and Russell*, 1997]. The phase change registered at the WEW station could imply a dilation of the Pi 2 pulse since the station was

located further north than the other stations. The origin of the Pi2 pulsations and the cause of the 180 degree phase change are beyond the scope of this thesis, and the pulsations are only used as an indication of the substorm onset.

At the CAN station the amplitude was in the order of 3 nT and at WEP, which was the most northern station, the amplitude was 1.5 nT. At all stations it was clear that the wave train got damped with time and at 09.45 UT the Pi 2 pulse had disappeared.

Figure 5-44 shows the measurements of the H-component from selected CPMN stations located in the northern hemisphere. The stations were arranged by latitude here as well, where the MGD station was located most north and the KAG station most south.

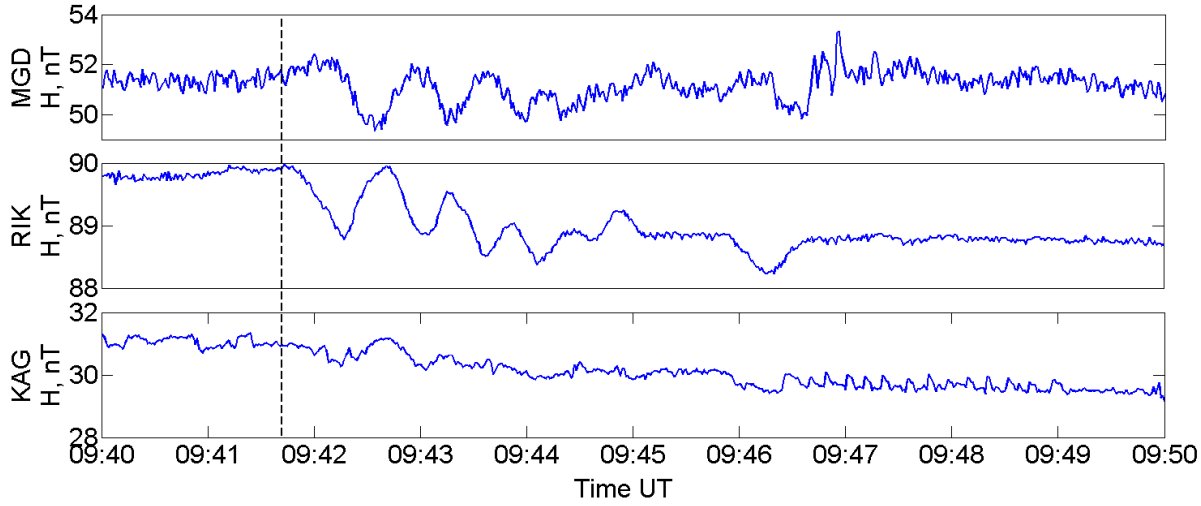

Figure 5-44: The Pi 2 pulsation registered at different stations in the CPMN chain in the northern hemisphere. As seen in the figure, the pulse was damped further south of the impact. The dashed line in the figure marks the start of the Pi 2 pulse wave train.

The Pi 2 pulse was first registered at the RIK and the KAG stations just before 09.42 UT. At the MGD station the Pi 2 pulse was registered at almost 09.42 UT (marked by the dashed line in Figure 5-44). The amplitude of the pulse was largest at the MGD station with a peak-to-peak value of 3 nT. The amplitudes of the pulses registered at the other stations were < 1 nT. The MGD station corresponded to an L=2.87, RIK to an L=1.5 and KAG to an L=1.2. The low L values may explain why the stations measured small amplitudes compared with the amplitude measured by the MCQ station which was located at L = 5.4.

According to *Rostocker et al.* [1980], a well-defined Pi 2 signature gives an accurate identification of a magnetospheric substorm onset within $\pm$ 1 minute, but it is difficult to find the exact start time of the pulses, so an additional minute is added to the uncertainty. Based on the CPMN data presented here, a magnetospheric substorm onset took place at 09.41 UT $\pm$ 2 minutes. Based on the large amplitude of the Pi 2 pulse in the data from the MCQ station, it seemed that the Pi 2 pulse started close to this station and propagated northward in the

southern hemisphere. The MGD station registered the largest amplitude in the northern hemisphere, but the magnitude was less than in the southern hemisphere suggesting the Pi 2 pulse started north of that station.

Auroral indices

As mentioned in chapter 2, there are several different auroral indices. The indices used here were the KP-index and the AE-index. The KP-index from the day of the event is presented in Table 5-4.

Time period	**00-03 UT**	**03-06 UT**	**06-09 UT**	**09-12 UT**	**12-15 UT**	**15-18 UT**	**18-21 UT**	**21-00 UT**
KP-index	4-	3	2	3-	4-	2+	3	3+

Table 5-4: The Kp-index during the 26th September 2005. One time period represents three hours. Time period from 09 UT to 12 UT represents the time interval where the active aurora, the magnetic bays and the Pi 2 pulsation were observed.

As seen in Table 5-4 the index increased from level 2 during the time period between 06.00 and 09.00 UT to 3 during the time period between 09.00 and 12.00 UT. It reached its maximum in the time period between 12.00 and 15.00 UT. Although the KP index has a time resolution of 3 hours, it shows the trend of a change in the geomagnetic activity.

The auroral electrojet index, AE-index, for the time period between 09.30 UT and 10.10 UT is presented in Figure 5-45. The resolution of the data was one minute. The dashed line in the figure is the time when the Cluster satellites observed the first magnetic reconnection signatures at ~-15 R_E (~ 09.35 UT). At ~ 09.46 UT the magnetometer stations which form the AE-index array measured a growth in the index. This is marked with the black line at "1" in the figure. The index increased until it reached a level of ~250 nT. This period is marked as "2" in the figure. The form of the curvature between index "1" and "2" suggested a development of an auroral electrojet flowing within the ionosphere, which meant that this period corresponded to the expansion phase (see Figure 2-19, chapter 2.6.1). At 09.54 UT the AE-index started to decrease which corresponded to the recovery phase of a substorm. The disturbance ended at ~10.06 UT. The substorm development identified by the AE-index did not, however, coincide with the magnetic bay developments registered by the ground stations located within the region of the footpoint.

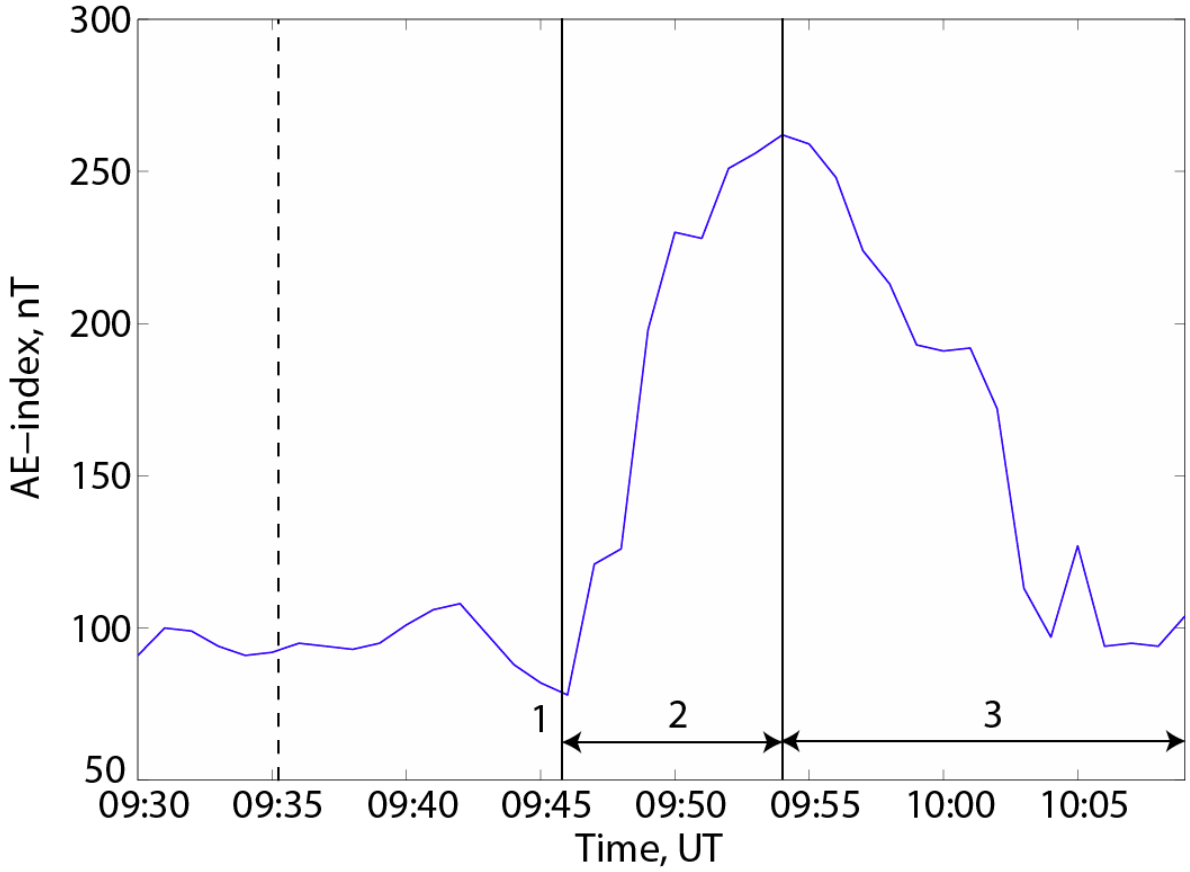

Figure 5-45: The AE-index during the active period. The different phases of the substorm are marked as 1, 2, and 3, where 1 is the growth phase, 2 is the expansion phase and 3 is the recovery phase. The dashed line in the figure is the time when the Cluster satellites observed the first magnetic reconnection signatures.

5.1.5 Timing of the 2005 event

The Cluster satellites were located in the near-Earth magnetotail at a distance ~ -15 R_E from the Earth, when detecting fast plasma jets (~1000 km/s) in both the earthward and the tailward directions. All the outflow periods registered by the Cluster satellites between 09.30 UT and 10.00 UT contained signatures of a magnetic reconnection. The first outflow was chosen as the start of the first magnetic reconnection period and is given in Table 5-5. The first indication of changes in the datasets after magnetic reconnection was from observations of the ionosphere from the IMAGE WIC. An auroral substorm appeared at ~09.41 UT in the pre-midnight sector ~ 23 MLT, close to the footpoint region. The next indications were the Pi 2 pulsations registered by the CPMN chain and the magnetic bay development at the CMO and at the MCQ stations. Both of these INTERMAGNET stations were located within the same region as the footpoint regions, and the Pi 2 signatures were also recorded almost simultaneously (~ 09.41 UT, see Table 5-5) with the outflow registered by the Cluster satellites. The largest Pi 2 pulsation amplitudes were registered at the stations located closest to the

footpoint region. The amplitudes became smaller at lower latitudes. The Pi 2 pulsations appeared in both hemispheres and they appeared at the same time as the other substorm signatures (~ 09.41 UT). The magnetic bay signatures suggested a formation of an auroral electrojet flowing in the dawn-to-dusk direction within the same region as the footpoints and the auroral brightening. Such an auroral electrojet acts as a closure of the SCW originating from a cross-tail current disruption in the near-Earth magnetotail.

The observed signatures	**Time onset [UT]**
Magnetic reconnection	~ 09.35
Aurora substorm onset	~ 09.41− 2 minutes
Start of Pi 2-wave train, south	~ 09.41 ± 2 minutes
Start of Pi 2-wave train, north	~ 09.41 ± 2 minutes
Magnetic bay, south	~ 09.41 ± 3 minutes
Magnetic bay, north	~ 09.39 ± 3 minutes
AE-index	~ 09.46 ± 1 minutes

Table 5-5: List of the signatures presented in previous chapter with the time of onsets as they appear in the datasets.

If a cross-tail current disruption formed the SCW, an auroral electrojet would form which would have contributed to an increase of the global AE-index. The final indication of changes was the increase in the AE-index ~ 11 minutes after the first magnetic reconnection. Such an increase is consistent with the substorm signatures given in chapter 2.6.1, although the magnitude was only ~250 nT. Based on the observation from the AE-index a substorm onset found place at 09.46 UT. The expansion phase lasted for a few minutes until the start of the recovery phase at 09.54. The proper order of the substorm signatures were, however, difficult to establish exactly due to the uncertainties of the measurements. This is also shown in Figure 5-46 where the black circles mark the onset of the substorm signatures and the horizontal black lines show the uncertainties related to the time of onset for each signature. The interval of the first magnetic reconnection observed by Cluster is marked with the red line in the figure, and the vertical dashed line marks the magnetic reconnection onset. Based on Figure 5-46 it seemed that the collisionless magnetic reconnection observed by the Cluster satellites started prior to the magnetic bays, the Pi 2 pulsations, the auroral substorm and the development of the AE-index.

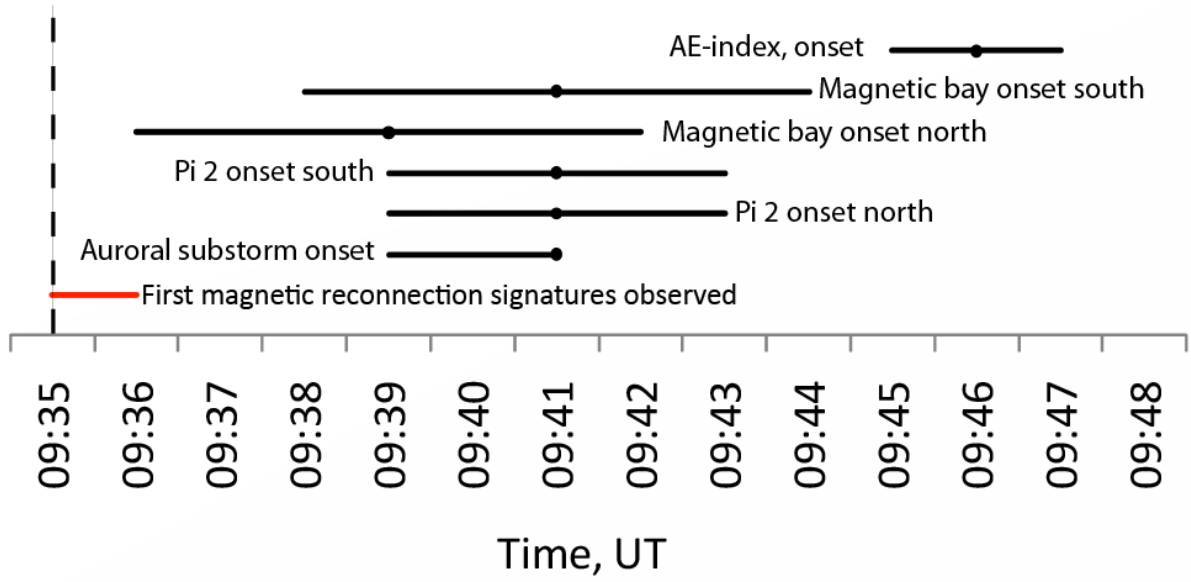

Figure 5-46: The time line when the first magnetic reconnection signatures (red line) were observed and the following substorm signatures. The onset of magnetic reconnection is marked with the dashed line. The onsets of the observed substorm signatures are marked as the black dots and the black horizontal lines are the uncertainties related to the timing of the substorm onset.

5.2 The 22nd August 2001 event

Some aspects of this magnetic reconnection event, registered on the 22nd August 2001, have been studied by *Volwerk et al.* [2003] and by *Louarn et al.* [2004]. The event was also one of a list created as a part of a Ph.D. thesis [*Borg*, 2006] where data from the Cluster satellites between 2001 and 2004 were investigated. In that study, 13 events of collisionless magnetic reconnection in the magnetotail were found.

In this thesis the time period to examine using Cluster data was set to between 09.40 UT and 10.15 UT. The rotation angle between the GSE and GSM coordinate system during this period varied from $-30.3°$ to $-30.9°$. A mean value of the rotation angle $\bar{\psi} = -30.6°$ was therefore used when transforming the datasets from the GSE system to the GSM system.

5.2.1 Data analysis and observations in the magnetotail

From 09.40 UT to 10.15 UT, on the 22nd August 2001, the Cluster constellation of satellites was located at $(x, y, z)_{GSM} = (-18, -3.4, -0{,}1)$ R_E which is 18 R_E from the Earth into the magnetotail.

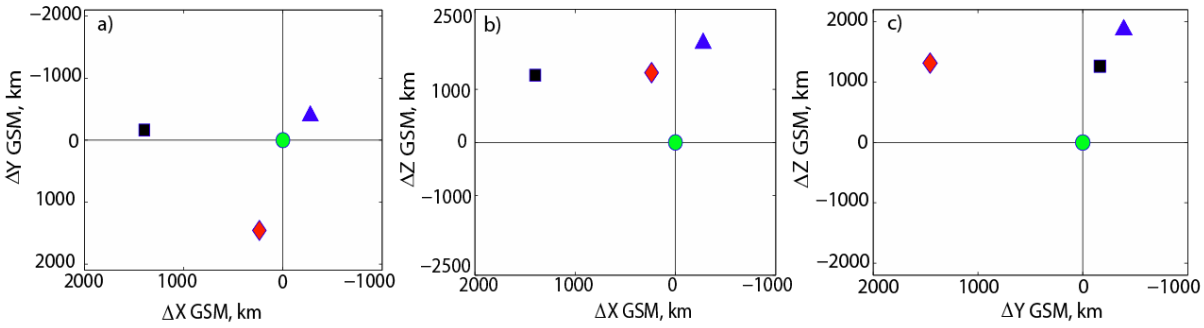

Figure 5-47: The position of the Cluster satellites in the GSM coordinate system, using the SC3 location as the origin. Each spacecraft is represented with its colour identifiers. The characteristic colours of the spacecraft are SC1-black, SC2-red, SC3-green and SC4-blue.

The Cluster tetrahedron configuration in the GSM coordinate system is shown in Figure 5-47 panel a) the xy_{GSM} plane, panel b) the xz_{GSM} plane and panel c) the yz_{GSM} plane. As seen in the figure, SC1 – the black square and SC2 – the red diamond – were located approximately on the same level in z_{GSM}. SC3 – the green circle – was located farthest south of the satellites while SC4 – the blue triangle – was located farthest north. SC1 was closest to the Earth. The maximum separation distance between the spacecraft during the examined time interval was $1.9 * 10^3$ km (between SC3 and SC4), and the minimum separation distance was $1.7 * 10^2$ km (between SC3 and SC1). During the chosen time interval, the Cluster barycentre moved at a speed of 1.1 km/s.

The location of the Cluster satellites in the magnetotail

The plasma β for this event was calculated using data from the FGM- and the CIS-experiment (see chapter 2.4.4 for details regarding the calculations). The CIS-experiment was operating on SC1, SC2 and SC4 during the selected time interval. Plasma β was therefore calculated for these spacecraft. The plasma β limits used in the previous event are also used here: Central plasma sheet $\beta > 0.3$, plasma sheet boundary layer $0.02 < \beta < 0.05$ and in the lobes $\beta < 0.02$ [*Baumjohann et al.*, 1988, *Baumjohann et al.*, 1989]. The spacecraft potential was also here used as a supplement to the β in order to establish the location of the Cluster satellites in the magnetotail. The spacecraft potential values for the different regions were: $|20| - |50|$ V for the lobe region and $|10| - |15|$ V for the plasma sheet region [*Lindquist*, 1983].

Figure 5-48 panel a) shows the calculated plasma β for SC1, SC3 and SC4 between 09.40 and 10.15 UT.

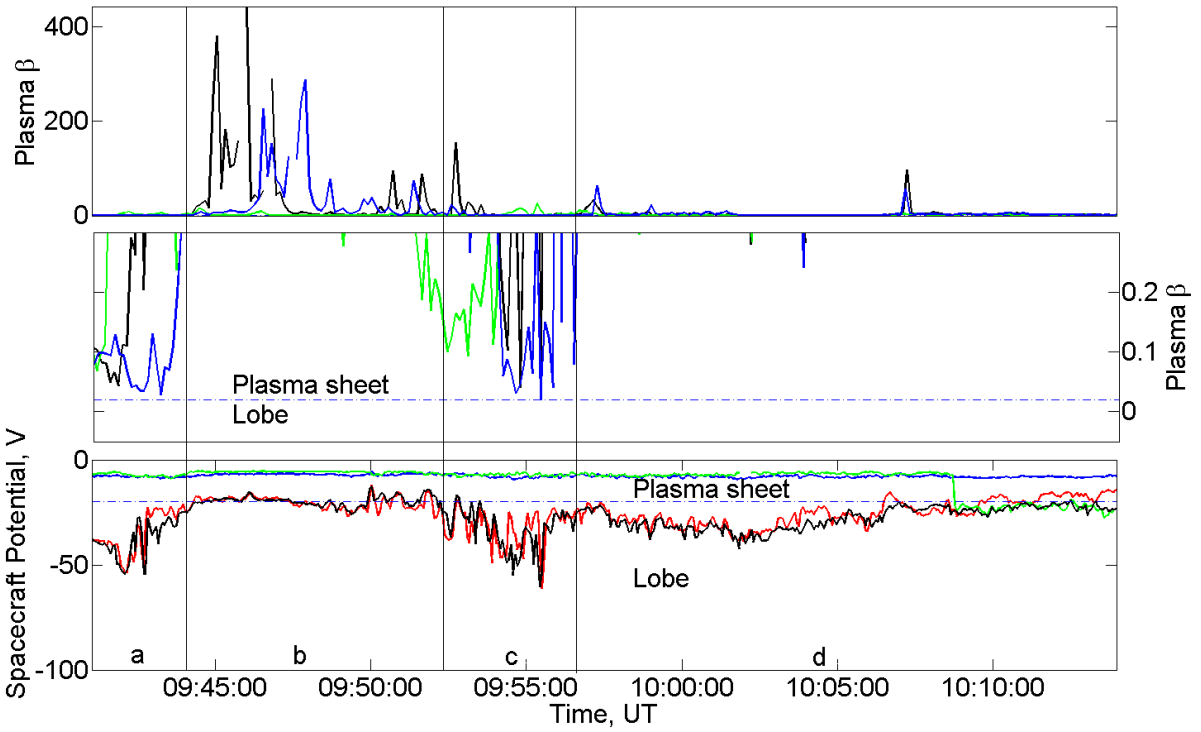

Figure 5-48: The calculated plasma β for SC1, SC3 and SC4 and the spacecraft potential of all four satellites. The spacecraft potential and the plasma β are plotted in the respective Cluster spacecraft colours: SC1-black, SC2-red, SC3-green and SC4-blue.

By zooming into the low plasma β values, which is done in panel b), it is possible to distinguish between the different regions of the plasma sheet. The values of β are limited between 0 – 0.3 in this panel, and the dashed line marks the β value 0.02.

Panel c) displays the spacecraft potential from all four spacecraft. The stable spacecraft potentials registered by SC3 and SC4 were a result of the Active Spacecraft Potential Control (ASPOC) [*Riedler et al.*, 1997] on the respective spacecraft during this time interval. The ASPOC instrument is an ion emitter instrument which controls the spacecraft potential and prevents any net transfer of charges between the spacecraft and the environment. This prevented the spacecraft from registering any electron flux during the time interval, so it was not possible to analyse the spacecraft potential data from SC3 and SC4.

If only the values of plasma β are considered in this event, the Cluster satellites were located within the plasma sheet during the whole time interval. During two periods, marked as "a" and "c" in the Figure 5-48, the plasma β approached a level of 0.02 which indicated that the spacecraft may have entered the plasma sheet boundary layer or the lobes during those periods. The measured spacecraft potential values throughout the whole time interval between 09.40 and 10.15 UT exceeded |20| V, which is marked by the dashed line in panel c).

With such spacecraft potential values it is reasonable to suggest that the spacecraft were located in the plasma sheet boundary layer or the lobe region during the whole interval. However, this observation does not agree with the plasma β values.

By studying the energy spectrograms (CIS) of the ion energy flux from SC1, SC3 and SC4, presented in Figure 5-49, it was found that the energy levels of the ions during interval "b" and "d" correspond to energy levels associated with the plasma sheet ($E_i > 10^3$ eV [*Kivelson and Russell*, 1997]).

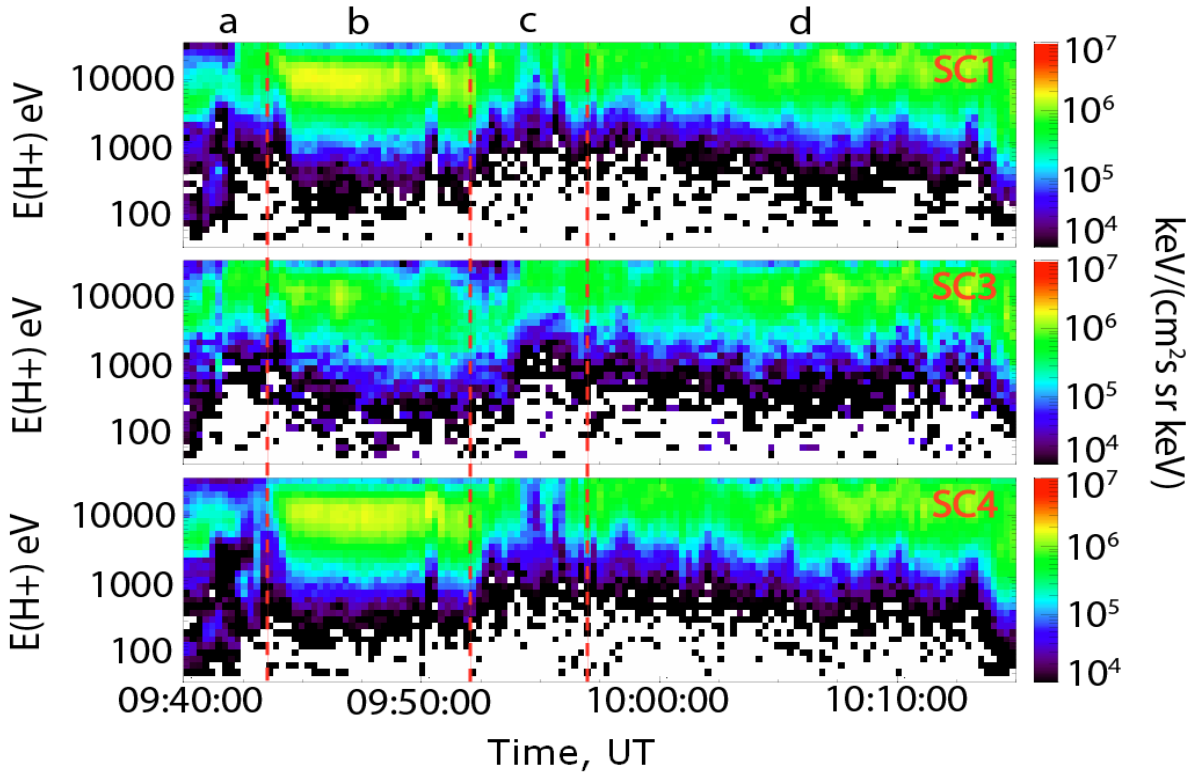

Figure 5-49: Energy spectrograms of H^+ obtained from the graphical products from the CAA. The red dashed lines indicate the same periods a – d as in Figure 5-48.

Observations in the Cluster data

The data from the Cluster satellites used in the examination of this event were CAA data. The data used were H^+ velocity data (CIS) from SC1, SC3 and SC4, magnetic field (FGM) and electric field (EFW) data from all four spacecraft and spacecraft potential data from SC1 (details regarding the instruments on the Cluster satellites are elaborated in chapter 3.2.1). The CIS data had a sampling rate of 8 seconds which corresponded to an average of two spin periods. The FGM and the EFW data have been averaged to a sampling rate of 4 seconds and are so- called spin resolution data. Figure 5-50 panel a) – i) display the data from the Cluster

satellites between 09.40 UT and 10.15 UT. The datasets were plotted in the Cluster satellites colours: SC1 – black, SC2 – red, SC3 – green and SC4 – blue, and the GSM coordinates was used unless otherwise specified.

The reconnection signatures searched for in the datasets were the same as in the previous event: Reversal of the V_x component, simultaneous reversal of B_z and observation of the quadrupole Hall magnetic field. As shown in Figure 5-50 panel a) SC1, SC3 and SC4 observed four intervals of earthward and tailward high speed flows. These intervals are marked by "1", "2", "3" and "4" in the figure. The outflows were identified by large positive and negative V_x values exceeding ± 500 km/s. The first earthward directed high speed flow reached a speed of ~ 1000 km/s at SC1 and SC3, and ~ 500 km/s at SC4. From 09.46 UT to ~ 09.50 UT V_x decreased and became slightly negative. At ~ 09.50 UT a tailward directed second high speed flow was observed with a speed reaching ~ 800 km/s. During the third interval the Cluster satellites registered a new earthward directed flow. The speed was larger than registered speed during the second outflow period, and all three spacecraft registered nearly the same values reaching ~ 1000 km/s. Between 10.03 UT and 10.04 UT V_x fluctuated around zero, before a new interval of a continuously earthward directed high speed flow was registered by all three spacecraft. The Cluster satellites measured B_z-components which are shown in panel e) Figure 5-50. The measurements showed the same tendency as the V_x data. B_z was postitive during the first outflow, negative during the second and positive during the third and fourth outflow intervals. The B_z-component was larger during the fourth interval compared with the other intervals, approaching values ~ 10 nT. During the first outflow interval the component reached ~ 5 nT. B_z changed simultaneously with the V_x-component, $B_z > 0$ when $V_x > 0$ and $B_z < 0$ when $V_x < 0$, which were consistent with the signatures expected in a dataset from satellites observing a magnetic reconnection. Even though the ion velocity was not available from SC2, it was possible to assume that the spacecraft measured the same outflows as the other spacecraft during the time interval. This assumption was based on the similarity of the B_x and B_z measurements from all four spacecraft displayed in Figure 5-50. From the results of the simultaneous changing V_x- and B_z-components together with the assumption that SC2 measured the same features in the velocity as the other spacecraft, it is possible to assume that the Cluster satellites were located earthward of the reconnection region during all outflows with the exception of the second. During the second outflow the Cluster satellites may have entered the tailward side of the outflow region.

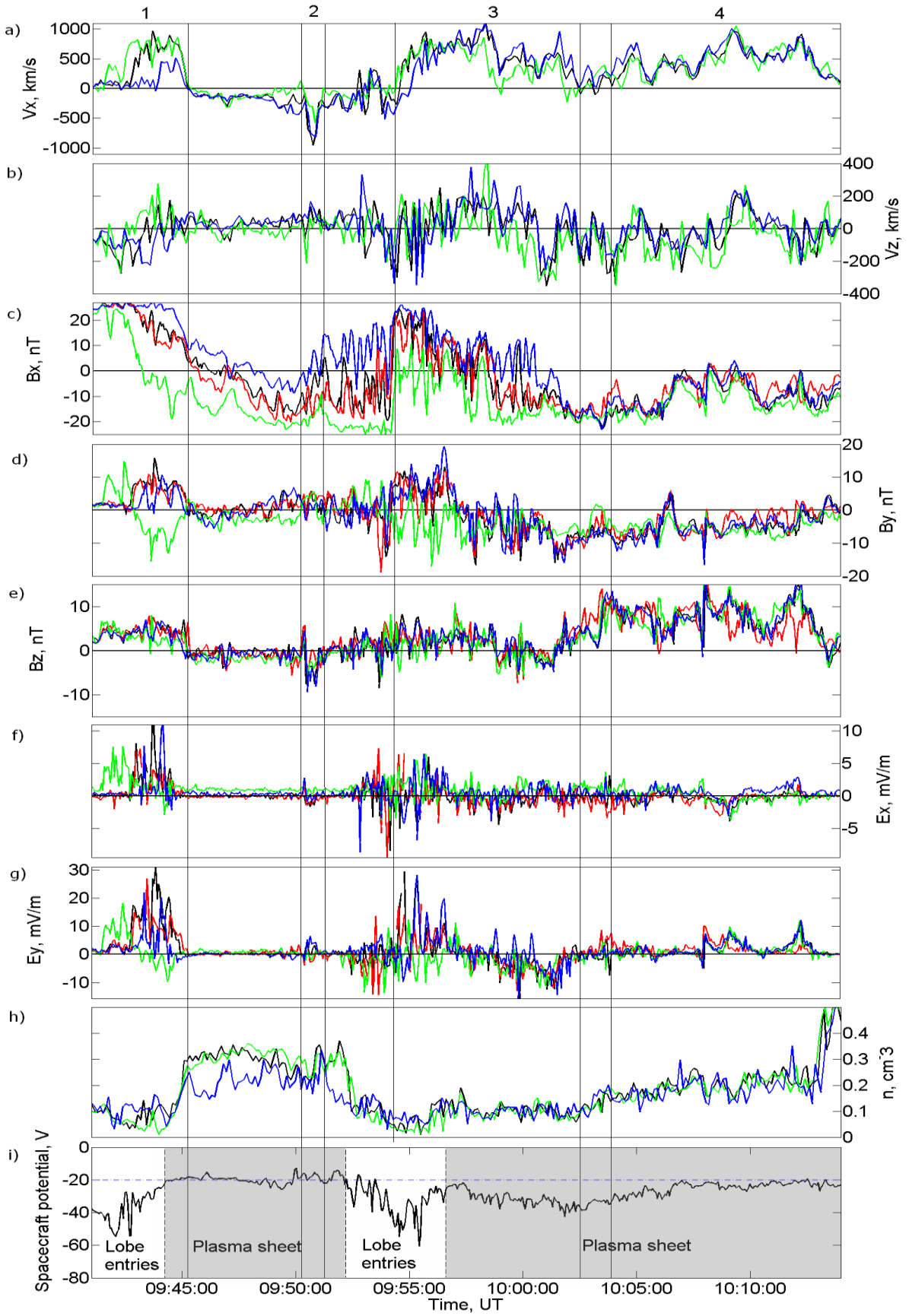

Figure 5-50: H^+ velocity, magnetic and electric fields, density and spacecraft potential data from the Cluster satellites. The velocity and the density are from SC1, SC3 and SC4 while the spacecraft potential are from SC1. Details regarding the data are given in the text.

During the time interval between 09.40 UT and 10.15 UT the Cluster satellites crossed the neutral sheet several times, i.e. the B_x-component changed polarity. The B_x measurements are displayed in Figure 5-50 panel c). The Cluster satellites were initially located in the northern hemisphere ($B_x > 0$). SC3 crossed the current sheet during the first outflow, while the other spacecraft crossed slightly after the outflow interval. The Cluster satellites stayed mainly south of the current sheet ($B_x < 0$) until the third interval, except for SC4 which was located mainly north of the neutral sheet ($B_x > 0$). SC1, SC2 and SC4 crossed the current sheet again during the third interval from south to north while SC3 was located close to the neutral sheet, and then from north to south. After the third interval the Cluster satellites stayed mainly south of the current sheet ($B_x < 0$). During the short interval between the third and the fourth outflow periods B_z increased. Such changes in the magnetic field topology suggest a dipolarization tailward of the Cluster satellites.

The V_z-component of the velocity is shown in Figure 5-50 panel b). If the Cluster satellites encountered the inflow region between the first and the second outflow interval, it would be recognised by an increasing V_z while V_x would be close to zero, as the Cluster satellites moved from a tailward to an earthward location of the reconnection region. During this interval the vertical velocity component fluctuated around zero. V_z was directed southward during the first part of the first outflow, and then the component turned northward during the last part of the outflow period. During this interval V_z reached a speed of ca 200 km/s. Such vertical velocities, directed both north and southward, were also present during the third and during the fourth outflow interval. *Volwerk et al.* [2003] explained these changes in both the V_x- the V_z-components by a standing wave in the current sheet during a reconnection event. Such an oscillating current sheet may explain why the Cluster satellites entered a tailward outflow region without passing through the inflow region.

The B_y measurements are presented in panel d). From the figure it seemed that the large B_y magnetic field measurements occurred during the outflow periods. The component changed polarity when the spacecraft crossed the current sheet. The magnitude of the measurements reached values of ~ 15 nT during the first and the third outflow intervals.

Strong electric fields were also detected during the outflow intervals, see Figure 5-50 panel f) and g). These electric field measurements are presented in the IRS2 coordinate system in order to avoid any uncertainties added to the field data when transforming the data into the GSM coordinate system. During the first interval of earthward directed high speed outflows E_x and E_y were mainly positive. The exception was the E_y-component measured by

SC3 which changed sign when the spacecraft crossed the current sheet. The electric field amplitudes reached ~ 30 mV/m in the y direction and ~ 10 mV/m in the x direction. During the third high speed outflow interval E_y fluctuated between positive (~ 20 mV/m) and negative values (~ 10 mV/m), where the E_x measurements were significantly less than the E_y-component. Further investigations of the electric fields are given in the next section.

The H^+ density measurements from SC1, SC3 and SC4 are shown in panel h). During the first plasma sheet encounter (see panel i)) the density was ~ 0.3 particles pr. cm^3, which corresponds to typical density values in the plasma sheet. However, during the second plasma sheet period the density was low (0.1 – 0.2 cm^{-3}). Such low density explains why the spacecraft potential decreased below -20 V during the second plasma sheet period, while the energy of the ions corresponded to energies within the plasma sheet (as shown in Figure 5-49).

The appearance of the measurements of the B_x- and B_z-components from all four spacecraft and the V_x measurements from SC1, SC3 and SC4 were similar. This suggest that the spatial extent of the reconnection region in the xz_{GSM}- plane was greater than the separation distances between the spacecraft in the same plane. The separation distance in the x direction was ~ $1.4 * 10^3$ km between SC1 and SC3, and in the z direction it was ~ $1.9 * 10^3$ km between SC3 and SC4.

The quality of the electric field data

Before proceeding with a further analysis of the electric fields, the quality of the measurements should be investigated. The quality flags of the electric field measurements during this event are given in appendix B together with the 2005 quality flags. The electric field measurements after 10.04 UT may have been influenced by wake effects (see appendix B, Figure 6-73) and are therefore not included in the following analysis.

Even though the quality flags for this event implied reliable electric field data, the E_sigma quantity should be investigated. The E_sigma quantities are presented in Figure 5-51. E_sigma reached large values (> 10 mV/m) during the outflow intervals. Such large values of E-sigma may occur if the spacecraft which measured the electric field influenced the measurements, or if there were actual large electric fields present near the spacecraft. Such large E_sigma quantities demand a further investigation of the raw data.

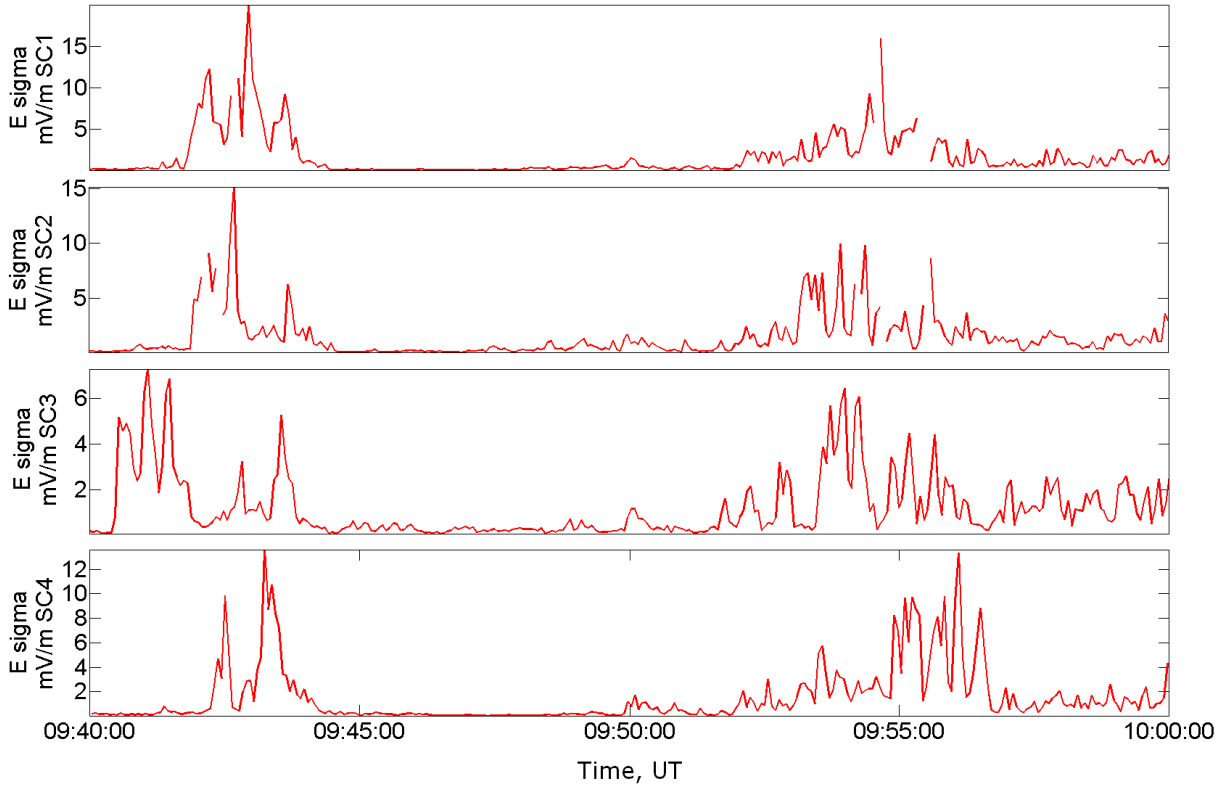

Figure 5-51: The quantity "E_sigma" from the EFW instrument during the time interval where the quality flags are of level three at all four spacecraft.

Figure 5-52 presents the raw data of the electric field from the time period between 09.40 and 10.00 UT. The data shows large electric field fluctuations (some exceed > 100 mV/m) during the same periods as the high speed flows occurred. When studying the data in details, the underlying sine wave (see chapter 3.2.2 for details) was found to be present, but there were also large amplitude fluctuations present. Since the spin resolution data (used in Figure 5-50) reflect an average of the spin wave, such large fluctuations have been removed. The large fluctuations shown in Figure 5-52 were real large amplitude electric fields in the vicinity of the spacecraft and were not caused by the spacecraft itself [personal conversation with Harri Laakso at ESTEC and a correspondence with Chris Cully at University of Stockholm]. When the relation between the E_y- and the B_x-components is studied in the next section, the full resolution electric field was therefore used.

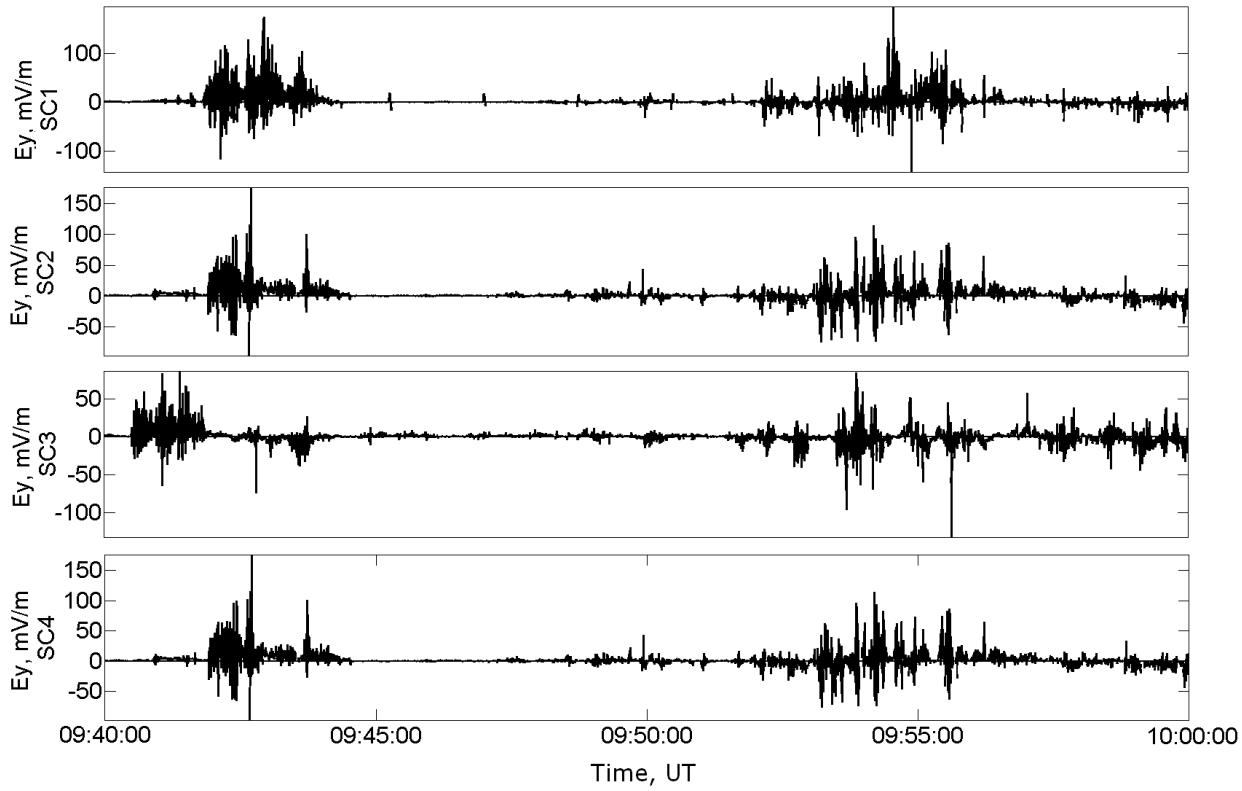

Figure 5-52: The electric field raw data from the time interval between 09.40 UT and 10.00 UT.

Electric fields in the magnetic reconnection interval

When investigating the relation between the E_y-component and the density the spin resolution electric field was used. The reason was the low resolution of the density (~8 seconds) data, which may prevent a possible relation between the density and electric field amplitudes to appear. Figure 5-53 presents plots of the ion density versus E_y for SC1, SC3 and SC4, respectively.

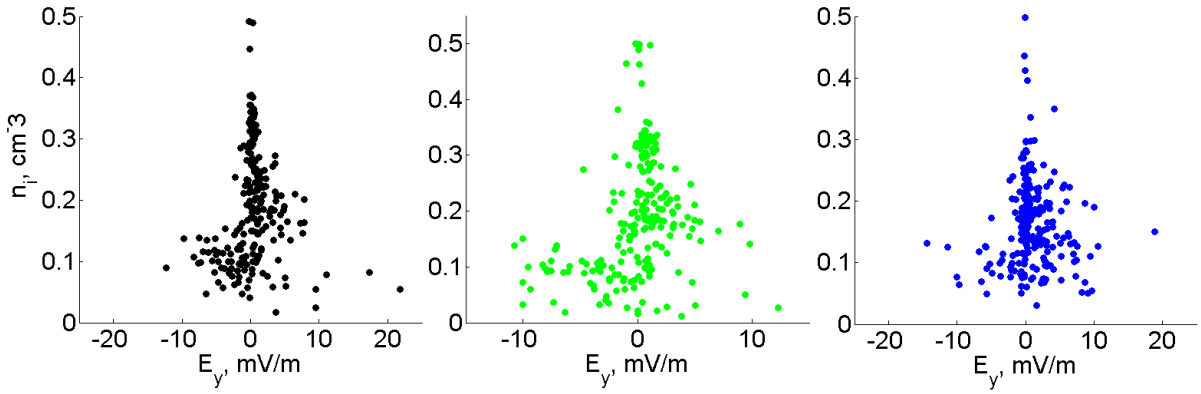

Figure 5-53: The E_y versus the density from SC1, SC3 and SC4.

As seen in the figure, the large electric fields (~ 10 mV/m) occurred more frequently in the regions with low ion density (0.1 – 0.2 cm^{-3}). Note that the axes are different in the panels.

Figure 5-54 displays scatter plots of E_y versus B_x. In these plots, the full resolution electric field and magnetic field data have been used.

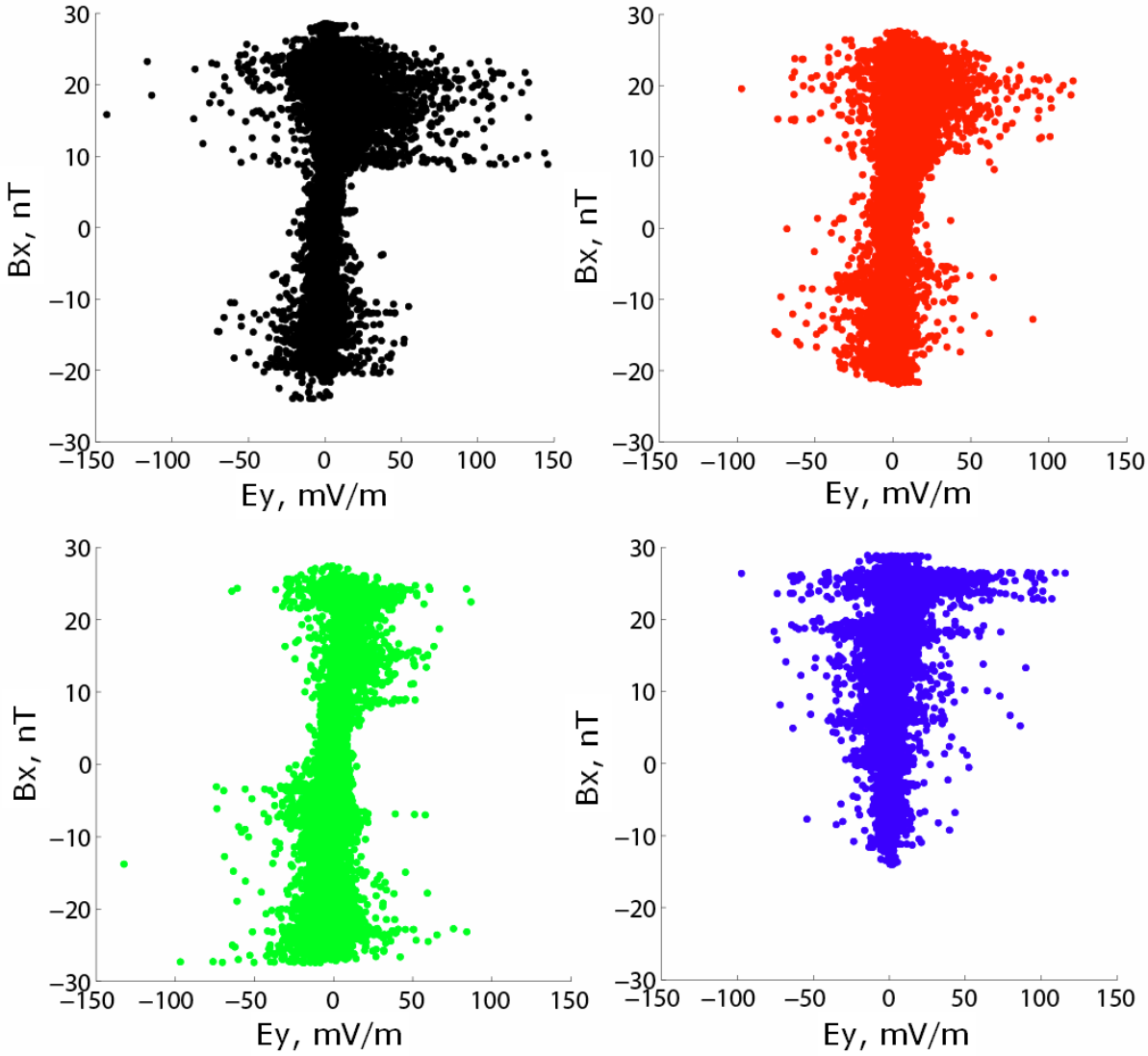

Figure 5-54: Scatter plot of B_x versus E_y from all four spacecraft. The plots are in the Cluster colours: SC1-black, SC2-red, SC3-green and SC4-blue.

The reason for using full resolution was to include the large electric field amplitudes which were removed during calibration. As seen from the figure, the largest electric field (> 50 mV/m) occurred mostly in the regions where the B_x-component was large ($\pm$ 30 nT). Close to the neutral sheet ($B_x = 0$) there were no such large electric field amplitudes, except for at SC3 and SC4. In the measurements from SC3 and SC4 the large electric fields appeared mostly in regions with large $|B_x|$, but also in regions where $B_x \approx 0$. When the spacecraft

crossed the current sheet during the first outflow, there were large electric fields present in the measurements from SC3 during that crossing.

The occurrence of the large electric fields in regions with low density and large $|B_x|$ values as presented in Figure 5-53 and Figure 5-54 from SC1 and SC2 were consistent with the observations done by *Borg et al.* [2005]. The signatures indicated that the large amplitude electric fields occurred mostly in the vicinity of the separatrices.

The variance analysis calculations and the Hall magnetic field

The variance analysis elaborated in chapter 2.5.3, was used for this event as well. The results from the calculation are given in Table 5-6, which contains the eigenvalues and the qualification multiplier for each spacecraft. The covariance matrix for this event was based on measurements from the time period between 09.30 and 10.15 UT. The time interval was chosen for the same reason as in the 2005 event: It should include the entire reconnection interval. The magnetic field data used in the calculations were full resolution data.

Spacecraft, SC	**Eigenvalues, λ**	$\omega = \frac{\lambda_{\max}}{\lambda_1 + \lambda_2 + \lambda_3}$
SC1	$\lambda_1 = 14, \lambda_2 = 23, \lambda_3 = 282$	$\omega = 0.88$
SC2	$\lambda_1 = 12, \lambda_2 = 23, \lambda_3 = 274$	$\omega = 0.87$
SC3	$\lambda_1 = 12, \lambda_2 = 21, \lambda_3 = 316$	$\omega = 0.91$
SC4	$\lambda_1 = 14, \lambda_2 = 21, \lambda_3 = 242$	$\omega = 0.87$

Table 5-6: The calculated eigenvalues and qualification multiplier for all four Cluster spacecraft in the time period between 09.30-10.00 UT.

The eigenvectors corresponding to the largest eigenvalues were used as the new x-axis when rotating the dataset. The largest eigenvalues were well determined at all four spacecraft which is seen by the large qualification multipliers (more than 87 % of the magnetic field is in the modified x direction). When calculating the modified coordinate system, it was assumed that the current sheet normal was directed along the $\hat{\boldsymbol{z}}_{GSM}$. When comparing the assumed current sheet direction with the normal calculated from the minimum variance analysis which yields $\hat{\boldsymbol{n}}_{VA} = (-0.02, 0.36, 0.93)$, it was clear that the assumption was at a sufficient level of accuracy. An additional verification of the assumption based on a current sheet normal directed along the $\hat{\boldsymbol{z}}_{GSM}$ was obtained from multipoint time analysis (MTA), see appendix D. From the MTA, the normal of the current sheet, when the Cluster satellites crossed the current sheet first time during the studied time interval, was found to be $\hat{\boldsymbol{n}}_{MTA} = (-0.1, -0.4, 0.9)$. The

rotation angles between the GSM coordinate system's and the modified system's x- and y-axis were of magnitude ~9° for SC1, ~6° for SC2, ~5° for SC3 and ~11° for SC4 during this interval.

The results from the dataset rotation are shown in Figure 5-55 where the black curves represent the original magnetic field B_y and the red curves show the B_y. As seen from the figure, there was a significant difference between the components at the beginning of the interval, and the largest differences were found in the measurements from SC1 and SC4, which were in the range of 3 nT. This difference was larger than the uncertainty of the FGM instrument when measuring magnetic field with magnitude less than 64 nT (see chapter 3.2.2). Thus, when using the modified coordinate system, any effects related to flaring of the magnetic field would be reduced. Measurements in the modified coordinate system were written with a ' (for example B_y').

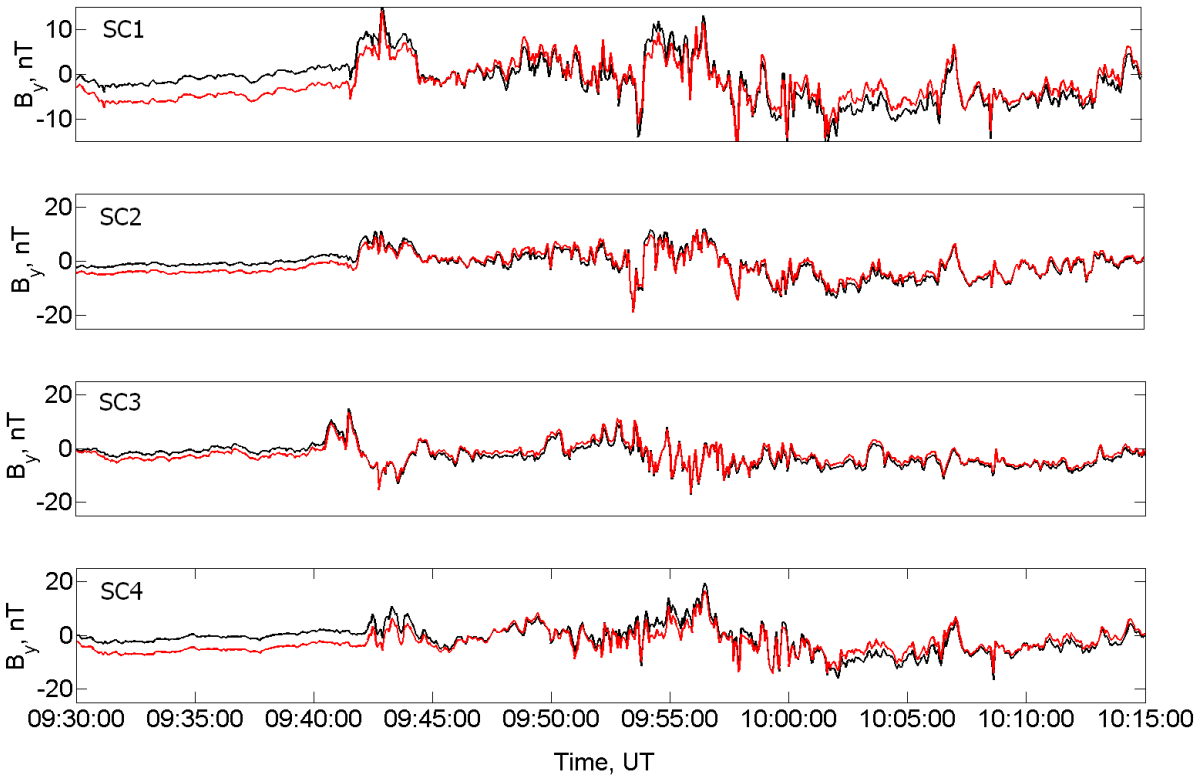

Figure 5-55: The result of the variance analysis on the magnetic field B_y-component. The black curve show the original magnetic field and the red curve show the corrected magnetic field.

When plotting the Hall magnetic field, the time intervals chosen for the examination must satisfy the following criteria [*Borg*, 2006]: The spacecraft had to observe a positive or negative outflow where V_x reached large values, and the spacecraft must be located within the plasma sheet. The SC1, SC3 and SC4 satisfied those criteria's during the outflow periods ex-

cept for some short possible crossings into the lobe. Based on the B_z measurements from SC2 which coincided with the other B_z measurements, it was assumed that SC2 also registered the high speed outflow as the other three spacecraft did.

In Figure 5-56 panel a) – panel e), each panel contains data from a high speed outflow periods. The scatter plots were based on spin resolution data transformed into the modified coordinate system, and the plots were presented in the Cluster satellites colours.

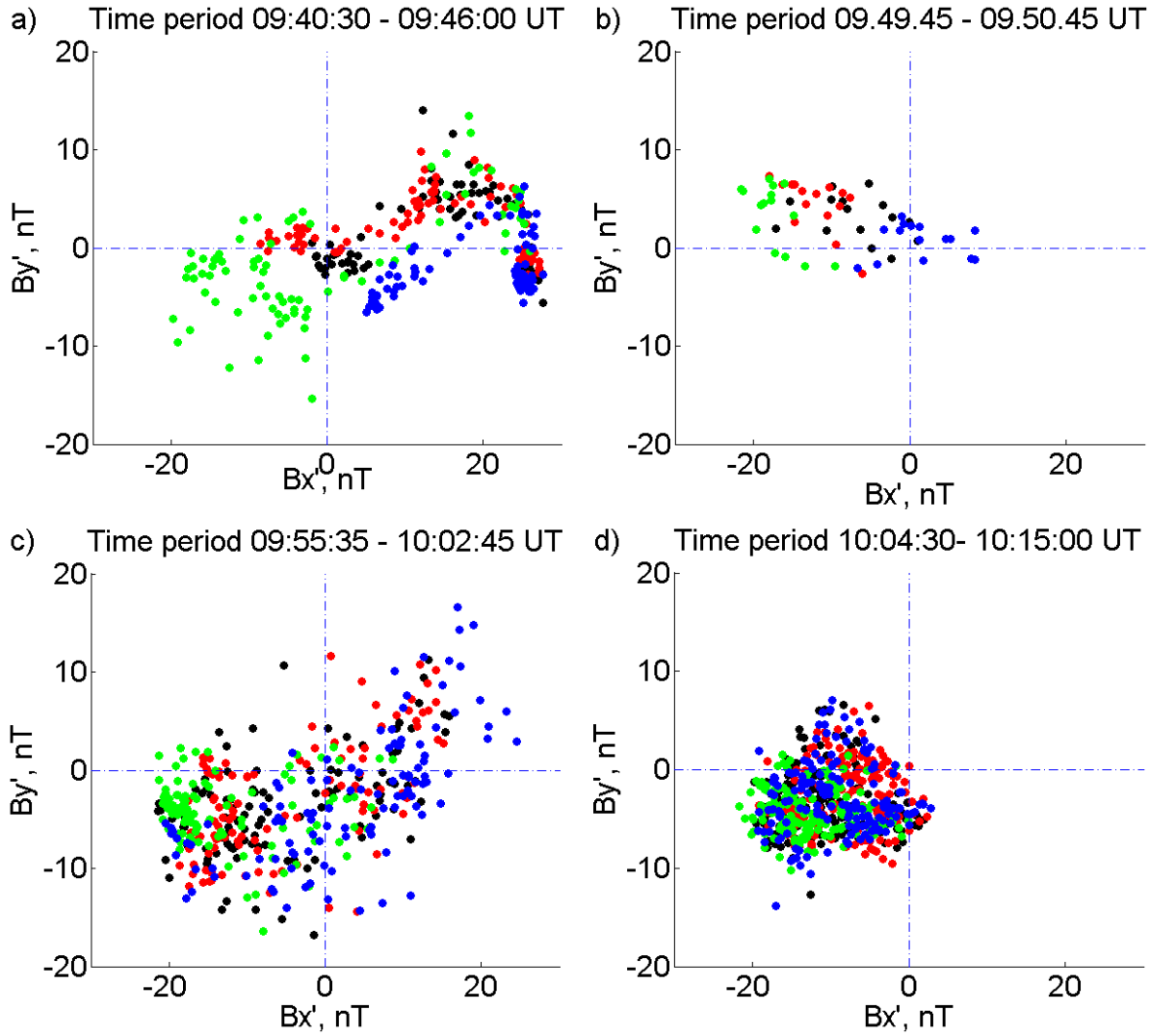

Figure 5-56: Scatter plots of the relation between the $B_x{}'$ and $B_y{}'$ magnetic field components during the four registered high speed outflows. The colours represent Cluster colours. Details regarding the figure are given in the text.

Panel a) shows a clear correlation between the B'_x and the B'_y measurements as would be expected if a quadrupole Hall magnetic field was present. The sense of the correlation corresponds to the relation earthward of the reconnection region, and is consistent with the earthward directed high speed outflow during this interval. In panel b) the correlation has changed to an anti-correlation between the B'_x, and $B_y{}'$. The sense of the correlation corresponds to a

location tailward of the reconnection region, in consistence with the direction of the second high speed outflow, which was tailward. In panel c) a new quadrupole Hall magnetic field signature was observed in the correlation between the B'_x and the B'_y measurements. The sense of the correlation again corresponds to a location earthward of the reconnection region. In panel d) the picture is somewhat cluttered and it is not possible to recognise any quadrupole Hall signature. This may be due to the fact the spacecraft stayed south of the current sheet during the last earthward high speed outflow.

In Figure 5-57 displays the modified out-of-plane Hall magnetic field (B_y') from SC1, SC3 and SC4, respectively, containing data from the three first outflows where the quadrupolar Hall signature was in apparent Figure 5-56.

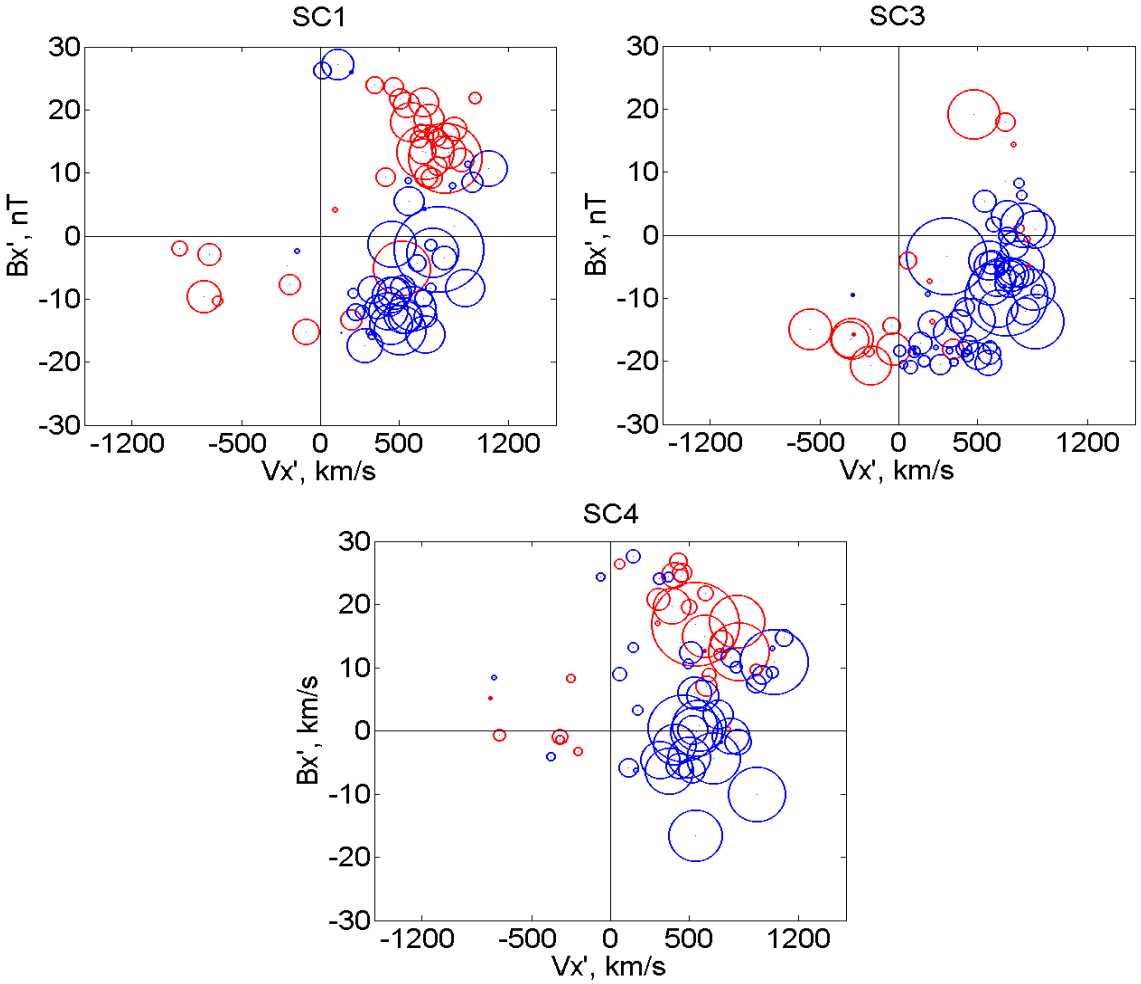

Figure 5-57: The Hall-bubble plot from the three first outflows periods from SC1, SC3 and SC4. The red circles represent negative B_y' while the blue circles represent negative B_y'-components. The size of the bubbles depends on the B_y' magnitude.

In Figure 5-57 the blue circles indicates a B'_y-component out of the plane (positive) while the red circles indicates a B_y'-component into the plane (negative). In the figure, negative B'_y-

dominated in the positive B_x'- and positive V_x'-quadrant and in the negative B_x'- and negative V_x'- quadrant. The positive B_y' dominated in the region of negative B_x'- and positive V_x'-quadrant. SC1 and SC3 observed three of four Hall-magnetic field branches during the time interval from 09.40 UT to 10.03 UT as presented in Figure 5-57. SC4 observed only two of the branches during the studied time interval.

These results indicate that the Cluster satellites entered a collisionless magnetic reconnection during each of the high speed outflows in the time interval between 09.40 UT and 10.15 UT. However, during the last high speed outflow, the satellites were probably located too far away from the region in order to observe the quadrupole Hall magnetic field. Note that each of the panels in Figure 5-56 contains measurements from one outflow each, while each of the panels in Figure 5-57 contains measurements from all three outflows. Based on the sense of the correlation between the B_x' and B_y' components, the Cluster satellites were located both earthward and tailward of the reconnection region during the outflows.

The scatter plots presented in Figure 5-56 and in Figure 5-57 were also made using measurements in the GSM coordinate system. The relation between the B_x and B_y measurements revealed the same signatures as the ones presented in Figure 5-56. When using the GSM measurements in order to present the bubble plots as in Figure 5-57, SC1 observed only two of the quadrupole Hall signature branches. The scatter plots using measurements rotated into a new coordinate system revealed clearer signatures of the quadrupole Hall magnetic field.

The Cluster satellites' location in the reconnection region

Based on the signatures seen in the preceding sections: An earthward directed high speed flow with a positive excursion in the B_z-component and the quadrupole Hall magnetic field, a rough estimate of the location of the spacecraft was determined as presented Figure 5-58. The signatures suggest a location of the Cluster satellites earthward of the reconnection region.

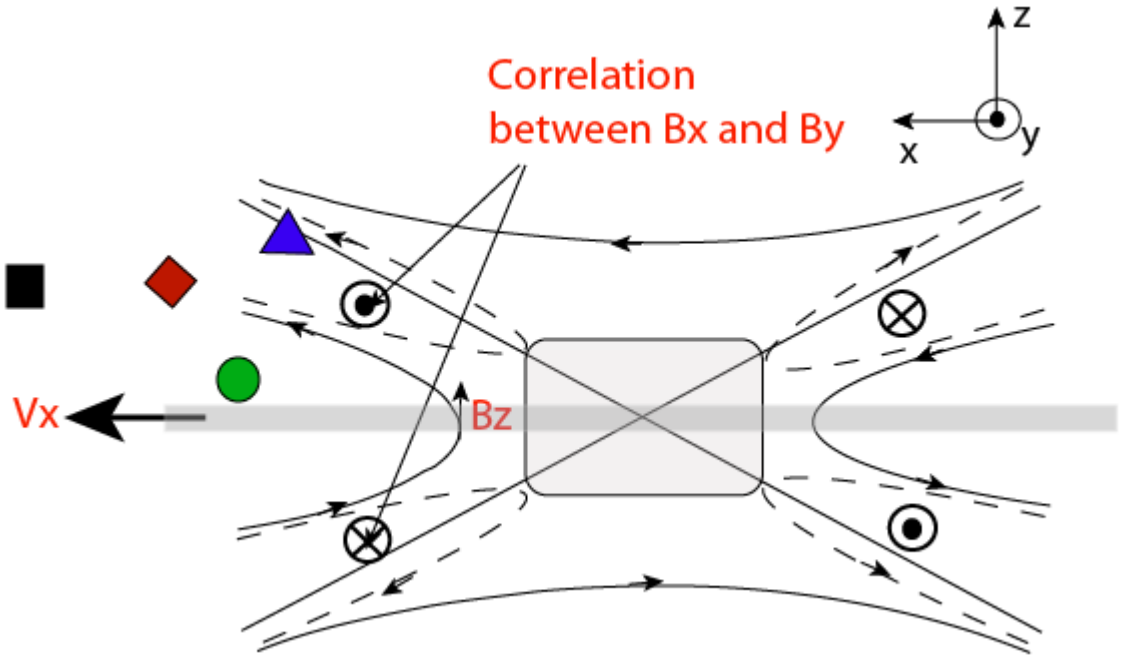

Figure 5-58: A rough sketch of the Cluster satellites' location with respect to the reconnection region during the event 22nd August 2001 between 09.40 UT and 09.44 UT. The red font marks the observed signatures in the data from the Cluster satellites. The signatures are not to scale.

5.2.2 Magnetic field line footpoint in the ionosphere

The OVT program simulated three different footpoints, using three models, of magnetic field lines from the same region where the Cluster satellites were located. The parameters used when simulating the footpoints using the T87, T89 and T96 models [*Tsyganenko*, 1987, *Tsyganenko*, 1989, *Tsyganenko*, 1995], are given in appendix C (see chapter 4.3 regarding the details of the simulations). The time of mapping the footpoints was set to 09.40 UT, just when the Cluster satellites entered the magnetic reconnection region. The region surrounding the footpoints calculated by T87, T89 and T96 models are shown as the red circles in Figure 5-59, panel a) and panel b). The red circles are from now on referred to as the footpoint regions. The grey circles in the figures are geographic latitudes and longitudes. In the northern hemisphere the footpoint region was located west of Hudson Bay in northern Canada between 55° and 65° north. In the southern hemisphere the footpoint region was located in the ocean between Antarctica and New Zealand around 60° south. It should be pointed out that the calculations of the footpoints were very uncertain also in this event, and therefore the simulations only provide a rough determination of the footpoint region.

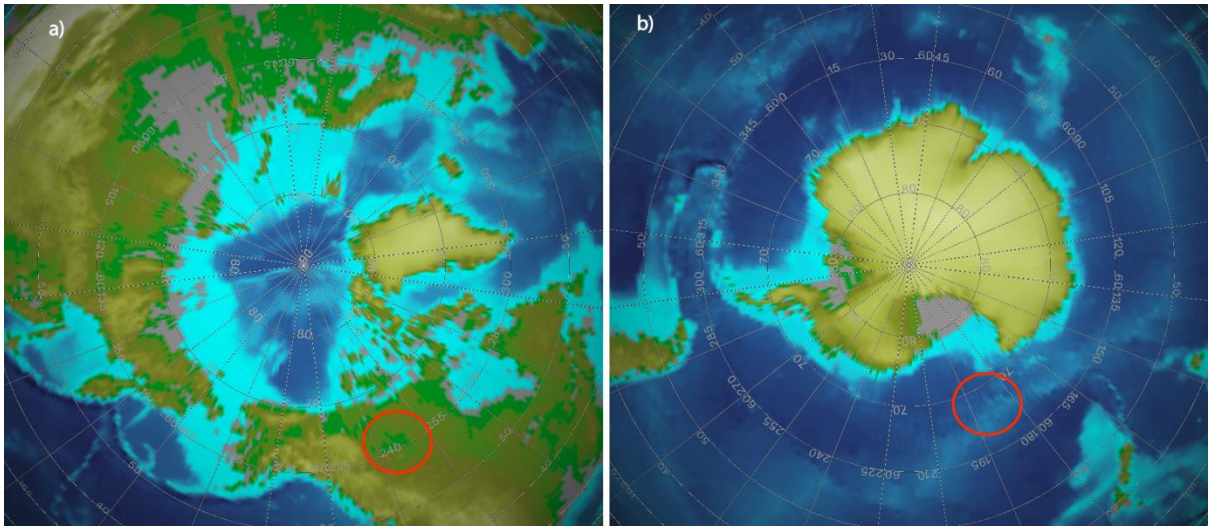

Figure 5-59: The footpoint region marked as the red circles in the northern and southern hemisphere. The gray lines illustrate the geographical latitudes and longitudes.

5.2.3 Data analysis and observations in the ionosphere

Enhanced auroral activity in the auroral oval was reported by the FUV WIC [*Mende et al.*, 2000a] on the IMAGE satellite during the time period when the Cluster satellites observed signatures of a collisionless magnetic reconnection (see chapter 3.3 regarding details of IMAGE). Figure 5-60 shows the UV pictures taken by the IMAGE WIC instrument of the auroral oval in the northern hemisphere during the time period from 09.37 UT to 10.13 UT. The auroral intensity was measured in rayleighs.

At 09.39 UT an auroral intensification appeared in the post-midnight sector at ~01 MLT between 60° and 70° magnetic latitude, west of the region where the footpoint region was located (see Figure 5-60). The aurora became more intense while the poleward boundary of the oval moved poleward filling the southern part of the footpoint region at 09.43 UT. This first period of intensification corresponded in time to when the Cluster satellites encountered the first earthward directed high speed flow at ~18 R_E. At 09.45 an auroral bulge developed in the footpoint region and the intense auroral region moved westward filling large parts of the midnight sector. At 09.49 UT the aurora became more intense and the oval started to expand poleward until 09.55 when parts of the aurora located in the pre-midnight sector became slightly weaker in intensity. This intensification at ~09.49 UT happened at the same time as the Cluster satellites encountered the tailward directed high speed flow. At 09.59 the aurora again grew in size and covered the whole footpoint region, where the aurora in the pre- and post-midnight sectors reached an intensity of 2000 R.

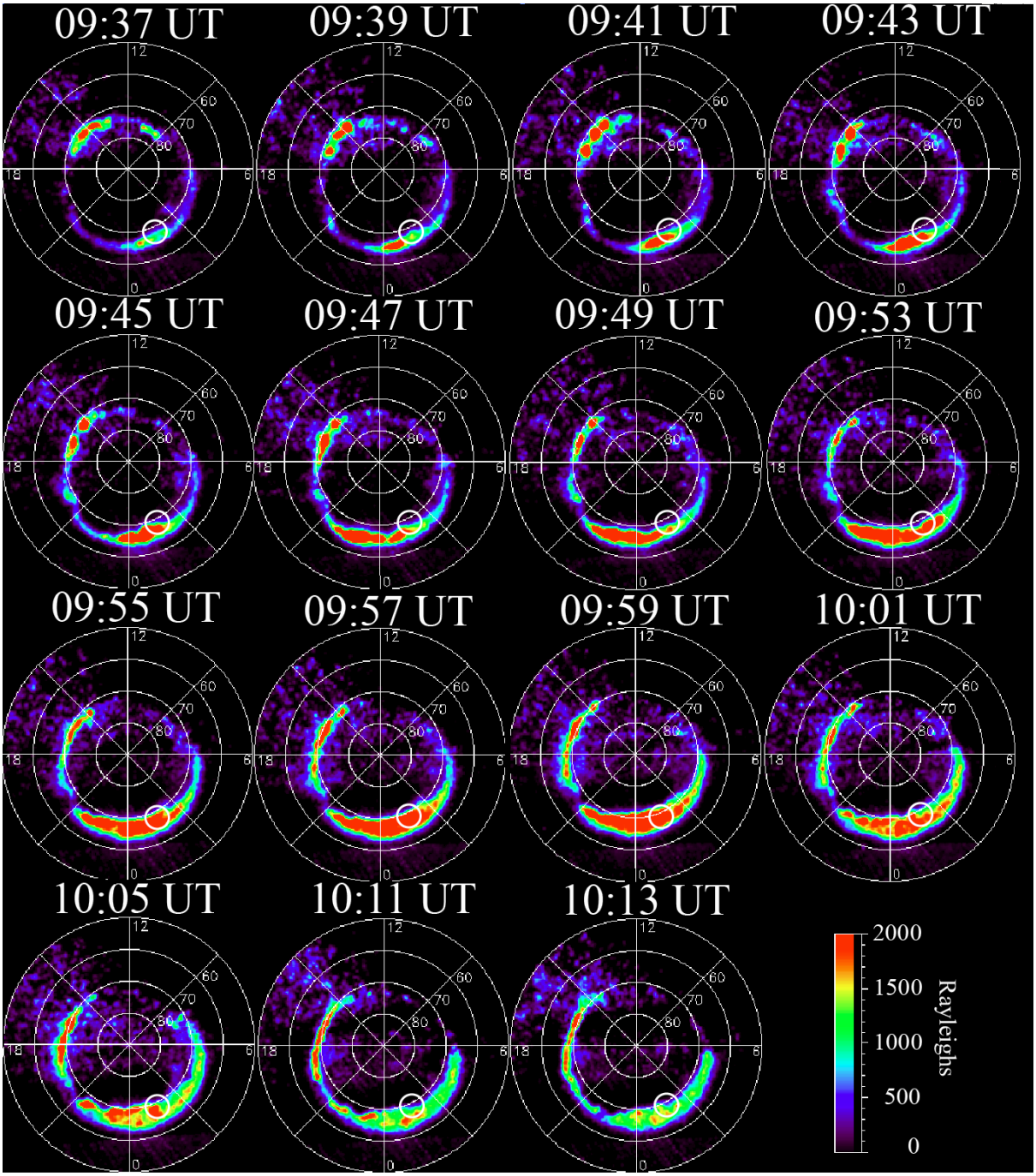

Figure 5-60: Selected pictures from the IMAGE WIC of the auroral oval before, during and after the reconnection interval observed by the Cluster satellites. Image observed the northern hemisphere at this time which is seen by the positive latitudes. The colour bar represents the intensity of the aurora measured in Rayleighs. The small white circle indicates the region where the footpoints of the Cluster satellites magnetic field lines are located.

The aurora moved poleward and had a spatial extent covering the pre- and post-midnight sectors, almost filling the magnetic latitude between 60° and 70° north. At 10.01 UT the aurora started to break up and move equatorward. At 10.13 UT the aurora was almost dissolved. The aurora which developed at ~09.57 UT corresponded in time to the Cluster satellites measuring the third earthward directed high speed outflow. The footpoint region was located within

the region of the intense auroral breakout during the whole period. Note that there is a ~2 minute difference between each IMAGE WIC picture in Figure 5-60 except between 10.05 UT and 10.11 UT. The reason is that the two pictures between these time intervals showed the same auroral dissipation as the shown in the picture at 10.11 UT.

5.2.4 Ground measurements

Magnetic bays

Based on the position of the footpoint region data from the magnetometer stations Cambridge Bay (CBB), Yellowknife (YKC) and Meanook (MEA) were used. The locations of the stations vary in geographical latitude and longitude. In the light of the footpoint location in the southern hemisphere, which was in the ocean south-east of New Zealand, the amount of available magnetometer stations were limited. The magnetometer stations Dumont d'Urville (DRV) in Antarctica, Macquarie Island (MCQ) and Eyrewell (EYR) on New Zealand were the closest stations to this region. The geographical latitude and longitude of the stations are given in Table 5-7 (A map of the stations is found in chapter 3.4.2).

Station name, north	**Geographical longitude**	**Geographical latitude**
Cambridge Bay, CBB	255°	69°
Yellowknife, YKC	246°	63°
Meanook, MEA	247°	55°
Station name, south		
Dumont d'Urville, DRV	140°	-67°
Macquarie Island, MCQ	159°	-55°
Eyrewell, EYR	172°	-43°

Table 5-7: The INTERMAGNET stations in the northern and southern hemispheres from which the geomagnetic field data is taken. The stations are sorted by geographical latitude.

Figure 5-61 shows the measurements of the horizontal (H) and the vertical (Z) components of the geomagnetic field during the time period between 09.00 UT and 11.00 UT measured by the stations located in the northern hemisphere. The stations are sorted by latitude in the figure, where CBB is located farthest north and MEA is located farthest south. The resolution of the data was one minute, and an error of ± 2 minutes should be added due to the manual reading from the graph when determining the onsets of signatures.

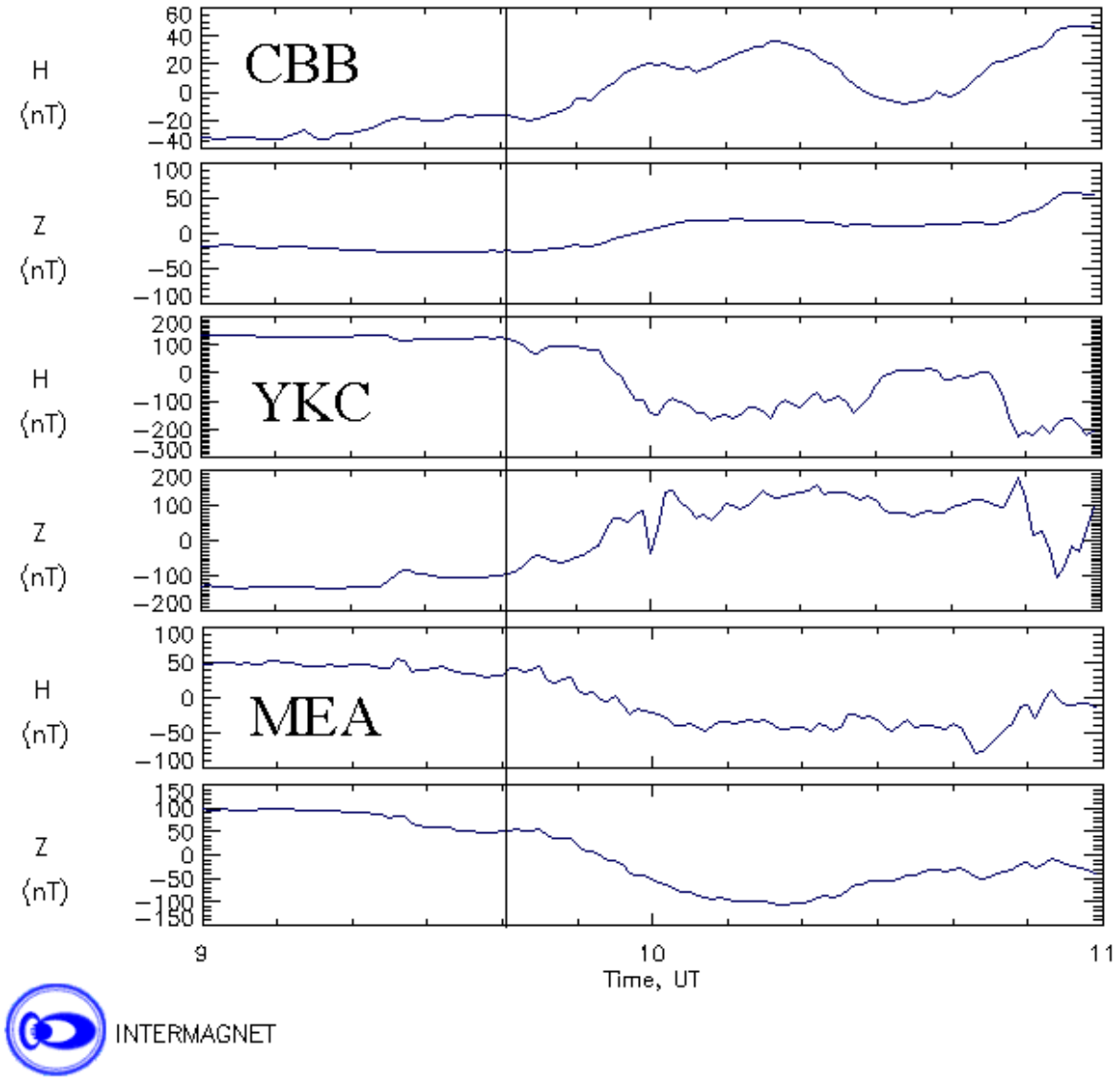

Figure 5-61: The ground magnetic field data from Cambridge Bay (CBB), Yellowknife (YKC) and Meanook (MEA) stations which are located in the Cluster satellites footpoint region in the northern hemisphere.

At ~ 09.41 UT a negative magnetic bay developed at the YKC station which is marked with the black line in Figure 5-61. This was seen in the negative excursion in the H-component in Figure 5-61. The bay lasted for ~ 50 minutes and reached a magnitude of ~200 nT. Almost at the same time as the horizontal intensity decreased, the Z-component suddenly changed with first a drop, then an increase. These signatures suggest that an auroral electrojet was flowing south of the station, and the negative bay (H < 0) indicated that a WTS was located close to the station [*Rostoker et al.*, 1980]. During the same interval, the MEA station registered a negative magnetic bay and a decrease in the Z-component. MEA was located further south than the YKC station (see Table 5-7). The signature in the Z-component was consistent with the expected signature if the station was located south of an auroral electrojet. The vertical

component at the CBB station registered a small increase which verified that the station was located north of the auroral electrojet. Based on the signatures in the measurements from the vertical component of the geomagnetic field, an auroral electrojet flowed between the YKC and CBB station in the northern hemisphere. A negative magnetic bay developed at the MEA station, but the deflection was less (~ 50 nT) than the bay which developed at the YKC station (~ 200 nT). The negative bays indicated that the WTS was closer to the YKC station than the MEA station. The footpoint region was located in the same region as the YKC station. The magnetic bay registered at the YKC station suggests a substorm onset at 09.41 UT in the northern hemisphere, 1 minute after the Cluster satellites registered the first earthward directed high speed outflow.

Figure 5-62 shows the measurements of the horizontal intensity and the Z-component of the geomagnetic field in the time period between 09.00 UT and 11.00 UT from stations located in the southern hemisphere. The stations are sorted by latitude, where the DRV station is farthest south and the EYR station is located farthest north. The stations were located further away from the footpoint region, compared with the location of the stations in the northern hemisphere.

At both the DRV and at the MCQ stations there were small but positive excursions in the horizontal intensity after 09.40 UT. The vertical component at the DRV station increased (~ 40 nT) while the same component at the MCQ station decreased (~ 50 nT). The fluctuations of the horizontal intensity at both the DRV and the MCQ station suggest that a WTS passed the stations at some distance. The WTS probably passed the MCQ station in the southern hemisphere at approximately the same distance as the WTS passed the MEA station in the northern hemisphere. This assumption is based on the same magnitudes in the magnetic bays and in the deflections of the vertical component being the same. Based on the magnetic bay signatures from the DRV and the MCQ stations, there may have been a dawn-to-dusk flowing auroral electrojet located between these stations in the northern hemisphere. The fluctuations at the EYR station were too small to use to locate the station's position with respect to the auroral electrojet.

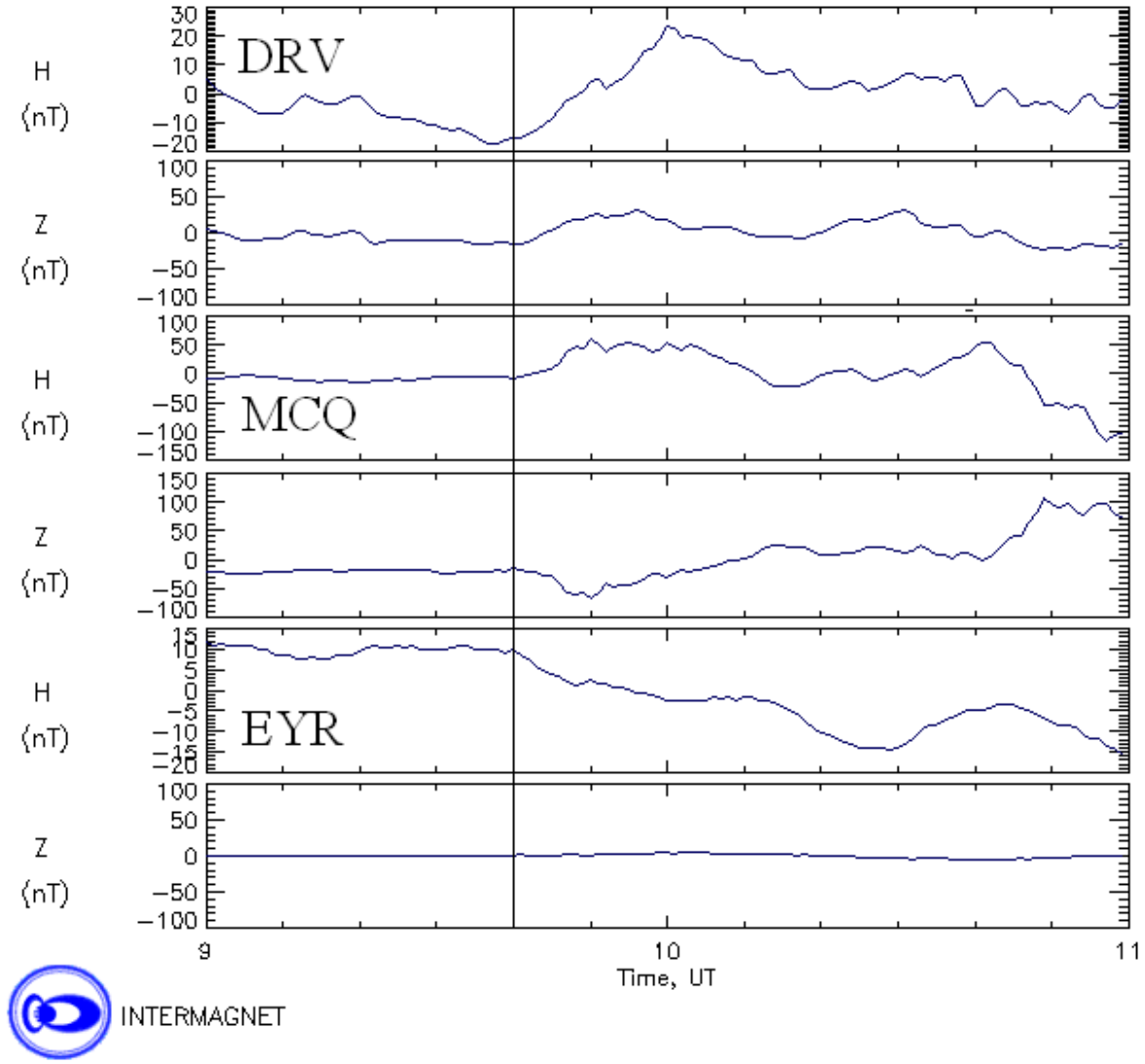

Figure 5-62: The ground magnetic field data from Dumont d'Urville (DRV) in Antarctica and Macquarie Island (MCQ) and Eyrewell (EYR) on New Zealand. The stations were the ones located closest to the region where the footpoint region was located in the southern hemisphere.

Pi 2 signatures

The Pi 2 signatures were described in chapter 2.6.1, and the stations used from the CPMN-network are listed in Table 5-8. The stations were selected due to their geographical location which varies in latitude (see map of the stations in chapter 3.4.1). The stations are arranged in Table 5-3 with respect to their geographical latitudes in the northern and southern hemisphere. The H-component of the geomagnetic field measurements from the stations listed in Table 5-3 table is presented in Figure 5-63 and Figure 5-64 for the northern and southern hemispheres, respectively. During the time period between 08.00 UT and 10.15 UT the stations in the CPMN-network were located in the pre-midnight sector close to 20 MLT. Be-

tween 08.00 UT and 10.15 UT there were no registrations of Pi 2 pulsations in the CPMN-chain. As seen from the figures there were disturbances registered at 08.27 UT and just before 10.00 UT, but the period of these disturbances was larger than the characteristic period of the Pi 2 pulsations, which are between 40-150 seconds [*Olson*, 1999].

Station name(North)	**Geographic latitude**	**Geographic longitude**
Chokurdakh, CHD	71º	148 º
Zyryanka, ZYK	60 º	151 º
Moshiri, MSR	44 º	142 º
Onagawa, ONW	38 º	142 º
Stations name(South)	**Geographic latitude**	**Geographic longitude**
Macquarie Isl., MCQ	-55 º	159 º
Canberra, CAN	-35 º	149 º
Dalby, DAL	-27 º	151 º
Weipa, WEP	-13 º	142 º

Table 5-8: The geographic locations of the selected stations in the CPMN chain used in this thesis. Their location is rewritten from the homepage of the CPMN stations[*CPMN*, 1995].

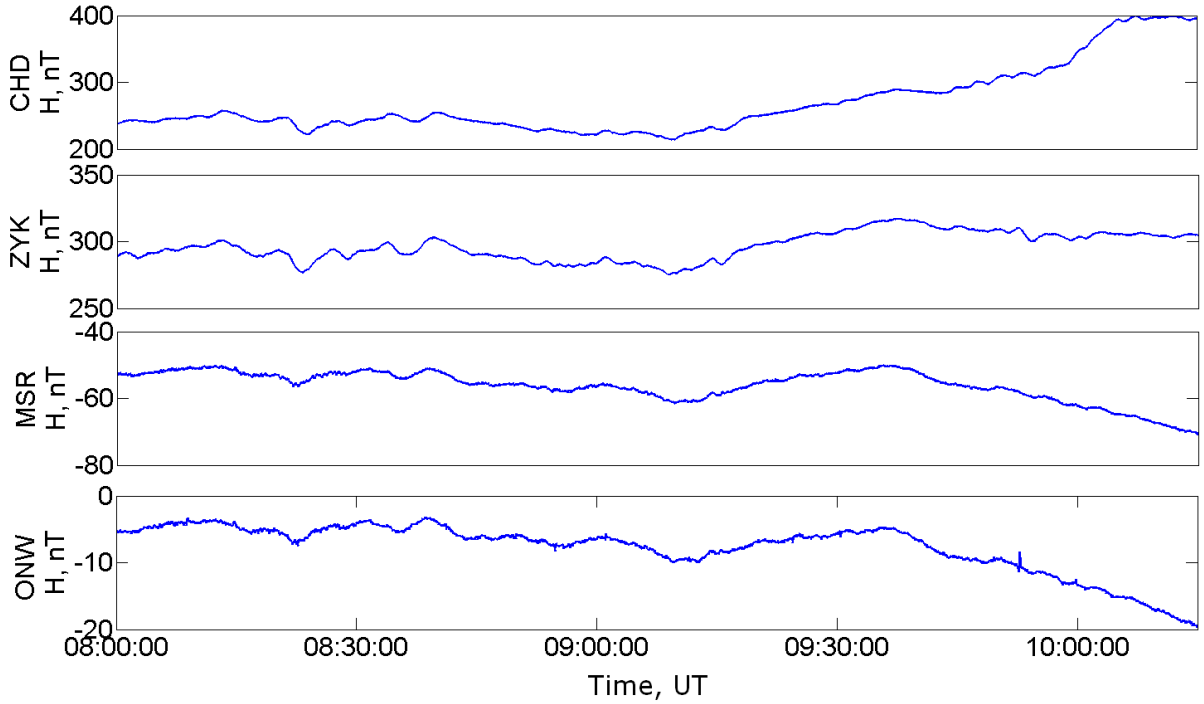

Figure 5-63: Horizontal component o the magnetic field used in order to identify Pi 2 pulsation seen by the northern hemisphere stations in the CPMN chain. No signatures of the Pi 2 pulsations were registered during this interval.

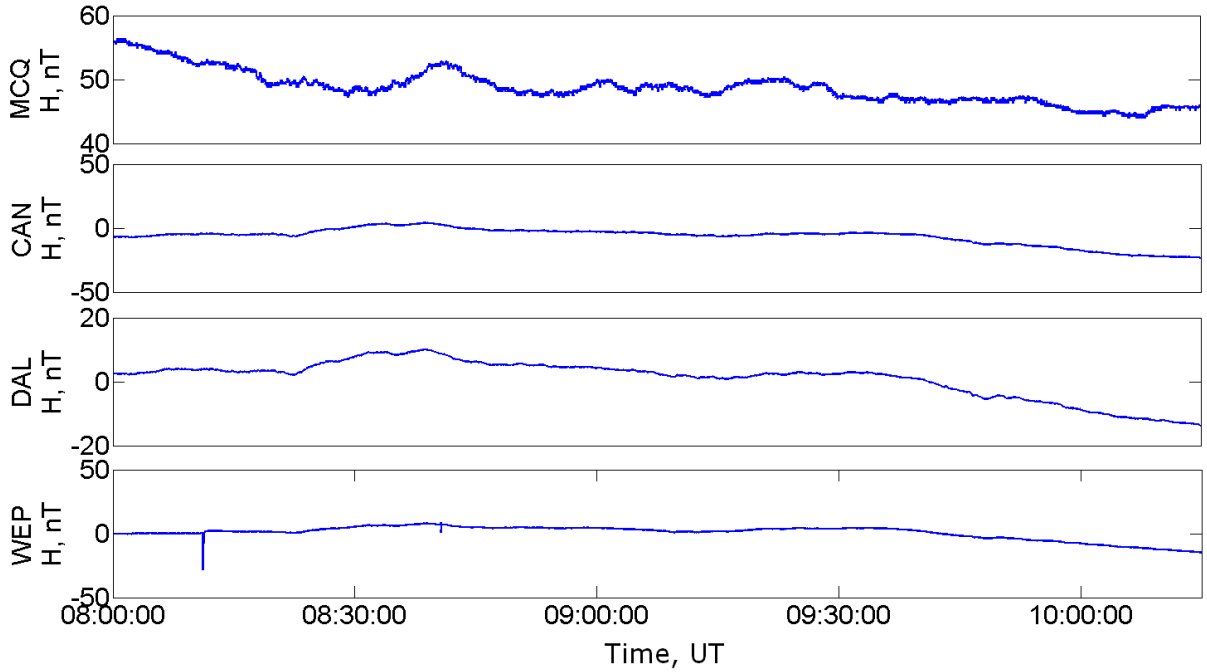

Figure 5-64: Horizontal component of the magnetic field used in order to identify Pi 2 pulsations seen by the southern stations in the CPMN chain. No signatures of the Pi 2 pulsations were registered.

The probability of one-to-one correspondence between auroral breakups, located between 60° N and 73° N, and Pi 2 pulsations registered at a low-latitude magnetometer station (latitude < 60°) has been investigated. It was found that if the station was located within 20 to 03 MLT there was a 79 % correspondence between the observation of the auroral breakup and the observation of a Pi 2 pulsation [*Yumoto and Grp*, 2001]. Since the stations during this event were located towards 18 MLT the probability of observing the Pi 2 pulsations during the studied time interval decreased.

Auroral indices

The AE-index and the Kp index are used as a measure of the substorm activity level. The values which constitute the Kp-index on the 22nd August 2001 are presented in Table 5-9. As seen from the table, the Kp-index increased from a level 3- up to a level 4 in the period between 06.00 UT and 12.00 UT. Although the KP index has a time resolution of 3 hours, it shows the trend of the geomagnetic activity this day.

Time period	00-03 UT	03-06 UT	06-09 UT	09-12 UT	12-15 UT	15-18 UT	18-21 UT	21-00 UT
KP-index	1+	2	3-	4	4	3+	4	4+

Table 5-9: The Kp-index during the 22.08.2001. One time period represents three hours. Time period between 9 UT and 12 UT represents the time interval where the active aurora and the magnetic bays were presented.

The auroral electrojet index, AE-index, for the period between 09.00 UT and 14.05 UT is shown in Figure 5-65.

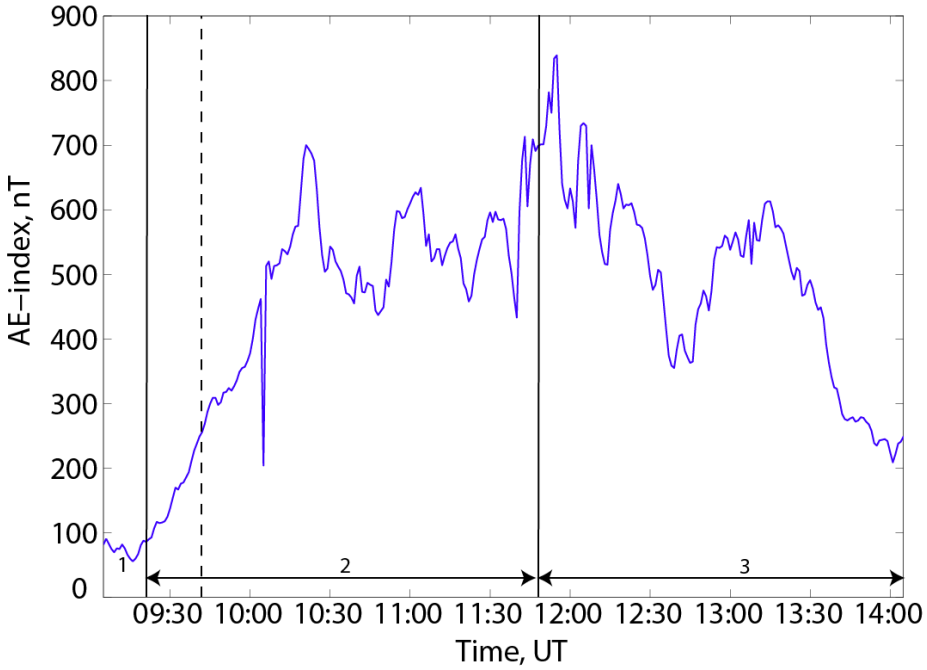

Figure 5-65: The AE-index during the active period. The different phases of the substorm are marked as 1, 2, and 3, where 1 is the growth phase, 2 is the expansion phase and 3 is the recovery phase. The dashed line marks the time when the Cluster satellites observed the first high speed ion outflow at ~09.40 UT.

The dashed line in the figure marks the time when the Cluster satellites encountered the magnetic reconnection region and observed the first high speed ion outflow (~ 09.40 UT). The index reached values larger than 500 nT with a peak reaching ~ 800 nT. Such values correspond to a large geomagnetic disturbance. The shape of the disturbance indicated a substorm development, where the onset took place at ~09.20 UT marked with "1" in the figure. The expansion phase lasted for ~2.5 hours before the index was reduced, which means the auroral electrojet started to diminish. The recovery phase lasted for ~2.5 hours, marked as "3" in the figure. s

5.2.5 Timing of the 2001 event

The Cluster satellites were located in the near-Earth magnetotail at a distance ~ -18 R_E from the Earth on the 22nd August 2001 when it observed fast plasma jets in both the earthward and the tailward directions. The first outflow was detected at 09.40 UT and contained all the signatures of magnetic reconnection. This outflow was therefore chosen as the start of the magnetic reconnection event and the time is given in Table 5-10.

The observed signatures	Time start [UT]
Auroral Electrojet	~ 09.20 ± 1 minutes
Aurora substorm onset	~ 09.39 − 2 minutes
Magnetic reconnection	~ 09.40
Start of Pi 2-wave train, south	-
Start of Pi 2-wave train, north	-
Magnetic bay, north	~ 09.41 ± 3 minutes
Magnetic bay, south	~ 09.40 ± 3 minutes

Table 5-10: The start of the different signatures in the 2001 event.

The first indication of changes in the datasets after magnetic reconnection was first observed was in the observations of the ionosphere from the northern hemisphere by IMAGE WIC. However, the auroral intensification appeared a minute (~ 09.39 UT) before the magnetic reconnection was observed in the magnetotail (see Table 5-10). Due to the resolution of WIC (2 minutes) an exact timing of the auroral intensification was difficult, which means that the intensification could have started one minute or up to three minutes, before the first magnetic reconnection were observed by the Cluster satellites. The intensification appeared in the post-midnight sector ~ 01 MLT, and the most intense region was located south of the footpoint region. At ~ 09.41 UT the intensified region entered the footpoint region. The next indication of activity was a magnetic bay development at the YKC station in the northern hemisphere. The YKC station was located within the same region as the footpoint region. The start of the bay in the northern hemisphere was measured ~1 minute (~ 09.41 UT, see Table 5-10) after magnetic reconnection was registered by the Cluster satellites. There was also an indication of a magnetic bay development in the southern hemisphere at the MCQ station a minute earlier than in the northern hemisphere. The bay was smaller, which can be explained with that the station were probably located further away from the footpoint region than the YKC station.

The AE-index this day suggested a substorm onset at 09.20 UT, 20 minutes before the Cluster satellites observed a magnetic reconnection in the tail. The AE-index increased to a level of > 500 nT, which indicates a large disturbance. The shape of the AE-index implies several intensifications of the auroral electrojet during the time period between 09.20 UT and 14.00 UT.

The timing of the signatures was difficult to establish exactly. This is seen in Figure 5-66 where the circles mark the starting point of the signature and the lines before and after

illustrate the uncertainties related to the onset time. The red line marks the interval of the first magnetic reconnection signatures observed by the Cluster satellites.

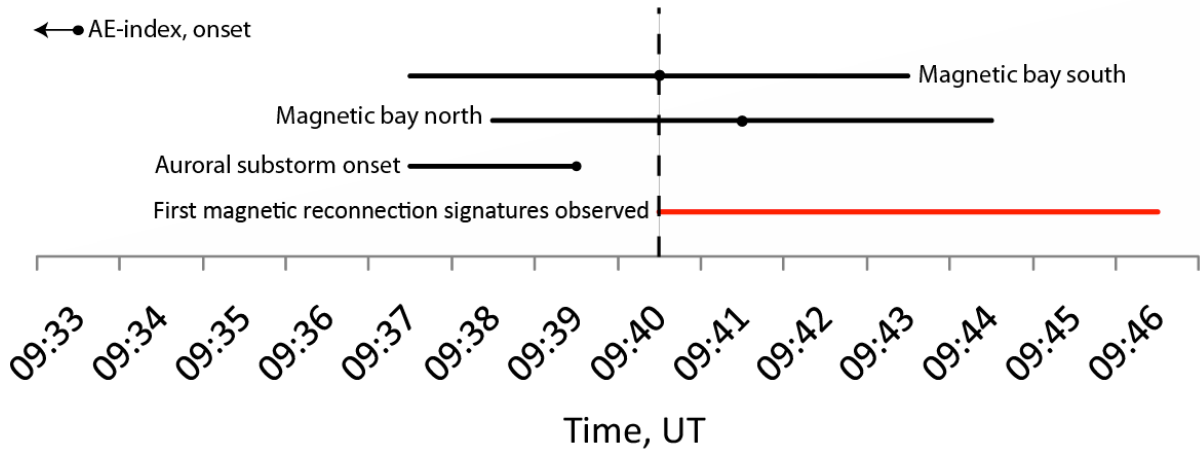

Figure 5-66: The time line when the first magnetic reconnection was observed and the following substorm signatures. The figure illustrates the difficulties regarding timing due to uncertainties of the signature onsets. The black dots represent the time of onset related the each of the substorm signatures. The horizontal lines are the uncertainties related to the onset time, and the vertical dashed line marks the start of the magnetic reconnection.

6 Summary and discussion

Two magnetic reconnection and substorm events have been presented using multi-instrument observations on the 22nd August 2001 and on the 26th September 2005 by the Cluster satellites, Image WIC and ground-based geomagnetic field measuring stations.

We have identified signatures of magnetic reconnection at distances ~ 18 R_E and ~ 15 R_E into the magnetotail from the Earth and identified geomagnetic activity. In the analysis presented in the preceding sections, the timing of the magnetic reconnection signatures and the substorm features has been studied. The main results from the studies are summarised and discussed in the following sections. At the end of the discussion the solar wind conditions in the time prior to the events are discussed, in order to investigate a possible relation between the geomagnetic activity and the energy input.

6.1 Flow reversals in the plasma sheet associated with reconnection

High speed ion flows in the plasma sheet have often been observed in the near-Earth magnetotail between 11 R_E – 20 R_E . The region outside 17 R_E is dominated by tailward directed high speed flows, while in the region inside 17 R_E is dominated by the earthward directed flows [*Petrukovich et al.*, 2009]. Such high speed plasma flows are associated with plasma sheet thinning [*Nakamura et al.*, 2002] which play an essential role during the substorm processes [*Sergeev et al.*, 1993].

Reversals of reconnection plasma outflows flows have been observed in the magnetotail reaching speeds of ~ 300 - ~ 900 km/s (e.g. [*Baker et al.*, 2002, *Borg et al.*, 2007, *Laitinen et al.*, 2007, *Runov et al.*, 2003]). The reversal of the plasma flows were associated with simultaneous reversals in the B_z-component and Hall magnetic field structures. Our results from both the 2005 and 2001 events are consistent with such findings. The tailward outflow velocity in the 2005 event reached a value of ~1000 km/s and the earthward ~ 500 - ~ 900 km/s. In the 2001 event both the tailward and the earthward directed high speed ion flows reached values of ~ 800 - ~ 1000 km/s. The outflow periods did, however, vary between the two events. In the 2005 event the outflow periods were sporadical and lasted for a short time (~ 3 minutes), while in the 2001 event the outflows lasted longer (~ 5 minutes) and did not emerge so bursty as in the 2005 event.

In the 2005 event, the magnetic reconnection seemed to consist of one bursty reconnection region reappearing at different locations in the near-Earth magnetotail. The first indications of a magnetic reconnection, which occurred earthward of the Cluster satellites, appeared at ~ 09.35 UT. Then after several minutes the reconnection reappeared at ~ 09.40 UT and the signatures contained a reversal of the outflow and a simultaneous reversal of the B_z. This reconnection period was the only one during the studied time interval which contained a continuous reversal in both V_x and B_z. The signatures suggest that the Cluster satellites were close to the reconnection region during this reconnection period. This is also confirmed by the clear quadrupole Hall magnetic field signatures registered by SC3 and SC4. At ~ 09.51 UT and at ~ 09.55 UT the reconnection reappeared, now located tailward of the Cluster satellites. The signatures of the reconnection region suggest a sporadic tailward movement of the disturbed region. Our results from the 2005 event are consistent with the findings by *Sergeev et al.* [2008]. They found that during the time interval between 08.00 UT and 10.00 UT magnetic reconnection operated in short pulses and that the V_x flow reversals was formed by a magnetic reconnection which reappeared at different locations in the near-Earth magnetotail.

In the 2001 event the outflow periods seemed continuous as if one outflow took over the for other, which indicates a continuously operating magnetic reconnection region moving across the Cluster satellites from 09.40 UT to 10.15 UT. Based on the direction of the high speed outflows and the B_z measurements, it seemes that the reconnection region was located mainly tailward of the Cluster satellites.

Based on the location of the Cluster satellites during observations of the collisionless magnetic reconnection intervals in the 2005 event, the reconnection occurred most likely on closed field lines within the plasma sheet. This conclusion is also consistent with the conclusion made by *Sergeev et al.*[2007].

The structure of the current sheet differs between the two events. During the 2001 event there was a kink mode oscillation of the current sheet during the magnetic reconnection interval [*Volwerk et al.*, 2003]. Such a kink mode wave is a standing wave, and it is an oscillation of the whole current sheet that was observed by all of the Cluster satellites. During the 2005 event there were two sequences of fluctuations. During the first period of the reconnection interval there were several small fluctuations in the B_x measurements from SC1 and SC3. These fluctuations were not large scale movements of the current sheet, but rather observations of strong turbulence within the current sheet. During the last part of the reconnection interval the small scale fluctuations disappeared and some large scale fluctuations ap-

peared. Those fluctuations were registered by SC1, SC3 and SC4 and were characterised by large changes in the B_x measurements. The fluctuations were first observed by SC1 followed by SC3 and SC4 which suggests an earthward motion of the flapping (SC1 more tailward than SC3 and SC4). This motion of the flapping is opposite to the motion of the reconnection region. *Sergeev et al.* [2008] explained this contrary direction of motion by a pause in the reconnection, which first was located earthward of the Cluster satellites then reappeared tailward of the Cluster satellites. In a survey of large amplitude flapping motions in the mid-tail *Sergeev et al.* [2006], they found that such fluctuations can be characterised as current sheet flapping motions. They tend to occur during the substorm expansion phase, and are associated with fast plasma flows. These results are consistent with our results where the large amplitude flapping motions appeared together with high speed ion outflows.

The observations of the current sheet wave in the 2001 event suggest a calmer current sheet than the one observed in the 2005 event where there were presence of turbulence and large amplitude flapping motions.

Based on the location of the Cluster satellites within the plasma sheet during the 2005 event, the reconnections happened most likely on closed field lines (plasma sheet reconnection). This assumption is also consistent with the conclusion from *Sergeev et al.* [2008]. In the 2001 event the inflow region did most likely not pass the Cluster satellites during the reconnection intervals. If the satellites did, we could have compared the inflow region with the plasma β values during that period in order to determine whether the inflow was located in the plasma sheet or in the lobe. This would have made it possible to determine whether the reconnection in the 2001 event occurred on open or closed field lines. Since the inflow region did not pass the Cluster satellites, we could not perform such an analysis, hence it is not possible to determine whether or not the reconnection occurred on open or closed magnetic field lines.

6.2 Electric fields associated with reconnection

The electric field measurements in the 2001 event contained large amplitude fluctuations. The large amplitudes ($|E_y| > 80$ mV/m) occurred in regions north and south of the neutral sheet where the B_x-components were large ($B_x \pm 30$ nT). The relation between the density and the E_y-component showed occurrence of large electric fields ($|E_y| > 10$ mV/m) in regions with low density ($\sim 0.1\ cm^{-3}$). In simulations large electric fields have been found in association with density depletions at the separatrices (see chapter 2.5.3) [*Shay et al.*, 2001].

Our results from the 2001 event are therefore consistent with the results reported by *Borg et al.* [2005]: That the electric fields in the 2001 event occurred within the vicinity of the separatrices.

The relation between the density and the E_y measurements from the 2005 event did not show clear correlation of high electric field amplitudes and regions with low density. The relation between the E_y- and the B_x-components showed that large, mostly positive electric fields ($|E_y| \sim 15$ mV/m) did appear in the regions with large B_x measurements ($B_x \pm 40$ nT). The large electric fields appeared during intervals when SC4 probably entered the plasma sheet boundary layer or lobes. Based on the unclear relation between the large E_y and density values, it is not possible to determine if the large electric fields were measured in the vicinity of the separatrices in the 2005 event.

6.3 Substorm signatures observed in association with reconnection

Table 6-11 presents the time difference in minutes between the first observed reconnection signature and the observed substorm signatures. The time differences are given for both the 2001 and the 2005 event. The uncertainties attached to the observations of the different signatures of substorm onsets are included as well.

The signatures	**Time after first observed reconnection Δt [min], 2005**	**Time after first observed reconnection Δt [min], 2001**
Magnetic reconnection	0	0
Aurora intensification	~ 6 – 2 minutes	~ –1 – 2 minutes
Start of Pi 2-wave train, south	~ 6 ± 2 minutes	-
Start of Pi 2-wave train, north	~ 6 ± 2 minutes	-
Magnetic bay, south	~ 6 ± 3 minutes	~ 0 ± 3 minutes
Magnetic bay, north	~ 4 ± 3 minutes	~ 1 ± 3 minutes
Onset in AE-index	~ 11 ± 1 minutes	~ -20 ± 1 minutes

Table 6-11: Time after the first ion outflow was detected at the Cluster satellites in the 2001 and in the 2005 event.

Auroral intensification has been observed in association with magnetic reconnection in the tail in several case studies (e.g. [*Angelopoulos et al.*, 2008, *Baker et al.*, 2002, *Borg et al.*, 2007, *Cao et al.*, 2008, *Ostgaard et al.*, 2009]), and data from IMAGE FUV have fre-

quently been used to establish a global auroral substorm development. The auroral substorm onset in the 2005 event appeared ~1 minute after the Cluster satellites observed the first reconnection. Prior to the auroral onset there was a small intensification which may correspond to a pseudobreakup. Such pseudobreakup has been reported during substorm growth phase [e.g., *Baker et al.*, 2002] (see chapter 2.6.1) as a result of fast plasma flows in the plasma sheet during current sheet thinning [*Nakamura et al.*, 2002]. The auroral activity which appeared after the magnetic reconnection was observed in the magnetotail, contained signatures of a developing auroral substorm and contained two intensifications (09.41 UT and 09.55 UT). The intensifications appeared in the footpoint region in the ionosphere at the same time as the Cluster satellites observed the high speed flows (at 09.40 at ~ 09.55 UT). The auroral substorm dissolved after ~20 minutes and during the substorm expansion phase, the aurora covered a region limited between 60° and 70° magnetic latitude in the pre-midnight sector at ~ 23 MLT. Figure 6-67 shows the time line of the 2005 event, where the red lines are the observed magnetic reconnection periods by the Cluster satellites. In the figure, the auroral intensifications, which appeared during the studied time interval, are included.

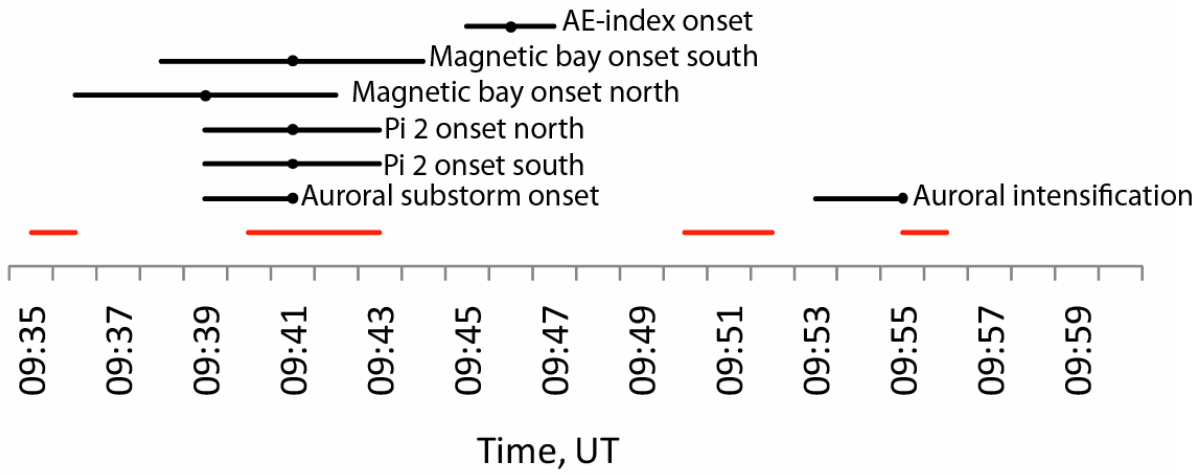

Figure 6-67: The time line showing when each magnetic reconnection was observed by the Cluster satellites in the 2005 event. The magnetic reconnection sequences are marked with the red lines. Each auroral intensification, including the uncertainties in the measurements, is plotted as well as the onset of the substorm signatures observed by different ground measurements. The black dots are the onset of the signature and the black lines are the uncertainties related to the onset of each signature.

As seen from the figure, the auroral intensification onsets (seen as the black dots) corresponded with the onset of the magnetic reconnection but the uncertainties in the data (marked with black lines) makes it impossible to determine whether the auroral intensification appeared before or after the magnetic reconnection onset. The auroral substorm activity dissolved at ~ 10.04 UT, 8 minutes after the last reconnection interval was observed by the Cluster satellites. The large flapping motions registered by the Cluster satellites during the

third and fourth reconnection interval (marked with red in Figure 6-67) did form during late substorm expansion phase, which is consistent with the results from the survey by *Sergeev et al.* [1993]

The auroral substorm on the 22nd August 2001 started (09.39 UT) prior to the first high speed outflow observations done by the Cluster satellites (09.40 UT). Figure 6-68 shows a time line of the observed reconnection (red lines) intervals and the auroral substorm intensifications (marked as 1, 2 and 3). The reconnection interval after 10.04 UT is not included in the figure due to the lack of the quadrupole Hall magnetic field signature during this interval. The black dots mark the onset of the signatures while the black lines are the uncertainty in time associated with each of the onsets. The auroral substorm contained three intensifications (09.39 UT, 09.49 UT and 09.57 UT), which coincided with the high speed flows observed by the Cluster satellites.

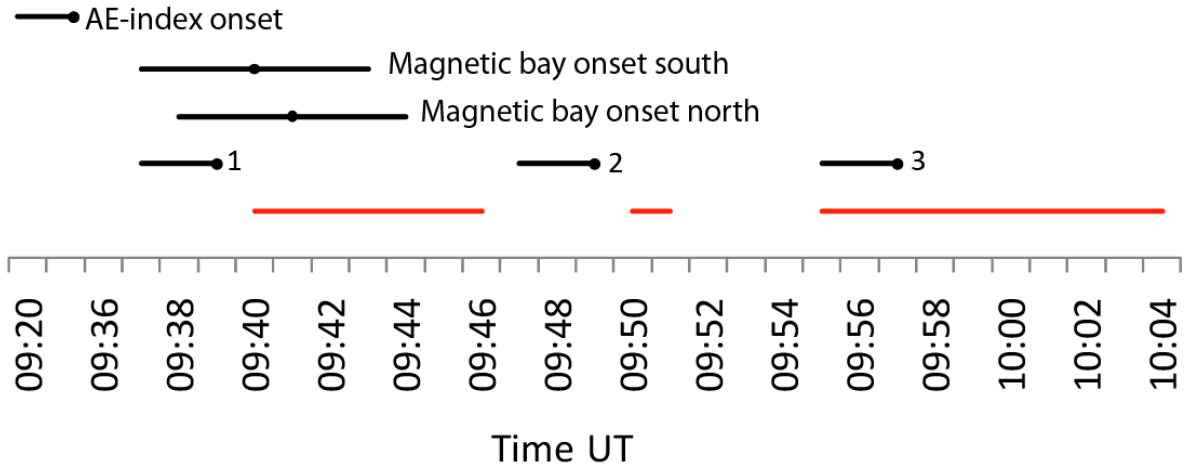

Figure 6-68: The time line showing when each magnetic reconnection was observed by the Cluster satellites for the 2001 event. The magnetic reconnection sequences are marked with the red lines. Each auroral intensification, including the uncertainties in the measurements, is plotted as well as the onset of the substorm signatures observed by different ground measurements. The numbers 1, 2 and 3 refers to each auroral intensification observed by IMAGE WIC. Note gap between the first time marker and the second time marker along the x-axis. The reason for this time gap is due to the early start of the auroral index.

During the most intensive period the aurora covered the night side of the oval from ~21 MLT to 04 MLT and between 60° and 70° magnetic latitude. The auroral substorm onset intensification occurred outside the footpoint region of Cluster, but when the Cluster satellites observed the first outflow, the auroral intensified region entered the footpoint region. This suggests that the Cluster satellites entered an ongoing magnetic reconnection, and may explain why the auroral substorm onset occurred prior to the first observed reconnection interval. The auroral substorm dissolved at ~ 10.13 UT, 7 minutes after the last magnetic reconnection was observed by the Cluster satellites.

Even though the intensifications in both the 2005 and in the 2001 events did coincide with the high speed outflows registered by the Cluster satellites, it is difficult to say whether the activity appeared prior to or after the high speed outflows due to the resolution of the IMAGE WIC data (2 minutes).

Geomagnetic activity has previously been reported during intervals of magnetic reconnection in the magnetotail. Positive and negative deflections in the vertical component of the geomagnetic magnetic field and a development of magnetic bays within the range of 3 minutes after magnetic reconnection have been reported [e.g., *Laitinen et al.*, 2007, *Nakamura*, 2006]. As seen from Figure 6-67, the deflections in both the vertical component and the horizontal intensity of the magnetic field in the 2005 event occurred during the same time period as the second reconnection flow was observed. The deflections occurred within ~10 minutes after the first magnetic reconnection signatures was observed in both the northern and in the southern hemispheres. This delay of the deflections is not consistent with the results from *Laitinen et al.* [2007] or *Nakamura et al.* [2006].

In the 2001 event the deflections appeared within ~1 minute after reconnection was observed (see Table 6-11 and Figure 6-68). The time difference between the observed signature in the southern hemisphere and in the northern hemisphere in the 2001 event may be caused by the locations of the stations which are located at different distances from the footpoint region. The uncertainties related to the substorm onset defined by the magnetic bay (5 minutes) makes it difficult to establish the actual start of the signature, hence it is not possible to determine whether the onset started prior to or after the first magnetic reconnection signatures was observed by the Cluster satellites.

Pi 2 pulsations are associated with auroral intensifications and substorm onsets. There is a 100 % correspondence between auroral intensifications and Pi2 pulsations if the pulsations are measured within the 23-01 hour MLT sector [*Yumoto and Grp*, 2001]. If the stations are located outside this region, the correspondence percentage is reduced. There has also been reported time coincident measurements of a positive magnetic bay development and onset of Pi 2 pulsations [*Nakamura et al.*, 2006]. In the 2005 event the onset of the Pi 2 pulsations coincided with the development of the magnetic bay and the onset of the auroral substorm appeared (see Table 6-11). The timing of the Pi 2 pulsations and the magnetic bay and auroral brightening suggests that the pulsations probably were formed during the formation of the SCW [*Olson*, 1999]. In the 2005 event is seems that the pulsations appeared in the high latitude at the same time as the second magnetic reconnection was observed by the Cluster satellites. During the 2001 event no Pi 2 pulsations were detected with the CPMN-chain data,

which may be explained by the locations of the stations in the dusk sector ~ 20 MLT, so that the possibility of observing the pulsations decreases. In order to investigate whether there were any pulsations prior to or after the observed reconnection and geomagnetic activity, data from the CPMN network from the time period between 06.00 UT and 13.00 UT was investigated. There were no signatures of such pulsations during the studied time interval.

In papers reporting observations of high speed flows in the magnetotail and the corresponding response in the AE-index, the signature of an auroral substorm appeared ~ 4 minutes after a magnetic reconnection was observed in the magnetotail [e.g., *Angelopoulos et al.*, 2008, *Baker et al.*, 2002]. Our results from the 2005 event are consistent with such findings. A substorm onset signature was apparent in the AE-index ~ 5 minutes after magnetic reconnection was observed by the Cluster satellites. The uncertainties in the timing of the substorm onset based on the AE-index are ~2 minutes, which suggests that the auroral electrojet most likely developed after the magnetic reconnection was observed by the Cluster satellites. If the substorm onset appeared after the magnetic reconnection within a time limit of 1-3 minutes the scenario fits the description of the NENL-model. In *Sergeev et al.* [2008] they concluded that the geomagnetic activity registered on the 26th September 2005 was generated by magnetic reconnection located in the near-Earth magnetotail at ~13 – ~15 R_E, which is an example of NENL [*Baker et al.*, 1996]. If the development of the substorm signatures were related to the first observed magnetic reconnection signatures, the scenario fits the description of the NENL model. It does, however, seem that the substorm signatures developed at the same time as the second magnetic reconnection flow was observed (see Figure 6-67). Without taking the uncertainties of timing into consideration, this reconnection-substorm scenario does also fit into the NENL model. However, when taking the uncertainties into consideration it is difficult to say whether the NENL model is the correct description of the second magnetic reconnection flow – substorm scenario in the event on 26th September 2005. The magnitude of the AE-index during the 2005 event was only ~250 nT. When comparing the AE-index during the studied time interval with the activity registered during the whole day (Figure 6-69) this individual substorm occurred just before a larger registered geomagnetic activity starting at ~11.30 UT. Whether the new disturbance at 11.30 UT was a substorm or not is beyond the scope of this thesis.

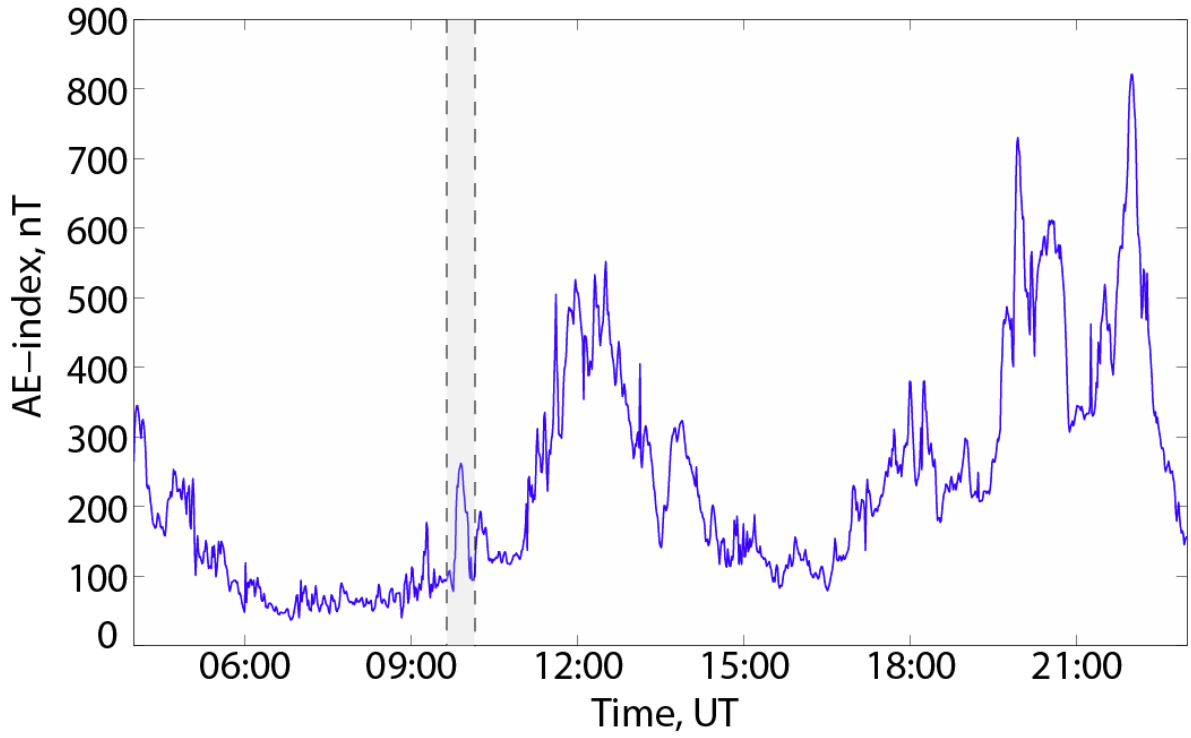

Figure 6-69: The AE-index from 26th September 2005 all day. The gray shaded area is the AE-index from when the Cluster satellites observed the high speed outflows.

The AE-index during the 2001 event showed a different trend than in the 2005 event. The index was much larger > 600 nT which suggests that there was a significant substorm occurring during the studied time interval. However, signatures of substorm onset appeared ~20 minutes before the high speed flows was observed by the Cluster satellites. When studying pictures of the ionosphere (not shown) from IMAGE WIC in the time period corresponding to the substorm onset in the AE-index, there was an auroral activity at ~ 09.16 UT with an auroral intensification appearing at ~ 09.24 UT. This may suggest that the Cluster satellites encountered an ongoing magnetic reconnection which started before the Cluster satellites reached the region. When studying the AE-index during the whole day on the 22nd August 2001 (Figure 6-70) it appears that the substorm was a part of a larger geomagnetic storm this day. Such continuous occurrence of increases in the AE-index was used as a definition of storm time in a statistical study by *Nakamura et al.*[1991] when studying the correspondence between ion flows near the neutral sheet and the substorm phases using the AE-index. This is further confirmed by the Kp-index which was on a level 4 from 09 UT and throughout the rest of the day (except for a small change to +3 between 15 UT and 18 UT, see Table 5-9). Based on the results presented here, with respect to timing and the geomagnetic activity during the whole day of the 2001 event, it is not possible to determine whether the magnetic re-

connection triggered the substorm, or that the substorm was generated by other features as plasma instabilities in the near-Earth region.

The differences between the AE-indices from the 2001 and the 2005 event accentuate the differences between the two studied magnetic reconnection and substorm events.

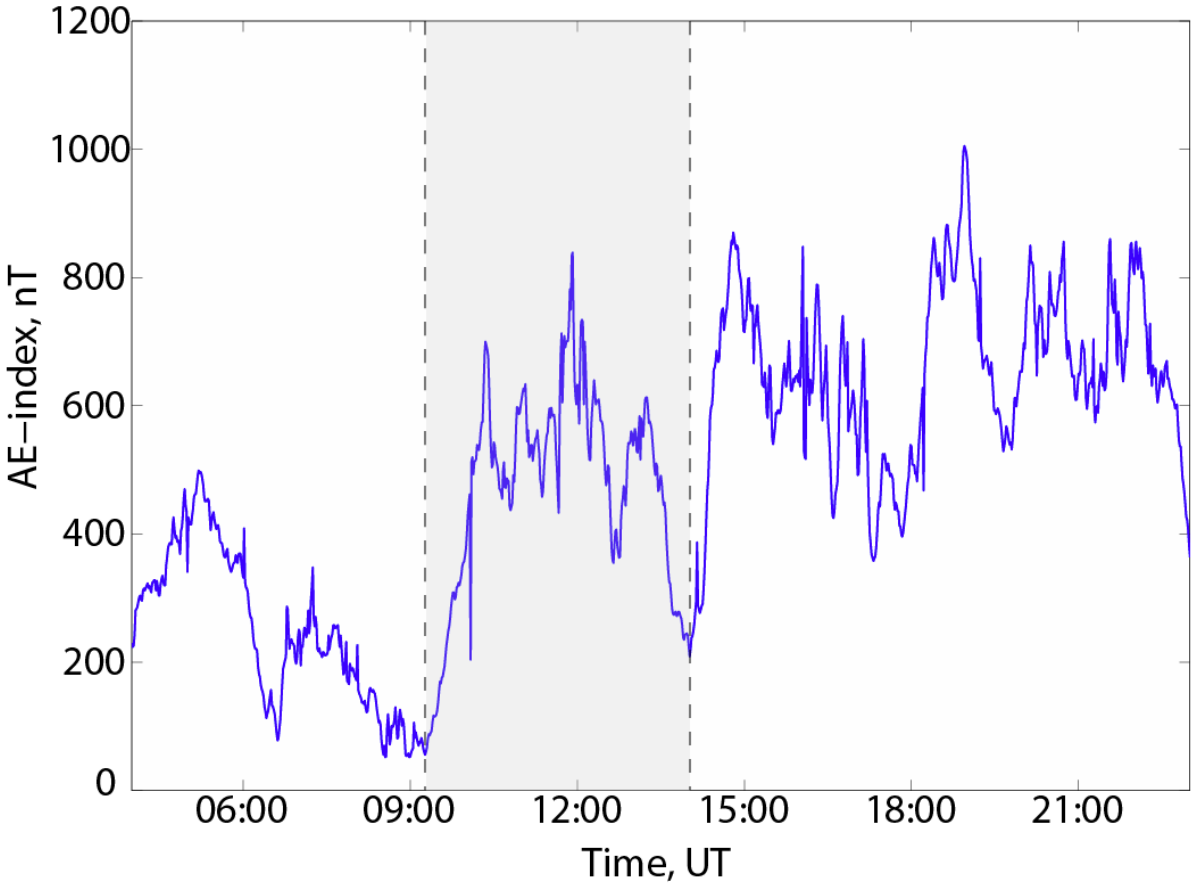

Figure 6-70: The AE-index from the 22nd August 2001 all day. The gray shaded are is the AE-index from when the Cluster satellites observed the high speed outflows at ~-18 R_E from the Earth.

6.4 The solar wind conditions prior to magnetic re-connection

The ultimate driver of the substorm process is the solar wind. The coupling function given as $E_I \sim V_p * B_S$, may provide a measure of the reconnection rate between the solar wind and the magnetosphere at the subsolar point [*Burton et al.*, 1975]. B_s is the southward component of IMF. When $B_z^{IMF} > 0$ then $B_s = 0$, and when $B_z^{IMF} < 0$ then $B_s = B_z^{IMF}$.

The solar wind data prior to the events are presented in Figure 6-71, where the red curves are solar wind data prior to the 2001 event and the black curves are solar wind data prior to the 2005 event.

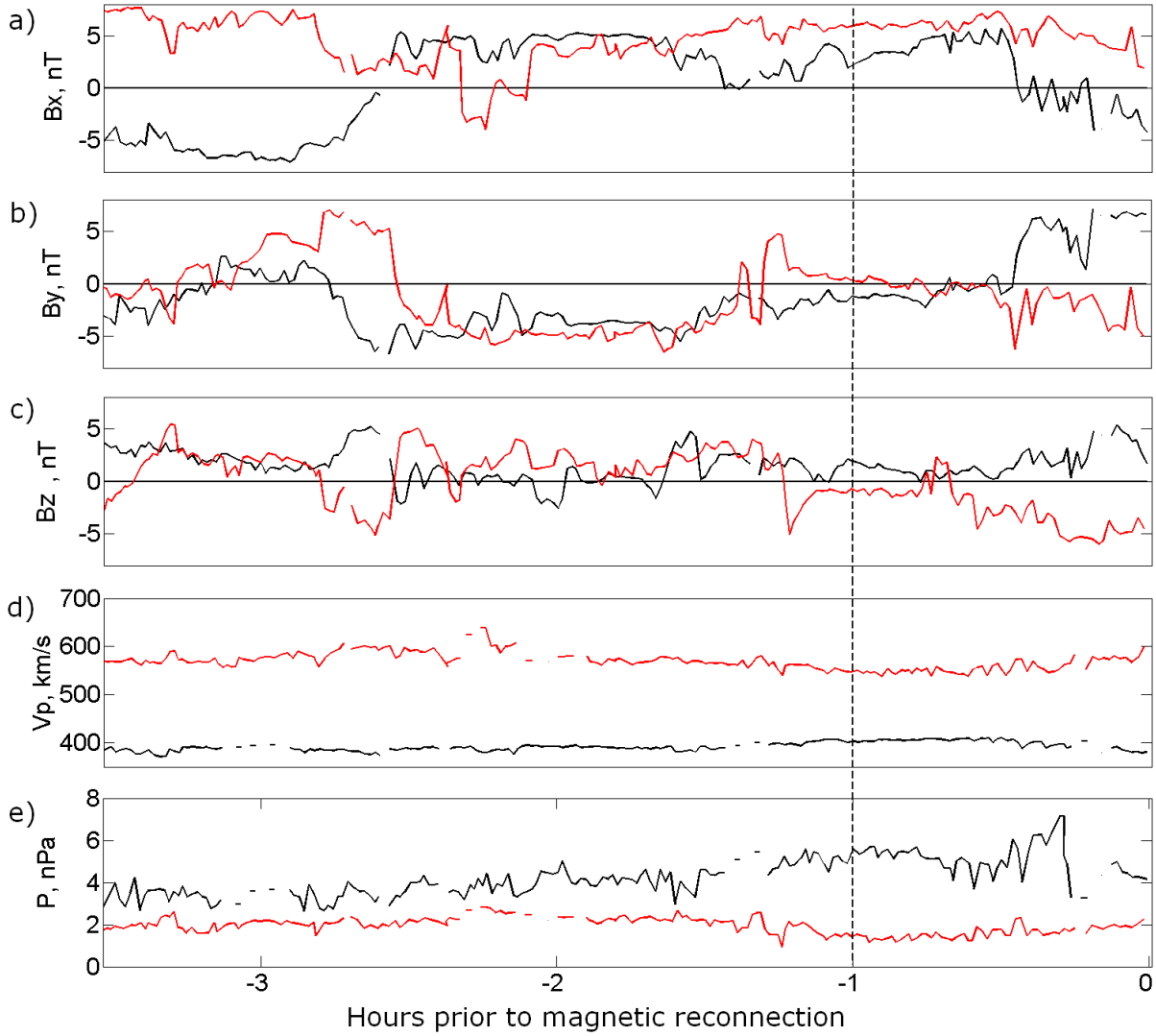

Figure 6-71: The solar wind measurements from OMNI-wed prior of the magnetic reconnection. The red plots are the solar wind parameters in front of the magnetic reconnection 22nd August 2001. The black plots are the solar wind parameters in front of the 26th September 2005 event. The dashed line in the figure marks one hour before the magnetic reconnections were observed.

Panel a) to c) show the solar wind magnetic field data, panel d) shows the proton velocity and panel e) shows the solar wind pressure. The datasets in panel a) to e) are from the OMNI-web (see chapter 3.5).The mean value of the proton velocity during the interval of one hour prior to the magnetic reconnection event in 2005 was ~400 km/s, and the B_z-component was positive. During the one hour prior to the 2001 event, the average proton velocity was ~550 km/s, and B_z was mainly negative reaching values of ~ - 5 nT. Such average values can be used in order to roughly determine the reconnection rate $E_I \sim 3$ mV/m prior to the 2001 event. This reconnection rate during an interval of one hour prior to the magnetic reconnection may provide favourable conditions in order to initiate a substorm caused by a magnetic

reconnection in the magnetotail [*Burton et al.*, 1975]. Whether this was the case in the 2001 event is, however, difficult to establish.

One hour prior of the 2005 event the B_z-component was positive, which means that $B_s = 0$ and consequently $E_l = 0$ in the interval. There was, however, a build-up in the dynamic pressure which reached values of ~ 7 nPa, see panel e). 15 minutes before reconnection the pressure dropped which may suggest an arrival of a discontinuity at the magnetopause. The sudden change was also apparent in the B_x-component of the IMF, which turned from positive to negative and in the dawn-to-dusk component, which went from fluctuating around zero to directing duskward reaching values of ~ 6 nT. Such pressure may stretch the magnetotail, in such a way that magnetic reconnection may occur very close to the Earth on closed field lines [*Sergeev et al.*, 2007]. But whether such changes were sufficient to initiate a magnetic reconnection in the magnetotail cannot be established.

The solar wind conditions prior to the 2001 event are consistent with the findings in a statistical study by Naga in 2005 [*Nagai et al.*, 2005] where one of the conclusions was that in distances between $-15 < x_{GSM} < -25$, the solar wind contained an averagely velocity of ~ 520 km/s and a southward directed component of the IMF.

As seen from Figure 6-71, the solar wind conditions prior to the magnetic reconnection in the 2001 event contained large velocities and a negative IMF B_z component that could provide an energy input to the magnetosphere, but there were no sudden changes which may have triggered the reconnection. Prior to the 2005 event there was a sudden change in both the IMF B_y, IMF B_z and in the solar wind pressure, which may have triggered the magnetic reconnection. The solar wind condition did, however, not provide a large energy input during the one hour prior to the magnetic reconnection ($E_l = 0$).

6.5 Future work

A natural expansion of this thesis would be to build on the results, for example in combination with the results of *Sergeev et al.* [2008], *Louarn et al.* [2004] and *Volwerk et al*. [2003]. By doing so, more details may be added to the magnetic reconnection-substorm issues and the substorm triggering processes, and maybe a more complete understanding of the processes can be achieved.

The STAFF [*Mirioni et al.*, 2005] experiment on Cluster indicates strong electromagnetic wave activity during the magnetic reconnection on the 22nd August 2001. A further

analysis of datasets from the 2001 and 2005 events using the STAFF experiments would provide important details on the magnetic reconnection process.

The electric fields registered during this magnetic reconnection can be studied in more detail by calibrating the raw data using different methods than the least-square-fit sine wave approximation. One example is to average over 5 seconds in order to produce "smoother" calibrated data. Such studies could be combined with a wider study of the large flapping motions observed in the 2005 event.

Another extension of this thesis can be achieved by using electron energy and electron flux data from the PEACE [*Johnstone et al.*, 1997] and RAPID [*Wilken et al.*, 1997] experiments on the Cluster satellites, in order to search for FACs from the magnetic reconnection region, especially from the separatrix region, and to investigate the electron energy distribution during the reconnection intervals.

Volwerk et al. [2008] investigated the Pi 2 waves using Cluster data in order to determine the direction of propagation of the waves. By using Cluster data from the 2005 event it would have been interesting to see the direction of the propagation of the Pi 2 pulsations since the pulsations are so clear on the ground.

A further investigation of the Pi 2 pulsations seen by the ground stations during the 2005 event could provide more information about the formation of the SCW. By studying the longitudinal structure of the Pi 2 pulsations using the polarization ellipse could determine the location of the downward and upward FACs associated with the SCW could be determined [*Lester et al.*, 1983, *Lester et al.*, 1984]. Data from other magnetometer chains can be used in order to search for Pi 2 pulsations linked to the substorm in the 2001 event. The Canadian Array for Realtime Investigations of Magnetic Activity (Carisma) data provides 5 second resolution data from magnetometer stations which were located in the footpoint region of the Cluster satellites during this event. It is also possible to search for other satellites either located in the footpoint region closer or farther from the Earth than the Cluster satellites which may have seen signatures of the geomagnetic activity or the magnetic reconnection.

The THEMIS mission [*Angelopoulos*, 2008] provides data from the magnetotail, near-Earth and the ground in order to investigate the initiation process of the substorm phenomena. If the satellites are located in the correct position, this mission can provide further details regarding the individual steps of the processes, and by using the knowledge from the Cluster data the issue regarding the triggering process may be further investigated.

Bibliography

ACUNA, M. H., OGILVIE, K. W., BAKER, D. N., CURTIS, S. A., FAIRFIELD, D. H. & MISH, W. H. (1995) The Global Geospace Science Program and its investigations *Space Science Reviews,* 71**,** 5-21.

AKASOFU, S. I. (1964) The development of the auroral substorm. *Planetary and Space Science,* 12**,** 273-282.

ANGELOPOULOS, V. (2008) The THEMIS Mission. *Space Science Reviews,* 141**,** 5-34.

ANGELOPOULOS, V., MCFADDEN, J. P., LARSON, D., CARLSON, C. W., MENDE, S. B., FREY, H., PHAN, T., SIBECK, D. G., GLASSMEIER, K. H., AUSTER, U., DONOVAN, E., MANN, I. R., RAE, I. J., RUSSELL, C. T., RUNOV, A., ZHOU, X. Z. & KEPKO, L. (2008) Tail reconnection triggering substorm onset. *Science,* 321**,** 931-935.

ANGELOPOULOS, V., MCFADDEN, J. P., LARSON, D., CARLSON, C. W., MENDE, S. B., FREY, H., PHAN, T., SIBECK, D. G., GLASSMEIER, K. H., AUSTER, U., DONOVAN, E., MANN, I. R., RAE, I. J., RUSSELL, C. T., RUNOV, A., ZHOU, X. Z. & KEPKO, L. (2009) Response to Comment on "Tail Reconnection Triggering Substorm Onset". *Science,* 324.

BAKER, D. N., PETERSON, W. K., ERIKSSON, S., LI, X., BLAKE, J. B., BURCH, J. L., DALY, P. W., DUNLOP, M. W., KORTH, A., DONOVAN, E., FRIEDEL, R., FRITZ, T. A., FREY, H. U., MENDE, S. B., ROEDER, J. & SINGER, H. J. (2002) Timing of magnetic reconnection initiation during a global magnetospheric substorm onset. *Geophysical Research Letters,* 29**,** 43, 1 - 43, 4.

BAKER, D. N., PULKKINEN, T. I., ANGELOPOULOS, V., BAUMJOHANN, W. & MCPHERRON, R. L. (1996) Neutral Line Model of Substorms: Past results and present view. *Journal of Geophysical Research,* 101**,** 12975-13010.

BALOGH, A., CARR, C. M., ACUÑA, M. H., DUNLOP, M. W., BEEK, T. J., BROWN, P., FORNACON, K.-H., GEORGESCU, E., GLASSMEIER, K.-H., HARRIS, J., MUSMANN, G., ODDY, T. & SCHWINGENSCHUH, K. (2001) The Cluster Magnetic Field Investigation: overview of in-flight performance and initial results. *Annales Geophysicae,* 19**,** 1207-1217.

BARTELS, J. (1950) *Geomagnetic K-indices, International Polar Year, August 1932 to August 1933,* International Union of Geodesy and geophysics Association of Terrestrial Magnetism and Electricity.

BAUMJOHANN, W., PASCHMANN, G. & CATTELL, C. A. (1989) Average Plasma Properties in the Central Plasma Sheet. *Journal of Geophysical Research,* 94**,** 6597-6606.

BAUMJOHANN, W., PASCHMANN, G. & LUHR, H. (1990) Characteristics of high-speed ion flows in the plasma sheet *Journal of Geophysical Research,* 95**,** 3801-3809.

BAUMJOHANN, W., PASCHMANN, G., SCKOPKE, N., CATTELL, C. A. & CARLSON, C. W. (1988) Average ion Moments in the Plasma Sheet Boundary layer. *Journal of Geophysical Research,* 93**,** 11,507-11,520.

BOGDANOVA, Y. V. *An Introduction to the Aurora*. UCL Department of Space & Climate Physics 2006 November 8 [cited 2009 4. April]; Available from: http://www.mssl.ucl.ac.uk/www_plasma/visitors/aurora.php.

BORG, A. L. (2006) A study of magnetic reconnection events observed by the cluster satellites in the Earth's magnetotail. *University of Oslo, Department of Physics.* Oslo, University of Oslo.

BORG, A. L., OIEROSET, M., PHAN, T. D., MOZER, F. S., PEDERSEN, A., MOUIKIS, C., MCFADDEN, J. P., TWITTY, C., BALOGH, A. & REME, H. (2005) Cluster encounter of a magnetic reconnection diffusion region in the near-Earth magnetotail on September 19, 2003. *Geophysical Research Letters,* 32**,** L19105, 4.

BORG, A. L., OSTGAARD, N., PEDERSEN, A., OIEROSET, M., PHAN, T. D., GERMANY, G., AASNES, A., LEWIS, W., STADSNES, J., LUCEK, E. A., REME, H. & MOUIKIS, C. (2007) Simultaneous observations of magnetotail reconnection and bright X-ray aurora on 2 October 2002. *Journal of Geophysical Research,* 112**,** A06215, 9.

BOYD, T. & SANDERSON, J. J. (2003) *The Physics of Plasma,* Cambridge, Cambridge University Press.

BURTON, R. K., MCPHERRON, R. L. & RUSSELL, C. T. (1975) Empirical relationship between interplanetary conditions and Dst *Journal of Geophysical Research-Space Physics,* 80**,** 4204-4214.

CAMPELL, W. H. (2003) *Introduction to Geomagnetic Fields,* Cambridge, Cambridge University Press.

CAO, X., PU, Z. Y., ZHANG, H., MISHIN, V. M., MA, Z. W., DUNLOP, M. W., FU, S. Y., XIE, L., XIAO, C. J., WANG, X. G., ZONG, Q. G., LIU, Z. X., KUBYSHKINA, M. V., PULKKINEN, T. I., FREY, H. U., KORTH, A., FRAENZ, M., LUCEK, E., CARR, C. M., REME, H., DANDOURAS, I., FAZAKERLEY, A. N., REEVES, G. D., FRIEDEL, R., GLASSMEIER, K. H. & ESCOUBET, C. P. (2008) Multispacecraft and ground-based observations of substorm timing and activations: Two case studies. *Journal of Geophysical Research,* 113**,** 1-13.

CHAPMAN, S. & FERRARO, V. C. A. (1930) A new theory of magnetic storms. *Nature,* 126**,** 129-130.

CHEN, F. F. (1983) *Introduction to Plasma Physics and Controlled Fusion,* New York and London, Plenum Press.

COWLEY, S. W. H. (2000) Magnetosphere-ionosphere interactions: A tutorial review. IN OHTANI, S., FUJII, R., HESSE, M. & LYSAK, R. L. (Eds.) *Magnetospheric Current Systems.* Washington, Amer Geophysical Union.

CPMN (1995) The Circum-pan Pasific Magnetometer Network. *Station List (1995) and Maps.* Space and Earth Electromagnetism Laboratory.

CUMMINGS, W. D. & DESSLER, A. J. (1967) Field-aligned currents in the magnetosphere *Journal of Geophysical Research,* 72**,** 1007-1013.

DALY, P., W. (2008) *Users Guide to the Cluster Science Data System,* European Space Agency.

DANDOURAS, I., BARTHE, A. & CIS-TEAM (2004) *User guide to the CIS measurements in the Cluster Active Archive*.

DAVIS, T. N. & SUGIURA, M. (1966) Auroral electrojet activity index AE and its universal time variations. *Journal of Geophysical Research,* 71**,** 785-801.

DECREAU, P. M. E., FERGEAU, P., KRANNOSELSKIKH, V., LEVEQUE, M., MARTIN, P., RANDRIAMBOARISON, O., SENE, F. X., TROTIGNON, J. G., CANU, P., MOGENSEN, P. B., VASILJEVIC, C., GUYOT, E., LAUNAY, L., CORNILLEAUWEHRLIN, N., DEFERAUDY, H., IVERSEN, I., GUSTAFSSON, G., GURNETT, D. & WOOLLISCROFT, L. (1997) Whisper, a resonance sounder and wave analyser: Performances and perspectives for the Cluster mission. *Space Science Reviews,* 79**,** 157-193.

DUNGEY, J. W. (1961) Interplanetary magnetic field and auroral zones. *Physical Review Letters,* 6**,** 47-48.

DUNLOP, M. W., WOODWARD, T. I. & FARRUGIA, C. J. (1995) Minimum variance analysis: Cluster Themes. *Cluster Workshop on Data Analysis Tools.* Braunschweig, Germany, ESA.

ELPHINSTONE, R. D., MURPHREE, J. S. & COGGER, L. L. (1996) What is a global auroral substorm? *Reviews of Geophysics,* 34**,** 169-232.

ELVEY, C. T. (1957) Problems of auroral morphology *Proceedings of the National Academy of Sciences of the United States of America,* 43**,** 63-75.

ESA. *Science and technology, Cluster*. European Space Agency 2000 [cited 2009 12. December]; Available from: http://sci.esa.int/science-e/www/area/index.cfm?fareaid=8.

ESA. *Space Science*. European Space Agency 2004 [cited 2010 04. January]; Available from: http://www.esa.int/esaSC/SEMLC2T1VED_index_0.html#subhead1.

ESA. *Earth's magnetic environment*. European Space Agency 2007a 06. December 2007 [cited 2009 01. October]; Available from: http://sci.esa.int/science-e/www/object/index.cfm?fobjectid=41918.

ESA. *Plot of Cluster Orbit and Spacecraft Configuration*. European Space Agency 2007b [cited 2010 6. January]; Available from: http://sci.esa.int/science-e/www/object/index.cfm?fobjectid=41122.

ESCOUBET, C. P., FEHRINGER, M. & GOLDSTEIN, M. (2001) Introduction The Cluster Mission. *Annales Geophysicae,* 19**,** 1197-1200.

FRENCH, P., LUCEK, E., BROWN, P., ODDY, T. & CARR, C. (2001) *User guide to the FGM instruments in the Cluster Active Archive*

GOSLING, J. T., BIRN, J. & HESSE, M. (1995) 3-dimensioal magnetic reconnection and the magnetic topology of coronal mass ejection events *Geophysical Research Letters,* 22**,** 869-872.

GURNETT, D. A. & BHATTACHARJEE, A. (2005) *Introduction to Plasma Physics: with Space and Laboratory Applications,* Cambridge, Cambridge University Press.

GUSTAFSSON, G., ANDRÉ, M., CAROZZI, T., ERIKSSON, A. I., FÄLTHAMMER, C.-G., GRARD, R., HOLMGREN, G., HOLTET, J. A., IVCHENKO, N., KARLSSON, T., KHOTYAINTSEV, Y., KLIMOV, S., LAAKSO, H., LINDQUIST, P.-A., LYBEKK, B., MARKLUND, G., MOZER, F., MURSULA, K., PEDERSEN, A., POPIELAWSKA, B., SAVIN, S., STASIEWICZ, K., TANSKANEN, P., VAIVADS, A. & WAHLUND, J.-E. (2001) First results of electric field and density observations by Cluster EFW based on initial months of operation. *Annales Geophysicae*
19**,** 1219-1240.

HARVEY, C. C., ALLEN, A. J., DÉRIOT, F., HUC, C., NONON-LATAPIE, M., PERRY, C. H., SCHWARTZ, S. J., ERIKSSON, T. & MCCAFFREY, S. (2008) Cluster Metadata Dictionary. IN ESA (Ed.). European Space Agency.

HESSE, M., SCHINDLER, K., BIRN, J. & KUZNETSOVA, M. (1999) The diffusion region in collisionless magnetic reconnection. *Physics of Plasmas,* 6**,** 1781-1795.

HESSE, M. & WINSKE, D. (1994) Hybrid simulations of collisionless reconnection in current sheets *Journal of Geophysical Research,* 99**,** 11177-11192.

HONES, E. W. (1984) *Magnetic Reconnection in Space and Laboratory Plasmas,* Washington D. C., American Geophysical Union.

HOSHINO, M., HIRAIDE, K. & MUKAI, T. (2000) Strong electron heating and non-Maxwellian behavior in magnetic reconnection. *Earth Plantes and Space* 53**,** 627-634.

INTERMAGNET. *INTERMAGNET*. INTERMAGNET 2009a [cited 2009 27. August]; Available from: http://www.intermagnet.org/apps/dataplot_e.php?plot_type=b_hdz_plot.

INTERMAGNET. *International Real-time Magentic Observatoriy Network*. 2009b [cited 2010 18. January]; Available from: www.intermagnet.org.
INTERMAGNET. *INTERMAGNET - Plot information*. INTERMAGNET 2010 [cited 2010 05 February]; Available from: http://www.intermagnet.org/apps/int_plots_def_e.php#undefined.
JACOBS, J. A. & SINNO, K. (1960) World-wide characteristics of the geomagnetic micropulsations *Geophysical Journal of the Royal Astronomical Society,* 3**,** 333-353.
JACQUEY, C., SAUVAUD, J. A. & DANDOURAS, J. (1991) Location and propagation of the magnetotail current disruption during substorm expansion-analysis and simulation of an ISEE multionset event *Geophysical Research Letters,* 18**,** 389-392.
JOHNSON, C. Y. (1966) Ionospheric composition and density from 90 to 1200 kilometres at solar minimum *Journal of Geophysical Research,* 71**,** 330-332.
JOHNSON, R. A. & WICHERN, D. W. (2007) *Applied Multivariate Statistical Analysis*, Pearson Education INC.
JOHNSTONE, A. D., ALSOP, C., BURGE, S., CARTER, P. J., COATES, A. J., COKER, A. J., FAZAKERLEY, A. N., GRANDE, M., GOWEN, R. A., GURGIOLO, C., HANCOCK, B. K., NARHEIM, B., PREECE, A., SHEATHER, P. H., WINNINGHAM, J. D. & WOODLIFFE, R. D. (1997) Peace: A plasma electron and current experiment. *Space Science Reviews,* 79**,** 351-398.
JORDAN, A. (2008) Plasmakonvektion in hohen Breiten. *Deutsches GeoForschungsZentrum.*
KAYMAZ, Z., SISCOE, G. L., TSYGANENKO, N. A. & LEPPING, R. P. (1994) Magnetotail views at 33 Re-IMP 8 magnetometer observations *Journal of Geophysical Research,* 99**,** 8705-8730.
KEPKO, L., KIVELSON, M. G., MCPHERRON, R. L. & SPENCE, H. E. (2004) Relative timing of substorm onset phenomena. *Journal of Geophysical Research-Space Physics,* 109**,** 1-17.
KHOTYAINTSEV, Y. *Orbit Visualization Tool*. Swedish Institute of Space Physics 2000 [cited 2009 3. December]; Available from: http://ovt.irfu.se./.
KING, J., PAPITASHVILI, N., GSFC/SPDF & QSS-GROUP. *One min and 5-min solar wind data sets at the Earth's bow shock nose*. NASA, Space Physics Data Facility 2006 [cited 2010 4. January]; Available from: http://omniweb.gsfc.nasa.gov/html/HROdocum.html#B.
KIVELSON, M. G. & RUSSELL, C. T. (1997) *Introduction to space physics,* Cambridge, Cambridge University Press.
KYOTO, W. *Geomagnetic Elements*. World data center for geomagnetism Kyoto 2010 [cited 2009 08. October]; Data analysis center for geomagnetism and space magnetism graduate school of science]. Available from: http://wdc.kugi.kyoto-u.ac.jp/element/eleexp.html.
LAITINEN, T. V., NAKAMURA, R., RUNOV, A., REME, H. & LUCEK, E. A. (2007) Global and local disturbances in the magnetotail during reconnection. *Annales Geophysicae,* 25**,** 1025-1035.
LANGEL, R. A. & HINZE, W. J. (1998) *The magnetic field of the Earth's Lithosphere,* Cambridge, Cambridge University Press.
LESTER, M., HUGHES, W. J. & SINGER, H. J. (1983) Polarization patterns pf Pi 2 magnetic pulsations and the substorm current wedge *Journal of Geophysical Research-Space Physics,* 88**,** 7958-7966.
LESTER, M., HUGHES, W. J. & SINGER, H. J. (1984) Longitudinal structure in Pi-2 pulsations and the substorm current wedge *Journal of Geophysical Research-Space Physics,* 89**,** 5489-5494.

LEVY, R. H., PETSCHEK, H. E. & SISCOE, G. L. (1964) Aerodynamic aspects of the magnetospheric flows *Aiaa Journal,* 2**,** 2065-2076.
LINDQUIST, P.-A. (1983) The potential of ISEE in different plasma environments *Proc. of the 17th ESLAB Symp on Spacecraft/Plasma Interactions and their Influence on Field and Particle Measurements.* Noordwijk, European Space Agency.
LINDQUIST, P.-A. & EFW-TEAM (2001) *User guide to the EFW measurements in the Cluster Active Archive,* European Space Agency.
LIOU, K., MENG, C. I., NEWELL, P. T., TAKAHASHI, K., OHTANI, S. I., LUI, A. T. Y., BRITTNACHER, M. & PARKS, G. (2000) Evaluation of low-latitude Pi2 pulsations as indicators of substorm onset using Polar ultraviolet imagery. *Journal of Geophysical Research,* 105**,** 2495-2505.
LOUARN, P., FRUIT, G., BUDNIK, E., SAUVAUD, J. A., JACQUEY, C., LE QUEAU, D., REME, H., LUCEK, E. & BALOGH, A. (2004) On the propagation of low-frequency fluctuations in the plasma sheet: 1. Cluster observations and magnetohydrodynamic analysis. *Journal of Geophysical Research,* 109**,** 11.
LUI, A. T. Y. (1991) A synthesis of magnetospheric substorm models. *Journal of Geophysical Research,* 96**,** 1849-1856.
LUI, A. T. Y. (2009) Comment on "Tail Reconnection Triggering Substorm Onset". *Science,* 324**,** 3.
MALTSEV, Y. P., LEONTYEV, S. V. & LYATSKY, W. B. (1974) Pi-2 pulsations as a result of evolution of an Alfvén impulse originating in the ionosphere during a brightening of aurora *Planetary and Space Science,* 22**,** 1519-1533.
MCPHERRON, R. L. (1979) Magnetospheric substorms *Reviews of Geophysics,* 17**,** 657-681.
MCPHERRON, R. L., RUSSELL, C. T. & AUBRY, M. P. (1973) Satellite studies of magnetospheric substorms on august 15, 1968 .9. Phenomenological model for substorms. *Journal of Geophysical Research,* 78**,** 3131-3149.
MENDE, S. B., HEETDERKS, H., FREY, H. U., LAMPTON, M., GELLER, S. P., ABIAD, R., SIEGMUND, O. H. W., TREMSIN, A. S., SPANN, J., DOUGANI, H., FUSELIER, S. A., MAGONCELLI, A. L., BUMALA, M. B., MURPHREE, S. & TRONDSEN, T. (2000a) Far ultraviolet imaging from the IMAGE spacecraft. 2. Wideband FUV imaging. *Space Science Reviews,* 91**,** 271-285.
MENDE, S. B., HEETDERKS, H., FREY, H. U., LAMPTON, M., GELLER, S. P., HABRAKEN, S., RENOTTE, E., JAMAR, C., ROCHUS, P., SPANN, J., FUSELIER, S. A., GERARD, J. C., GLADSTONE, R., MURPHREE, S. & COGGER, L. (2000b) Far ultraviolet imaging from the IMAGE spacecraft. 1. System design. *Space Science Reviews,* 91**,** 243-270.
MIRIONI, L., CORNILLEAU-WEHRLIN, N., ROBERT, P., MAKSIMOVIC, M., DE CONCHY, Y. & HARVEY, C. C. (2005) STAFF products for the Cluster Active Archive. *Proceedings of theCluster and Double Star Symposium 5th Anniversary of Cluster in Space.* Noordwijk, ESTEC.
MOZER, F. S., BALE, S. D. & PHAN, T. D. (2002) Evidence of diffusion regions at a subsolar magnetopause crossing. *Physical Review Letters,* 89**,** 4.
MOZER, F. S., BALE, S. D., PHAN, T. D. & OSBORNE, J. A. (2003) Observations of electron diffusion regions at the subsolar magnetopause. *Physical Review Letters,* 91**,** 4.
NAGAI, T., FUJIMOTO, M., NAKAMURA, R., BAUMJOHANN, W., IEDA, A., SHINOHARA, I., MACHIDA, S., SAITO, Y. & MUKAI, T. (2005) Solar wind control of the radial distance of the magnetic reconnection site in the magnetotail. *Journal of Geophysical Research,* 110**,** 11.

NAGAI, T., SHINOHARA, I., FUJIMOTO, M., HOSHINO, M., SAITO, Y., MACHIDA, S. & MUKAI, T. (2001) Geotail observations of the Hall current system: Evidence of magnetic reconnection in the magnetotail. *Journal of Geophysical Research-Space Physics,* 106**,** 25929-25949.

NAKAMURA, M., PASCHMANN, G., BAUMJOHANN, W. & SCHOPKE, N. (1991) Ion distributions and flows near the neutral sheet *Journal of Geophysical Research,* 96**,** 5631-5649.

NAKAMURA, R. (2006) Substorms and their solar wind causes. *Space Science Reviews,* 124**,** 91-101.

NAKAMURA, R., BAUMJOHANN, W., ASANO, Y., RUNOV, A., BALOGH, A., OWEN, C. J., FAZAKERLEY, A. N., FUJIMOTO, M., KLECKER, B. & REME, H. (2006) Dynamics of thin current sheets associated with magnetotail reconnection. *Journal of Geophysical Research,* 111**,** 14.

NAKAMURA, R., BAUMJOHANN, W., RUNOV, A., VOLWERK, M., ZHANG, T. L., KLECKER, B., BOGDANOVA, Y., ROUX, A., BALOGH, A., REME, H., SAUVAUD, J. A. & FREY, H. U. (2002) Fast flow during current sheet thinning. *Geophysical Research Letters,* 29**,** 4.

NESS, N. F. (1965) Earth's magnetic tail *Journal of Geophysical Research,* 70**,** 2989-3005.

NMOC. *Systems of time*. Naval Meteorology and Oceanography Command 2010 [cited 2010 19. February]; Available from: http://www.usno.navy.mil/USNO/time/master-clock/systems-of-time/?searchterm=universal%20time.

OIEROSET, M., PHAN, T. D., FUJIMOTO, M. & LEPPING, R. P. (2001) In situ detection of collisionless recconection in the Earth's magnetotail. *Letter to Nature,* 412**,** 414-417.

OLSON, J. V. (1999) Pi2 pulsations and substorm onsets: A review. *Journal of Geophysical Research,* 104**,** 499-520.

OSTGAARD, N., SNEKVIK, K., BORG, A. L., ASNES, A., PEDERSEN, A., OIEROSET, M., PHAN, T. & HAALAND, S. E. (2009) Can magnetotail reconnection produce the auroral intensities observed in the conjugate ionosphere? *Journal of Geophysical Research,* 114**,** 13.

PASCHMANN, G., HAALAND, S. & TREUMANN, R. A. (2002) *Auroral Plasma Physics,* Bern, Kluwer Academic Publishers.

PASCHMANN, G., SONNERUP, B. U. O., PAPAMASTORAKIS, I., SCKOPKE, N., HAERENDEL, G., BAME, S. J., ASBRIDGE, J. R., GOSLING, J. T., RUSSELL, C. T. & ELPHIC, R. C. (1979) Plasma acceleration at the Earths magnetopause - evidence for reconnection *Nature,* 282**,** 243-246.

PEDERSEN, A., LYBEKK, B., ANDRE, M., ERIKSSON, A., MASSON, A., MOZER, F. S., LINDQVIST, P. A., DECREAU, P. M. E., DANDOURAS, I., SAUVAUD, J. A., FAZAKERLEY, A., TAYLOR, M., PASCHMANN, G., SVENES, K. R., TORKAR, K. & WHIPPLE, E. (2008) Electron density estimations derived from spacecraft potential measurements on Cluster in tenuous plasma regions. *Journal of Geophysical Research,* 113**,** 19.

PETRUKOVICH, A. A., BAUMJOHANN, W., NAKAMURA, R. & REME, H. (2009) Tailward and earthward flow onsets observed by Cluster in a thin current sheet. *Journal of Geophysical Research,* 114**,** 1-7.

PETRUKOVICH, A. A., BAUMJOHANN, W., NAKAMURA, R., RUNOV, A. & BALOGH, A. (2005) Cluster vision of the magnetotail current sheet on a macroscale. *Journal of Geophysical Research-Space Physics,* 110**,** 7.

PRITCHETT, P. L. (2001) Collisionless magnetic reconnection in a three-dimensional open system. *Journal of Geophysical Research,* 106**,** 25961-25977.

PRÖLSS, G. W. (2003) *Physics of the Earth's space environment, an introduction,* Bonn, Springer.

RÉME, H. & AL., E. (2001) First multispacecraft ion measurements in and near the Earth's magnetospherewith the identical Cluster Ion Spectrometry (CIS) experiment. *Annales Geophysicae,* 19**,** 1303-1354.

RETINO, A., VAIVADS, A., ANDRE, M., SAHRAOUI, F., KHOTYAINTSEV, Y., PICKETT, J. S., CATTANEO, M. B. B., MARCUCCI, M. F., MOROOKA, M., OWEN, C. J., BUCHERT, S. C. & CORNILLEAU-WEHRLIN, N. (2006) Structure of the separatrix region close to a magnetic reconnection X-line: Cluster observations. *Geophysical Research Letters,* 33**,** 4.

RIDPATH, I. (2007) Oxford Dictionary of Astronomy. 2 ed. Oxford, Oxford University Press.

RIEDLER, W., TORKAR, K., RUDENAUER, F., FEHRINGER, M., PEDERSEN, A., SCHMIDT, R., GRARD, R. J. L., ARENDS, H., NARHEIM, B. T., TROIM, J., TORBERT, R., OLSEN, R. C., WHIPPLE, E., GOLDSTEIN, R., VALAVANOGLOU, N. & ZHAO, H. (1997) Active spacecraft potential control. *Space Science Reviews,* 79**,** 271-302.

ROSTOKER, G., S.-I., A., GREENWALD, R. A., KAMIDE, Y., KAWASAKI, K., LUI, A. T. Y., MCPHERRON, R. L. & RUSSEL, C. T. (1980) Magnetospheric substorms - Definitions and signatures. *Journal of Geophysical Research,* 85**,** 1663-1668.

RUNOV, A., NAKAMURA, R., BAUMJOHANN, W., TREUMANN, R. A., ZHANG, T. L., VOLWERK, M., VÖRÖS, Z., BALOGH, A., GLASSMEIER, K.-H., KLECKER, B., RÉME, A. & KISTLER, L. (2003) Current sheet structure near magnetic X-line observed by Cluster. *Geophysical Research Letter,* 30.

RUSSELL, C. T., SNARE, R. C., MEANS, J. D., PIERCE, D., DEARBORN, D., LARSON, M., BARR, G. & LE, G. (1995) THE GGS/POLAR magnetic-fields investigation. *Space Science Reviews,* 71**,** 563-582.

SCHINDLER, K. & BIRN, J. (1978) Magnetospheric physics *Physics Reports-Review Section of Physics Letters,* 47**,** 111-165.

SCHINDLER, K. & BIRN, J. (1993) On the cause of thin current sheets in the near-Earth magnetotail and their possible significance for magnetospheric substorms *Journal of Geophysical Research,* 98**,** 15477-15485.

SCUDDER, J. D., MOZER, F. S., MAYNARD, N. C. & RUSSELL, C. T. (2002) Fingerprints of collisionless reconnection at the separator, I, Ambipolar-Hall signatures. *Journal of Geophysical Research,* 107**,** 38.

SERGEEV, V., KUBYSHKINA, M., ALEXEEV, I., FAZAKERLEY, A., OWEN, C., BAUMJOHANN, W., NAKAMURA, R., RUNOV, A., VOROS, Z., ZHANG, T. L., ANGELOPOULOS, V., SAUVAUD, J. A., DALY, P., CAO, J. B. & LUCEK, E. (2008) Study of near-Earth reconnection events with Cluster and Double Star. *Journal of Geophysical Research,* 113**,** 19.

SERGEEV, V., RUNOV, A., BAUMJOHANN, W., NAKAMURA, R., ZHANG, T. L., BALOGH, A., LOUARND, P., SAUVAUD, J.-A. & REME, H. (2004) Orientation and propagation of currentsheet oscillations. *Geophysical Research Letter,* 31**,** L05807.

SERGEEV, V., RUNOV, A., BAUMJOHANN, W., NAKAMURA, R., ZHANG, T. L., VOLWERK, M., BALOGH, A., REME, H., SAUVAUD, J. A., ANDRE, M. & KLECKER, B. (2003) Current sheet flapping motion and structure observed by Cluster. *Geophysical Research Letters,* 30**,** 4.

SERGEEV, V., SEMENOV, V., KUBYSHKINA, M., IVANOVA, V., BAUMJOHANN, W., NAKAMURA, R., PENZ, T., RUNOV, A., ZANG, T. L., GLASSMEIER, K.-H.,

ANGELOPOULOS, V., FREY, H., SAUVAUD, J.-A., DALY, P., CAO, J. B., SINGER, H. & LUCEK, E. (2007) Observations of repeated intense near-Earth reconnection on closed field lines with Cluster, Double Star and other spacecraft. *Geophysical Research Letters,* 34**,** L02103,1 - L02103,6.

SERGEEV, V. A., MITCHELL, D. G., RUSSELL, C. T. & WILLIAMS, D. J. (1993) Structure of the tail plasma current sheet at similar-to-11 R (E) and its changes in the course of a substorm *Journal of Geophysical Research,* 98**,** 17345-17365.

SERGEEV, V. A., SORMAKOV, D. A., APATENKOV, S. V., BAUMJOHANN, W., NAKAMURA, R., RUNOV, A. V., MUKAI, T. & NAGAI, T. (2006) Survey of large-amplitude flapping motions in the midtail current sheet. *Annales Geophysicae,* 24**,** 2015-2024.

SHARMA, A. S., NAKAMURA, R., RUNOV, A., GRIGORENKO, E. E., HASEGAWA, H., HOSHINO, M., LOUARN, P., OWEN, C. J., PETRUKOVICH, A., SAUVAUD, J. A., SEMENOV, V. S., SERGEEV, V. A., SLAVIN, J. A., SONNERUP, B. U. O., ZELENYI, L. M., FRUIT, G., HAALAND, S., MALOVA, H. & SNEKVIK, K. (2008) Transient and localized processes in the magnetotail: a review. *Annales Geophysicae,* 26**,** 955-1006.

SHAY, M. A., DRAKE, J. F., ROGERS, B. N. & DENTON, R. E. (2001) Alfvenic collisionless magnetic reconnection and the Hall term. *Journal of Geophysical Research,* 106**,** 3759-3772.

SHIOKAWA, K., BAUMJOHANN, W. & HAERENDEL, G. (1997) Braking of high-speed flows in the near-Earth tail. *Geophysical Research Letters,* 24**,** 1179-1182.

SNEKVIK, K. (2009) Observations of field aligned currents in the plasma sheet. *University of Bergen, Department of Physics and Technology.* Bergen, University of Bergen.

SONNERUP, B. U. & CAHILL, L. J. (1967) A magnetopause structure and attitude from EXPLORER 12 observations *Journal of Geophysical Research,* 72**,** 171-183.

SONNERUP, B. U. O., PASCHMANN, G., PAPAMASTORAKIS, I., SCKOPKE, N., HAERENDEL, G., BAME, S. J., ASBRIDGE, J. R., GOSLING, J. T. & RUSSELL, C. T. (1981) Evidence for magnetic-field reconnection at the Earths magnetopause. *Journal of Geophysical Research-Space Physics,* 86**,** 49-67.

SONNERUP, B. U. Ö. (1979) *Solar System Plasma Physics,* North-Holland, New York.

STASIEWICZ, K., KHOTYAINTSEV, M. & KHOTYAINTSEV, Y. (2003) Orbit Visualization Tool *Swedish Institute of Space Physics.* Uppsala.

STØRMER, C. (1955) *The Polar Aurora,* Oxford, Clarendon Press.

TAKAHASHI, K., OHTANI, S. & ANDERSON, B. J. (1995) Statistical analysis of Pi 2 pulsations observed by the AMPTE-CCE spacecraft in the inner magnetosphere *Journal of Geophysical Research-Space Physics,* 100**,** 21929-21941.

TSYGANENKO, N. A. (1987) Global quantitative models of the geomagnetic-field in the cislunar magnetosphere for different disturbance levels. *Planetary and Space Science,* 35**,** 1347-1358.

TSYGANENKO, N. A. (1989) A magnetospheric magnetic-field model with a warped tail current sheet. *Planetary and Space Science,* 37**,** 5-20.

TSYGANENKO, N. A. (1995) Modeling the Earth's magnetospheric magnetic-field confined within a realistic magnetopause. *Journal of Geophysical Research* 100**,** 5599-5612.

TSYGANENKO, N. A. (2002) A model of the near magnetosphere with a dawn-dusk asymmetry - 2. Parameterization and fitting to observations. *Journal of Geophysical Research,* 107**,** 17.

UENO, G., OHTANI, S., MUKAI, T., SAITO, Y. & HAYAKAWA, H. (2003) Hall current system around the magnetic neutral line in the magnetotail: Statistical study. *Journal of Geophysical Research-Space Physics,* 108**,** 9.1-9.7.

VAIVADS, A., RETINO, A. & ANDRE, M. (2006) Microphysics of magnetic reconnection. *Space Science Reviews,* 122**,** 19-27.

VASYLIUNAS, V. M. (1975) Theoretical models of magnetic-field line merging.1. *Reviews of Geophysics,* 13**,** 303-336.

VOLWERK, M., GLASSMEIER, K. H., RUNOV, A., BAUMJOHANN, W., NAKAMURA, R., ZHANG, T. L., KLECKER, B., BALOGH, A. & REME, H. (2003) Kink mode oscillation of the current sheet. *Geophysical Research Letters,* 30**,** 4.

VOLWERK, M., NAKAMURA, R., BAUMJOHANN, W., UOZUMI, T., YUMOTO, K. & BALOGH, A. (2008) Tailward propagation of Pi2 waves in the Earth's magnetotail lobe. *Annales Geophysicae,* 26**,** 4023-4030.

WEBSTER, J. G. (1999) *The measurement, instrumentation, and sensors handbook,* Boca Ration, CRC Press LLC.

WEIMER, D. R. (1994) Substorm time constants. *Journal of Geophysical Research,* 99**,** 11005-11015.

WHISPER-TEAM (2009) *User guide to the Whisper measurements in the Cluster Active Archive.*

WILKEN, B., AXFORD, W. I., DAGLIS, I., DALY, P., GUTTLER, W., IP, W. H., KORTH, A., KREMSER, G., LIVI, S., VASYLIUNAS, V. M., WOCH, J., BAKER, D., BELIAN, R. D., BLAKE, J. B., FENNELL, J. F., LYONS, L. R., BORG, H., FRITZ, T. A., GLIEM, F., RATHJE, R., GRANDE, M., HALL, D., KECSUEMETY, K., MCKENNALAWLOR, S., MURSULA, K., TANSKANEN, P., PU, Z., SANDAHL, I., SARRIS, E. T., SCHOLER, M., SCHULZ, M., SORASS, F. & ULLALAND, S. (1997) RAPID - The imaging energetic particle spectrometer on Cluster. *Space Science Reviews,* 79**,** 399-473.

WUTEAM. *Biomes and Ecosystems*. University Corporation for Atmospheric Research (UCAR), Michigan 2008 [cited 2009 08. October]; The Earth magnetic field]. Available from: http://www.windows.ucar.edu.

XIAO, C. J., WANG, X. G., PU, Z. Y., ZHAO, H., WANG, J. X., MA, Z. W., FU, S. Y., KIVELSON, M. G., LIU, Z. X., ZONG, Q. G., GLASSMEIER, K. H., BALOGH, A., KORTH, A., REME, H. & ESCOUBET, C. P. (2006) In situ evidence for the structure of the magnetic null in a 3D reconnection event in the Earth'smagnetotail. *Nature Physics,* 2**,** 478-483.

YUMOTO, K. (1996) The STEP 210 degrees magnetic meridian network project. *Journal of Geomagnetism and Geoelectricity,* 48**,** 1297-1309.

YUMOTO, K. & GRP, C. (2001) Characteristics of Pi 2 magnetic pulsations observed at the CPMN stations: A review of the STEP results. *Earth Planets and Space,* 53**,** 981-992.

ZHANG, T. L., BAUMJOHANN, W., NAKAMURA, R., BALOGH, A. & GLASSMEIER, K. H. (2002) A wavy twisted neutral sheet observed by CLUSTER. *Geophysical Research Letters,* 29**,** 4.

Appendix A: List of acronyms and abbreviations

ACE – Advanced Composition Explorer

AE-index – Auroral Electrojet index

AL-index – Auroral Lower index

AU-index – Auroral Upper index

BRW – Barrow

CAA – Cluster Active Archive

CAN – Canberra

CBB – Cambridge Bay

CHD – Chokurdakh

CIS – Cluster Ion Spectrometry

CME – Coronal Mass Ejections

CMO – Collage

CODIF – COmposition and Distribution Function

CPMN – Circum-pan Pacific Magnetometer Network

DAL – Dalby

DRV - Dumont d'Urville

EFW – Electric Field and Wave

ESA - European Space Agency

EUV – Extreme Ultra-Violet

EYR – Eyrewell

FAC – Field Aligned Current

FGM – Fluxgate Magnetometer

FUV – Far Ultraviolet

GEO – Geocorona

GSE - Geocentric Solar Ecliptic

GSM - Geocentric Solar Magnetospheric

IMAGE – Imager for Magnetopause-to-Aurora Global Exploration

IMF – Interplanetary Magnetic Field

INTERMAGNET – INTErnational Real-time MAGnetic Observatory NETwork

IR – Infrared

ISTP – International Solar Terrestrial Physics

KAG – Kagoshima

MCQ – Macquarie Island

MEA – Meanook

MGD – Magadan

MHD – Magnetohydrodynamic

MLT – Magnetic Local Time

MSR – Moshiri

NENL – Near-Earth Neutral Line

NECD – Near-Earth Current Disruption

ONW – Onagawa

OTV – Orbit Visualization Tool

R_E – Earth radii

RIK – Rikubetsu

SCW – Substorm Current Wedge

SI - Spectrographic Imager

SIT –Sitka

THEMIS - Time History of Events and Macroscale Interactions during Substorms

UT – Universal Time

UV – Ultra-Violet

WDC - World Data Center

WEP – Weipa

WEW – Wewak

WIC – Wideband Imaging Camera

WTS – Westward Travelling Surge

YKC – Yellowknife

ZYK – Zyryanka

Appendix B: The electric field quality flags

The quality of the electric field from EFW [*Gustafsson et al.*, 2001] experiment is investigated in this appendix. The quality flags of the electric fields are defined as (taken from the user guide for the EFW-experiment): 0 - bad data, 1 - known problems, use at your own risk, 2 - survey data, not for publication, 3 - good for publication, subject to PI approval and 4 - excellent data which has received special treatment. Level 4 is never used by the CAA because the data are generated automatically [*Lindquist and EFW-Team*, 2001]. Figure 6-72 and Figure 6-73 show plots of the quality flags of the data from the datasets in 2005 and 2001 used in this thesis.

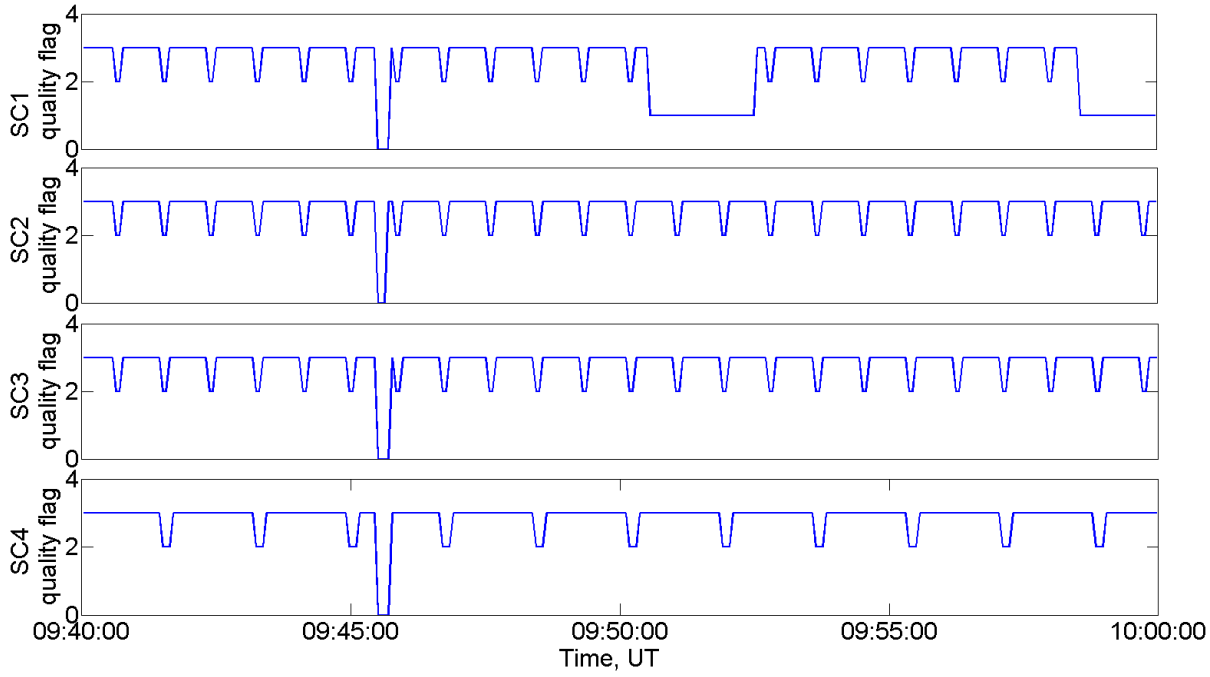

Figure 6-72: The quality flag from the electric field measurements from the 2005 dataset. The data should be used with caution if the quality flags fall below 3. The periodic drops are Whisper emitting waves from the spacecraft.

As seen from the figures, the quality flags are mainly of level three with a periodical change to level 2. This periodical change is due to the Whisper [*Decreau et al.*, 1997] experiment operating [*Lindquist and EFW-Team*, 2001]. The Whisper experiment uses radio technique in order to identify the electron density in the plasma [*Whisper-Team*, 2009]. The small emitted waves are seen as small spikes in the potential data presented in Figure 6-72 and in Figure 6-73. The larger periods with a level 1 quality range are due to cold ion drift wakes [*Lindquist and EFW-Team*, 2001]. This effect is difficult to detect in the raw data because it is similar to the real electric field measured in the are close to the spacecraft. There

has not being developed any algorithm taking this wake effect into account and therefore the data are flagged with quality flag 1. This means that the electric field data the period where the quality flag is 1 or 0 should be used with caution. Those periods are from 09.45.15 UT to 09.45.40 UT for all four spacecraft, and at SC1 between 09.50.30 UT and 09.52.25 UT at SC1 in the electric field dataset from 2005, and some intervals for SC1, SC2 and SC3 and the time period after 10.04.30 in the electric field dataset for the 2001 event.

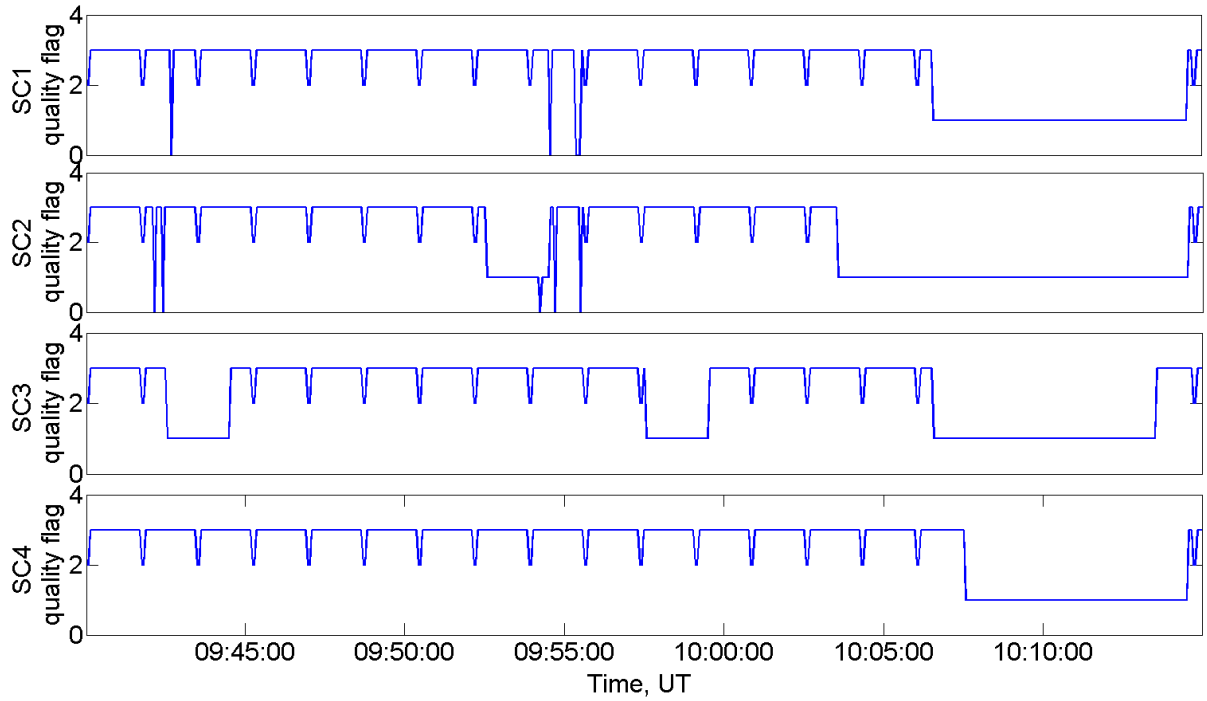

Figure 6-73: The quality flag of the electric field data from the 2001 dataset. The data should be used with caution if the quality flags fall below 3. The periodic drops are Whisper emitting waves from the spacecraft.

Appendix C: The parameters used for the Tsyganenko models

Table 6-12 contains the values used when simulating the footpoints in the 2005 event, using the T87, T89 and T96 models. The IMF values are obtained by calculating the average value of the solar wind pressure, B_x, B_y and B_z during a time interval of 1 hour (between 09.00 and 10.00 UT, see chapter 4.3). The simulations of the footpoints were done in OVT and the calculations of the average values were done in the solarwind.m file in appendix E. Details regarding the parameters are given in the main text of the thesis in chapter 4.3.

Parameters	**T87/T89**	**T96**
K_P- index	3	-
D_{ST} -index	-	-9
IMF B_x	-	-2
IMF B_y	-	5
IMF B_z	-	1
Solar wind pressure	-	5

Table 6-12: The parameters used in the different Tsyganenko mapping models when simulating the footpoints for the 2005 event. T87 and T89 use the same parameters.

Table 6-13 contains the values used when simulating the footpoints in the 2001 event, using the same models and calculations as for the 2005 event.

Parameters	**T87/ T89**	**T96**
K_P- index	4	-
D_{ST} -index	-	-14
IMF B_x	-	5
IMF B_y	-	-1
IMF B_z	-	-5
Solar wind pressure	-	2

Table 6-13: The parameters used in the different Tsyganenko mapping models when simulating the footpoints for the 2001 event. T87 and T89 models use the same parameters.

Appendix D: Multipoint timing analysis (MTA)

In order to calculate the normal of any plane surface passing the Cluster satellites, there should be a point in the dataset where a similar feature was measured by all four spacecraft. The simplest way of doing so is by using the point where the Cluster satellites cross the neutral sheet, i.e. when B_x changes its polarity. Figure 6-74 shows the B_x-measurements from the 2001 event between 09.40 UT and 09.50 UT, which was the first time the Cluster satellites crossed the current sheet during this event. The time of crossing for each satellite is marked with a pink circle in the figure, and is given in Table 6-14 together with the separation distances between the satellites during that crossing.

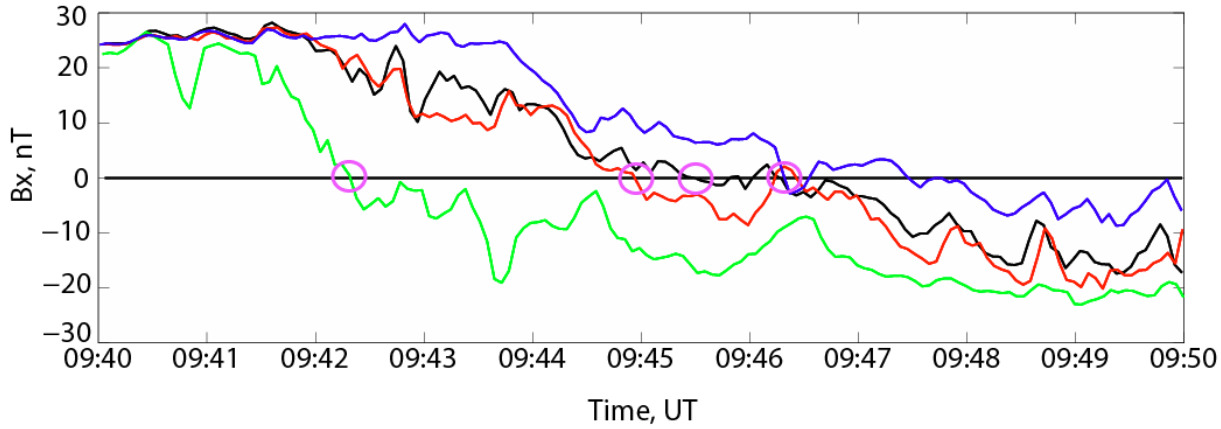

Figure 6-74: Plot of the B_x-component of the magnetic field measurements. The pink circles indicate the crossing of the current sheet of each Cluster spacecraft. The magnetic field measurements are given in the Cluster colours: SC1-black, SC2-red, SC3-green, and SC4-blue.

The calculations of the movement were done by a program created by A. L. Borg, and the calculations were based on the position of SC3 and the time when this spacecraft crossed the current sheet. Based on the current sheet crossing within the limited time interval between 09.42 UT and 09.47 UT, the normal of the plane was found to point in the direction $\hat{\boldsymbol{n}}_{MTA} = (-0.1, -0.4, 0.9)$. The normal to the current sheet was found to be almost parallel with the z_{GSM} direction, while the current sheet itself was oriented approximately in the xy_{GSM} plane. Since the calculations were based on a short time interval, it was difficult to say whether this normal was the same during the rest of the reconnection time interval or not. Nevertheless, the normal direction calculated by the multipoint timing analysis strengthens the assumption that the normal of the current sheet was pointing along the z_{GSM} direction.

Spacecraft, SC	Distance from SC3 $(x, y, z)_{GSM}$ $[10^3\ km]$	Time when crossing [UT]
SC1	$(1.4, -0.16, 1.3)$	09.45.25
SC2	$(0.22, 1.5, 1.3)$	09.44.54
SC3	$(0, 0, 0)$	09.42.11
SC4	$(-0.29, -0.39, 1.9)$	09.46.17

Table 6-14: The crossing time of each spacecraft when crossing the current sheet. The internal separation distance between each spacecraft is given when using SC3 as a reference.

MTA has not been used on the 2005 event, since there was no time during the studied event at which all the Cluster satellites observed a similar feature.

Appendix E: The program codes

In this section the programs used in this thesis are presented. The programming language used is Matlab 7.7.0. The programs shown are from the 2005 event only but there are similar programs for the 2001 event for the data presented in chapter 5. The programs have mainly been used in order to present data from satellites and ground measurements, but also for calculations. There has not been any focus on making the programs as effective as possible. The datasets are loaded into the codes .txt files. Previous to each code there is a short explanation of the code and a comment on the difference between the 2005 code and the 2001 code. In some occasions there is an explanation of some of the mathematics used in the code and how the results are given.

Create_GSM_from_GSE.m

The difference between the GSE - and GSM - coordinate system is a rotation about the x-axis. The transformation between the two coordinate systems is given mathematically as

$$\begin{pmatrix} x \\ y \\ z \end{pmatrix}_{GSM} = \begin{pmatrix} 1 & 0 & 0 \\ 0 & \cos\psi & -\sin\psi \\ 0 & \sin\psi & \cos\psi \end{pmatrix} \cdot \begin{pmatrix} x \\ y \\ z \end{pmatrix}_{GSE} \qquad (2.1)$$

where the parameters x, y and z are the measured quantities. The program Create_GSM_from_GSE.m transforms the CAA data from the GSE coordinate system into the GSM coordinate system. The program uses the rotation angle from the auxiliary file from CAA. The program consists of two parts: Create_GSM_from_GSE_load.m which loads the data into arrays and the other part which Create_GSM_from_GSE_process.m which does the calculations.

```
% Create_GSM_from_GSE_load
clc;
clear;

Year = 2005;
Month = 09;
Day = 26;

%defining the time for analysing the data
time_start = datenum(Year, Month, Day, 9, 30,
00);
time_end = datenum(Year, Month, Day, 10, 00, 00);

%loading the data files
% MF_C1 = 'C1_CP_FGM_spin.txt';
% MF_C2 = 'C2_CP_FGM_spin.txt';
% MF_C3 = 'C3_CP_FGM_spin.txt';
% MF_C4 = 'C4_CP_FGM_spin.txt';
MF_C1 = 'C1_CP_FGM_full.txt';
MF_C2 = 'C2_CP_FGM_full.txt';
MF_C3 = 'C3_CP_FGM_full.txt';
MF_C4 = 'C4_CP_FGM_full.txt';

E_C1 = 'C1_CP_EFW_EX_EY.txt';
E_C2 = 'C2_CP_EFW_EX_EY.txt';
E_C3 = 'C3_CP_EFW_EX_EY.txt';
E_C4 = 'C4_CP_EFW_EX_EY.txt';

Ez_C1 = 'C1_CP_EFW_EZ.txt';
Ez_C2 = 'C2_CP_EFW_EZ.txt';
Ez_C3 = 'C3_CP_EFW_EZ.txt';
Ez_C4 = 'C4_CP_EFW_EZ.txt';

V_C4 = 'C4_CP_CIS_CODIF.txt';

AUX = 'CL_SP_AUX.txt';

SCPOT_C1 = 'C1_CP_EFW_SCPOT.txt';
SCPOT_C2 = 'C2_CP_EFW_SCPOT.txt';
SCPOT_C3 = 'C3_CP_EFW_SCPOT.txt';
SCPOT_C4 = 'C4_CP_EFW_SCPOT.txt';

A = load(E_C1);
B = load(E_C2);
C = load(E_C3);
D = load(E_C4);

E = load(MF_C1);
F = load(MF_C2);
```

```
G = load(MF_C3);
H = load(MF_C4);

J = load(V_C4);

K = load(Ez_C1);
L = load(Ez_C2);
M = load(Ez_C3);
N = load(Ez_C4);

O = load(AUX);

P = load (SCPOT_C1);
Q = load (SCPOT_C2);
R = load (SCPOT_C3);
S = load (SCPOT_C4);

%Removing data which are not real data
invalidA=(A(:,5)==-
1000000000.000);A(invalidA,5)=NaN;
invalidA=(A(:,6)==-
1000000000.000);A(invalidA,6)=NaN;
invalidB=(B(:,5)==-
1000000000.000);B(invalidB,5)=NaN;
invalidB=(B(:,6)==-
1000000000.000);B(invalidB,6)=NaN;
invalidC=(C(:,5)==-
1000000000.000);C(invalidC,5)=NaN;
invalidC=(C(:,6)==-
1000000000.000);C(invalidC,6)=NaN;
invalidD=(D(:,5)==-
1000000000.000);D(invalidD,5)=NaN;
invalidD=(D(:,6)==-
1000000000.000);D(invalidD,6)=NaN;

invalidK=(K(:,7)==-
1000000000.000);K(invalidK,7)=NaN;
invalidL=(L(:,7)==-
1000000000.000);L(invalidL,7)=NaN;
invalidM=(M(:,7)==-
1000000000.000);M(invalidM,7)=NaN;
invalidN=(N(:,7)==-
1000000000.000);N(invalidN,7)=NaN;

invalidJ=(J(:,6)>=3);J(invalidJ,6)=NaN;

invalidC1=(P(:,5)==-
1000000000.000);P(invalidC1,5)=NaN;
invalidC2=(Q(:,5)==-
1000000000.000);Q(invalidC2,5)=NaN;
invalidC3=(R(:,5)==-
1000000000.000);R(invalidC3,5)=NaN;
invalidC4=(S(:,5)==-
1000000000.000);S(invalidC4,5)=NaN;

Ex_C1 = A(:,5);
Ey_C1 = A(:,6);
Ez_C1 = K(:,7);

Ex_C2 = B(:,5);
Ey_C2 = B(:,6);
Ez_C2 = L(:,7);

Ex_C3 = C(:,5);
Ey_C3 = C(:,6);
Ez_C3 = M(:,7);

Ex_C4 = D(:,5);
Ey_C4 = D(:,6);
Ez_C4 = N(:,7);

bx_C1 = E(:,6);
by_C1 = E(:,7);
bz_C1 = E(:,8);

bx_C2 = F(:,6);
by_C2 = F(:,7);
bz_C2 = F(:,8);

bx_C3 = G(:,6);
by_C3 = G(:,7);
bz_C3 = G(:,8);

bx_C4 = H(:,6);
by_C4 = H(:,7);
bz_C4 = H(:,8);

vx_C4 = J(:,7);
vy_C4 = J(:,8);
vz_C4 = J(:,9);

n_C4 = J(:,6);

potential_C1 = P(:,5);
potential_C2 = Q(:,5);
potential_C3 = R(:,5);
potential_C4 = S(:,5);

%reading the auxiliry data
GSE_GSM = O(:,41);%rotation angle
Sep_min = O(:,39);
Sep_max = O(:,40);
Vel_SC3_x = O(:,14);%velocity of the referance
spacecraft
Vel_SC3_y = O(:,15);
Vel_SC3_z = O(:,16);
pos_GSE_x = O(:,11);
pos_GSE_y = O(:,12);
pos_GSE_z = O(:,13);
C1_off_x = O(:,17);%separation distance between
SC1 and SC3
C1_off_y = O(:,18);
C1_off_z = O(:,19);
C2_off_x = O(:,20);%separation distance between
SC2 and SC3
C2_off_y = O(:,21);
C2_off_z = O(:,22);
C4_off_x = O(:,26);%separation distance between
SC4 and SC3
C4_off_y = O(:,27);
C4_off_z = O(:,28);

potential_C1_time = P(:,2); potential_C1_min =
P(:,3); potential_C1_sec = P(:,4);

%reading time arrays from the files
T_pot_C1 = datenum(Year, Month, Day, poten-
tial_C1_time, potential_C1_min, poten-
tial_C1_sec);

v_time_C4 = J(:,2); v_min_C4 = J(:,3); v_sek_C4 =
J(:,4);

Ez_time_C1 = K(:,2); Ez_min_C1 = K(:,3);
Ez_sek_C1 = K(:,4);
Ez_time_C2 = L(:,2); Ez_min_C2 = L(:,3);
Ez_sek_C2 = L(:,4);
Ez_time_C3 = M(:,2); Ez_min_C3 = M(:,3);
Ez_sek_C3 = M(:,4);
Ez_time_C4 = N(:,2); Ez_min_C4 = N(:,3);
Ez_sek_C4 = N(:,4);


E_time_C1 = A(:,2); E_min_C1 = A(:,3); E_sek_C1 =
A(:,4);
E_time_C2 = B(:,2); E_min_C2 = B(:,3); E_sek_C2 =
B(:,4);
E_time_C3 = C(:,2); E_min_C3 = C(:,3); E_sek_C3 =
C(:,4);
E_time_C4 = D(:,2); E_min_C4 = D(:,3); E_sek_C4 =
D(:,4);

b_time_C1 = E(:,2); b_min_C1 = E(:,3); b_sek_C1 =
E(:,4);
b_time_C2 = F(:,2); b_min_C2 = F(:,3); b_sek_C2 =
F(:,4);
b_time_C3 = G(:,2); b_min_C3 = G(:,3); b_sek_C3 =
G(:,4);
b_time_C4 = H(:,2); b_min_C4 = H(:,3); b_sek_C4 =
H(:,4);

T_b_C1 = datenum(Year, Month, Day, b_time_C1,
b_min_C1, b_sek_C1);
T_b_C2 = datenum(Year, Month, Day, b_time_C2,
b_min_C2, b_sek_C2);
T_b_C3 = datenum(Year, Month, Day, b_time_C3,
b_min_C3, b_sek_C3);
T_b_C4 = datenum(Year, Month, Day, b_time_C4,
b_min_C4, b_sek_C4);

T_E_C1 = datenum(Year, Month, Day, E_time_C1,
E_min_C1, E_sek_C1);
T_E_C2 = datenum(Year, Month, Day, E_time_C2,
E_min_C2, E_sek_C2);
```

```
T_E_C3 = datenum(Year, Month, Day, E_time_C3,
E_min_C3, E_sek_C3);
T_E_C4 = datenum(Year, Month, Day, E_time_C4,
E_min_C4, E_sek_C4);

T_Ez_C1 = datenum(Year, Month, Day, Ez_time_C1,
Ez_min_C1, Ez_sek_C1);
T_Ez_C2 = datenum(Year, Month, Day, Ez_time_C2,
Ez_min_C2, Ez_sek_C2);
T_Ez_C3 = datenum(Year, Month, Day, Ez_time_C3,
Ez_min_C3, Ez_sek_C3);
T_Ez_C4 = datenum(Year, Month, Day, Ez_time_C4,
Ez_min_C4, Ez_sek_C4);

T_v_C4 = datenum(Year, Month, Day, v_time_C4,
v_min_C4, v_sek_C4);

%Adjusting the data into the specified time in-
terval
index_time_interval_b_C1 = find(T_b_C1 >=
time_start & T_b_C1 <= time_end);
index_time_interval_b_C2 = find(T_b_C2 >=
time_start & T_b_C2 <= time_end);
index_time_interval_b_C3 = find(T_b_C3 >=
time_start & T_b_C3 <= time_end);
index_time_interval_b_C4 = find(T_b_C4 >=
time_start & T_b_C4 <= time_end);
T_b_C1 = T_b_C1(index_time_interval_b_C1);
T_b_C2 = T_b_C2(index_time_interval_b_C2);
T_b_C3 = T_b_C3(index_time_interval_b_C3);
T_b_C4 = T_b_C4(index_time_interval_b_C4);
bx_C1 = bx_C1(index_time_interval_b_C1);by_C1 =
by_C1(index_time_interval_b_C1);bz_C1 =
bz_C1(index_time_interval_b_C1);
bx_C2 = bx_C2(index_time_interval_b_C2);by_C2 =
by_C2(index_time_interval_b_C2);bz_C2 =
bz_C2(index_time_interval_b_C2);
bx_C3 = bx_C3(index_time_interval_b_C3);by_C3 =
by_C3(index_time_interval_b_C3);bz_C3 =
bz_C3(index_time_interval_b_C3);
bx_C4 = bx_C4(index_time_interval_b_C4);by_C4 =
by_C4(index_time_interval_b_C4);bz_C4 =
bz_C4(index_time_interval_b_C4);
index_time_interval_v_C4 = find(T_v_C4 >=
time_start & T_v_C4 <= time_end);
T_v_C4 = T_v_C4(index_time_interval_v_C4);
vx_C4 = vx_C4(index_time_interval_v_C4);vy_C4 =
vy_C4(index_time_interval_v_C4);vz_C4 =
vz_C4(index_time_interval_v_C4);
n_C4 = n_C4(index_time_interval_v_C4);
index_time_interval_E_C1 = find(T_E_C1 >=
time_start & T_E_C1<= time_end);
index_time_interval_E_C2 = find(T_E_C2 >=
time_start & T_E_C2<= time_end);
index_time_interval_E_C3 = find(T_E_C3 >=
time_start & T_E_C3<= time_end);
index_time_interval_E_C4 = find(T_E_C4 >=
time_start & T_E_C4<= time_end);
T_E_C1 = T_E_C1(index_time_interval_E_C1);
T_E_C2 = T_E_C2(index_time_interval_E_C2);
T_E_C3 = T_E_C3(index_time_interval_E_C3);
T_E_C4 = T_E_C4(index_time_interval_E_C4);
Ex_C1 = Ex_C1(index_time_interval_E_C1);
Ex_C2 = Ex_C2(index_time_interval_E_C2);
Ex_C3 = Ex_C3(index_time_interval_E_C3);
Ex_C4 = Ex_C4(index_time_interval_E_C4);
Ey_C1 = Ey_C1(index_time_interval_E_C1);
Ey_C2 = Ey_C2(index_time_interval_E_C2);
Ey_C3 = Ey_C3(index_time_interval_E_C3);
Ey_C4 = Ey_C4(index_time_interval_E_C4);
index_time_interval_Ez_C1 = find(T_Ez_C1 >=
time_start & T_Ez_C1<= time_end);
index_time_interval_Ez_C2 = find(T_Ez_C2 >=
time_start & T_Ez_C2<= time_end);
index_time_interval_Ez_C3 = find(T_Ez_C3 >=
time_start & T_Ez_C3<= time_end);
index_time_interval_Ez_C4 = find(T_Ez_C4 >=
time_start & T_Ez_C4<= time_end);
T_Ez_C1 = T_Ez_C1(index_time_interval_Ez_C1);
T_Ez_C2 = T_Ez_C2(index_time_interval_Ez_C2);
T_Ez_C3 = T_Ez_C3(index_time_interval_Ez_C3);
T_Ez_C4 = T_Ez_C4(index_time_interval_Ez_C4);
Ez_C1 = Ez_C1(index_time_interval_Ez_C1);
Ez_C2 = Ez_C2(index_time_interval_Ez_C2);
Ez_C3 = Ez_C3(index_time_interval_Ez_C3);
Ez_C4 = Ez_C4(index_time_interval_Ez_C4);
index_time_interval_C1 = find(T_pot_C1 >=
time_start & T_pot_C1 <= time_end);
T_pot_C1 = T_pot_C1(index_time_interval_C1);
potential_C1 = poten-
tial_C1(index_time_interval_C1);
potential_C2 = poten-
tial_C2(index_time_interval_C1);
potential_C3 = poten-
tial_C3(index_time_interval_C1);
potential_C4 = poten-
tial_C4(index_time_interval_C1);
```

%% *Create_GSM_from_GSE_process*

```
%Determing the auxiliary data
psi_deg = mean(GSE_GSM);%mean value of the rota-
tion angle
psi = deg2rad(psi_deg);
mean_vx_SC3 = mean(Vel_SC3_x);
mean_vy_SC3 = mean(Vel_SC3_y);
mean_vz_SC3 = mean(Vel_SC3_z);
%pos_GSE = [mean(pos_GSE_x); mean(pos_GSE_y);
mean(pos_GSE_z)];
vel = sqrt(mean_vx_SC3^2 + mean_vy_SC3^2 +
mean_vy_SC3^2);
max_dist = max(Sep_max);
min_dist = min(Sep_min);

%Changing the coordinate system between the GSE
and GSM coordinate systems.
rot_matrix = [1 0 0; 0 cos(psi) -sin(psi); 0
sin(psi) cos(psi)];

%change the magnetic field
b_C1 = [bx_C1 by_C1 bz_C1];
b_C1_GSM = zeros(length(b_C1(:,1)),3);
b_C2 = [bx_C2 by_C2 bz_C2];
b_C2_GSM = zeros(length(b_C2(:,1)),3);
b_C3 = [bx_C3 by_C3 bz_C3];
b_C3_GSM = zeros(length(b_C3(:,1)),3);
b_C4 = [bx_C4 by_C4 bz_C4];
b_C4_GSM = zeros(length(b_C4(:,1)),3);
for i=1:length(b_C1(:,1))
    b_C1_GSM(i,:) = rot_matrix*b_C1(i,:)';
end
for i=1:length(b_C2(:,1))
    b_C2_GSM(i,:) = rot_matrix*b_C2(i,:)';
end
for i=1:length(b_C3(:,1))
    b_C3_GSM(i,:) = rot_matrix*b_C3(i,:)';
end
for i=1:length(b_C4(:,1))
    b_C4_GSM(i,:) = rot_matrix*b_C4(i,:)';
end
%change the velocity
v_C4 = [vx_C4 vy_C4 vz_C4];
v_GSM_C4 = zeros(length(v_C4(:,1)),3);
for i=1:length(v_C4(:,1))
    v_GSM_C4(i,:) = rot_matrix*v_C4(i,:)';
end
%change the position
pos_GSE = [pos_GSE_x pos_GSE_y pos_GSE_z];
pos_GSM = zeros(length(pos_GSE(:,1)), 3);
for i=1:length(pos_GSE(:,1))
    pos_GSM(i,:) = rot_matrix*pos_GSE(i,:)';
end
%change the standoff distance
soff_C1 = [C1_off_x C1_off_y C1_off_z];
soff_C1_GSM = zeros(length(soff_C1(:,1)), 3);
soff_C2 = [C2_off_x C2_off_y C2_off_z];
soff_C2_GSM = zeros(length(soff_C2(:,1)), 3);
soff_C4 = [C4_off_x C4_off_y C4_off_z];
soff_C4_GSM = zeros(length(soff_C4(:,1)), 3);
for i=1:length(soff_C1(:,1))
    soff_C1_GSM(i,:) = rot_matrix*soff_C1(i,:)';
end
for i=1:length(soff_C2(:,1))
    soff_C2_GSM(i,:) = rot_matrix*soff_C2(i,:)';
end
for i=1:length(soff_C4(:,1))
    soff_C4_GSM(i,:) = rot_matrix*soff_C4(i,:)';
end

% fid_C1_B=fopen('GSM_data_SC1_B.txt','w');
% fid_C2_B=fopen('GSM_data_SC2_B.txt','w');
```

```
% fid_C3_B=fopen('GSM_data_SC3_B.txt','w');
% fid_C4_B=fopen('GSM_data_SC4_B.txt','w');
% fid_C4_V=fopen('GSM_data_SC4_V.txt','w');

fid_C1_B=fopen('GSM_data_SC1_B_full.txt','w');
fid_C2_B=fopen('GSM_data_SC2_B_full.txt','w');
fid_C3_B=fopen('GSM_data_SC3_B_full.txt','w');
fid_C4_B=fopen('GSM_data_SC4_B_full.txt','w');

for i=1:length(b_C1_GSM(:,1))
    fprintf(fid_C1_B,[datestr(T_b_C1(i),'yyyy mm
dd HH MM SS.FFF') ' %12.8f %12.8f %12.8f \n'],
b_C1_GSM(i,1), b_C1_GSM(i,2), b_C1_GSM(i,3));
end
for i=1:length(b_C2_GSM(:,1))
    fprintf(fid_C2_B,[datestr(T_b_C2(i),'yyyy mm
dd HH MM SS.FFF') ' %12.8f %12.8f %12.8f \n'],
b_C2_GSM(i,1), b_C2_GSM(i,2), b_C2_GSM(i,3));
end
for i=1:length(b_C3_GSM(:,1))
    fprintf(fid_C3_B,[datestr(T_b_C3(i),'yyyy mm
dd HH MM SS.FFF') ' %12.8f %12.8f %12.8f \n'],
b_C3_GSM(i,1), b_C3_GSM(i,2), b_C3_GSM(i,3));
end
for i=1:length(b_C4_GSM(:,1))
    fprintf(fid_C4_B,[datestr(T_b_C4(i),'yyyy mm
dd HH MM SS.FFF') ' %12.8f %12.8f %12.8f \n'],
b_C4_GSM(i,1), b_C4_GSM(i,2), b_C4_GSM(i,3));
end
for i=1:length(v_GSM_C4(:,1))
    fprintf(fid_C4_V,[datestr(T_v_C4(i),'yyyy mm
dd HH MM SS') ' %12.8f %12.8f %12.8f \n'],
v_GSM_C4(i,1), v_GSM_C4(i,2), v_GSM_C4(i,3));
end


fclose(fid_C1_B);
fclose(fid_C2_B);
fclose(fid_C3_B);
fclose(fid_C4_B);
fclose(fid_C4_V);
```

MVA.m

The program MVA.m calculates the covariance matrix of the magnetic field measurements, the eigenvalues and the eigenvectors in order to use the variance analysis elaborated in chapter 4.1. The program returns two matrices, V and E,

$$V = \begin{pmatrix} \lambda_1 & 0 & 0 \\ 0 & \lambda_2 & 0 \\ 0 & 0 & \lambda_3 \end{pmatrix}, E = \begin{pmatrix} x_1 & x_2 & x_3 \\ y_1 & y_2 & y_3 \\ z_1 & z_3 & z_3 \end{pmatrix} \quad (2.2)$$

where the E-matrix is the eigenvalue matrix where the diagonal contains the three eigenvalues. The V-matrix is the eigenvector matrix where each column is an eigenvector. The function *cov* used in the Matlab calculations of the covariance matrix, removes the sample mean of the data before calculating the variance matrix. The program calculates the covariance matrix and the eigenvectors and eigenvalues for each satellite from Cluster.

```
%% MVA.m

clc;
clear;

%Date
Year = 2005;
Month = 09;
Day = 26;

%Saving file for the MVA vectors
fid_C1=fopen('MVA_vectors_SC1.txt','w');
fid_C2=fopen('MVA_vectors_SC2.txt','w');
fid_C3=fopen('MVA_vectors_SC3.txt','w');
fid_C4=fopen('MVA_vectors_SC4.txt','w');

%Defines the choosen time interval for preforming
the MVA analysis
time_start_C1 = datenum(Year, Month, Day, 9, 30,
00);
time_end_C1 = datenum(Year, Month, Day, 10, 00,
00);
time_start_C2 = datenum(Year, Month, Day, 9, 30,
00);
time_end_C2 = datenum(Year, Month, Day, 10, 00,
00);
time_start_C3 = datenum(Year, Month, Day, 9, 30,
00);
time_end_C3 = datenum(Year, Month, Day, 10, 00,
00);
time_start_C4 = datenum(Year, Month, Day, 9, 30,
00);
time_end_C4 = datenum(Year, Month, Day,  10, 00,
00);

%Read from file
C1 = 'sep_C1_C3.txt';
C2 = 'sep_C2_C3.txt';
C4 = 'sep_C4_C3.txt';

MF_C1 = 'GSM_data_SC1_B_full.txt';
MF_C2 = 'GSM_data_SC2_B_full.txt';
MF_C3 = 'GSM_data_SC3_B_full.txt';
MF_C4 = 'GSM_data_SC4_B_full.txt';

%loading data
A = load(C1);
B = load(C2);
C = load(C4);
D = load (MF_C1);
E = load (MF_C2);
F = load (MF_C3);
G = load (MF_C4);

%defining the parameters
x_C1 = A(:,5);
y_C1 = A(:,6);
z_C1 = A(:,7);
x_C2 = B(:,5);
y_C2 = B(:,6);
z_C2 = B(:,7);
x_C4 = C(:,5);
y_C4 = C(:,6);
z_C4 = C(:,7);

%magnetic field
bx_C1 = D(:,7);
by_C1 = D(:,8);
```

```
bz_C1 = D(:,9);

bx_C2 = E(:,7);
by_C2 = E(:,8);
bz_C2 = E(:,9);

bx_C3 = F(:,7);
by_C3 = F(:,8);
bz_C3 = F(:,9);

bx_C4 = G(:,7);
by_C4 = G(:,8);
bz_C4 = G(:,9);

%Reading time from datafile
b_C1_time = D(:,4); b_C1_min = D(:,5); b_C1_sek =
D(:,6);
b_C2_time = E(:,4); b_C2_min = E(:,5); b_C2_sek =
E(:,6);
b_C3_time = F(:,4); b_C3_min = F(:,5); b_C3_sek =
F(:,6);
b_C4_time = G(:,4); b_C4_min = G(:,5); b_C4_sek =
G(:,6);

T_b_C1 = datenum(Year, Month, Day, b_C1_time,
b_C1_min, b_C1_sek);
T_b_C2 = datenum(Year, Month, Day, b_C2_time,
b_C2_min, b_C2_sek);
T_b_C3 = datenum(Year, Month, Day, b_C3_time,
b_C3_min, b_C3_sek);
T_b_C4 = datenum(Year, Month, Day, b_C4_time,
b_C4_min, b_C4_sek);

%limiting the time interval
index_time_interval_a = find(T_b_C1 >=
time_start_C1 & T_b_C1 <= time_end_C1);
T_b_C1 = T_b_C1(index_time_interval_a);
bx_C1 = bx_C1(index_time_interval_a);
by_C1 = by_C1(index_time_interval_a);
bz_C1 = bz_C1(index_time_interval_a);
b_C1 = [bx_C1 by_C1 bz_C1];
index_time_interval_b = find(T_b_C2 >=
time_start_C2 & T_b_C2 <= time_end_C2);
T_b_C2 = T_b_C2(index_time_interval_b);
bx_C2 = bx_C2(index_time_interval_b);
by_C2 = by_C2(index_time_interval_b);
bz_C2 = bz_C2(index_time_interval_b);
b_C2 = [bx_C2 by_C2 bz_C2];

index_time_interval_c = find(T_b_C3 >=
time_start_C3 & T_b_C3 <= time_end_C3);
T_b_C3 = T_b_C3(index_time_interval_c);
bx_C3 = bx_C3(index_time_interval_c);
by_C3 = by_C3(index_time_interval_c);
bz_C3 = bz_C3(index_time_interval_c);
b_C3 = [bx_C3 by_C3 bz_C3];

index_time_interval_d = find(T_b_C4 >=
time_start_C4 & T_b_C4 <= time_end_C4);
T_b_C4 = T_b_C4(index_time_interval_d);
bx_C4 = bx_C4(index_time_interval_d);
by_C4 = by_C4(index_time_interval_d);
bz_C4 = bz_C4(index_time_interval_d);
b_C4 = [bx_C4 by_C4 bz_C4];


%calculating the variance matrix, the eigenvalue
matrix E and the
%eigenvector matrix V for SC1
M_C1 = cov(b_C1);
[V_C1,E_C1] = eig(M_C1) %returns a matrix V whose
columns are eigenvectors and a diagonal matrix E
containing eigenvalues
x = 'V is the matrix containing the eigen vectors
and E is the corresponding eigenvalues for SC2';
variance_C1 = trace(M_C1)

%Selects the eigenvalues and the corresponding
eigen vectors in order to
%change he coordiante system
%Finds the largest eigenvalue and the location of
it for each covariance
%matrix
SizeData_C1 = size(E_C1);
Vec_C1 = reshape(E_C1, [prod(SizeData_C1), 1]);
[Max_C1, MaxInd_C1] = max(Vec_C1)

%calculating the variance matrix, the eigenvalue
matrix E and the
%eigenvector matrix V for SC2
M_C2 = cov(b_C2);
variance_C2 = trace(M_C2)
%find the eigenvalues and the corresponding ei-
genvectors for SC2
[V_C2,E_C2] = eig(M_C2) %returns a matrix V whose
columns are eigenvectors and a diagonal matrix E
containing eigenvalues
y = 'V is the matrix containing the eigen vectors
and E is the corresponding eigenvalues for SC2';

%Selects the eigenvalues and the corresponding
eigen vectors in order %to
%change he coordiante system
%Finds the largest eigenvalue and the location of
it for each M
SizeData_C2 = size(E_C2);
Vec_C2 = reshape(E_C2, [prod(SizeData_C2), 1]);
[Max_C2, MaxInd_C2] = max(Vec_C2)

%calculating the variance matrix, the eigenvalue
matrix E and the
%eigenvector matrix V for SC3
M_C3 = cov(b_C3);
variance_C3 = trace(M_C3)
%find the eigenvalues and the corresponding ei-
genvectors for SC3
[V_C3,E_C3] = eig(M_C3) %returns a matrix V whose
columns are eigenvectors and a diagonal matrix E
containing eigenvalues
z = 'V is the matrix containing the eigen vectors
and E is the corresponding eigenvalues for SC3';

%Selects the eigenvalues and the corresponding
eigen vectors in order to
%change he coordiante system
%Finds the largest eigenvalue and the location of
it for each M
SizeData_C3 = size(E_C3);
Vec_C3 = reshape(E_C3, [prod(SizeData_C3), 1]);
[Max_C3, MaxInd_C3] = max(Vec_C3)

%calculating the variance matrix, the eigenvalue
matrix E and the
%eigenvector matrix V for SC4
M_C4 = cov(b_C4);
variance_C4 = trace(M_C4)
%find the eigenvalues and the corresponding ei-
genvectors for SC4
[V_C4,E_C4] = eig(M_C4) %returns a matrix V whose
columns are eigenvectors and a diagonal matrix E
containing eigenvalues
w = 'V is the matrix containing the eigen vectors
and E is the corresponding eigenvalues for SC4';
%Selects the eigenvalues and the corresponding
eigen vectors in order to
%change he coordiante system
%Finds the largest eigenvalue and the location of
it for each M
SizeData_C4 = size(E_C4);
Vec_C4 = reshape(E_C4, [prod(SizeData_C4), 1]);
[Max_C4, MaxInd_C4] = max(Vec_C4)


% Save to file:
fprintf(fid_C1,'Eigenvalues: %12.8f %12.8f %12.8f
\n',E_C1(1,1),E_C1(2,2),E_C1(3,3));
fprintf(fid_C1,'Eigenvector 1: \n %12.8f %12.8f
%12.8f% \n',V_C1(1,1),V_C1(2,1),V_C1(3,1));
fprintf(fid_C1,'Eigenvector 2: \n %12.8f %12.8f
%12.8f% \n',V_C1(1,2),V_C1(2,2),V_C1(3,2));
fprintf(fid_C1,'Eigenvector 3: \n %12.8f %12.8f
%12.8f% \n',V_C1(1,3),V_C1(2,3),V_C1(3,3));

fprintf(fid_C2,'Eigenvalues: %12.8f %12.8f %12.8f
\n',E_C2(1,1),E_C2(2,2),E_C2(3,3));
fprintf(fid_C2,'Eigenvector 1: \n %12.8f %12.8f
%12.8f% \n',V_C2(1,1),V_C2(2,1),V_C2(3,1));
fprintf(fid_C2,'Eigenvector 2: \n %12.8f %12.8f
%12.8f% \n',V_C2(1,2),V_C2(2,2),V_C2(3,2));
fprintf(fid_C2,'Eigenvector 3: \n %12.8f %12.8f
%12.8f% \n',V_C2(1,3),V_C2(2,3),V_C2(3,3));

fprintf(fid_C3,'Eigenvalues: %12.8f %12.8f %12.8f
\n',E_C3(1,1),E_C3(2,2),E_C3(3,3));
```

```
fprintf(fid_C3,'Eigenvector 1: \n %12.8f %12.8f
%12.8f% \n',V_C3(1,1),V_C3(2,1),V_C3(3,1));
fprintf(fid_C3,'Eigenvector 2: \n %12.8f %12.8f
%12.8f% \n',V_C3(1,2),V_C3(2,2),V_C3(3,2));
fprintf(fid_C3,'Eigenvector 3: \n %12.8f %12.8f
%12.8f% \n',V_C3(1,3),V_C3(2,3),V_C3(3,3));

fprintf(fid_C4,'Eigenvalues: %12.8f %12.8f %12.8f
\n',E_C4(1,1),E_C4(2,2),E_C4(3,3));
fprintf(fid_C4,'Eigenvector 1: \n %12.8f %12.8f
%12.8f% \n',V_C4(1,1),V_C4(2,1),V_C4(3,1));
fprintf(fid_C4,'Eigenvector 2: \n %12.8f %12.8f
%12.8f% \n',V_C4(1,2),V_C4(2,2),V_C4(3,2));
fprintf(fid_C4,'Eigenvector 3: \n %12.8f %12.8f
%12.8f% \n',V_C4(1,3),V_C4(2,3),V_C4(3,3));

fclose(fid_C4);
fclose(fid_C1);
fclose(fid_C2);
fclose(fid_C3);
```

Hall_field_all.m

The program Hall_field_all.m plots the Hall- magnetic field during the high speed outflow intervals observed by Cluster. The program the consists of two parts, one which first loades the data, then transforms the data into a modified coordinate system based on the MVA analysis and finally calculates the angle between the modified coordinate system and the GSM coordinate system. The other part plots the Hall magnetic field.

```
%% Loading the data for creating the Hall_plots

clc;
clear;

Year = 2005;
Month = 09;
Day = 26;

%defines the timeintervals when teh high speed
outflows are observed by
%Cluster
time_start_0 = datenum(Year, Month, Day, 9, 35,
30);
time_end_0 = datenum(Year, Month, Day, 9, 36,
25);

time_start_1 = datenum(Year, Month, Day, 9, 38,
45);
time_end_1 = datenum(Year, Month, Day, 9, 40,
30);

time_start_2 = datenum(Year, Month, Day, 9, 40,
30);
time_end_2 = datenum(Year, Month, Day, 9, 43,
00);

time_start_3 = datenum(Year, Month, Day, 9, 50,
00);
time_end_3 = datenum(Year, Month, Day, 09, 51,
35);

time_start_4 = datenum(Year, Month, Day, 09, 52,
40);
time_end_4 = datenum(Year, Month, Day, 09, 56,
10);

% MF_C1 = 'C1_CP_FGM_full.txt';
% MF_C2 = 'C2_CP_FGM_full.txt';
% MF_C3 = 'C3_CP_FGM_full.txt';
% MF_C4 = 'C4_CP_FGM_full.txt';

%the eigen vector from the MVA analysis in the
2005 event
e_C1 = -[-0.98751694   0.15745669   0.00420526];
e_C2 = -[-0.97820140   0.20334257  -0.04211672];
e_C3 = [0.98326128  -0.18216190   0.00378152];
e_C4 = -[-0.98460863   0.17462467   0.00721601];

%loading the data
MF_C1 = 'GSM_data_SC1_B.txt';
MF_C2 = 'GSM_data_SC2_B.txt';
MF_C3 = 'GSM_data_SC3_B.txt';
MF_C4 = 'GSM_data_SC4_B.txt';

E = load(MF_C1);
F = load(MF_C2);
G = load(MF_C3);
H = load(MF_C4);

bx_gsm_C1 = E(:,7);
by_gsm_C1 = E(:,8);
bz_gsm_C1 = E(:,9);

bx_gsm_C2 = F(:,7);
by_gsm_C2 = F(:,8);
bz_gsm_C2 = F(:,9);

bx_gsm_C3 = G(:,7);
by_gsm_C3 = G(:,8);
bz_gsm_C3 = G(:,9);

bx_gsm_C4 = H(:,7);
by_gsm_C4 = H(:,8);
bz_gsm_C4 = H(:,9);

b_time_C1 = E(:,4); b_min_C1 = E(:,5); b_sek_C1 =
E(:,6);
b_time_C2 = F(:,4); b_min_C2 = F(:,5); b_sek_C2 =
F(:,6);
b_time_C3 = G(:,4); b_min_C3 = G(:,5); b_sek_C3 =
G(:,6);
b_time_C4 = H(:,4); b_min_C4 = H(:,5); b_sek_C4 =
H(:,6);

T_b_C1 = datenum(Year, Month, Day, b_time_C1,
b_min_C1, b_sek_C1);
T_b_C2 = datenum(Year, Month, Day, b_time_C2,
b_min_C2, b_sek_C2);
T_b_C3 = datenum(Year, Month, Day, b_time_C3,
b_min_C3, b_sek_C3);
T_b_C4 = datenum(Year, Month, Day, b_time_C4,
b_min_C4, b_sek_C4);

b_C1 = [bx_gsm_C1 by_gsm_C1 bz_gsm_C1];
b_C2 = [bx_gsm_C2 by_gsm_C2 bz_gsm_C2];
b_C3 = [bx_gsm_C3 by_gsm_C3 bz_gsm_C3];
b_C4 = [bx_gsm_C4 by_gsm_C4 bz_gsm_C4];

%Calculating the change i the vectorfields
%details regaring the method are elaborated in
chapter 4.1 in the main
%document
ex_gsm = [1 0 0];
ey_gsm = [0 1 0];
ez_gsm = [0 0 1];

%the new eigenvectors
ex_new_C1 = e_C1;
ey_new_C1 = cross(ez_gsm,ex_new_C1);
ez_new_C1 = ez_gsm;

%the new eigenvectors for C2
ex_new_C2 = e_C2;
ey_new_C2 = cross(ez_gsm, ex_new_C2);
ez_new_C2 = ez_gsm
```

```
%the new eigenvectors for C3
ex_new_C3 = e_C3;
ey_new_C3 = cross(ez_gsm, ex_new_C3);
ez_new_C3 = ez_gsm

%the new eigenvectors for C4
ex_new_C4 = e_C4;
ey_new_C4 = cross(ez_gsm, ex_new_C4);
ez_new_C4 = ez_gsm

%changing the B-vector into the new coordinate
system form SC1
for i=1:length(b_C1(:,1))
    b_koord_C1(i,1) = dot([b_C1(i,1) b_C1(i,2)
b_C1(i,3)],ex_new_C1);
    b_koord_C1(i,2) = dot([b_C1(i,1) b_C1(i,2)
b_C1(i,3)],ey_new_C1);
    b_koord_C1(i,3) = dot([b_C1(i,1) b_C1(i,2)
b_C1(i,3)],ez_new_C1);
end
 bx_new_C1 = b_koord_C1(:,1);
 by_new_C1 = b_koord_C1(:,2);
 bz_new_C1 = b_koord_C1(:,3);

 %changing the B-vector into the new coordinate
system for SC2
for i=1:length(b_C2(:,1))
    b_koord_C2(i,1) = dot([b_C2(i,1) b_C2(i,2)
b_C2(i,3)],ex_new_C2);
    b_koord_C2(i,2) = dot([b_C2(i,1) b_C2(i,2)
b_C2(i,3)],ey_new_C2);
    b_koord_C2(i,3) = dot([b_C2(i,1) b_C2(i,2)
b_C2(i,3)],ez_new_C2);
end
 bx_new_C2 = b_koord_C2(:,1);
 by_new_C2 = b_koord_C2(:,2);
 bz_new_C2 = b_koord_C2(:,3);

 %changing the b-vector into the new coordinate
system for SC4
for i=1:length(b_C3(:,1))
    b_koord_C3(i,1) = dot([b_C3(i,1) b_C3(i,2)
b_C3(i,3)],ex_new_C3);
    b_koord_C3(i,2) = dot([b_C3(i,1) b_C3(i,2)
b_C3(i,3)],ey_new_C3);
    b_koord_C3(i,3) = dot([b_C3(i,1) b_C3(i,2)
b_C3(i,3)],ez_new_C3);
end
 bx_new_C3 = b_koord_C3(:,1);
 by_new_C3 = b_koord_C3(:,2);
 bz_new_C3 = b_koord_C3(:,3);

 %changing the b-vector into the new coordinate
system for SC5
for i=1:length(b_C4(:,1))
    b_koord_C4(i,1) = dot([b_C4(i,1) b_C4(i,2)
b_C4(i,3)],ex_new_C4);
    b_koord_C4(i,2) = dot([b_C4(i,1) b_C4(i,2)
b_C4(i,3)],ey_new_C4);
    b_koord_C4(i,3) = dot([b_C4(i,1) b_C4(i,2)
b_C4(i,3)],ez_new_C4);
end
 bx_new_C4 = b_koord_C4(:,1);
 by_new_C4 = b_koord_C4(:,2);
 bz_new_C4 = b_koord_C4(:,3);
%%
%The differences

%plotting the differences between the By compo-
nents before and after changing into the
%modified coordinate system
figure(1)
subplot(4,1,1), plot(T_b_C1, by_gsm_C1, 'k',
'LineWidth', 2)
hold on;
plot(T_b_C1, by_new_C1, 'r', 'LineWidth', 2)
ylabel('B_y, nT', 'FontSize', 16);
ylim([-15, 15]);
xlim([T_b_C1(1) T_b_C1(length(T_b_C1))]);
hold off;
subplot(4,1,2), plot(T_b_C2, by_gsm_C2, 'k',
'LineWidth', 2)
ylabel('B_y, nT', 'FontSize', 16)
ylim([-25, 25]);
hold on;
plot(T_b_C2, by_new_C2, 'r', 'LineWidth', 2)
xlim([T_b_C2(1) T_b_C2(length(T_b_C2))]);
hold off;
subplot(4,1,3), plot(T_b_C3, by_gsm_C3, 'k',
'LineWidth', 2)
ylabel('B_y, nT', 'FontSize', 16);
ylim([-25, 25]);
hold on;
plot(T_b_C3, by_new_C3, 'r', 'LineWidth', 2)
xlim([T_b_C3(1) T_b_C3(length(T_b_C3))]);
hold off;
subplot(4,1,4), plot(T_b_C4, by_gsm_C4, 'k',
'LineWidth', 2)
ylabel('B_y, nT', 'FontSize', 16)
ylim([-25, 25]);
hold on;
plot(T_b_C4, by_new_C4, 'r', 'LineWidth', 2)
xlim([T_b_C4(1) T_b_C4(length(T_b_C4))]);
xlabel('Time, UT')
datetick('x', 13)

%Calculated the difference between the modified
By and the GSM by
%measurements
difference_C1 = zeros([length(by_gsm_C1),1]);

for i=1:length(bx_gsm_C1)
    difference_C1(i) = abs(by_gsm_C1(i) -
by_new_C1(i));
end


difference_C2 = zeros([length(by_gsm_C2),1]);

for i=1:length(by_gsm_C2)
    difference_C2(i) = abs(by_gsm_C2(i)-
by_new_C2(i));
end

difference_C3 = zeros([length(by_gsm_C3),1]);

for i=1:length(by_gsm_C3)
    difference_C3(i) = abs(by_gsm_C3(i) -
by_new_C3(i));
end

difference_C4 = zeros([length(by_gsm_C4),1]);

for i=1:length(by_gsm_C4)
    difference_C4(i) = abs(by_gsm_C4(i) -
by_new_C4(i));
end

%%
%Hall field time limitation
%choosing the data in the right timeinterval when
the high speed outflows
%are observed
zero_index_time_interval_b_C1 = find(T_b_C1 >=
time_start_0 & T_b_C1 <= time_end_0);
zero_index_time_interval_b_C2 = find(T_b_C2 >=
time_start_0 & T_b_C2 <= time_end_0);
zero_index_time_interval_b_C3 = find(T_b_C3 >=
time_start_0 & T_b_C3 <= time_end_0);
zero_index_time_interval_b_C4 = find(T_b_C4 >=
time_start_0 & T_b_C4 <= time_end_0);
bx_zero_C1 =
bx_new_C1(zero_index_time_interval_b_C1);by_zero_
C1 =
by_new_C1(zero_index_time_interval_b_C1);bz_zero_
C1 = bz_new_C1(zero_index_time_interval_b_C1);
bx_zero_C2 =
bx_new_C2(zero_index_time_interval_b_C2);by_zero_
C2 =
by_new_C2(zero_index_time_interval_b_C2);bz_zero_
C2 = bz_new_C2(zero_index_time_interval_b_C2);
bx_zero_C3 =
bx_new_C3(zero_index_time_interval_b_C3);by_zero_
C3 =
by_new_C3(zero_index_time_interval_b_C3);bz_zero_
C3 = bz_new_C3(zero_index_time_interval_b_C3);
bx_zero_C4 =
bx_new_C4(zero_index_time_interval_b_C4);by_zero_
C4 =
by_new_C4(zero_index_time_interval_b_C4);bz_zero_
C4 = bz_new_C4(zero_index_time_interval_b_C4);
```

```
first_index_time_interval_b_C1 = find(T_b_C1 >=
time_start_1 & T_b_C1 <= time_end_1);
first_index_time_interval_b_C2 = find(T_b_C2 >=
time_start_1 & T_b_C2 <= time_end_1);
first_index_time_interval_b_C3 = find(T_b_C3 >=
time_start_1 & T_b_C3 <= time_end_1);
first_index_time_interval_b_C4 = find(T_b_C4 >=
time_start_1 & T_b_C4 <= time_end_1);
bx_first_C1 =
bx_new_C1(first_index_time_interval_b_C1);by_firs
t_C1 =
by_new_C1(first_index_time_interval_b_C1);bz_firs
t_C1 = bz_new_C1(first_index_time_interval_b_C1);
bx_first_C2 =
bx_new_C2(first_index_time_interval_b_C2);by_firs
t_C2 =
by_new_C2(first_index_time_interval_b_C2);bz_firs
t_C2 = bz_new_C2(first_index_time_interval_b_C2);
bx_first_C3 =
bx_new_C3(first_index_time_interval_b_C3);by_firs
t_C3 =
by_new_C3(first_index_time_interval_b_C3);bz_firs
t_C3 = bz_new_C3(first_index_time_interval_b_C3);
bx_first_C4 =
bx_new_C4(first_index_time_interval_b_C4);by_firs
t_C4 =
by_new_C4(first_index_time_interval_b_C4);bz_firs
t_C4 = bz_new_C4(first_index_time_interval_b_C4);

second_index_time_interval_b_C1 = find(T_b_C1 >=
time_start_2 & T_b_C1 <= time_end_2);
second_index_time_interval_b_C2 = find(T_b_C2 >=
time_start_2 & T_b_C2 <= time_end_2);
second_index_time_interval_b_C3 = find(T_b_C3 >=
time_start_2 & T_b_C3 <= time_end_2);
second_index_time_interval_b_C4 = find(T_b_C4 >=
time_start_2 & T_b_C4 <= time_end_2);
bx_second_C1 =
bx_new_C1(second_index_time_interval_b_C1);by_sec
ond_C1 =
by_new_C1(second_index_time_interval_b_C1);bz_sec
ond_C1 =
bz_new_C1(second_index_time_interval_b_C1);
bx_second_C2 =
bx_new_C2(second_index_time_interval_b_C2);by_sec
ond_C2 =
by_new_C2(second_index_time_interval_b_C2);bz_sec
ond_C2 =
bz_new_C2(second_index_time_interval_b_C2);
bx_second_C3 =
bx_new_C3(second_index_time_interval_b_C3);by_sec
ond_C3 =
by_new_C3(second_index_time_interval_b_C3);bz_sec
ond_C3 =
bz_new_C3(second_index_time_interval_b_C3);
bx_second_C4 =
bx_new_C4(second_index_time_interval_b_C4);by_sec
ond_C4 =
by_new_C4(second_index_time_interval_b_C4);bz_sec
ond_C4 =
bz_new_C4(second_index_time_interval_b_C4);

third_index_time_interval_b_C1 = find(T_b_C1 >=
time_start_3 & T_b_C1 <= time_end_3);
third_index_time_interval_b_C2 = find(T_b_C2 >=
time_start_3 & T_b_C2 <= time_end_3);
third_index_time_interval_b_C3 = find(T_b_C3 >=
time_start_3 & T_b_C3 <= time_end_3);
third_index_time_interval_b_C4 = find(T_b_C4 >=
time_start_3 & T_b_C4 <= time_end_3);
bx_third_C1 =
bx_new_C1(third_index_time_interval_b_C1);by_thir
d_C1 =
by_new_C1(third_index_time_interval_b_C1);bz_thir
d_C1 = bz_new_C1(third_index_time_interval_b_C1);
bx_third_C2 =
bx_new_C2(third_index_time_interval_b_C2);by_thir
d_C2 =
by_new_C2(third_index_time_interval_b_C2);bz_thir
d_C2 = bz_new_C2(third_index_time_interval_b_C2);
bx_third_C3 =
bx_new_C3(third_index_time_interval_b_C3);by_thir
d_C3 =
by_new_C3(third_index_time_interval_b_C3);bz_thir
d_C3 = bz_new_C3(third_index_time_interval_b_C3);
bx_third_C4 =
bx_new_C4(third_index_time_interval_b_C4);by_thir
d_C4 =
by_new_C4(third_index_time_interval_b_C4);bz_thir
d_C4 = bz_new_C4(third_index_time_interval_b_C4);

fourth_index_time_interval_b_C1 = find(T_b_C1 >=
time_start_4 & T_b_C1 <= time_end_4);
fourth_index_time_interval_b_C2 = find(T_b_C2 >=
time_start_4 & T_b_C2 <= time_end_4);
fourth_index_time_interval_b_C3 = find(T_b_C3 >=
time_start_4 & T_b_C3 <= time_end_4);
fourth_index_time_interval_b_C4 = find(T_b_C4 >=
time_start_4 & T_b_C4 <= time_end_4);
bx_fourth_C1 =
bx_new_C1(fourth_index_time_interval_b_C1);by_fou
rth_C1 =
by_new_C1(fourth_index_time_interval_b_C1);bz_fou
rth_C1 =
bz_new_C1(fourth_index_time_interval_b_C1);
bx_fourth_C2 =
bx_new_C2(fourth_index_time_interval_b_C2);by_fou
rth_C2 =
by_new_C2(fourth_index_time_interval_b_C2);bz_fou
rth_C2 =
bz_new_C2(fourth_index_time_interval_b_C2);
bx_fourth_C3 =
bx_new_C3(fourth_index_time_interval_b_C3);by_fou
rth_C3 =
by_new_C3(fourth_index_time_interval_b_C3);bz_fou
rth_C3 =
bz_new_C3(fourth_index_time_interval_b_C3);
bx_fourth_C4 =
bx_new_C4(fourth_index_time_interval_b_C4);by_fou
rth_C4 =
by_new_C4(fourth_index_time_interval_b_C4);bz_fou
rth_C4 =
bz_new_C4(fourth_index_time_interval_b_C4);

%the new coordinate system SC1
ex_new_C1_ang = ex_new_C1;
ey_new_C1_ang = ey_new_C1;
ez_new_C1_ang = ez_new_C1;

%the angle between the two x-vectors from GSM
coordinates and the modified
%x-axis for SC1
angle_C1_x = rad2deg((acos(dot(ex_gsm,
ex_new_C1_ang))));
angle_C1_y = rad2deg((acos(dot(ey_gsm,
ey_new_C1_ang))));
angle_C1_z = rad2deg((acos(dot(ez_gsm,
ez_new_C1_ang))));

if angle_C1_x > 90
    angle_C1_new_x = 180 - angle_C1_x;
else
    angle_C1_new_x = angle_C1_x;
end
if angle_C1_y > 90
    angle_C1_new_y = 180 - angle_C1_y;
else
    angle_C1_new_y = angle_C1_y;
end
if angle_C1_z > 90
    angle_C1_new_z = 180 - angle_C1_z;
else
    angle_C1_new_z = angle_C1_z;
end
angle_C1 = [angle_C1_new_x angle_C1_new_y an-
gle_C1_new_z]

%the new coordinate system SC2
ex_new_C2_ang = ex_new_C2;
ey_new_C2_ang = ey_new_C2;
ez_new_C2_ang = ez_new_C2;


%the angle between the two x-vectors from GSM
coordinates and the modified
%x-axis for SC2
angle_C2_x = rad2deg((acos(dot(ex_gsm,
ex_new_C2_ang))));
angle_C2_y = rad2deg((acos(dot(ey_gsm,
ey_new_C2_ang))));
angle_C2_z = rad2deg((acos(dot(ez_gsm,
ez_new_C2_ang))));

if angle_C2_x > 90
```

```
    angle_C2_new_x = 180 - angle_C2_x;
else
    angle_C2_new_x = angle_C2_x;
end
if angle_C2_y > 90
    angle_C2_new_y = 180 - angle_C2_y;
else
    angle_C2_new_y = angle_C2_y;
end
if angle_C2_z > 90
    angle_C2_new_z = 180 - angle_C2_z;
else
    angle_C2_new_z = angle_C2_z;
end
angle_C2 = [angle_C2_new_x angle_C2_new_y an-
gle_C2_new_z]


%the new coordinate system SC3
ex_new_C3_ang = ex_new_C3;
ey_new_C3_ang = ey_new_C3;
ez_new_C3_ang = ez_new_C3;


%the angle between the two x-vectors from GSM
coordinates and the modified
%x-axis for SC3
angle_C3_x = rad2deg((acos(dot(ex_gsm,
ex_new_C3_ang))));
angle_C3_y = rad2deg((acos(dot(ey_gsm,
ey_new_C3_ang))));
angle_C3_z = rad2deg((acos(dot(ez_gsm,
ez_new_C3_ang))));

if angle_C3_x > 90
    angle_C3_new_x = 180 - angle_C3_x;
else
    angle_C3_new_x = angle_C3_x;
end
if angle_C3_y > 90
    angle_C3_new_y = 180 - angle_C3_y;
else
    angle_C3_new_y = angle_C3_y;
end
if angle_C3_z > 90
    angle_C3_new_z = 180 - angle_C3_z;
else
    angle_C3_new_z = angle_C3_z;
end
angle_C3 = [angle_C3_new_x angle_C3_new_y an-
gle_C3_new_z]

%the new coordinate system SC4
ex_new_C4_ang = ex_new_C4;
ey_new_C4_ang = ey_new_C4;
ez_new_C4_ang = ez_new_C4;


%the angle between the two x-vectors from GSM
coordinates and the modified
%x-axis for SC4
angle_C4_x = rad2deg((acos(dot(ex_gsm,
ex_new_C4_ang))));
angle_C4_y = rad2deg((acos(dot(ey_gsm,
ey_new_C4_ang))));
angle_C4_z = rad2deg((acos(dot(ez_gsm,
ez_new_C4_ang))));

if angle_C4_x > 90
    angle_C4_new_x = 180 - angle_C4_x;
else
    angle_C4_new_x = angle_C4_x;
end
if angle_C4_y > 90
    angle_C4_new_y = 180 - angle_C4_y;
else
    angle_C4_new_y = angle_C4_y;
end
if angle_C4_z > 90
    angle_C4_new_z = 180 - angle_C4_z;
else
    angle_C4_new_z = angle_C4_z;
end
angle_C4 = [angle_C4_new_x angle_C4_new_y an-
gle_C4_new_z]
```

```
%% PLotting the Hall magnetic field for all
spacecrafts
figure(1)
scatter(bx_zero_C1, by_zero_C1, 'k', 'filled')
scatter(bx_zero_C2, by_zero_C2, 'r', 'filled')
hold on;
scatter(bx_zero_C3, by_zero_C3, 'g', 'filled')
scatter(bx_zero_C4, by_zero_C4, 'b', 'filled')
ylim([-30 30])
xlim([-50 50])
plot([-50 50],[0 0],'LineStyle', '-.');
plot([0 0],[-30 30],'LineStyle', '-.');
xlabel('Bx, nT', 'FontSize', 24);
ylabel('By, nT', 'FontSize', 24);
title('Time period 09:35:30 - 09:36:25 UT',
'FontSize', 24);

figure(2)
scatter(bx_first_C1, by_first_C1, 'k', 'filled')
hold on;
scatter(bx_first_C2, by_first_C2, 'r', 'filled')
scatter(bx_first_C3, by_first_C3, 'g', 'filled')
scatter(bx_first_C4, by_first_C4, 'b', 'filled')
ylim([-30 30])
xlim([-50 50])
hold on;
plot([-50 50],[0 0],'LineStyle', '-.');
plot([0 0],[-30 30],'LineStyle', '-.');
xlabel('Bx, nT', 'FontSize', 24);
ylabel('By, nT', 'FontSize', 24);
title('Time period 09:38:45 - 09:40:30 UT',
'FontSize', 24);

figure(3)
scatter(bx_second_C1, by_second_C1, 'k',
'filled')
title('MVA');
hold on;
scatter(bx_second_C2, by_second_C2, 'r',
'filled')
scatter(bx_second_C3, by_second_C3, 'g',
'filled')
scatter(bx_second_C4, by_second_C4, 'b',
'filled')
ylim([-30 30])
xlim([-50 50])
plot([-50 50],[0 0],'LineStyle', '-.');
plot([0 0],[-30 30],'LineStyle', '-.');
xlabel('Bx, nT', 'FontSize', 24);
ylabel('By, nT', 'FontSize', 24);
title('Time period 09.40.30 - 09.43.00 UT',
'FontSize', 24);

figure(4)
scatter(bx_third_C1, by_third_C1, 'k', 'filled')
title('MVA');
hold on;
%scatter(bx_third_C2, by_third_C2, 'r', 'filled')
scatter(bx_third_C3, by_third_C3, 'g', 'filled')
scatter(bx_third_C4, by_third_C4, 'b', 'filled')
ylim([-30 30])
xlim([-50 50])
plot([-50 50],[0 0],'LineStyle', '-.');
plot([0 0],[-30 30],'LineStyle', '-.');
xlabel('Bx, nT', 'FontSize', 24);
ylabel('By, nT', 'FontSize', 24);
title('Time period 09:50:00 - 09:51:35 UT',
'FontSize', 24);

figure(5)
scatter(bx_fourth_C1, by_fourth_C1, 'k',
'filled')
title('MVA');
hold on;
%scatter(bx_fourth_C2, by_fourth_C2, 'r',
'filled')
scatter(bx_fourth_C3, by_fourth_C3, 'g',
'filled')
scatter(bx_fourth_C4, by_fourth_C4, 'b',
'filled')
ylim([-30 30])
xlim([-50 50])
plot([-50 50],[0 0],'LineStyle', '-.');
plot([0 0],[-30 30],'LineStyle', '-.');
xlabel('Bx, nT', 'FontSize', 24);
ylabel('By, nT', 'FontSize', 24);
```

```
title('Time period 09:52:40- 09:56:10 UT', 'Font-        Size', 24);
```

Hall_bubles_C4.m

The program Hall_bubles_C4.m generates the quadrupole Hall out-of-plane magnetic field using the velocity and the magnetic field components. The program plots the field by using the GSM data and the modified dataset from variance analysis. The program provides the user with two plots in order to compare the changes between the GSM measurements and the modified measurements based on the variance analysis.

```
%% Hall bubles

%Programme which defines the MVA the vector,
plots the changes and
%plots the Hall-plot.
clc;
clear;

Year = 2005;
Month = 09;
Day = 26;


%Defines the different timeintervals for the
registered outflow
time_outflow_1_start = datenum(Year, Month, Day,
9, 35, 30);
time_outflow_1_stop = datenum(Year, Month, Day,
9, 36, 25);

time_outflow_2_start = datenum(Year, Month, Day,
9, 38, 45);
time_outflow_2_stop = datenum(Year, Month, Day,
9, 43, 00);

time_outflow_3_start = datenum(Year, Month, Day,
9, 50, 00);
time_outflow_3_stop = datenum(Year, Month, Day,
9, 51, 30);

time_outflow_4_start = datenum(Year, Month, Day,
9, 52, 40);
time_outflow_4_stop = datenum(Year, Month, Day,
9, 56, 10);

%Reading the different data types from file
MF = 'GSM_data_SC4_B.txt';
V = 'GSM_data_SC4_V.txt';
%Loading the different files into arrays
M = load (MF);V = load (V);
%Reading the different parts of the arrays con-
taining the velocity and the
%magnetic field and time
bx = M(:,7);by = M(:,8);bz = M(:,9);
vx = V(:,7);vy = V(:,8);vz = V(:,9);

% by = by-1e-9;%removing the background field

b_time = M(:,4);b_min = M(:,5);b_sek = M(:,6);
v_time = V(:,4);v_min = V(:,5);v_sek = V(:,6);
%Changes the time into serial numbers
T_b = datenum(Year, Month, Day, b_time, b_min,
b_sek);
T_v = datenum(Year, Month, Day, v_time, v_min,
v_sek);

%Creates arrays with the data in the first out-
flow region
index_time_interval_B_1 = find(T_b >=
time_outflow_1_start & T_b <=
time_outflow_1_stop);
T_b_1 = T_b(index_time_interval_B_1);bx_1 =
bx(index_time_interval_B_1);
by_1 = by(index_time_interval_B_1);bz_1 =
bz(index_time_interval_B_1);
index_time_interval_V_1 = find(T_v >=
time_outflow_1_start & T_v <=
time_outflow_1_stop);
T_v_1= T_v(index_time_interval_V_1);vx_1 =
vx(index_time_interval_V_1);
vy_1 = vy(index_time_interval_V_1);vz_1 =
vz(index_time_interval_V_1);
%Creates arrays with the data in the second out-
flow region
index_time_interval_B_2 = find(T_b >=
time_outflow_2_start & T_b <=
time_outflow_2_stop);
T_b_2 = T_b(index_time_interval_B_2);bx_2 =
bx(index_time_interval_B_2);
by_2 = by(index_time_interval_B_2);bz_2 =
bz(index_time_interval_B_2);
index_time_interval_V_2 = find(T_v >=
time_outflow_2_start & T_v <=
time_outflow_2_stop);
T_v_2= T_v(index_time_interval_V_2);vx_2 =
vx(index_time_interval_V_2);
vy_2 = vy(index_time_interval_V_2);vz_2 =
vz(index_time_interval_V_2);
%Creates arrays with the data in the third out-
flow region
index_time_interval_B_3 = find(T_b >=
time_outflow_3_start & T_b <=
time_outflow_3_stop);
T_b_3 = T_b(index_time_interval_B_3);bx_3 =
bx(index_time_interval_B_3);
by_3 = by(index_time_interval_B_3);bz_3 =
bz(index_time_interval_B_3);
index_time_interval_V_3 = find(T_v >=
time_outflow_3_start & T_v <=
time_outflow_3_stop);
T_v_3= T_v(index_time_interval_V_3);vx_3 =
vx(index_time_interval_V_3);
vy_3 = vy(index_time_interval_V_3);vz_3 =
vz(index_time_interval_V_3);
%Creates arrays with the data in the fourth out-
flow region
index_time_interval_B_4 = find(T_b >=
time_outflow_4_start & T_b <=
time_outflow_4_stop);
T_b_4 = T_b(index_time_interval_B_4);bx_4 =
bx(index_time_interval_B_4);
by_4 = by(index_time_interval_B_4);bz_4 =
bz(index_time_interval_B_4);
index_time_interval_V_4 = find(T_v >=
time_outflow_4_start & T_v <=
time_outflow_4_stop);
T_v_4= T_v(index_time_interval_V_4);vx_4 =
vx(index_time_interval_V_4);
vy_4 = vy(index_time_interval_V_4);vz_4 =
vz(index_time_interval_V_4);


%Defines the reduction matrix
index_red = zeros(length(T_v_1));
%Checks the data series for the closest times in
the shortest array and
%picks the entries in the long array. This is
done in order to get the
%arrays to have the same length
for i=1:length(T_v_1)
    subtracted = abs(T_b_1 - T_v_1(i));
    sorted = sort(subtracted);
    min_value = sorted(1);
    index = find(subtracted == min_value);
    index_red(i) = index(1);
end;
```

```
%Fjerner overflødige entries i matrisen
index_red_1 = index_red(find(index_red ~= 0));
%Reduserer B-feltmatrisene slik at b-felt data og
v data er av samme mengde
t_red_1 = T_b_1(index_red_1);
bx_red_1 = bx_1(index_red_1);
by_red_1 = by_1(index_red_1);
bz_red_1 = bz_1(index_red_1);
b_red_1 = [bx_red_1 by_red_1 bz_red_1];
v_1 = [vx_1 vy_1 vz_1];

index_red = zeros(length(T_v_2));
%Checks the data series for the closest times in
the shortest array and
%picks the entries in the long array. This is
done in order to get the
%arrays to have the same length
for i=1:length(T_v_2)
    subtracted = abs(T_b_2 - T_v_2(i));
    sorted = sort(subtracted);
    min_value = sorted(1);
    index = find(subtracted == min_value);
    index_red(i) = index(1);
end;
%Fjerner overflødige entries i matrisen
index_red_2 = index_red(find(index_red ~= 0));
%Reduserer B-feltmatrisene slik at b-felt data og
v data er av samme mengde
t_red_2 = T_b_2(index_red_2);
bx_red_2 = bx_2(index_red_2);
by_red_2 = by_2(index_red_2);
bz_red_2 = bz_2(index_red_2);
b_red_2 = [bx_red_2 by_red_2 bz_red_2];
v_2 = [vx_2 vy_2 vz_2];

index_red = zeros(length(T_v_3));
%Checks the data series for the closest times in
the shortest array and
%picks the entries in the long array. This is
done in order to get the
%arrays to have the same length
for i=1:length(T_v_3)
    subtracted = abs(T_b_3 - T_v_3(i));
    sorted = sort(subtracted);
    min_value = sorted(1);
    index = find(subtracted == min_value);
    index_red(i) = index(1);
end;
%Fjerner overflødige entries i matrisen
index_red_3 = index_red(find(index_red ~= 0));
%Reduserer B-feltmatrisene slik at b-felt data og
v data er av samme mengde
t_red_3 = T_b_3(index_red_3);
bx_red_3 = bx_3(index_red_3);
by_red_3 = by_3(index_red_3);
bz_red_3 = bz_3(index_red_3);
b_red_3 = [bx_red_3 by_red_3 bz_red_3];
v_3 = [vx_3 vy_3 vz_3];

index_red = zeros(length(T_v_4));
%Checks the data series for the closest times in
the shortest array and
%picks the entries in the long array. This is
done in order to get the
%arrays to have the same length
for i=1:length(T_v_4)
    subtracted = abs(T_b_4 - T_v_4(i));
    sorted = sort(subtracted);
    min_value = sorted(1);
    index = find(subtracted == min_value);
    index_red(i) = index(1);
end;
%Removes the abundant entries in the matrix
index_red_4 = index_red(find(index_red ~= 0));
%Reduces the size of the matrix so the velocity
matrix and the magnetic
%field matrix is of the same order.
t_red_4 = T_b_4(index_red_4);
bx_red_4 = bx_4(index_red_4);
by_red_4 = by_4(index_red_4);
bz_red_4 = bz_4(index_red_4);
b_red_4 = [bx_red_4 by_red_4 bz_red_4];
v_4 = [vx_4 vy_4 vz_4];
%-------------------------------------------------
-------------------------
%Starts the plotting of the Hallfield without any
coordinate changes

%Removes all the values which are not supposed to
be in the Hall field i.e.
%the valuse of positive vx is removed when by is
less than 0 and the other
%way around
vx_byp_1=vx_1+(by_red_1<0)*1e6;
vx_byn_1=vx_1+(by_red_1>=0)*1e6;
bx_byp_1=bx_red_1+(by_red_1<0)*1e6;
bx_byn_1=bx_red_1+(by_red_1>=0)*1e6;

vx_byp_2=vx_2+(by_red_2<0)*1e6;
vx_byn_2=vx_2+(by_red_2>=0)*1e6;
bx_byp_2=bx_red_2+(by_red_2<0)*1e6;
bx_byn_2=bx_red_2+(by_red_2>=0)*1e6;

vx_byp_3=vx_3+(by_red_3<0)*1e6;
vx_byn_3=vx_3+(by_red_3>=0)*1e6;
bx_byp_3=bx_red_3+(by_red_3<0)*1e6;
bx_byn_3=bx_red_3+(by_red_3>=0)*1e6;

vx_byp_4=vx_4+(by_red_4<0)*1e6;
vx_byn_4=vx_4+(by_red_4>=0)*1e6;
bx_byp_4=bx_red_4+(by_red_4<0)*1e6;
bx_byn_4=bx_red_4+(by_red_4>=0)*1e6;


%plotting the Hallfield
figure(1)
for i = 1:length(bx_red_1)
    color_dot='r';
    dot_size=2*abs(by_red_1(i));
    if by_red_1(i) <= 0, color_dot='b'; end;
    plot(vx_1(i), bx_red_1(i),
'Marker','o','MarkerSize',dot_size,'MarkerEdgeCol
or',color_dot);
    hold on
end

hold on;
for i = 1:length(bx_red_2)
    color_dot='r';
    dot_size=2*abs(by_red_2(i));
    if by_red_2(i) <= 0, color_dot='b'; end;
    plot(vx_2(i), bx_red_2(i),
'Marker','o','MarkerSize',dot_size,'MarkerEdgeCol
or',color_dot);
    hold on
end

hold on;
for i = 1:length(bx_red_3)
    color_dot='r';
    dot_size=2*abs(by_red_3(i));
    if by_red_3(i) <= 0, color_dot='b'; end;
    plot(vx_3(i), bx_red_3(i),
'Marker','o','MarkerSize',dot_size,'MarkerEdgeCol
or',color_dot);
    hold on
end

hold on;
for i = 1:length(bx_red_4)
    color_dot='r';
    dot_size=2*abs(by_red_4(i));
    if by_red_4(i) <= 0, color_dot='b'; end;
    plot(vx_4(i), bx_red_4(i),
'Marker','o','MarkerSize',dot_size,'MarkerEdgeCol
or',color_dot);
    hold on
end
plot([-1500 1500],[0 0],'k-');
plot([0 0],[-50 50],'k-');
title('Hall quadrupole, red: By>0, blue: By<0,
C1');
hold off;
xlabel('Vx');
ylabel('Bx');
axis([-1500 1500 -50 50]);

% plot(vx)
%
%
%% Introducing the MVA coordinate system
%-------------------------------------------------
-------------------------
%the MVA vectors
```

```
e_C1 = -[-0.98751694   0.15745669   0.00420526];
e_C2 = -[-0.97820140   0.20334257  -0.04211672];
e_C3 = [0.98326128  -0.18216190   0.00378152];
e_C4 = -[-0.98460863   0.17462467   0.00721601];

%-----------------------------------------------
-------------------------
%Change the coordinates to the plane with MVA
analysis. Assuming that the
%eigenvectors in the chartesian coordinate system
ex_cartesian = [1 0 0];
ey_cartesian = [0 1 0];
ez_cartesian = [0 0 1];

%New coordinatesystem for the first outflow
ex_new = e_C4; %ex_new_1 is set to the eigenvec-
tor from the MVA analysis which
                          %corresponds to the
largest eigenvalue.
ey_new = cross(ez_cartesian, ex_new);
ez_new = ez_cartesian;

v_coord_1 = zeros(length(v_1),3);
b_coord_1 = zeros(length(b_red_1), 3);

%Changes the magnetic field components to the new
coordinate system
for i=1:length(b_red_1(:,1))
    b_coord_1(i,1) = dot([b_red_1(i,1)
b_red_1(i,2) b_red_1(i,3)],ex_new);
    b_coord_1(i,2) = dot([b_red_1(i,1)
b_red_1(i,2) b_red_1(i,3)],ey_new);
    b_coord_1(i,3) = dot([b_red_1(i,1)
b_red_1(i,2) b_red_1(i,3)],ez_new);
end
 bx_new_1 = b_coord_1(:,1);
 by_new_1 = b_coord_1(:,2);
 bz_new_1 = b_coord_1(:,3);

%Changes the velocity components to the new coor-
dinate system
for i=1:length(vx_1(:,1))
    v_coord_1(i,1) = dot([v_1(i,1) v_1(i,2)
v_1(i,3)],ex_new);
    v_coord_1(i,2) = dot([v_1(i,1) v_1(i,2)
v_1(i,3)],ey_new);
    v_coord_1(i,3) = dot([v_1(i,1) v_1(i,2)
v_1(i,3)],ez_new);
end
 vx_new_1 = v_coord_1(:,1);


v_coord_2 = zeros(length(v_2),3);
b_coord_2 = zeros(length(b_red_2), 3);

%Changes the magnetic field components to the new
coordinate system
for i=1:length(b_red_2(:,1))
    b_coord_2(i,1) = dot([b_red_2(i,1)
b_red_2(i,2) b_red_2(i,3)],ex_new);
    b_coord_2(i,2) = dot([b_red_2(i,1)
b_red_2(i,2) b_red_2(i,3)],ey_new);
    b_coord_2(i,3) = dot([b_red_2(i,1)
b_red_2(i,2) b_red_2(i,3)],ez_new);
end
 bx_new_2 = b_coord_2(:,1);
 by_new_2 = b_coord_2(:,2);
 bz_new_2 = b_coord_2(:,3);

%Changes the velocity components to the new coor-
dinate system
for i=1:length(vx_2(:,1))
    v_coord_2(i,1) = dot([v_2(i,1) v_2(i,2)
v_2(i,3)],ex_new);
    v_coord_2(i,2) = dot([v_2(i,1) v_2(i,2)
v_2(i,3)],ey_new);
    v_coord_2(i,3) = dot([v_2(i,1) v_2(i,2)
v_2(i,3)],ez_new);
end
 vx_new_2 = v_coord_2(:,1);


v_coord_3 = zeros(length(v_3),3);
b_coord_3 = zeros(length(b_red_3), 3);

%Changes the magnetic field components to the new
coordinate system
for i=1:length(b_red_3(:,1))
    b_coord_3(i,1) = dot([b_red_3(i,1)
b_red_3(i,2) b_red_3(i,3)],ex_new);
    b_coord_3(i,2) = dot([b_red_3(i,1)
b_red_3(i,2) b_red_3(i,3)],ey_new);
    b_coord_3(i,3) = dot([b_red_3(i,1)
b_red_3(i,2) b_red_3(i,3)],ez_new);
end
 bx_new_3 = b_coord_3(:,1);
 by_new_3 = b_coord_3(:,2);
 bz_new_3 = b_coord_3(:,3);

%Changes the velocity components to the new coor-
dinate system
for i=1:length(vx_3(:,1))
    v_coord_3(i,1) = dot([v_3(i,1) v_3(i,2)
v_3(i,3)],ex_new);
    v_coord_3(i,2) = dot([v_3(i,1) v_3(i,2)
v_3(i,3)],ey_new);
    v_coord_3(i,3) = dot([v_3(i,1) v_3(i,2)
v_3(i,3)],ez_new);
end
 vx_new_3 = v_coord_3(:,1);

%New coordinatesystem for the fourth outflow
v_coord_4 = zeros(length(v_4),3);
b_coord_4 = zeros(length(b_red_4), 3);

%Changes the magnetic field components to the new
coordinate system
for i=1:length(b_red_4(:,1))
    b_coord_4(i,1) = dot([b_red_4(i,1)
b_red_4(i,2) b_red_4(i,3)],ex_new);
    b_coord_4(i,2) = dot([b_red_4(i,1)
b_red_4(i,2) b_red_4(i,3)],ey_new);
    b_coord_4(i,3) = dot([b_red_4(i,1)
b_red_4(i,2) b_red_4(i,3)],ez_new);
end
 bx_new_4 = b_coord_4(:,1);
 by_new_4 = b_coord_4(:,2);
 bz_new_4 = b_coord_4(:,3);

%Changes the velocity components to the new coor-
dinate system
for i=1:length(vx_4(:,1))
    v_coord_4(i,1) = dot([v_4(i,1) v_4(i,2)
v_4(i,3)],ex_new);
    v_coord_4(i,2) = dot([v_4(i,1) v_4(i,2)
v_4(i,3)],ey_new);
    v_coord_4(i,3) = dot([v_4(i,1) v_4(i,2)
v_4(i,3)],ez_new);
end
 vx_new_4 = v_coord_4(:,1);


%Removes all the values which are not supposed to
be in the Hall field i.e.
%the valuse of positive vx is removed when by is
less than 0 and the other
%way around
vx_byp_1_new=vx_new_1+(by_new_1<0)*1e6;
vx_byn_1_new=vx_new_1+(by_new_1>=0)*1e6;
bx_byp_1_new=bx_new_1+(by_new_1<0)*1e6;
bx_byn_1_new=bx_new_1+(by_new_1>=0)*1e6;

vx_byp_2_new=vx_new_2+(by_new_2<0)*1e6;
vx_byn_2_new=vx_new_2+(by_new_2>=0)*1e6;
bx_byp_2_new=bx_new_2+(by_new_2<0)*1e6;
bx_byn_2_new=bx_new_2+(by_new_2>=0)*1e6;

vx_byp_3_new=vx_new_3+(by_new_3<0)*1e6;
vx_byn_3_new=vx_new_3+(by_new_3>=0)*1e6;
bx_byp_3_new=bx_new_3+(by_new_3<0)*1e6;
bx_byn_3_new=bx_new_3+(by_new_3>=0)*1e6;

vx_byp_4_new=vx_new_4+(by_new_4<0)*1e6;
vx_byn_4_new=vx_new_4+(by_new_4>=0)*1e6;
bx_byp_4_new=bx_new_4+(by_new_4<0)*1e6;
bx_byn_4_new=bx_new_4+(by_new_4>=0)*1e6;


%plotting the Hallfield in the modified coordi-
nate system.
figure(7)
for i = 1:length(bx_new_1)
    color_dot='r';
    dot_size=4.5*abs(by_new_1(i));
```

```
    if by_new_1(i) <= 0, color_dot='b'; end;
    plot(vx_new_1(i), bx_new_1(i), 'LineWidth',
2,
'Marker','o','MarkerSize',dot_size,'MarkerEdgeCol
or',color_dot);
    hold on
end

hold on;
for i = 1:length(bx_new_2)
    color_dot='r';
    dot_size=4.5*abs(by_new_2(i));
    if by_new_2(i) <= 0, color_dot='b'; end;
    plot(vx_new_2(i), bx_new_2(i), 'LineWidth',
2,
'Marker','o','MarkerSize',dot_size,'MarkerEdgeCol
or',color_dot);
    hold on
end

hold on;
for i = 1:length(bx_new_3)
    color_dot='r';
    dot_size=4.5*abs(by_new_3(i));
    if by_new_3(i) <= 0, color_dot='b'; end;
    plot(vx_new_3(i), bx_new_3(i), 'LineWidth',
2,
'Marker','o','MarkerSize',dot_size,'MarkerEdgeCol
or',color_dot);
    hold on
end
%
% hold on;
% for i = 1:length(bx_new_4)
%     color_dot='r';
%     dot_size=4.5*abs(by_new_4(i));
%     if by_new_4(i) <= 0, color_dot='b'; end;
%     plot(vx_new_4(i), bx_new_4(i), 'LineWidth',
2,
'Marker','o','MarkerSize',dot_size,'MarkerEdgeCol
or',color_dot);
%     hold on
% end

plot([-1500 1500],[0 0],'k-');
plot([0 0],[-50 50],'k-');
title('Hall quadrupole in a new coordinate sys-
tem, red: By>0, blue: By<0, C1');
hold off;
xlabel('Vx');
ylabel('Bx');
axis([-1500 1500 -50 50]);
```

ALL_SC_plot_B_V_E_N_GSM.m

When plotting all the data from Cluster the program ALL_SC_plot_B_V_E_N_GSM.m has been used. This program consists of two parts, one which loads the data used and another part which plots the data. The loading part is also used when running the scatter_E_B_n_plot.m program.

```
%% Loading the data from Cluster Active Archive


clc;
clear;

%date
Year = 2005;
Month = 09;
Day = 26;
%defining the time for analysing data
time_start = datenum(Year, Month, Day, 9, 33,
00);
time_end = datenum(Year, Month, Day, 09, 57, 00);

%loading data from .txt files
MF_C1 = 'GSM_data_SC1_B.txt';
MF_C2 = 'GSM_data_SC2_B.txt';
MF_C3 = 'GSM_data_SC3_B.txt';
MF_C4 = 'GSM_data_SC4_B.txt';

E_C1 = 'C1_CP_EFW_EX_EY.txt';
E_C2 = 'C2_CP_EFW_EX_EY.txt';
E_C3 = 'C3_CP_EFW_EX_EY.txt';
E_C4 = 'C4_CP_EFW_EX_EY.txt';

Ez_C1 = 'C1_CP_EFW_EZ.txt';
Ez_C2 = 'C2_CP_EFW_EZ.txt';
Ez_C3 = 'C3_CP_EFW_EZ.txt';
Ez_C4 = 'C4_CP_EFW_EZ.txt';

n_C4 = 'C4_CP_CIS_CODIF.txt';
V_C4 = 'GSM_data_SC4_V.txt';

A = load(E_C1);
B = load(E_C2);
C = load(E_C3);
D = load(E_C4);

E = load(MF_C1);
F = load(MF_C2);
G = load(MF_C3);
H = load(MF_C4);

J = load(n_C4);

K = load(Ez_C1);
L = load(Ez_C2);
M = load(Ez_C3);
N = load(Ez_C4);

O = load(V_C4);

%removing values which are fillvalus in the .txt
files
invalidA=(A(:,5)==-
1000000000.000);A(invalidA,5)=NaN;
invalidA=(A(:,6)==-
1000000000.000);A(invalidA,6)=NaN;
invalidB=(B(:,5)==-
1000000000.000);B(invalidB,5)=NaN;
invalidB=(B(:,6)==-
1000000000.000);B(invalidB,6)=NaN;
invalidC=(C(:,5)==-
1000000000.000);C(invalidC,5)=NaN;
invalidC=(C(:,6)==-
1000000000.000);C(invalidC,6)=NaN;
invalidD=(D(:,5)==-
1000000000.000);D(invalidD,5)=NaN;
invalidD=(D(:,6)==-
1000000000.000);D(invalidD,6)=NaN;

invalidK=(K(:,7)==-
1000000000.000);K(invalidK,7)=NaN;
invalidL=(L(:,7)==-
1000000000.000);L(invalidL,7)=NaN;
invalidM=(M(:,7)==-
1000000000.000);M(invalidM,7)=NaN;
invalidN=(N(:,7)==-
1000000000.000);N(invalidN,7)=NaN;

invalidJ=(J(:,6)>=3);J(invalidJ,6)=NaN;

Ex_C1 = A(:,5);
Ey_C1 = A(:,6);
Ez_C1 = K(:,7);

Ex_C2 = B(:,5);
Ey_C2 = B(:,6);
Ez_C2 = L(:,7);

Ex_C3 = C(:,5);
```

```
Ey_C3 = C(:,6);
Ez_C3 = M(:,7);

Ex_C4 = D(:,5);
Ey_C4 = D(:,6);
Ez_C4 = N(:,7);

bx_C1 = E(:,7);
by_C1 = E(:,8);
bz_C1 = E(:,9);

bx_C2 = F(:,7);
by_C2 = F(:,8);
bz_C2 = F(:,9);

bx_C3 = G(:,7);
by_C3 = G(:,8);
bz_C3 = G(:,9);

bx_C4 = H(:,7);
by_C4 = H(:,8);
bz_C4 = H(:,9);

vx_C4 = O(:,7);
vy_C4 = O(:,8);
vz_C4 = O(:,9);

n_C4 = J(:,6);

b_C1 = [bx_C1 by_C1 bz_C1];
b_C2 = [bx_C2 by_C2 bz_C2];
b_C3 = [bx_C3 by_C3 bz_C3];
b_C4 = [bx_C4 by_C4 bz_C4];
%leser inn tid
v_time_C4 = O(:,4); v_min_C4 = O(:,5); v_sek_C4 =
O(:,6);

n_time_C4 = J(:,2); n_min_C4 = J(:,3); n_sek_C4 =
J(:,4);

Ez_time_C1 = K(:,2); Ez_min_C1 = K(:,3);
Ez_sek_C1 = K(:,4);
Ez_time_C2 = L(:,2); Ez_min_C2 = L(:,3);
Ez_sek_C2 = L(:,4);
Ez_time_C3 = M(:,2); Ez_min_C3 = M(:,3);
Ez_sek_C3 = M(:,4);
Ez_time_C4 = N(:,2); Ez_min_C4 = N(:,3);
Ez_sek_C4 = N(:,4);


E_time_C1 = A(:,2); E_min_C1 = A(:,3); E_sek_C1 =
A(:,4);
E_time_C2 = B(:,2); E_min_C2 = B(:,3); E_sek_C2 =
B(:,4);
E_time_C3 = C(:,2); E_min_C3 = C(:,3); E_sek_C3 =
C(:,4);
E_time_C4 = D(:,2); E_min_C4 = D(:,3); E_sek_C4 =
D(:,4);

b_time_C1 = E(:,4); b_min_C1 = E(:,5); b_sek_C1 =
E(:,6);
b_time_C2 = F(:,4); b_min_C2 = F(:,5); b_sek_C2 =
F(:,6);
b_time_C3 = G(:,4); b_min_C3 = G(:,5); b_sek_C3 =
G(:,6);
b_time_C4 = H(:,4); b_min_C4 = H(:,5); b_sek_C4 =
H(:,6);

T_b_C1 = datenum(Year, Month, Day, b_time_C1,
b_min_C1, b_sek_C1);
T_b_C2 = datenum(Year, Month, Day, b_time_C2,
b_min_C2, b_sek_C2);
T_b_C3 = datenum(Year, Month, Day, b_time_C3,
b_min_C3, b_sek_C3);
T_b_C4 = datenum(Year, Month, Day, b_time_C4,
b_min_C4, b_sek_C4);

T_E_C1 = datenum(Year, Month, Day, E_time_C1,
E_min_C1, E_sek_C1);
T_E_C2 = datenum(Year, Month, Day, E_time_C2,
E_min_C2, E_sek_C2);
T_E_C3 = datenum(Year, Month, Day, E_time_C3,
E_min_C3, E_sek_C3);
T_E_C4 = datenum(Year, Month, Day, E_time_C4,
E_min_C4, E_sek_C4);

T_Ez_C1 = datenum(Year, Month, Day, Ez_time_C1,
Ez_min_C1, Ez_sek_C1);
T_Ez_C2 = datenum(Year, Month, Day, Ez_time_C2,
Ez_min_C2, Ez_sek_C2);
T_Ez_C3 = datenum(Year, Month, Day, Ez_time_C3,
Ez_min_C3, Ez_sek_C3);
T_Ez_C4 = datenum(Year, Month, Day, Ez_time_C4,
Ez_min_C4, Ez_sek_C4);

T_n_C4 = datenum(Year, Month, Day, n_time_C4,
n_min_C4, n_sek_C4);
T_v_C4 = datenum(Year, Month, Day, v_time_C4,
v_min_C4, v_sek_C4);


%Adjusting the data to the time interval defined
in the beginning of the
%program.
index_time_interval_b_C1 = find(T_b_C1 >=
time_start & T_b_C1 <= time_end);
index_time_interval_b_C2 = find(T_b_C2 >=
time_start & T_b_C2 <= time_end);
index_time_interval_b_C3 = find(T_b_C3 >=
time_start & T_b_C3 <= time_end);
index_time_interval_b_C4 = find(T_b_C4 >=
time_start & T_b_C4 <= time_end);

T_b_C1 = T_b_C1(index_time_interval_b_C1);
T_b_C2 = T_b_C2(index_time_interval_b_C2);
T_b_C3 = T_b_C3(index_time_interval_b_C3);
T_b_C4 = T_b_C4(index_time_interval_b_C4);
bx_C1 = bx_C1(index_time_interval_b_C1);by_C1 =
by_C1(index_time_interval_b_C1);bz_C1 =
bz_C1(index_time_interval_b_C1);
bx_C2 = bx_C2(index_time_interval_b_C2);by_C2 =
by_C2(index_time_interval_b_C2);bz_C2 =
bz_C2(index_time_interval_b_C2);
bx_C3 = bx_C3(index_time_interval_b_C3);by_C3 =
by_C3(index_time_interval_b_C3);bz_C3 =
bz_C3(index_time_interval_b_C3);
bx_C4 = bx_C4(index_time_interval_b_C4);by_C4 =
by_C4(index_time_interval_b_C4);bz_C4 =
bz_C4(index_time_interval_b_C4);

index_time_interval_v_C4 = find(T_v_C4 >=
time_start & T_v_C4 <= time_end);
T_v_C4 = T_v_C4(index_time_interval_v_C4);
vx_C4 = vx_C4(index_time_interval_v_C4);vy_C4 =
vy_C4(index_time_interval_v_C4);vz_C4 =
vz_C4(index_time_interval_v_C4);
index_time_interval_n_C4 = find(T_n_C4 >=
time_start & T_n_C4 <= time_end);
T_n_C4 = T_n_C4(index_time_interval_n_C4);
n_C4 = n_C4(index_time_interval_n_C4);

index_time_interval_E_C1 = find(T_E_C1 >=
time_start & T_E_C1<= time_end);
index_time_interval_E_C2 = find(T_E_C2 >=
time_start & T_E_C2<= time_end);
index_time_interval_E_C3 = find(T_E_C3 >=
time_start & T_E_C3<= time_end);
index_time_interval_E_C4 = find(T_E_C4 >=
time_start & T_E_C4<= time_end);
T_E_C1 = T_E_C1(index_time_interval_E_C1);
T_E_C2 = T_E_C2(index_time_interval_E_C2);
T_E_C3 = T_E_C3(index_time_interval_E_C3);
T_E_C4 = T_E_C4(index_time_interval_E_C4);
Ex_C1 = Ex_C1(index_time_interval_E_C1);
Ex_C2 = Ex_C2(index_time_interval_E_C2);
Ex_C3 = Ex_C3(index_time_interval_E_C3);
Ex_C4 = Ex_C4(index_time_interval_E_C4);
Ey_C1 = Ey_C1(index_time_interval_E_C1);
Ey_C2 = Ey_C2(index_time_interval_E_C2);
Ey_C3 = Ey_C3(index_time_interval_E_C3);
Ey_C4 = Ey_C4(index_time_interval_E_C4);
index_time_interval_Ez_C1 = find(T_Ez_C1 >=
time_start & T_Ez_C1<= time_end);
index_time_interval_Ez_C2 = find(T_Ez_C2 >=
time_start & T_Ez_C2<= time_end);
index_time_interval_Ez_C3 = find(T_Ez_C3 >=
time_start & T_Ez_C3<= time_end);
index_time_interval_Ez_C4 = find(T_Ez_C4 >=
time_start & T_Ez_C4<= time_end);
T_Ez_C1 = T_Ez_C1(index_time_interval_Ez_C1);
T_Ez_C2 = T_Ez_C2(index_time_interval_Ez_C2);
T_Ez_C3 = T_Ez_C3(index_time_interval_Ez_C3);
T_Ez_C4 = T_Ez_C4(index_time_interval_Ez_C4);
```

```
Ez_C1 = Ez_C1(index_time_interval_Ez_C1);
Ez_C2 = Ez_C2(index_time_interval_Ez_C2);
Ez_C3 = Ez_C3(index_time_interval_Ez_C3);
Ez_C4 = Ez_C4(index_time_interval_Ez_C4);

%% Plotting the data from Cluster Active Archive

figure(1)
subplot(2,1,1),plot(T_v_C4,vx_C4,'b',[T_v_C4(1)
T_v_C4(length(T_v_C4))],[0 0],'k', 'LineWidth',
2);
ylabel('Vx, km/s','FontSize', 24);
datetick('x',13);
set(gca,'xtick',[],'FontSize', 24,
'xlim',[T_v_C4(1) T_v_C4(length(T_v_C4))]);
ylim([-1100 1100]);
subplot(2,1,2),plot(T_v_C4,vz_C4,'b',[T_v_C4(1)
T_v_C4(length(T_v_C4))],[0 0],'k', 'LineWidth',
2);
ylabel('Vz, km/s','FontSize', 24);
datetick('x',13);
set(gca,'xtick',[], 'YAxisLocation','right',
'FontSize', 24, 'xlim', [T_v_C4(1)
T_v_C4(length(T_v_C4))]);
ylim([-250 250]);

figure(2)
subplot(2,1,1), plot(T_b_C1,bx_C1,'k',[T_b_C1(1)
T_b_C1(length(T_b_C1))],[0 0],'k', 'LineWidth',
2);
hold on;
plot(T_b_C2,bx_C2,'r', 'LineWidth', 2);
plot(T_b_C3,bx_C3,'g', 'LineWidth', 2);
plot(T_b_C4,bx_C4,'b', 'LineWidth', 2);
ylabel('Bx, nT','FontSize', 24);
ylim([-inf inf])
set(gca,'xtick',[], 'xlim', [T_v_C4(1)
T_v_C4(length(T_v_C4))],'FontSize', 24);
hold off;
subplot(2,1,2), plot(T_b_C1,by_C1,'k',[T_b_C1(1)
T_b_C1(length(T_b_C1))],[0 0],'k', 'LineWidth',
2);
hold on;
plot(T_b_C2,by_C2,'r','LineWidth', 2);
plot(T_b_C3,by_C3,'g', 'LineWidth', 2);
plot(T_b_C4,by_C4,'b', 'LineWidth', 2);
ylabel('By, nT','FontSize', 24);
ylim([-25 25]);
set(gca,'xtick',[], 'xlim', [T_b_C4(1)
T_b_C4(length(T_b_C4))],'FontSize', 24, 'YAxisLo-
cation','right');
hold off;


figure(3)
plot(T_b_C1,bz_C1,'k',[T_b_C1(1)
T_b_C1(length(T_b_C1))],[0 0],'k', 'LineWidth',
2);
hold on;
plot(T_b_C2,bz_C2,'r',[T_b_C2(1)
T_b_C2(length(T_b_C2))],[0 0],'k', 'LineWidth',
2);
plot(T_b_C3,bz_C3,'g',[T_b_C3(1)
T_b_C3(length(T_b_C3))],[0 0],'k', 'LineWidth',
2);
plot(T_b_C4,bz_C4,'b',[T_b_C4(1)
T_b_C4(length(T_b_C4))],[0 0],'k', 'LineWidth',
2);
ylabel('Bz, nT','FontSize', 24);
datetick('x',13);
ylim([-15 15])
set(gca,'xtick',[], 'xlim', [T_b_C1(1)
T_b_C1(length(T_b_C1))],'FontSize', 24);
hold off;

figure(4)
subplot(2,1,1), plot(T_E_C1,Ex_C1,'k',[T_E_C1(1)
T_E_C1(length(T_E_C1))],[0 0],'k', 'LineWidth',
2);
hold on;
plot(T_E_C2,Ex_C2,'r',[T_E_C2(1)
T_E_C2(length(T_E_C2))],[0 0],'k', 'LineWidth',
2);
plot(T_E_C3,Ex_C3,'g',[T_E_C3(1)
T_E_C3(length(T_E_C3))],[0 0],'k', 'LineWidth',
2);
plot(T_E_C4,Ex_C4,'b',[T_E_C4(1)
T_E_C4(length(T_E_C4))],[0 0],'k', 'LineWidth',
2);
ylabel('Ex, mV/m','FontSize', 24);
datetick('x',13);
ylim([-5 5]);
set(gca,'xtick',[], 'xlim', [T_E_C4(1)
T_E_C4(length(T_E_C4))],'FontSize', 24, 'YAxisLo-
cation','right');
hold off;
subplot(2,1,2), plot(T_E_C1,Ey_C1,'k',[T_E_C1(1)
T_E_C1(length(T_E_C1))],[0 0],'k', 'LineWidth',
2);
hold on;
plot(T_E_C2,Ey_C2,'r',[T_E_C2(1)
T_E_C2(length(T_E_C2))],[0 0],'k', 'LineWidth',
2);
plot(T_E_C3,Ey_C3,'g',[T_E_C3(1)
T_E_C3(length(T_E_C3))],[0 0],'k', 'LineWidth',
2);
plot(T_E_C4,Ey_C4,'b',[T_E_C4(1)
T_E_C4(length(T_E_C4))],[0 0],'k', 'LineWidth',
2);
ylabel('Ey, mV/m','FontSize', 24);
datetick('x',13);
ylim([-10 30]);
set(gca,'xtick',[], 'xlim', [T_E_C4(1)
T_E_C4(length(T_E_C4))],'FontSize', 24);
hold off;

figure(5)
plot(T_n_C4,n_C4,'b','LineWidth', 2);
hold on;
plot([T_n_C4(1) T_n_C4(length(T_n_C4))],[0
0],'k','LineStyle', '-.', 'LineWidth', 2);
ylabel('n, cm^-3','FontSize', 24);
ylim([-0.05 inf])
datetick('x',13);
set(gca, 'xlim', [T_n_C4(1)
T_n_C4(length(T_n_C4))], 'FontSize', 14, 'YAxis-
Location','right');
xlabel('Time, UT','FontSize', 14);

%plot presentation
% figure(6)
% subplot(3,1,1), plot(T_v_C4,
vx_C4,'k',[T_v_C4(1) T_v_C4(length(T_v_C4))],[0
0],'k', 'LineWidth', 2)
% ylabel('Vx, km/s','FontSize', 24);
% datetick('x',13);
% set(gca,'xtick',[],'FontSize', 24,
'xlim',[T_v_C4(1) T_v_C4(length(T_v_C4))]);
% ylim([-1100 1100]);
% subplot(3,1,2),
plot(T_b_C4,bx_C4,'k',[T_b_C4(1)
T_b_C4(length(T_b_C4))],[0 0],'k', 'LineWidth',
2)
% ylim([-50 50])
% set(gca,'xtick',[], 'xlim', [T_v_C4(1)
T_v_C4(length(T_v_C4))],'FontSize', 24);
% subplot(3,1,3),
plot(T_b_C4,bz_C4,'k',[T_b_C4(1)
T_b_C4(length(T_b_C4))],[0 0],'k', 'LineWidth',
2)
% ylabel('Bz, nT','FontSize', 24);
% datetick('x',13);
% ylim([-15 15])
% xlim([T_b_C1(1) T_b_C1(length(T_b_C1))]);
```

NaN_inter.m

This small program removes data from the .txt file which is fill values and sets the value to NaN.

```
%% NaN inter
% removes unvalid data from a file and sets the
value to NaN
%%
function y = NaN_inter(x)
%x=[1 2 3 4 NaN NaN 6 8]

s=1;
if isnan(x(1))
    x(1)=nanmean(x);
end


for i= 2:length(x);
    if isnan(x(i))
        s=i-1;
        j=i;
        while (isnan(x(j)) & j<length(x))
            j=j+1;
            %j
            %x(j)
        end
        x(i)=x(s)+(x(s)-x(j))./(i-j);
        if j>=(length(x)-1); x(i)=x(i-1); end
    end
end
y=x;
y(find(isnan(y)))=0;
end
```

scatter_E_B_n_plot.m

The program used when creating the scatter plots of the E_y versus B_x, and the density versus the E_y is the scatter_E_B_n_plot.m program. The program loads the data from the ALL_SC_plot_B_V_E_N_GSM_load.m file. In this program, the dataset with high resolution are reduced to the same length as the datasets with the lower resolution in order to fit into the same plots. In the 2005 event this program is used only for SC4. In the 2001 program data from SC1 and SC3 are also included.

```
%% Scatterplot of the electric field, the mag-
netic field and the density
%%
index_red_1 = zeros(length(T_n_C4));
%Checks the data series for the closest times in
the shortest array and
%picks the entries in the long array. This is
done in order to get the
%arrays to have the same length
for i=1:length(T_n_C4)
    subtracted = abs(T_E_C4 - T_n_C4(i));
    sorted = sort(subtracted);
    min_value = sorted(1);
    index = find(subtracted == min_value);
    index_red_1(i) = index(1);
end;
%Fjerner overflødige entries i matrisen
index_red_1 = index_red_1(find(index_red_1 ~=
0));
%Reduserer B-feltmatrisene slik at b-felt data og
v data er av samme mengde
Ey_C4_red = Ey_C4(index_red_1);

index_red_2 = zeros(length(T_b_C4));
%Checks the data series for the closest times in
the shortest array and
%picks the entries in the long array. This is
done in order to get the
%arrays to have the same length
for i=1:length(T_b_C4)
    subtracted = abs(T_E_C4 - T_b_C4(i));
    sorted = sort(subtracted);
    min_value = sorted(1);
    index = find(subtracted == min_value);
    index_red_2(i) = index(1);
end;
%removing the redundant entries i matrisen
index_red_2 = index_red_2(find(index_red_2 ~=
0));
Ey_red_4_2 = Ey_C4(index_red_2);

length(n_C4)
length(Ey_C4_red)
% length(Ey_red_4_2)
% length(bx_C4)
%----------------------------------------
figure(1)
scatter(Ey_red_4_2, bx_C4)
ylim([-45 45]);
xlim([-20 20]);
xlabel('E_y, mV/m', 'FontSize', 24)
ylabel('B_x, nT', 'FontSize', 24)

figure(2)
scatter(Ey_C4_red, n_C4)
ylim([0 1.6]);
xlim([-20 20]);
xlabel('E_y, mV/m', 'FontSize', 24)
ylabel('n_i, cm^-3', 'FontSize', 24)
```

E_field_quality.m

The E_field_quality.m program is used when investigating the quality flags of the electric field measurements presented in appendix B.

```
%% The electric field quality
% plotting the standard deviation of the electric
field measurements and
% the quality flags

clc;
clear;
%date
Year = 2005;
Month = 09;
Day = 26;
%Defining the time interval used when investigat-
ing the quality of the
%electric fields
time_start = datenum(Year, Month, Day, 9, 33,
00);
time_end = datenum(Year, Month, Day, 09, 57, 00);

E_C1 = 'C1_CP_EFW_EX_EY.txt';
E_C2 = 'C2_CP_EFW_EX_EY.txt';
E_C3 = 'C3_CP_EFW_EX_EY.txt';
E_C4 = 'C4_CP_EFW_EX_EY.txt';


A = load(E_C1);
B = load(E_C2);
```

```
C = load(E_C3);
D = load(E_C4);

%removing bad data
invalidA=(A(:,5)==-
1000000000.000);A(invalidA,5)=NaN;
invalidA=(A(:,6)==-
1000000000.000);A(invalidA,6)=NaN;
invalidA=(A(:,7)==-
1000000000.000);A(invalidA,7)=NaN;

invalidB=(B(:,5)==-
1000000000.000);B(invalidB,5)=NaN;
invalidB=(B(:,6)==-
1000000000.000);B(invalidB,6)=NaN;
invalidB=(B(:,7)==-
1000000000.000);B(invalidB,7)=NaN;

invalidC=(C(:,5)==-
1000000000.000);C(invalidC,5)=NaN;
invalidC=(C(:,6)==-
1000000000.000);C(invalidC,6)=NaN;
invalidC=(C(:,7)==-
1000000000.000);C(invalidC,7)=NaN;

invalidD=(D(:,5)==-
1000000000.000);D(invalidD,5)=NaN;
invalidD=(D(:,6)==-
1000000000.000);D(invalidD,6)=NaN;
invalidD=(D(:,7)==-
1000000000.000);D(invalidD,7)=NaN;

Ex_C1 = A(:,5);
Ey_C1 = A(:,6);
q_1 = A(:,9);%the quality flag from SC1
dE_1 = A(:,7);%the standard deviation from SC1

Ex_C2 = B(:,5);
Ey_C2 = B(:,6);
q_2 = B(:,9);
dE_2 = B(:,7);

Ex_C3 = C(:,5);
Ey_C3 = C(:,6);
q_3 = C(:,9);
dE_3 = C(:,7);

Ex_C4 = D(:,5);
Ey_C4 = D(:,6);
q_4 = D(:,9);
dE_4 = D(:,7);

E_time_C1 = A(:,2); E_min_C1 = A(:,3); E_sek_C1 =
A(:,4);
E_time_C2 = B(:,2); E_min_C2 = B(:,3); E_sek_C2 =
B(:,4);
E_time_C3 = C(:,2); E_min_C3 = C(:,3); E_sek_C3 =
C(:,4);
E_time_C4 = D(:,2); E_min_C4 = D(:,3); E_sek_C4 =
D(:,4);

T_E_C1 = datenum(Year, Month, Day, E_time_C1,
E_min_C1, E_sek_C1);
T_E_C2 = datenum(Year, Month, Day, E_time_C2,
E_min_C2, E_sek_C2);
T_E_C3 = datenum(Year, Month, Day, E_time_C3,
E_min_C3, E_sek_C3);
T_E_C4 = datenum(Year, Month, Day, E_time_C4,
E_min_C4, E_sek_C4);

%Adjusting the dataset into the selected time
interval.
index_time_interval_E_C1 = find(T_E_C1 >=
time_start & T_E_C1<= time_end);
index_time_interval_E_C2 = find(T_E_C2 >=
time_start & T_E_C2<= time_end);
index_time_interval_E_C3 = find(T_E_C3 >=
time_start & T_E_C3<= time_end);
index_time_interval_E_C4 = find(T_E_C4 >=
time_start & T_E_C4<= time_end);
T_E_C1 = T_E_C1(index_time_interval_E_C1);
T_E_C2 = T_E_C2(index_time_interval_E_C2);
T_E_C3 = T_E_C3(index_time_interval_E_C3);
T_E_C4 = T_E_C4(index_time_interval_E_C4);
Ex_C1 = Ex_C1(index_time_interval_E_C1);
Ex_C2 = Ex_C2(index_time_interval_E_C2);
Ex_C3 = Ex_C3(index_time_interval_E_C3);
Ex_C4 = Ex_C4(index_time_interval_E_C4);
Ey_C1 = Ey_C1(index_time_interval_E_C1);
Ey_C2 = Ey_C2(index_time_interval_E_C2);
Ey_C3 = Ey_C3(index_time_interval_E_C3);
Ey_C4 = Ey_C4(index_time_interval_E_C4);
q_1 = q_1(index_time_interval_E_C1);
q_2 = q_2(index_time_interval_E_C2);
q_3 = q_3(index_time_interval_E_C3);
q_4 = q_4(index_time_interval_E_C4);
dE_1 = dE_1(index_time_interval_E_C1);
dE_2 = dE_2(index_time_interval_E_C2);
dE_3 = dE_3(index_time_interval_E_C3);
dE_4 = dE_4(index_time_interval_E_C4);

%%
%plotting the electric field standard deviations
and the quality flags
figure(1)
subplot(4,1,1),plot(T_E_C1,Ey_C1,'k',[T_E_C1(1)
T_E_C1(length(T_E_C1))],[0 0],'k', 'LineWidth',
1.5);
title('Electric field and standard deviation,
2005', 'FontSize', 24);
ylabel('Ey, mV/m SC1','FontSize', 24);
xlabel('Time, UT','FontSize', 24);
ylim([-inf inf]);
xlim([T_E_C1(1) T_E_C1(length(T_E_C1))]);
subplot(4,1,2), plot(T_E_C2,Ey_C2,'k',[T_E_C2(1)
T_E_C2(length(T_E_C2))],[0 0],'k', 'LineWidth',
1.5);
ylabel('Ey, mV/m SC2','FontSize', 24);
xlabel('Time, UT','FontSize', 24);
ylim([-inf inf]);
xlim([T_E_C2(1) T_E_C2(length(T_E_C2))]);
subplot(4,1,3), plot(T_E_C3,Ey_C3,'k',[T_E_C3(1)
T_E_C3(length(T_E_C3))],[0 0],'k', 'LineWidth',
1.5);
ylabel('Ey, mV/m SC3','FontSize', 24);
xlabel('Time, UT','FontSize', 24);
ylim([-inf inf]);
xlim([T_E_C3(1) T_E_C3(length(T_E_C3))]);
hold off;
subplot(4,1,4),plot(T_E_C4,Ey_C4,'k',[T_E_C4(1)
T_E_C4(length(T_E_C4))],[0 0],'k', 'LineWidth',
1.5);
ylabel('Ey, mV/m SC4','FontSize', 24);
xlabel('Time, UT','FontSize', 24);
datetick('x',13);
ylim([-inf inf]);
xlim([T_E_C4(1) T_E_C4(length(T_E_C4))]);

% figure(2)
% subplot(4, 1, 1), plot(T_E_C1, q_1,
'LineWidth', 2)
% title('Qualification number EFW-experiment,
2005', 'FontSize', 24)
% ylim([0 4])
% ylabel('Quality flag', 'FontSize', 24)
% xlabel('Time, UT', 'FontSize', 24)
% xlim([T_E_C1(1) T_E_C1(length(T_E_C1))])
% datetick('x', 13);
% subplot(4, 1, 2), plot(T_E_C2, q_2,
'LineWidth', 2)
% ylim([0 4])
% ylabel('Quality flag', 'FontSize', 24)
% xlim([T_E_C1(1) T_E_C1(length(T_E_C1))])
% xlabel('Time, UT', 'FontSize', 24)
% datetick('x', 13);
% subplot(4, 1, 3), plot(T_E_C3, q_3,
'LineWidth', 2)
% ylim([0 4])
% ylabel('Quality flag', 'FontSize', 24)
% xlim([T_E_C1(1) T_E_C1(length(T_E_C1))])
% xlabel('Time, UT', 'FontSize', 24)
% datetick('x', 13);
% subplot(4, 1, 4), plot(T_E_C4, q_4,
'LineWidth', 2)
% ylim([0 4])
% ylabel('Quality flag', 'FontSize', 24)
% xlim([T_E_C1(1) T_E_C1(length(T_E_C1))])
% xlabel('Time, UT', 'FontSize', 24)
% datetick('x', 13);

figure(3)
subplot(4,1,1),plot(T_E_C1,dE_1,'r', 'LineWidth',
2')
ylabel('E_sigma, mV/m SC1','FontSize', 24);
```

```
xlabel('Time, UT','FontSize', 24);
datetick('x',13);
ylim([-inf inf]);
xlim([T_E_C1(1) T_E_C1(length(T_E_C1))])
subplot(4,1,2), plot(T_E_C2,dE_2,'r',
'LineWidth', 2);
ylabel('E_sigma, mV/m SC2','FontSize', 24);
xlabel('Time, UT','FontSize', 24);
datetick('x',13);
ylim([-inf inf]);
xlim([T_E_C2(1) T_E_C2(length(T_E_C2))])
subplot(4,1,3), plot(T_E_C3,dE_3, 'r',
'LineWidth', 2')
ylabel('E_sigma, mV/m SC3','FontSize', 24);
xlabel('Time, UT','FontSize', 24);
datetick('x',13);
ylim([-inf inf]);
xlim([T_E_C3(1) T_E_C3(length(T_E_C3))])
subplot(4,1,4),plot(T_E_C4,dE_4, 'r','LineWidth',
2')
ylabel('E_sigma, mV/m SC4','FontSize', 24);
xlabel('Time, UT','FontSize', 24);
datetick('x',13);
ylim([-inf inf]);
xlim([T_E_C4(1) T_E_C4(length(T_E_C4))])
```

positions.m

The positions.m program plots the position of the Cluster satellites in both the GSE and the GSM coordinate system. The program uses SC3 as the origo and calculates the positions of the other spacecrafts relative to SC3.

```
%% Generates the postition plot of the satellites
%
clc;
clear;

C1 = 'sep_C1_C3.txt';
C2 = 'sep_C2_C3.txt';
C4 = 'sep_C4_C3.txt';

AUX = 'CL_SP_AUX.txt';

A = load(C1);
B = load(C2);
C = load(C4);
D = load(AUX);


%loading the position data from the auxillary
file
x_gse_C1 = A(:,5);
y_gse_C1 = A(:,6);
z_gse_C1 = A(:,7);

pos_C1 = [x_gse_C1 y_gse_C1 z_gse_C1];

x_gse_C2 = B(:,5);
y_gse_C2 = B(:,6);
z_gse_C2 = B(:,7);

pos_C2 = [x_gse_C2 y_gse_C2 z_gse_C2];

x_gse_C4 = C(:,5);
y_gse_C4 = C(:,6);
z_gse_C4 = C(:,7);
pos_C4 = [x_gse_C4 y_gse_C4 z_gse_C4];


Sep_min = D(:,39);
Sep_max = D(:,40);
GSE_GSM = D(:,41);%rotation angle
C1_off_x = D(:,17);%separation distance between
SC1 and SC3
C1_off_y = D(:,18);
C1_off_z = D(:,19);
C2_off_x = D(:,20);%separation distance between
SC2 and SC3
C2_off_y = D(:,21);
C2_off_z = D(:,22);
C4_off_x = D(:,26);%separation distance between
SC4 and SC3
C4_off_y = D(:,27);
C4_off_z = D(:,28);
pos_GSE_x = D(:,11);
pos_GSE_y = D(:,12);
pos_GSE_z = D(:,13);

%Calculations
psi_deg = mean(GSE_GSM)%mean value of the rota-
tion angle
psi = deg2rad(psi_deg);%transforming the angle
into radians
max_dist = max(Sep_max);%calculating the maximum
separation distance
min_dist = min(Sep_min);%calculates the minimum
separation distance
%The rotation matrix from GSE to GSM
rot_matrix = [1 0 0; 0 cos(psi) -sin(psi); 0
sin(psi) cos(psi)];

%Changing the coordinate system from GSE into GSM
pos_C1 = [x_gse_C1 y_gse_C1 z_gse_C1];
pos_C1_GSM = zeros(length(pos_C1(:,1)),3);
for i=1:length(pos_C1(:,1))
    pos_C1_GSM(i,:) = rot_matrix*pos_C1(i,:)';
end
pos_C2 = [x_gse_C2 y_gse_C2 z_gse_C2];
pos_C2_GSM = zeros(length(pos_C2(:,1)),3);
for i=1:length(pos_C1(:,1))
    pos_C2_GSM(i,:) = rot_matrix*pos_C2(i,:)';
end
pos_C4 = [x_gse_C4 y_gse_C4 z_gse_C4];
pos_C4_GSM = zeros(length(pos_C4(:,1)),3);
for i=1:length(pos_C1(:,1))
    pos_C4_GSM(i,:) = rot_matrix*pos_C4(i,:)';
end

soff_C1 = [C1_off_x C1_off_y C1_off_z];
soff_C1_GSM = zeros(length(soff_C1(:,1)), 3);
soff_C2 = [C2_off_x C2_off_y C2_off_z];
soff_C2_GSM = zeros(length(soff_C2(:,1)), 3);
soff_C4 = [C4_off_x C4_off_y C4_off_z];
soff_C4_GSM = zeros(length(soff_C4(:,1)), 3);
for i=1:length(soff_C1(:,1))
    soff_C1_GSM(i,:) = rot_matrix*soff_C1(i,:)';
end
for i=1:length(soff_C2(:,1))
    soff_C2_GSM(i,:) = rot_matrix*soff_C2(i,:)';
end
for i=1:length(soff_C4(:,1))
    soff_C4_GSM(i,:) = rot_matrix*soff_C4(i,:)';
end

%change the position from GSE into GSM
pos_GSE = [pos_GSE_x pos_GSE_y pos_GSE_z];
pos_GSM = zeros(length(pos_GSE(:,1)), 3);
for i=1:length(pos_GSE(:,1))
    pos_GSM(i,:) = rot_matrix*pos_GSE(i,:)';
end
pos_GSM_x = mean(pos_GSM(:,1))/6378
pos_GSM_y = mean(pos_GSM(:,2))/6378
pos_GSM_z = mean(pos_GSM(:,3))/6378

x_C1_gjsnitt = mean(x_gse_C1);
y_C1_gjsnitt = mean(y_gse_C1);
z_C1_gjsnitt = mean(z_gse_C1);
D_C1 = [x_C1_gjsnitt y_C1_gjsnitt z_C1_gjsnitt];
dist_C1 = norm(D_C1);
x_C2_gjsnitt = mean(x_gse_C2);
y_C2_gjsnitt = mean(y_gse_C2);
z_C2_gjsnitt = mean(z_gse_C2);
D_C2 = [x_C2_gjsnitt y_C2_gjsnitt z_C2_gjsnitt];
dist_C2 = norm(D_C2);
x_C4_gjsnitt = mean(x_gse_C4);
```

```
y_C4_gjsnitt = mean(y_gse_C4);
z_C4_gjsnitt = mean(z_gse_C4);
D_C4 = [x_C2_gjsnitt y_C2_gjsnitt z_C2_gjsnitt];
dist_C4 = norm(D_C2);


%%
%Plotting GSM position
figure(11)
plot(mean(soff_C1_GSM(:,1)),
mean(soff_C1_GSM(:,2)),'Marker','s','MarkerSize',
15,'MarkerFaceColor','k')
hold on;
plot([-9000 3000],[0 0], '-k');
plot([0 0], [-6000 6000], '-k');
title('The xy-plane', 'FontSize', 14);
xlabel('\DeltaX GSM, km', 'FontSize', 14);
ylabel('\DeltaY GSM, km', 'FontSize', 14);
ylim([-6000 6000])
xlim([-9000 3000])
set(gca,'XTick',[-9000 -6000 -3000 0 3000],
'XDir', 'reverse',  'YDir', 'reverse');
plot(mean(soff_C2_GSM(:,1)),
mean(soff_C2_GSM(:,2)),
'Marker','d','MarkerSize',15,'MarkerFaceColor','r
');
plot(mean(soff_C4_GSM(:,1)),
mean(soff_C4_GSM(:,2)),
'Marker','^','MarkerSize',15,'MarkerFaceColor','b
');
plot(0,0,
'Marker','o','MarkerSize',15,'MarkerFaceColor','g
');
hold off;

figure(12)
plot(mean(soff_C1_GSM(:,2)),
mean(soff_C1_GSM(:,3)),'Marker','s','MarkerSize',
15,'MarkerFaceColor','k')
hold on;
plot([-6000 6000],[0 0], '-k');
plot([0 0], [-2500 2500], '-k');
title('The yz-plane', 'FontSize', 14);
xlabel('\DeltaY GSM, km', 'FontSize', 14);
ylabel('\DeltaZ GSM, km', 'FontSize', 14);
set(gca,'yTick',[-2500 -1500 -500 0 500 1500
2500], 'XDir', 'reverse');
ylim([-2500 2500])
xlim([-6000 6000])
plot(mean(soff_C2_GSM(:,2)),
mean(soff_C2_GSM(:,3)),
'Marker','d','MarkerSize',15,'MarkerFaceColor','r
');
plot(mean(soff_C4_GSM(:,2)),
mean(soff_C4_GSM(:,3)),
'Marker','^','MarkerSize',15,'MarkerFaceColor','b
');
plot(0,0,
'Marker','o','MarkerSize',15,'MarkerFaceColor','g
');
hold off;

figure(13)
plot(mean(soff_C1_GSM(:,1)),
mean(soff_C1_GSM(:,3)),'Marker','s','MarkerSize',
15,'MarkerFaceColor','k')
hold on;
plot([-10000 3000],[0 0], '-k');
plot([0 0], [-2500 2500], '-k');
title('The xz-plane', 'FontSize', 14);
xlabel('\DeltaX GSM, km', 'FontSize', 14);
ylabel('\DeltaZ GSM, km', 'FontSize', 14);
set(gca,'XTick',[-9000 -6000 -3000 0 3000],
'XDir', 'reverse');
set(gca,'YTick',[-2500 -1500 -500 0 500 1500
2500]);
ylim([-2500 2500])
xlim([-10000 3000])
plot(mean(soff_C2_GSM(:,1)),
mean(soff_C2_GSM(:,3)),
'Marker','d','MarkerSize',15,'MarkerFaceColor','r
');
plot(mean(soff_C4_GSM(:,1)),
mean(soff_C4_GSM(:,3)),
'Marker','^','MarkerSize',15,'MarkerFaceColor','b
');
plot(0,0,
'Marker','o','MarkerSize',15,'MarkerFaceColor','g
');
hold off;

%%
%Plotting the position in GSE
figure(1)
plot(x_C1_gjsnitt, y_C1_gjsnitt,
'Marker','s','MarkerSize',15,'MarkerFaceColor','k
');
hold on;
plot([0 0],[0 0],'k');
title('The xy-plane');
xlabel('x-km');
ylabel('y-km');
ylim([-6500 6500])
xlim([-10000 1500])
plot(x_C2_gjsnitt, y_C2_gjsnitt,
'Marker','d','MarkerSize',15,'MarkerFaceColor','r
');
plot(x_C4_gjsnitt, y_C4_gjsnitt,
'Marker','^','MarkerSize',15,'MarkerFaceColor','b
');
plot(0,0,
'Marker','o','MarkerSize',15,'MarkerFaceColor','g
');
hold off;

figure(2)
plot(x_C1_gjsnitt, z_C1_gjsnitt,
'Marker','s','MarkerSize',15,'MarkerFaceColor','k
');
hold on; grid on;
title('The xz-plane');
xlabel('x-km');
ylabel('y-km');
plot(x_C2_gjsnitt, z_C2_gjsnitt,
'Marker','d','MarkerSize',15,'MarkerFaceColor','r
');
plot(x_C4_gjsnitt, z_C4_gjsnitt,
'Marker','^','MarkerSize',15,'MarkerFaceColor','b
');
plot(0,0,
'Marker','o','MarkerSize',15,'MarkerFaceColor','g
');
hold off;

figure(3)
plot(y_C1_gjsnitt, z_C1_gjsnitt,
'Marker','s','MarkerSize',15,'MarkerFaceColor','k
');
hold on; grid on;
title('The yz-plane')
xlabel('x-km');
ylabel('y-km');
plot(y_C2_gjsnitt, z_C2_gjsnitt,
'Marker','d','MarkerSize',15,'MarkerFaceColor','r
');
plot(y_C4_gjsnitt, z_C4_gjsnitt,
'Marker','^','MarkerSize',15,'MarkerFaceColor','b
');
plot(0,0,
'Marker','o','MarkerSize',15,'MarkerFaceColor','g
');
hold off;
```

plasma_beta_C4.m

The plasma_beta_C4.m program plots the plasma beta and the spacecraft potential which is used when determine the spacecraft location in the magnetotail. This program includes only

data from SC4 in the 2005 event, but in the plots from the 2001 event data from SC1 and SC3 is included.

```
%% Generates the postition plot of the satellites
%
clc;
clear;

C1 = 'sep_C1_C3.txt';
C2 = 'sep_C2_C3.txt';
C4 = 'sep_C4_C3.txt';

AUX = 'CL_SP_AUX.txt';

A = load(C1);
B = load(C2);
C = load(C4);
D = load(AUX);


%loading the position data from the auxillary
file
x_gse_C1 = A(:,5);
y_gse_C1 = A(:,6);
z_gse_C1 = A(:,7);

pos_C1 = [x_gse_C1 y_gse_C1 z_gse_C1];

x_gse_C2 = B(:,5);
y_gse_C2 = B(:,6);
z_gse_C2 = B(:,7);

pos_C2 = [x_gse_C2 y_gse_C2 z_gse_C2];

x_gse_C4 = C(:,5);
y_gse_C4 = C(:,6);
z_gse_C4 = C(:,7);
pos_C4 = [x_gse_C4 y_gse_C4 z_gse_C4];


Sep_min = D(:,39);
Sep_max = D(:,40);
GSE_GSM = D(:,41);%rotation angle
C1_off_x = D(:,17);%separation distance between
SC1 and SC3
C1_off_y = D(:,18);
C1_off_z = D(:,19);
C2_off_x = D(:,20);%separation distance between
SC2 and SC3
C2_off_y = D(:,21);
C2_off_z = D(:,22);
C4_off_x = D(:,26);%separation distance between
SC4 and SC3
C4_off_y = D(:,27);
C4_off_z = D(:,28);
pos_GSE_x = D(:,11);
pos_GSE_y = D(:,12);
pos_GSE_z = D(:,13);

%Calculations
psi_deg = mean(GSE_GSM)%mean value of the rota-
tion angle
psi = deg2rad(psi_deg);%transforming the angle
into radians
max_dist = max(Sep_max);%calculating the maximum
separation distance
min_dist = min(Sep_min);%calculates the minimum
separation distance
%The rotation matrix from GSE to GSM
rot_matrix = [1 0 0; 0 cos(psi) -sin(psi); 0
sin(psi) cos(psi)];

%Changing the coordinate system from GSE into GSM
pos_C1 = [x_gse_C1 y_gse_C1 z_gse_C1];
pos_C1_GSM = zeros(length(pos_C1(:,1)),3);
for i=1:length(pos_C1(:,1))
    pos_C1_GSM(i,:) = rot_matrix*pos_C1(i,:)';
end
pos_C2 = [x_gse_C2 y_gse_C2 z_gse_C2];
pos_C2_GSM = zeros(length(pos_C2(:,1)),3);
for i=1:length(pos_C1(:,1))
    pos_C2_GSM(i,:) = rot_matrix*pos_C2(i,:)';
end
pos_C4 = [x_gse_C4 y_gse_C4 z_gse_C4];
pos_C4_GSM = zeros(length(pos_C4(:,1)),3);
for i=1:length(pos_C1(:,1))
    pos_C4_GSM(i,:) = rot_matrix*pos_C4(i,:)';
end

soff_C1 = [C1_off_x C1_off_y C1_off_z];
soff_C1_GSM = zeros(length(soff_C1(:,1)), 3);
soff_C2 = [C2_off_x C2_off_y C2_off_z];
soff_C2_GSM = zeros(length(soff_C2(:,1)), 3);
soff_C4 = [C4_off_x C4_off_y C4_off_z];
soff_C4_GSM = zeros(length(soff_C4(:,1)), 3);
for i=1:length(soff_C1(:,1))
    soff_C1_GSM(i,:) = rot_matrix*soff_C1(i,:)';
end
for i=1:length(soff_C2(:,1))
    soff_C2_GSM(i,:) = rot_matrix*soff_C2(i,:)';
end
for i=1:length(soff_C4(:,1))
    soff_C4_GSM(i,:) = rot_matrix*soff_C4(i,:)';
end

%change the position from GSE into GSM
pos_GSE = [pos_GSE_x pos_GSE_y pos_GSE_z];
pos_GSM = zeros(length(pos_GSE(:,1)), 3);
for i=1:length(pos_GSE(:,1))
    pos_GSM(i,:) = rot_matrix*pos_GSE(i,:)';
end
pos_GSM_x = mean(pos_GSM(:,1))/6378
pos_GSM_y = mean(pos_GSM(:,2))/6378
pos_GSM_z = mean(pos_GSM(:,3))/6378

x_C1_gjsnitt = mean(x_gse_C1);
y_C1_gjsnitt = mean(y_gse_C1);
z_C1_gjsnitt = mean(z_gse_C1);
D_C1 = [x_C1_gjsnitt y_C1_gjsnitt z_C1_gjsnitt];
dist_C1 = norm(D_C1);
x_C2_gjsnitt = mean(x_gse_C2);
y_C2_gjsnitt = mean(y_gse_C2);
z_C2_gjsnitt = mean(z_gse_C2);
D_C2 = [x_C2_gjsnitt y_C2_gjsnitt z_C2_gjsnitt];
dist_C2 = norm(D_C2);
x_C4_gjsnitt = mean(x_gse_C4);
y_C4_gjsnitt = mean(y_gse_C4);
z_C4_gjsnitt = mean(z_gse_C4);
D_C4 = [x_C2_gjsnitt y_C2_gjsnitt z_C2_gjsnitt];
dist_C4 = norm(D_C2);


%%
%Plotting GSM position
figure(11)
plot(mean(soff_C1_GSM(:,1)),
mean(soff_C1_GSM(:,2)),'Marker','s','MarkerSize',
15,'MarkerFaceColor','k')
hold on;
plot([-9000 3000],[0 0], '-k');
plot([0 0], [-6000 6000], '-k');
title('The xy-plane', 'FontSize', 14);
xlabel('\DeltaX GSM, km', 'FontSize', 14);
ylabel('\DeltaY GSM, km', 'FontSize', 14);
ylim([-6000 6000])
xlim([-9000 3000])
set(gca,'XTick',[-9000 -6000 -3000 0 3000],
'XDir', 'reverse',  'YDir', 'reverse');
plot(mean(soff_C2_GSM(:,1)),
mean(soff_C2_GSM(:,2)),
'Marker','d','MarkerSize',15,'MarkerFaceColor','r
');
plot(mean(soff_C4_GSM(:,1)),
mean(soff_C4_GSM(:,2)),
'Marker','^','MarkerSize',15,'MarkerFaceColor','b
');
plot(0,0,
'Marker','o','MarkerSize',15,'MarkerFaceColor','g
');
hold off;

figure(12)
plot(mean(soff_C1_GSM(:,2)),
mean(soff_C1_GSM(:,3)),'Marker','s','MarkerSize',
15,'MarkerFaceColor','k')
```

```
hold on;
plot([-6000 6000],[0 0], '-k');
plot([0 0], [-2500 2500], '-k');
title('The yz-plane', 'FontSize', 14);
xlabel('\DeltaY GSM, km', 'FontSize', 14);
ylabel('\DeltaZ GSM, km', 'FontSize', 14);
set(gca,'yTick',[-2500 -1500 -500 0 500 1500
2500], 'XDir', 'reverse');
ylim([-2500 2500])
xlim([-6000 6000])
plot(mean(soff_C2_GSM(:,2)),
mean(soff_C2_GSM(:,3)),
'Marker','d','MarkerSize',15,'MarkerFaceColor','r
');
plot(mean(soff_C4_GSM(:,2)),
mean(soff_C4_GSM(:,3)),
'Marker','^','MarkerSize',15,'MarkerFaceColor','b
');
plot(0,0,
'Marker','o','MarkerSize',15,'MarkerFaceColor','g
');
hold off;

figure(13)
plot(mean(soff_C1_GSM(:,1)),
mean(soff_C1_GSM(:,3)),'Marker','s','MarkerSize',
15,'MarkerFaceColor','k')
hold on;
plot([-10000 3000],[0 0], '-k');
plot([0 0], [-2500 2500], '-k');
title('The xz-plane', 'FontSize', 14);
xlabel('\DeltaX GSM, km', 'FontSize', 14);
ylabel('\DeltaZ GSM, km', 'FontSize', 14);
set(gca,'XTick',[-9000 -6000 -3000 0 3000],
'XDir', 'reverse');
set(gca,'YTick',[-2500 -1500 -500 0 500 1500
2500]);
ylim([-2500 2500])
xlim([-10000 3000])
plot(mean(soff_C2_GSM(:,1)),
mean(soff_C2_GSM(:,3)),
'Marker','d','MarkerSize',15,'MarkerFaceColor','r
');
plot(mean(soff_C4_GSM(:,1)),
mean(soff_C4_GSM(:,3)),
'Marker','^','MarkerSize',15,'MarkerFaceColor','b
');
plot(0,0,
'Marker','o','MarkerSize',15,'MarkerFaceColor','g
');
hold off;

%%
%Plotting the position in GSE
figure(1)
plot(x_C1_gjsnitt, y_C1_gjsnitt,
'Marker','s','MarkerSize',15,'MarkerFaceColor','k
');
hold on;
plot([0 0],[0 0],'k');
title('The xy-plane');
xlabel('x-km');
ylabel('y-km');
ylim([-6500 6500])
xlim([-10000 1500])
plot(x_C2_gjsnitt, y_C2_gjsnitt,
'Marker','d','MarkerSize',15,'MarkerFaceColor','r
');
plot(x_C4_gjsnitt, y_C4_gjsnitt,
'Marker','^','MarkerSize',15,'MarkerFaceColor','b
');
plot(0,0,
'Marker','o','MarkerSize',15,'MarkerFaceColor','g
');
hold off;

figure(2)
plot(x_C1_gjsnitt, z_C1_gjsnitt,
'Marker','s','MarkerSize',15,'MarkerFaceColor','k
');
hold on; grid on;
title('The xz-plane');
xlabel('x-km');
ylabel('y-km');
plot(x_C2_gjsnitt, z_C2_gjsnitt,
'Marker','d','MarkerSize',15,'MarkerFaceColor','r
');
plot(x_C4_gjsnitt, z_C4_gjsnitt,
'Marker','^','MarkerSize',15,'MarkerFaceColor','b
');
plot(0,0,
'Marker','o','MarkerSize',15,'MarkerFaceColor','g
');
hold off;

figure(3)
plot(y_C1_gjsnitt, z_C1_gjsnitt,
'Marker','s','MarkerSize',15,'MarkerFaceColor','k
');
hold on; grid on;
title('The yz-plane')
xlabel('x-km');
ylabel('y-km');
plot(y_C2_gjsnitt, z_C2_gjsnitt,
'Marker','d','MarkerSize',15,'MarkerFaceColor','r
');
plot(y_C4_gjsnitt, z_C4_gjsnitt,
'Marker','^','MarkerSize',15,'MarkerFaceColor','b
');
plot(0,0,
'Marker','o','MarkerSize',15,'MarkerFaceColor','g
');
hold off;
```

solarwind.m

This program is used when plotting the solar wind data from OMNI web. The program plots the data from the 2001 and the 2005 event into the same plot. The x-axis is set to indicate the time interval prior to magnetic reconnection. In the program, the IMF clock angle is calculated as well as the epsilon parameter ϵ and the reconnection rate E_I.

```
%% Solar wind data from OMNI web
%data from 2005 event are named _269 and data
from the 2001 event are named
%_234
%%
clc;
clear;

Year_269 = 2005;
Month_269 = 09;
Day_269 = 26;

Year_234 = 2001;
Month_234 = 08;
Day_234 = 22;

%Defining the timeinterval which are studied
time_start_269 = datenum(Year_269, Month_269,
Day_269, 06, 00, 00);
time_end_269 = datenum(Year_269, Month_269,
Day_269, 09, 33, 00);

time_start_234 = datenum(Year_234, Month_234,
Day_234, 06, 00, 00);
time_end_234 = datenum(Year_234, Month_234,
Day_234, 09, 40, 00);


%loading data from OMNI
SW_269 = 'OMNI_269.txt';
```

```
SW_234 = 'omni_234.txt';

A = load(SW_269);
B = load(SW_234);

%Replasces fill values with NaN
invalidA=(A(:,15)==9999.99);A(invalidA,15)=NaN;
invalidB=(A(:,16)==9999.99);A(invalidB,16)=NaN;
invalidC=(A(:,17)==9999.99);A(invalidC,17)=NaN;
invalidD=(A(:,22)==99999.9);A(invalidD,22)=NaN;
invalidE=(A(:,26)==999.99);A(invalidE,26)=NaN;
invalidF=(A(:,27)==9999999.);A(invalidF,27)=NaN;
invalidG=(A(:,28)==99.99);A(invalidG,28)=NaN;
invalidH=(A(:,29)==999.99);A(invalidH,29)=NaN;
invalidI=(A(:,30)==999.99);A(invalidI,30)=NaN;

in-
validA_234=(B(:,15)==9999.99);B(invalidA_234,15)=
NaN;
in-
validB_234=(B(:,16)==9999.99);B(invalidB_234,16)=
NaN;
in-
validC_234=(B(:,17)==9999.99);B(invalidC_234,17)=
NaN;
in-
validD_234=(B(:,22)==99999.9);B(invalidD_234,22)=
NaN;
in-
validE_234=(B(:,26)==999.99);B(invalidE_234,26)=N
aN;
in-
validF_234=(B(:,27)==9999999.);B(invalidF_234,27)
=NaN;
in-
validG_234=(B(:,28)==99.99);B(invalidG_234,28)=Na
N;
in-
validH_234=(B(:,29)==999.99);B(invalidH_234,29)=N
aN;
in-
validI_234=(B(:,30)==999.99);B(invalidI_234,30)=N
aN;

%reading time data
h_269 = A(:,3);
min_269 = A(:,4);
sec_269 = A(:,38);

h_234 = B(:,3);
min_234 = B(:,4);
sec_234 = B(:,38);

%reading the physical parameters from the data-
fiels
bx_gse_269 = A(:,15); %nT
by_gse_269 = A(:,16); %nT
bz_gse_269 = A(:,17); %nT

bx_gse_234 = B(:,15); %nT
by_gse_234 = B(:,16); %nT
bz_gse_234 = B(:,17); %nT

vp_269 = A(:,22); %flow speed
np_269 = A(:,26); %proton density
tp_269 = A(:,27); %proton temerature
P_269 = A(:,28); %flow pressure (calculated in
the data file)
E_269 = A(:,29); %Eletric field (calculated in
the data file)
beta_269 = A(:,30); %plasma beta (calculated in
the data file)


vp_234 = B(:,22); %flow speed
np_234 = B(:,26); %proton density
tp_234 = B(:,27); %proton temperature
P_234 = B(:,28); %flow pressure (calculated in
the data file)
E_234 = B(:,29); %Eletric field (calculated in
the data file)
beta_234 = B(:,30); %plasma betha (calculated in
the data file)


% bx_gse_269 = NaN_inter(bx_gse_269);
% by_gse_269 = NaN_inter(by_gse_269);
% bz_gse_269 = NaN_inter(bz_gse_269);
% vp_269 = NaN_inter(vp_269);
% np_269 = NaN_inter(np_269);
%
% bx_gse_234 = NaN_inter(bx_gse_234);
% by_gse_234 = NaN_inter(by_gse_234);
% bz_gse_234 = NaN_inter(bz_gse_234);
% vp_234 = NaN_inter(vp_234);
% np_234 = NaN_inter(np_234);


%Creating the time array
T_269 = datenum(Year_269, Month_269, Day_269,
h_269, min_269, sec_269);
T_234 = datenum(Year_234, Month_234, Day_234,
h_234, min_234, sec_234);

%Adjusting the dataset into the selected timein-
terval
index_time_interval_269 = find(T_269 >=
time_start_269 & T_269 <= time_end_269);
T_269 = T_269(index_time_interval_269);
bx_gse_269 = bx_gse_269(index_time_interval_269);
by_gse_269 = by_gse_269(index_time_interval_269);
bz_gse_269 = bz_gse_269(index_time_interval_269);
np_269 = np_269(index_time_interval_269);
tp_269 = tp_269(index_time_interval_269);
vp_269 = vp_269(index_time_interval_269);
P_269 = P_269(index_time_interval_269);
E_269 = E_269(index_time_interval_269);
beta_269 = beta_269(index_time_interval_269);

%Adjusting the dataset into the selected timein-
terval
index_time_interval_234 = find(T_234 >=
time_start_234 & T_234 <= time_end_234);
T_234 = T_234(index_time_interval_234);
bx_gse_234 = bx_gse_234(index_time_interval_234);
by_gse_234 = by_gse_234(index_time_interval_234);
bz_gse_234 = bz_gse_234(index_time_interval_234);
np_234 = np_234(index_time_interval_234);
tp_234 = tp_234(index_time_interval_234);
vp_234 = vp_234(index_time_interval_234);
P_234 = P_234(index_time_interval_234);
E_234 = E_234(index_time_interval_234);
beta_234 = beta_234(index_time_interval_234);

%% calculating the energy input
%The epsilon parameter
IMF_clock = zeros(length(bx_gse_269),1);

% for i=1:length(testy),if
testz(i)>0,test_IMF_clock(i) =
atan((abs(testy(i)))/testz(i));else,test_IMF_cloc
k(i) = 180 - atan(abs(testy(i)/testz(i))); end,
end

for i=1:length(bz_gse_269)
    if bz_gse_269(i)>0
        IMF_clock(i) =
atan((abs(by_gse_269(i)))/bz_gse_269(i));
    else
        IMF_clock(i) = 3.1415 -
atan(abs(by_gse_269(i)/bz_gse_269(i)));
    end
end

%IMF_clock = atan(by_gse_269./bz_gse_269)
B =
sqrt(bx_gse_269.^2+by_gse_269.^2+bz_gse_269.^2);
epsilon_1 = (vp_269*1000).*(B*1e-9).^2;
epsilon_2 = (sin(IMF_clock/2)).^4;
epsilon_3 = (7*6370*1000)^2;
epsilon_269 = epsi-
lon_1.*epsilon_2.*epsilon_3*10^7;

IMF_clock_234= zeros(length(bx_gse_234),1);

for i=1:length(bz_gse_234)
    if bz_gse_234(i)>0
        IMF_clock_234(i) =
atan((abs(by_gse_234(i)))/bz_gse_234(i));
    else
        IMF_clock_234(i) = 3.1415 -
atan(abs(by_gse_234(i)/bz_gse_234(i)));
    end
end
```

```
IMF_clock_234 = atan(by_gse_234./bz_gse_234);

B_234 =
sqrt(bx_gse_234.^2+by_gse_234.^2+bz_gse_234.^2);
epsilon_1_234 = (vp_234*1000).*(B_234*1e-9).^2;
espilon_2_234 = (sin(IMF_clock_234/2)).^4;
epsilon_3_234 = (7*6370*1000)^2;
epsilon_234 = epsi-
lon_1_234.*espilon_2_234.*epsilon_3_234*10^7;

%the reconnection rate
for i=1:length(bz_gse_269)
    if bz_gse_269(i)<0
        E_269(i) =
abs(((vp_269(i))*1000)*((bz_gse_269(i))*1e-9)) ;
    else
        E_269(i) = 0;
    end
end

for i=1:length(bz_gse_234)
    if bz_gse_234(i)<0
        E_234(i) =
abs((vp_234(i)*1000)*(bz_gse_234(i)*1e-9));
    else
        E_234(i) = 0;
    end
end
%% plotting the solar wind data
subplot(2,1,2), plot(T_269, P_269,
'k','LineWidth', 2)
hourindatenums=datenum(2001,01,01,02,00,00)-
datenum(2001,01,01,01,00,00);
time_reconnection_269=datenum(2005,09,26,09,33,00
);
newxticks=fliplr(time_reconnection_269:-
hourindatenums:T_269(1));
set(gca,'xtick',newxticks);
newxticklabels=(1:length(newxticks))-
(length(newxticks));
set(gca,'xticklabel',newxticklabels)
minuteindatenums=datenum(2001,01,01,01,01,00)-
datenum(2001,01,01,01,00,00);
xlim([T_269(1)
T_269(length(T_269))+minuteindatenums]);
ylim([-0 8]);
ylabel('P, nPa', 'FontSize', 24);
hold on
time_reconnection_234=datenum(2001,08,22,09,40,00
);
plot(T_234+(time_reconnection_269-
time_reconnection_234),P_234,'r','LineWidth', 2)


figure(1)
subplot(3,1,1), plot(T_269, bx_gse_269,
'k',[T_269(1) T_269(length(T_269))],[0
0],'k','LineWidth', 2)
hourindatenums=datenum(2001,01,01,02,00,00)-
datenum(2001,01,01,01,00,00);
time_reconnection_269=datenum(2005,09,26,09,33,00
);
newxticks=fliplr(time_reconnection_269:-
hourindatenums:T_269(1));%rotates the axis in
order to display the hours from reconection
started
set(gca,'xtick',newxticks);
newxticklabels=(1:length(newxticks))-
(length(newxticks));%labeling the axes with the
hour intervals since reconnection
set(gca,'xticklabel',newxticklabels)
minuteindatenums=datenum(2001,01,01,01,01,00)-
datenum(2001,01,01,01,00,00);
xlim([T_269(1)
T_269(length(T_269))+minuteindatenums]);
ylim([-8 8]);
ylabel('Bx, nT', 'FontSize', 24);
hold on
time_reconnection_234=datenum(2001,08,22,09,40,00
);
plot(T_234+(time_reconnection_269-
time_reconnection_234),bx_gse_234,'r','LineWidth'
, 2)%adjusting the time in the 2001 event so it
fits into the timeinterval from the 2005 event

subplot(3,1,2), plot(T_269, by_gse_269,
'k',[T_269(1) T_269(length(T_269))],[0
0],'k','LineWidth', 2)
hourindatenums=datenum(2001,01,01,02,00,00)-
datenum(2001,01,01,01,00,00);
time_reconnection_269=datenum(2005,09,26,09,33,00
);
newxticks=fliplr(time_reconnection_269:-
hourindatenums:T_269(1));
set(gca,'xtick',newxticks);
newxticklabels=(1:length(newxticks))-
(length(newxticks));
set(gca,'xticklabel',newxticklabels)
minuteindatenums=datenum(2001,01,01,01,01,00)-
datenum(2001,01,01,01,00,00);
xlim([T_269(1)
T_269(length(T_269))+minuteindatenums]);
ylim([-8 8]);
ylabel('By, nT', 'FontSize', 24);
hold on
time_reconnection_234=datenum(2001,08,22,09,40,00
);
plot(T_234+(time_reconnection_269-
time_reconnection_234),by_gse_234,'r','LineWidth'
, 2)

subplot(3,1,3), plot(T_269, bz_gse_269,
'k',[T_269(1) T_269(length(T_269))],[0
0],'k','LineWidth', 2)
hourindatenums=datenum(2001,01,01,02,00,00)-
datenum(2001,01,01,01,00,00);
time_reconnection_269=datenum(2005,09,26,09,33,00
);
newxticks=fliplr(time_reconnection_269:-
hourindatenums:T_269(1));
set(gca,'xtick',newxticks);
newxticklabels=(1:length(newxticks))-
(length(newxticks));
set(gca,'xticklabel',newxticklabels)
minuteindatenums=datenum(2001,01,01,01,01,00)-
datenum(2001,01,01,01,00,00);
xlim([T_269(1)
T_269(length(T_269))+minuteindatenums]);
ylim([-8 8]);
ylabel('By, nT', 'FontSize', 24);
hold on
time_reconnection_234=datenum(2001,08,22,09,40,00
);
plot(T_234+(time_reconnection_269-
time_reconnection_234),bz_gse_234,'r','LineWidth'
, 2)

figure(2)

subplot(2,1,1), plot(T_269, vp_269,
'k','LineWidth', 2)
hourindatenums=datenum(2001,01,01,02,00,00)-
datenum(2001,01,01,01,00,00);
time_reconnection_269=datenum(2005,09,26,09,33,00
);
newxticks=fliplr(time_reconnection_269:-
hourindatenums:T_269(1));
set(gca,'xtick',newxticks);
newxticklabels=(1:length(newxticks))-
(length(newxticks));
set(gca,'xticklabel',newxticklabels)
minuteindatenums=datenum(2001,01,01,01,01,00)-
datenum(2001,01,01,01,00,00);
xlim([T_269(1)
T_269(length(T_269))+minuteindatenums]);
ylim([350 700]);
ylabel('Vp, km/s', 'FontSize', 24);
hold on
time_reconnection_234=datenum(2001,08,22,09,40,00
);
plot(T_234+(time_reconnection_269-
time_reconnection_234),vp_234,'r','LineWidth', 2)

subplot(2,1,2), plot(T_269, P_269,
'k','LineWidth', 2)
hourindatenums=datenum(2001,01,01,02,00,00)-
datenum(2001,01,01,01,00,00);
time_reconnection_269=datenum(2005,09,26,09,33,00
);
newxticks=fliplr(time_reconnection_269:-
hourindatenums:T_269(1));
```

```
set(gca,'xtick',newxticks);
newxticklabels=(1:length(newxticks))-
(length(newxticks));
set(gca,'xticklabel',newxticklabels)
minuteindatenums=datenum(2001,01,01,01,01,00)-
datenum(2001,01,01,01,00,00);
xlim([T_269(1)
T_269(length(T_269))+minuteindatenums]);
ylim([-0 8]);
ylabel('P, nPa', 'FontSize', 24);
hold on
time_reconnection_234=datenum(2001,08,22,09,40,00
);
plot(T_234+(time_reconnection_269-
time_reconnection_234),P_234,'r','LineWidth', 2)

figure(3)
subplot(2,1,1), plot(T_269, epsilon_269,
'k','LineWidth', 2)
hourindatenums=datenum(2001,01,01,02,00,00)-
datenum(2001,01,01,01,00,00);
time_reconnection_269=datenum(2005,09,26,09,33,00
);
newxticks=fliplr(time_reconnection_269:-
hourindatenums:T_269(1));
set(gca,'xtick',newxticks);
newxticklabels=(1:length(newxticks))-
(length(newxticks));
set(gca,'xticklabel',newxticklabels)
minuteindatenums=datenum(2001,01,01,01,01,00)-
datenum(2001,01,01,01,00,00);
xlim([T_269(1)
T_269(length(T_269))+minuteindatenums]);
% ylim([-0 8]);
ylabel('\epsilon , W', 'FontSize', 24);
hold on
time_reconnection_234=datenum(2001,08,22,09,40,00
);
plot(T_234+(time_reconnection_269-
time_reconnection_234),epsilon_234,'r','LineWidth
', 2)

subplot(2,1,2), plot(T_269, E_269*1000,
'k','LineWidth', 2)
hourindatenums=datenum(2001,01,01,02,00,00)-
datenum(2001,01,01,01,00,00);
time_reconnection_269=datenum(2005,09,26,09,33,00
);
newxticks=fliplr(time_reconnection_269:-
hourindatenums:T_269(1));
set(gca,'xtick',newxticks);
newxticklabels=(1:length(newxticks))-
(length(newxticks));
set(gca,'xticklabel',newxticklabels)
minuteindatenums=datenum(2001,01,01,01,01,00)-
datenum(2001,01,01,01,00,00);
xlim([T_269(1)
T_269(length(T_269))+minuteindatenums]);
ylim([-0.05 4]);
ylabel('E_I , mV/m', 'FontSize', 24);
hold on
time_reconnection_234=datenum(2001,08,22,09,40,00
);
plot(T_234+(time_reconnection_269-
time_reconnection_234),
E_234*1000,'r','LineWidth', 2)
```

AE_index.m

The program is used when plotting the AE-index. The program does not use a .txt file with data, but the data are loaded into the program as arrays. This program contains data from the 2005 event from 04.00 UT until 23.59 UT. The 2001 program contains the data from the 2001 AE-index obtained from the WDC Geomagnetism, Kyoto.

```
%% AE-index
clc;
clear;

%The data from the Kyoto Geocenter from 04.00 UT
to 23.59 UT
AE_04 = [265   308   333   344   345   337   326
309   298   322   325   317   300   275   232
226   230   224   208   199   186   175   173
169   170   177   190   187   181   171   169
171   166   159   158   172   196   209   211
212   221   214   226   253   246   250   240
222   222   225   225   214   210   232   240
222   210   189   220   220   230];
AE_05 = [174   168   214   240   218   134   101
134   158   136   127   128   123   118   120
135   136   151   145   127   111   113   115
111   142   127   144   123    99   110   127
150   140   132   150   145   141   131   117
114   109    97    85    78    84    91    92
93    94    94    91    92    82    74    76
71    62    57    52    48   119];
AE_06 = [62    89    91    84    95    95    87
91    94    71    79    89    98    87    83
84    68    64    65    75    67    55    56
54    60    61    61    59    57    53    50
50    56    53    46    45    45    48    48
47    47    47    48    51    53    52    43
41    37    38    40    45    52    60    71
73    56    40    62    94    63];
AE_07 = [76    75    84    86    76    58    65
52    53    50    74    60    61    73    86
75    60    55    49    53    59    59    68
72    67    61    58    57    50    46    60
73    71    64    66    61    52    49    53
55    65    86    90    85    81    75    75
78    73    67    64    62    63    63    60
62    59    65    68    63    65];
AE_08 = [63    64    68    69    64    56    58
58    68    62    61    61    64    65    51
50    53    54    65    72    70    88    85
72    63    61    66    66    65    59    57
55    61    76    79    82    82    66    63
63    75    75    75    76    76    58    40
51    57    88    94   103    82    61    68
91    91   113   110    90    70];
AE_09 = [84    81    65    77    89    83    80
100    95   135   130   138   177   167   102
83    69    88    78    84   110    98    83
88    86    91   100    99    94    91    92
95    94    93    95   101   106   108    98
88    82    78   121   126   198   230   228
251   256   262   259   248   224   213   193
191   192   172   113    97   127];
AE_10 = [94    95    94   104   137   153   167
167   183   193   191   168   163   160   168
170   160   142   125   122   125   124   119
124   123   124   127   126   128   135   135
126   119   121   128   133   135   129   119
118   118   117   118   121   124   129   130
130   133   131   129   126   124   129   137
138   150   155   173   204   137];
AE_11 = [238   243   221   214   231   206   216
210   237   287   312   279   275   271   249
249   273   328   335   305   248   222   267
281   275   295   303   322   378   427   505
405   375   305   302   303   298   318   365
396   403   416   447   473   486   485   480
482   472   462   506   526   514   508   506
495   478   464   450   437   354];
AE_12 = [445   445   439   420   388   389   409
406   397   430   492   533   519   486   489
488   449   431   447   458   466   492   534
552   511   476   479   453   433   432   415
410   396   374   378   400   420   437   424
394   380   358   363   376   365   346   347
```

```
343   324   321   315   296   289   269   275
290   287   303   307   284   405];
AE_13 = [271   256   275   300   307   316   312
295   288   292   288   270   262   244   227
221   202   190   185   170   149   143   141
155   178   201   201   194   197   204   227
252   277   293   302   304   312   313   303
293   298   309   318   320   323   323   313
299   287   274   269   272   269   260   260
252   247   242   233   229   257];
AE_14 = [226   214   216   200   192   191   184
182   173   150   150   153   144   147   157
182   199   202   195   184   169   153   151
136   117   134   150   148   154   153   126
115   113   139   125   115   114   128   123
130   180   165   158   186   162   117   145
124   117   148   175   128   128   144   164
135   140   154   142   147   155];
AE_15 = [167   188   158   142   135   135   133
143   131   127   127   124   126   123   114
117   118   121   113   109    99    92    98
92   109   116   111    89    83    86    85
89   100   107   108   116   115   111   123
131   124   114   116   124   146   156   152
142   137   131   132   123   123   124   123
132   138   128   118   115   122];
AE_16 = [110   103   102    98    98   103   105
102    98    96   100   108   113   114   109
102    91    85    82    79    84    88    95
102   108   118   132   154   144   125   122
123   129   128   122   125   130   124   125
129   133   136   142   164   165   179   222
230   228   223   195   206   194   179   184
198   210   208   208   196   137];
AE_17 = [218   239   220   223   216   201   188
186   190   195   197   194   193   201   201
211   216   214   219   229   239   250   249
243   259   270   261   257   283   280   311
296   260   265   248   251   259   260   243
259   273   287   285   291   288   301   342
380   378   346   313   289   260   238   230
238   240   248   270   313   253];
AE_18 = [348   380   380   340   335   312   284
275   283   291   276   260   257   268   245
206   180   183   184   177   180   195   209
219   221   232   231   228   223   221   236
243   236   224   230   232   224   232   240
248   239   235   250   258   270   282   298
295   295   283   262   239   222   213   215
216   218   222   219   213   249];
AE_19 = [208   207   208   208   211   222   222
222   219   221   222   218   226   238   262
268   264   264   272   283   297   294   303
311   392   413   459   468   463   471   487
478   473   464   454   470   412   401   516
586   673   722   730   713   707   657   637
613   616   552   510   512   501   507   461
447   557   566   520   476   416];
AE_20 = [493   500   529   544   550   557   567
561   574   587   588   572   561   576   599
611   605   610   611   606   610   584   564
567   568   576   556   575   554   541   522
507   474   439   395   350   318   307   314
318   323   316   320   329   337   345   344
344   342   338   344   338   331   325   331
332   334   333   334   344   462];
AE_21 = [335   330   332   338   351   378   371
436   425   405   462   468   479   499   519
507   475   454   453   462   449   408   400
389   413   433   478   507   522   555   566
574   572   571   610   634   624   641   662
692   760   795   811   821   820   804   773
756   705   635   593   585   571   522   471
487   541   536   493   468   535];
AE_22 = [456   439   429   408   387   354   337
330   336   320   328   316   307   300   287
283   284   277   257   250   256   258   265
258   248   250   251   241   235   220   190
179   194   206   186   171   162   165   161
145   151   156   156   157   155   152   154
149   138   122   130   145   143   123   118
122   135   131   112    98   228];
AE_23 = [93    88    77    75    76    82    90
96    92    84    82    88    92    99    99
103    97    81    72    74    71    64    59
52    49    46    57    62    51    70   107
132    84    81   127    83   107   128    90
89    57    66   120   134   107    70   177
157   165   124    54    63    65    60    88
64    59    59    69    77    86];
AE_time = (240:1380)';
AE_data = [AE_04 AE_05 AE_06 AE_07 AE_08 AE_09
AE_10 AE_11 AE_12 AE_13 AE_14 AE_15 AE_16 AE_17
AE_18 AE_19 AE_20 AE_21 AE_22 AE_23]';

time_start_h = 04;
time_start_m = 00;

time_end_h = 23;
time_end_m = 59;

%transform start and end time into minutes
start_min = time_start_h*60 + time_start_m;
end_min = time_end_h*60 + time_end_m;

%adjusting the datasets according to the given
time interval
index_time_interval = find(AE_time >= start_min &
AE_time <= end_min);
AE_time = AE_time(index_time_interval);
length(AE_time);
AE_data = AE_data(index_time_interval);
length(AE_data);
time_sec = zeros(size(AE_time));

%transforming the time in order to use datetick
function
hour_AE = floor(AE_time/60);
minute_AE = floor((AE_time-60.*hour_AE));
time_array_AE = [0*(1:length(hour_AE))'
0*(1:length(hour_AE))' 0*(1:length(hour_AE))'
hour_AE minute_AE time_sec];
newAE_min= datenum(time_array_AE);

figure(1)
plot(newAE_min, AE_data, 'LineWidth', 1.5)
ylabel('AE-index, nT', 'FontSize', 14);
datetick('x',15);
xlabel('Time, UT', 'FontSize', 14);
set(gca, 'xLim', [newAE_min(1) ne-
wAE_min(length(newAE_min))])
```

Pi2_pulse.m

The program Pi2_pulse.m loads and plots the data from the CPMN network. The time in the data arrays in the .txt file are originally in seconds. The program transforms the time series into the format HH:MM:SS.

```
%% Pi2_pulse

%%
%Code for recognizing a Pi2 event at the Asian
coast from Russia to
%Australia
clc;
clear;

%loading the date
Year = 2005;
Month = 09;
Day = 26;

%difining the starting time
time_start_h = 09;
```

```
time_start_m = 40;
time_start_s = 00;
%defining the stop time
time_end_h = 09;
time_end_m = 45;
time_end_s = 00;

%changes the time array from seconds to hour,
minute and second
start_sec = time_start_h*3600 + time_start_m*60 +
time_start_s;
end_sec = time_end_h*3600 + time_end_m*60 +
time_end_s;


%Loading the magnetic field data from heighest
latitude to the lowest
%latitude magnetic stations in the northern hemi-
sphere
stationNames_high = {'MGD' 'RIK' 'KAG'};%stations
above 50 lat

for i=1:length(stationNames_high), file-
Names_high{i}=[stationNames_high{i} '.txt']; end
loadedData_high = cell(1,length(fileNames_high));
for i=1:length(fileNames_high), loaded-
Data_high{i}={load(fileNames_high{i})}; end

%Filtering and plotting the H components of the
magnetic field data from
%teh stations
for i=1:(length(fileNames_high))

    file_high = loadedData_high{i}; fileCont_high
= file_high{1};
    time_high = fileCont_high(:,1); H_high =
fileCont_high(:,2); D_high = fileCont_high(:,3);
Z_high = fileCont_high(:,4);


    index_time_interval = find(time_high >=
start_sec & time_high <= end_sec);

    time_high = time_high(index_time_interval);
    H_high = H_high(index_time_interval);
    D_high = D_high(index_time_interval);
    Z_high = Z_high(index_time_interval);

    %transforms the timearray into a readable
format
    hour_high=floor(time_high/3600);
    minute_high=floor((time_high-
3600.*hour_high)/60);
    second_high=floor(time_high-3600.*hour_high-
60.*minute_high);
    time_array_high = [0*(1:length(hour_high))'
0*(1:length(hour_high))' 0*(1:length(hour_high))'
hour_high minute_high second_high];
    newTime_high=datenum(time_array_high);

    figure(1);
    sub-
plot(length(fileNames_high),1,i),plot(newTime_hig
h, H_high),ylabel(stationNames_high{i},
'Linewidth', 2, 'FontSize', 14)
    xlim([newTime_high(1) new-
Time_high(length(newTime_high))])
    datetick('x', 13)
    xlabel('Time UT')


%     figure(2);
%     sub-
plot(length(fileNames_high),1,i),plot(newTime_hig
h, D_high),ylabel(stationNames_high{i})
%     title('Magnetic D-component');
%     datetick('x',13);
%
%     figure(3);
%     sub-
plot(length(fileNames_high),1,i),plot(newTime_hig
h, Z_high),ylabel(stationNames_high{i})
%     title('Magnetic Z-component');
%     datetick('x',13);
%

end
```